Compressible turbulent convection at extreme Rayleigh numbers

A thesis submitted

in partial fulfillment of the requirements

for the degree of

Doctor of Philosophy

by

Harshit Tiwari

Roll No.: 21109866

to the

DEPARTMENT OF PHYSICS

INDIAN INSTITUTE OF TECHNOLOGY KANPUR

February, 2026

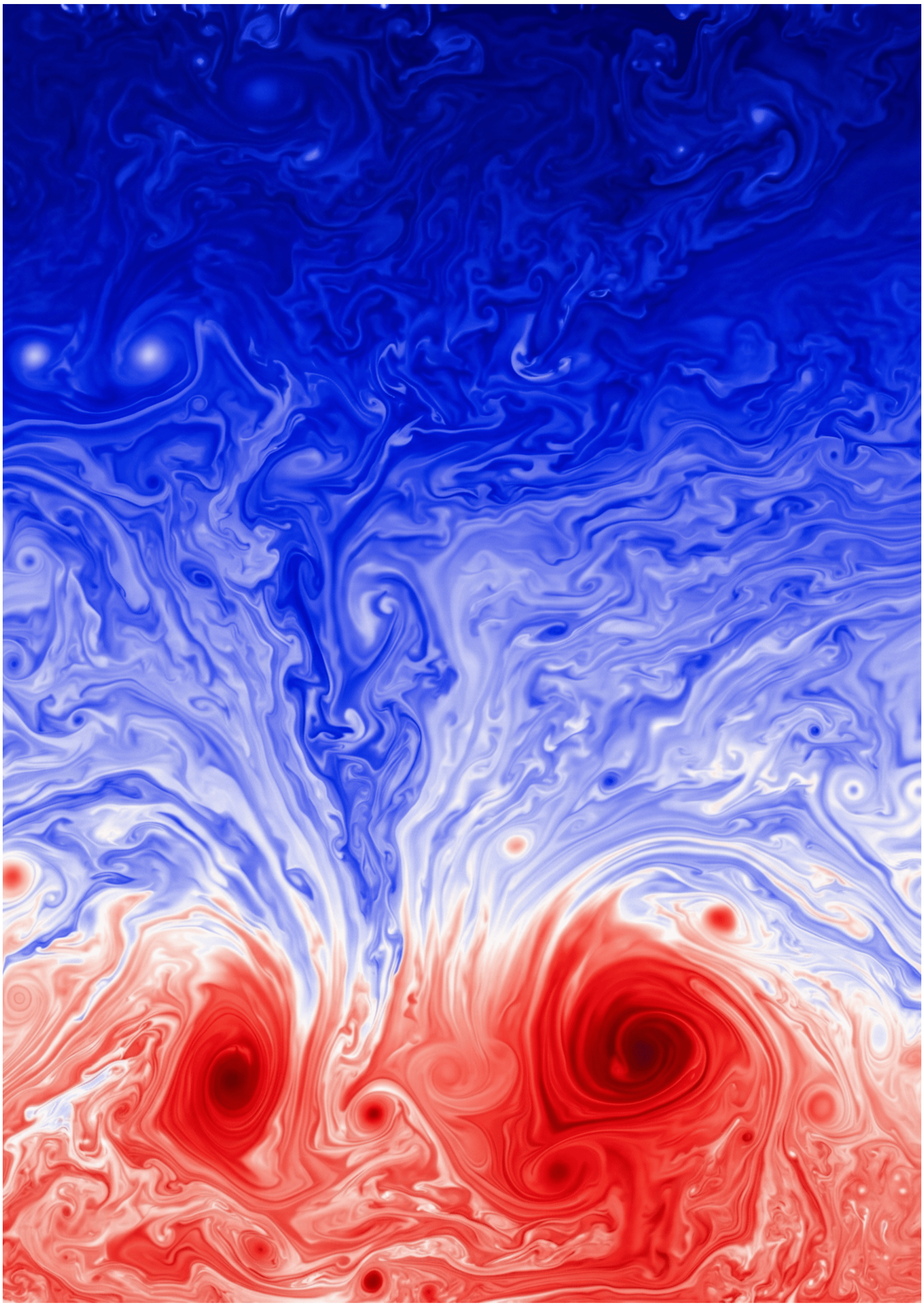

Hot and cold plumes in compressible convection

Certificate

It is certified that the work contained in this thesis entitled **"Compressible turbulent convection at extreme Rayleigh numbers"** by **Harshit Tiwari** has been carried out under my supervision and that it has not been submitted elsewhere for a degree.

Rajesh Ranjan

Prof. Mahendra K. Verma
(Thesis supervisor)
Department of Physics
Indian Institute of Technology Kanpur
Kanpur - 208016, India

Prof. Rajesh Ranjan
(Thesis co-supervisor)
Department of Aerospace Engineering
Indian Institute of Technology Kanpur
Kanpur - 208016, India

February, 2026

Declaration

This is to certify that the thesis titled **"Compressible turbulent convection at extreme Rayleigh numbers"** has been authored by me. It presents the research conducted by me under the supervision of **Prof. Mahendra K. Verma** and **Prof. Rajesh Ranjan**.

To the best of my knowledge, it is an original work, both in terms of research content and narrative, and has not been submitted elsewhere, in part or in full, for a degree. Further, due credit has been attributed to the relevant state-of-the-art and collaborations with appropriate citations and acknowledgments, in line with established norms and practices.

Harshit Tiwari.

Harshit Tiwari

Programme: PhD
Roll No.: 21109866
Department: Physics
Indian Institute of Technology Kanpur

Kanpur 208016

Synopsis

Name of the student: **Harshit Tiwari**

Roll No.: **21109866**

Degree for which submitted: **Doctor of Philosophy**

Department: **Department of Physics**

Thesis title: **Compressible turbulent convection at extreme Rayleigh numbers**

Thesis supervisor: **Prof. Mahendra K. Verma** and **Prof. Rajesh Ranjan**

Month and year of thesis submission: **February, 2026**

Thermal convection drives heat transport across a wide range of natural and engineered flows. Quantifying heat transport in turbulent convection remains a fundamental challenge, centered on the relationship between two dimensionless parameters: the Rayleigh number (Ra), which measures the strength of the buoyancy, and the Nusselt number (Nu), which represents the efficiency of convective heat transport. Two competing models predict the scaling of heat transport: the *classical* scaling ($\mathrm{Nu} \propto \mathrm{Ra}^{1/3}$) [1–3], governed by boundary layers in a state of marginal stability, and the *ultimate-regime* scaling ($\mathrm{Nu} \propto \mathrm{Ra}^{1/2}$) [4], which is expected to emerge when the boundary layers become fully turbulent. While some experiments and simulations report that the Nusselt number transitions from the near-classical scaling, $\mathrm{Ra}^{0.30}$, toward a larger power law near $\mathrm{Ra} \approx 10^{14}$ [5–7], others find that the near-classical scaling persists even at larger Rayleigh numbers [8–10].

[1] Malkus, W. V. R., *Proc. R. Soc. London A* **225**, 196 (1954).
[2] Priestley, C. H. B., *Aust. J. Phys.* **7**, 176 (1954).
[3] Howard, L. N., *Proc. 11th Int. Congr. Appl. Mech.*, Munich, 1109 (1966).
[4] Kraichnan, R. H., *Phys. Fluids* **5**, 1374 (1962).
[5] Chavanne, X., Chillà, F., Castaing, B., Hebral, B., Chabaud, B., and Chaussy, J., *Phys. Rev. Lett.* **79**, 3648 (1997).
[6] He, X., Funfschilling, D., Nobach, H., Bodenschatz, E., and Ahlers, G., *Phys. Rev. Lett.* **108**, 024502 (2012).
[7] Zhu, X., Mathai, V., Verzicco, R., and Lohse, D., *Phys. Rev. Lett.* **120**, 144502 (2018).
[8] Castaing, B., Gunaratne, G., Heslot, F., Kadanoff, L., Libchaber, A., Thomae, S., Wu, X. Z., Zaleski, S., and Zanetti, G., *J. Fluid Mech.* **204**, 1 (1989).
[9] Niemela, J. J., Skrbek, L., Sreenivasan, K. R., and Donnelly, R. J., *Nature* **404**, 837 (2000).
[10] Iyer, K. P., Scheel, J. D., Schumacher, J., and Sreenivasan, K. R., *Proc. Natl. Acad. Sci. U.S.A.* **117**, 7528 (2020).

Most studies in the literature have focused on *Rayleigh-Bénard convection* (RBC) under the Oberbeck-Boussinesq (OB) approximation, which assumes that density is constant everywhere except for buoyancy [11–13]. However, many astrophysical and geophysical flows exhibit significant density stratification and are *compressible* [14–16]. In this thesis, we investigate turbulent compressible convection using high-resolution direct numerical simulations (DNS). In contrast to the constant bulk temperature of RBC, the bulk temperature in compressible convection decreases adiabatically with height even at high Ra. We show that up to $\mathrm{Ra} = 10^{16}$ in two dimensions (2D) and $\mathrm{Ra} = 10^{13}$ in three dimensions (3D), heat transport in compressible convection follows the near-classical scaling ($\mathrm{Nu} \sim \mathrm{Ra}^{0.30}$).

To explain the persistence of the near-classical scaling in compressible convection and RBC, we decompose the vertical heat flux into positive and negative components. Normally, hot plumes rise and cold plumes sink, resulting in a positive heat flux. However, we show that deflection from the walls and turbulent mixing cause heat to move against buoyancy, generating negative heat flux. The positive and negative heat fluxes are nearly equal in magnitude. However, in the distribution function, the positive heat fluxes have longer tails than the negative ones, and the differences between the positive and negative heat fluxes scale as $\mathrm{Ra}^{-0.20}$, which leads to $\mathrm{Nu} \sim \mathrm{Ra}^{0.30}$. The robust and universal properties described above, even in the presence of a logarithmic layer in compressible convection, indicate the likely absence of the ultimate regime in turbulent thermal convection. In contrast, periodic convection (without walls), which is related to the ultimate regime, exhibits a predominantly positive heat flux [17, 18].

A brief outline of the thesis is as follows.

In Chapter 1, we introduce the governing equations of fully compressible convection along with the non-dimensional parameters. We derive the hydrostatic equilibrium profiles and detail the onset of instability in compressible convection, governed by the *Schwarzschild criterion* [19], which requires the vertical temperature gradient to exceed the adiabatic temperature gradient. We also provide a literature review of the scaling laws for the heat and momentum transport in turbulent convection.

[11] Ahlers, G., Grossmann, S., and Lohse, D., *Rev. Mod. Phys.* **81**, 503 (2009).
[12] Chillà, F. and Schumacher, J., *Eur. Phys. J. E* **35**, 58 (2012).
[13] Verma, M. K., *Physics of Buoyant Flows: From Instabilities to Turbulence* (World Scientific, Singapore, 2018).
[14] Spiegel, E. A. and Veronis, G., *Astrophys. J.* **131**, 442 (1960).
[15] Hansen, C. J., Kawaler, S. D., and Trimble, V., *Stellar Interiors* (Springer, New York, 2004).
[16] Schumacher, J. and Sreenivasan, K. R., *Rev. Mod. Phys.* **92**, 041001 (2020).
[17] Lohse, D. and Toschi, F., *Phys. Rev. Lett.* **90**, 034502 (2003).
[18] Verma, M. K., Mishra, P. K., Pandey, A., and Paul, S., *Phys. Rev. E* **85**, 016310 (2012).
[19] Schwarzschild, K., *Nachr. Ges. Wiss. Göttingen, Math.-Phys. Kl.* **1906**, 41 (1906).

In Chapter 2, we discuss the numerical formulation and software architecture of the solver DHARA, which was developed to perform simulations reported in this thesis. We describe the MacCormack-TVD (total variation diminishing) scheme employed to handle compressible flows. We detail the Python-based design utilizing the `CuPy` library for GPU acceleration, which ensures portability across heterogeneous architectures, including NVIDIA and AMD GPUs. We describe the code's performance, highlighting super-linear scaling on CPUs in Shaheen III (KAUST) and sub-linear scaling on GPUs in Frontier (OLCF) and Polaris (ALCF). Additionally, we validate the solver against established benchmarks for compressible convection and turbulence. Beyond the primary focus of this work, DHARA has been instrumental in investigating the Prandtl number dependence in compressible convection [20, 21] and analyzing scale-by-scale energy transfers in compressible turbulence [22].

In Chapter 3, we present results from numerical simulations of compressible convection in a box of aspect ratio $\Gamma = 4$, reaching $\mathrm{Ra} = 10^{15}$ in 2D and 10^{11} in 3D. We show that the Nusselt number $\mathrm{Nu} \propto \mathrm{Ra}^{0.30}$ (near-classical scaling) that differs strongly from the ultimate-regime scaling, which is $\mathrm{Nu} \propto \mathrm{Ra}^{1/2}$. The bulk temperature drops adiabatically along the vertical even for high Ra, which is in contrast to the constant bulk temperature in RBC. Unlike RBC, the density decreases with height. Additionally, the vertical pressure-gradient ($-dp/dz$) nearly matches the buoyancy term (ρg). But, the difference, $-dp/dz - \rho g$, is equal to the nonlinear term that leads to Reynolds number $\mathrm{Re} \propto \mathrm{Ra}^{1/2}$.

In Chapter 4, we perform a comparative study of Rayleigh-Bénard, compressible, and periodic convection in two and three dimensions. We compare our DNS of compressible convection and periodic convection with high-fidelity RBC datasets [23–25]. We show that up to $\mathrm{Ra} = 10^{16}$ in 2D and up to $\mathrm{Ra} = 10^{13}$ in 3D, the positive and negative heat fluxes in RBC and compressible convection are nearly equal in magnitude. However, in the distribution function, the positive fluxes have longer tails than the negative ones. Furthermore, the positive heat flux decreases faster than the negative heat flux with increasing Ra, resulting in the difference between them scaling as $\mathrm{Ra}^{-0.20}$, leading to $\mathrm{Nu} \sim \mathrm{Ra}^{0.30}$. The imbalance of positive and negative heat fluxes remains robust even in the presence of logarithmic boundary layers in compressible convection, suggesting that the ultimate regime is likely absent in standard RBC and compressible convection. Finally, we show

[20] Sharma, L., Pathak, M., Tiwari, H., and Verma, M. K., *Phys. Rev. Fluids* **10**, 114611 (2025).
[21] Pathak, M., Sharma, L., Tiwari, H., and Verma, M. K., *CTR Annu. Res. Briefs*, 263-274 (2025).
[22] Singh, D., Tiwari, H., Sharma, L., and Verma, M. K., *Phys. Rev. Fluids* **10**, 114609 (2025).
[23] Samuel, S., Bhattacharya, S., and Verma, M. K., *Phys. Rev. Fluids* **9**, 013501 (2024).
[24] Samuel, S., *Ph.D. thesis*, Indian Institute of Technology Kanpur (2024).
[25] Bhattacharya, S., Samuel, S., and Verma, M. K., *Phys. Rev. Fluids* **6**, 073501 (2021).

that in the absence of walls, periodic convection exhibits a predominantly positive heat flux and follows the ultimate regime scaling.

In Chapter 5, addressing the need for robust shock capturing and low dissipation in compressible turbulence simulations, we extend the capabilities of DHARA by integrating a general-purpose high-order finite volume module. We implement the Riemann-solver-free semi-discrete scheme of Kurganov and Tadmor [26] combined with weighted and targeted essentially non-oscillatory (WENO/TENO) reconstructions [27–29]. Leveraging the Python-CuPy framework for high GPU throughput, we evaluate these schemes against canonical benchmarks, including the isentropic vortex, Kelvin-Helmholtz instability, and the supersonic Taylor-Green vortex. We demonstrate that TENO schemes significantly minimize numerical dissipation and better resolve small-scale structures compared to traditional WENO-based formulations. Finally, we present high-resolution DNS of supersonic turbulence (turbulent Mach number, $M_t = 3.0$) using the seventh-order TENO scheme, demonstrating the solver's capability to resolve complex shock structures and establishing a framework for future studies on inter-scale energy transfers.

In Chapter 6, we present the conclusions drawn from the thesis. We also outline the scope for future work building upon the findings of this study.

[26] Kurganov, A. and Tadmor, E., *J. Comput. Phys.* **160**, 241 (2000).
[27] Jiang, G. S. and Shu, C. W., *J. Comput. Phys.* **126**, 202 (1996).
[28] Borges, R., Carmona, M., Costa, B., and Don, W. S., *J. Comput. Phys.* **227**, 3191 (2008).
[29] Fu, L., Hu, X. Y., and Adams, N. A., *J. Comput. Phys.* **305**, 333 (2016).

Acknowledgements

"Beauty will save the world."

– Fyodor Dostoevsky, *The Idiot*

My journey at IIT Kanpur began in 2019 as a Master's student. When the chance to pursue a PhD arose, I initially wavered, unsure if this path was truly for me. However, the enforced quietude of the COVID-19 lockdowns proved to be a turning point; the solitude granted me the space to resolve my doubts and commit sincerely to the pursuit of science. Reflecting on this, I realize how pivotal IIT Kanpur has been in that transformation. Beyond its academic infrastructure, the institute provided a nurturing ecosystem that challenges and inspires in equal measure. I am profoundly grateful to this community, which has served as both the bedrock of my research and a cherished home for my personal growth.

I owe my deepest thanks to my supervisor, Prof. Mahendra K. Verma, for his unwavering guidance and support throughout my doctoral journey. I have rarely met someone with such tireless energy and absolute dedication to research. He has been incredibly approachable and supportive; our regular meetings were instrumental in shaping my understanding of physics, and he always pushed me to tackle fundamental, challenging problems rather than settling for easy answers. His ability to maintain enthusiasm even during the most challenging phases of research has been truly inspiring to witness, and I feel fortunate to have trained under him. I also extend my sincere thanks to my co-supervisor, Prof. Rajesh Ranjan, whose insight and friendly counsel have been a constant source of encouragement. His passion for his work is contagious and has motivated me significantly. I cherish the bond I have formed with both of them, and I sincerely hope to maintain this collaborative spirit and remain in close contact with them in the years to come.

I am also indebted to Prof. Katepalli R. Sreenivasan, whose profound contributions to fluid dynamics form the foundation of much of this thesis. He has been supportive of our work from the very beginning, and I cherish the opportunity to interact with him personally. I am incredibly grateful for his generous hospitality during my visit to New York University in November; the time spent in his company was inspiring, and our discussions have left a lasting impression on me. My journey has been further enriched by the motivating support of Prof. David Keyes; his thoughtful correspondence and respectful guidance have meant a lot to me. I also thank Dr. Samar Aseeri, a wonderful mentor from whom I have gained invaluable insights.

I extend my sincere thanks to Prof. Shashwat Bhattacharya, whom I visited last summer; he has been supportive throughout my research. My thanks also go to Prof. Ambrish Pandey for his constant positivity, and to Prof. S. Ravichandran, who has been a friendly mentor. I am also thankful to Prof. Sarosh Alam Ghausi for his consistent support. Finally, I would like to express my gratitude to Prof. Jörg Schumacher and Prof. Sanjeeva Lele for their insightful suggestions that have greatly enriched this work.

A large part of this thesis is based on high-fidelity direct numerical simulations, which would not have been possible without access to world-class supercomputing facilities. I am deeply grateful for the generous computational time provided by the Argonne Leadership Computing Facility (ALCF), the Oak Ridge Leadership Computing Facility (OLCF), and the King Abdullah University of Science and Technology (KAUST). I also acknowledge the Param Sanganak facility at IIT Kanpur, where the initial simulations were conducted, as well as the resources provided by the Kotak School of Sustainability (KSS).

The development of the DHARA solver relied heavily on the in-house GPU laboratory established by my supervisors, which served as the essential testing ground for debugging and validation. The code's performance was significantly enhanced during the Frontier Hackathon in March 2024. I extend my sincere thanks to Dr. Gina Sitaraman, Dr. Mark J. Stock, and Dr. Michael Sandoval for their expert guidance on optimization. A special note of gratitude goes to Samar and Gina for their extensive help with code profiling, which was instrumental in ensuring the smooth execution of our large-scale simulations.

Building this solver was a collective feat, and I am indebted to the team that helped us achieve it. I specifically thank Manthan Verma for his initial guidance in getting me started with coding and setting up the computational environments; his early inputs were vital. I also acknowledge the significant contributions of Shashwat Nirgudkar, Abhay Kumar, Siddharth Rana, and Akash Rodhiya, who helped with the code structure and optimization. I must also mention the technical contributions of Dhananjay Singh, who built several key modules that are now integral to the code.

My daily life in the lab has been enriched by a wonderful group of colleagues who became close friends. I extend my heartfelt gratitude to Dr. Lekha Sharma, who joined our group as a postdoctoral fellow. We collaborated on numerous projects, and her profound sincerity and commitment to research played a pivotal role in giving shape to this thesis. I am equally grateful to my labmates Dhananjay Singh, Abhishek Jha, Sachin Rawat, and Mayank Pathak, who have been not just brilliant colleagues but great friends. My long discussions with Dhananjay were crucial for both my work and personal clarity, while Abhishek's friendship and constant readiness to help made the daily challenges of research much lighter. I also cherish the support and camaraderie shared with Sachin and Mayank, whose presence contributed significantly to the positive atmosphere in our group.

I was fortunate to be guided by supportive seniors—Roshan Samuel, Shadab Alam, Mohammad Anas, Soumyadeep Chatterjee, and Manohar Sharma—who patiently helped me grasp the fundamentals of turbulence and HPC during my early days. A special thanks to Roshan, whose deep expertise in thermal convection and our continued discussions significantly influenced the physical insights presented in this thesis. Finally, I express my sincere gratitude to Mr. Manmohan Dewbanshi for his dedication in keeping our lab running seamlessly. He is always willing to help, whether with administrative paperwork or daily operations, and his reliability has been a great asset to our group.

Beyond the academic grind, the Adventure Sports Club at IIT Kanpur became a vital source of balance and joy in my life. The early morning conditioning sessions and the treks we undertook together were the true highlights of my time here, offering a much-needed escape from the rigors of research. I am grateful to this vibrant community for prioritizing health, adventure, and personal growth. A special shout-out to my trekking companions and friends—Vivek, Saumya, Krushna (KP), Kushal, Chidanand, Poonam Di, Utsav, Subhrajyoti, Neetu Di, Neelakshi Di, Mridusmita, and many others. Their energy and friendship turned every expedition into a cherished memory. These shared experiences kept my spirits high and helped me navigate the highs and lows of the PhD journey with a clearer mind.

Life in the Hall of Residence VII was made memorable by a fantastic group of friends who made the campus feel like home. I extend my thanks to Vaibhav Sharma, Pranay Mohta, Ojasvi Rajput, Satyam Kumar, Dushyanth Kumar Reddy G, and Ratnesh Kushwaha; our time together provided the laughter and relaxation that one inevitably needs after a long day at work. I also wish to thank Akash for his exceptional hospitality and care during my visit to New York. I am also grateful to the mess and sanitation workers of the Hall. Their friendly faces, hard work, and behind-the-scenes support made my daily life comfortable, and I appreciate the warmth they showed me throughout my stay.

I would not be where I am today without the unconditional love and sacrifices of my family. My sister, Preeti, has been my constant cheerleader, always believing in me even when I doubted myself; I wouldn't be here without her support. I owe everything to my parents, whose silent resilience and hard work laid the foundation for my dreams. I am especially grateful to my mother, who has always been my greatest source of strength. She took immense pride in my goals and consistently taught me to aim higher, never letting me settle for less than my potential. Her belief in me has been the driving force behind every success I have achieved.

Finally, I reserve my deepest gratitude for my fiancée, Disha. This journey would have been infinitely more difficult without her by my side. She has been my emotional anchor, keeping me motivated during the toughest days and celebrating every small victory with me. Her patience and unwavering belief in my abilities gave me the strength to keep pushing forward. I also extend my sincere thanks to my future in-laws, whose warmth and support have made me feel truly welcome in their family. I look forward to the life we will build together.

February, 2026 Harshit Tiwari

Dedicated to my parents.

List of publications

Published:

1. **Tiwari, H.**, Sharma, L., and Verma, M. K.*, "On the absence of the ultimate regime in turbulent thermal convection", *Proc. Natl. Acad. Sci. U.S.A.* 122 (44) e2513474122 (2025).

2. **Tiwari, H.**, Sharma, L., and Verma, M. K.*, "Compressible turbulent convection at very high Rayleigh numbers", *Int. J. Heat Mass Transfer* 242, 126821 (2025).

3. Singh, D., **Tiwari, H.**, Sharma, L., and Verma, M. K.*, "Mathematical formulation of mode-to-mode energy transfers and energy fluxes in compressible turbulence", *Phys. Rev. Fluids* 10, 114609 (2025).

4. Sharma, L.*, Pathak, M., **Tiwari, H.**, and Verma, M. K., "Prandtl number dependence in turbulent compressible convection", *Phys. Rev. Fluids* 10, 114611 (2025).

5. Pathak, M., Sharma, L., **Tiwari, H.**, and Verma, M. K.*, "Variation of convective heat flux imbalance with Prandtl number", *CTR Annu. Res. Briefs* (2025).

6. Singh, D., **Tiwari, H.***, Sharma, L., and Verma, M. K., "Scale-by-scale energy transfers and fluxes in compressible turbulence", *Europhys. Lett.* 154, 53001 (2026).

Under review:

1. **Tiwari, H.**, Singh, D., Verma, M. K., and Ranjan, R.*, "Scaling in supersonic turbulence: Energy spectra and fluxes using high-fidelity direct numerical simulations", *Phys. Rev. E.*

2. Pandey, A.*, **Tiwari, H.**, and Sreenivasan, K. R., "Thermal convection in 1, 2, 3 and 4 dimensions", *J. Fluid Mech.*

3. Pathak, M., Sharma, L.*, **Tiwari, H.**, Aseeri, S., Keyes, D., and Verma, M. K., "Prandtl-number dependence of positive and negative heat fluxes in turbulent compressible convection", *Phys. Rev. Fluids.*

*Corresponding author

Under preparation:

1. Singh, D., **Tiwari, H.**, and Verma, M. K.,, "Thermalization in compressible Euler and quantum turbulence".
2. Kumar, N., **Tiwari, H.**, Verma, M. K., and Ravichandran, S., "Intermittency in conditionally unstable moist convection".
3. **Tiwari, H.**, Pandey, A., and Sreenivasan, K. R., "Scaling laws in four-dimensional turbulent convection".

Contents

List of figures

List of tables

Chapter 1

Introduction

Thermal convection is a ubiquitous transport mechanism in nature and engineering. In this process, buoyancy forces resulting from density variations drive the collective fluid motion. In astrophysical settings, convection dictates the thermal evolution of stars and giant planets. For example, the solar convection zone transports heat from the radiative interior to the surface (Spruit et al., 1990; Schumacher and Sreenivasan, 2020). Due to the immense spatial scales of this region, the flow is highly turbulent. These turbulent motions are also the origin of the solar dynamo, which generates the magnetic fields driving sunspots and solar flares (Parker, 1955; Miesch, 2005). Similar large-scale convective flows in gas giants like Jupiter and Saturn drive the zonal winds and atmospheric storms observed from the Earth (Ingersoll, 1990; Jones and Kuzanyan, 2009).

On Earth, convection plays a critical role in geophysics and meteorology. The vigorous motion of the liquid iron outer core acts as a geodynamo, generating the geomagnetic field (Glatzmaiers and Roberts, 1995). In the atmosphere, thermal convection is the primary driver of cloud formation and global circulation patterns (Houze, 1993). Apart from natural flows, controlling convection is essential in engineering applications, ranging from the cooling of nuclear reactors and electronic devices to the thermal management of high-speed aerospace vehicles (Incropera et al., 2007).

To unravel the complex physics governing these systems, researchers rely on simplified theoretical frameworks. The canonical model used to study these flows is Rayleigh-Bénard convection (RBC). In this setup, a fluid layer confined between two plates is heated from

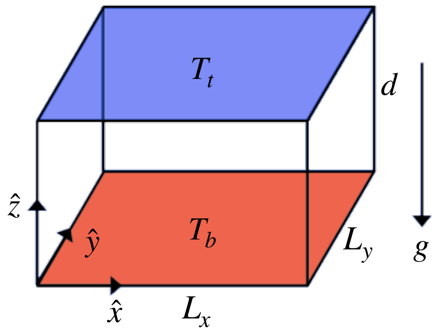

FIGURE 1.1: Schematic diagram of the Rayleigh-Bénard convection system with height d. The bottom and top plates are maintained at constant temperatures T_b and T_t, respectively, with gravity g acting in the downward direction.

below and cooled from above. The standard theoretical framework for RBC relies on the Oberbeck-Boussinesq (OB) approximation, which assumes that density remains constant except for small variations in the buoyancy term.

While the OB approximation is valid for most laboratory-scale liquids, it is insufficient for strongly stratified natural systems. In the solar convection zone, planetary atmospheres, and high-speed gas flows, the fluid density varies significantly with depth. In such regimes, the flow is not merely buoyant but compressible. This thesis focuses on numerical simulations of highly turbulent compressible convection. Before addressing the complexities of compressibility, we first establish the fundamental concepts using the standard RBC framework.

1.1 Rayleigh-Bénard convection

Rayleigh-Bénard convection (RBC) serves as the fundamental paradigm for studying thermally driven turbulence. It provides a canonical framework to investigate the interplay between buoyancy forces and dissipative mechanisms in a controlled setting (Siggia, 1994; Ahlers et al., 2009; Lohse and Xia, 2010; Chillà and Schumacher, 2012; Verma et al., 2017; Verma, 2018). The physical system consists of a fluid confined within a rectangular domain of dimensions $L_x \times L_y \times d$, where L_x and L_y denote the horizontal lengths and d represents the vertical height. The bottom and top plates are maintained at constant temperatures T_b and T_t, respectively, imposing a destabilizing temperature difference $\Delta T = T_b - T_t > 0$ between the plates. A constant downward gravitational acceleration $\mathbf{g} = -g\hat{z}$ acts on the fluid. A schematic illustration of the system is presented in Fig. 1.1.

The theoretical description of RBC typically employs the Oberbeck-Boussinesq (OB) approximation. This approximation assumes that the fluid properties—viscosity, thermal diffusivity, and specific heat—are constant throughout the flow. Furthermore, it assumes that density variations are negligible, except in the gravitational force term of the momentum equation, where density $\tilde{\rho}$ varies linearly with temperature $\tilde{T}$ according to

$$\tilde{\rho}(\tilde{T}) = \rho_b[1 - \alpha(\tilde{T} - T_b)], \tag{1.1}$$

where ρ_b is the reference density at the bottom plate at temperature T_b and α is the thermal expansion coefficient.

The dynamics of the system are governed by the incompressible Navier-Stokes equations under the OB approximation. In terms of the dimensional variables (velocity and thermodynamic variables are denoted by tildes, and the dimensional spatial gradient operator by ∇'), the equations for the conservation of mass, momentum, and energy are (Chandrasekhar, 1961; Ahlers et al., 2009; Verma, 2018)

$$\nabla' \cdot \tilde{\mathbf{u}} = 0, \tag{1.2}$$

$$\frac{\partial \tilde{\mathbf{u}}}{\partial \tilde{t}} + (\tilde{\mathbf{u}} \cdot \nabla')\tilde{\mathbf{u}} = -\frac{1}{\rho_b}\nabla'\tilde{p} + \alpha g(\tilde{T} - T_b)\hat{z} + \nu\nabla'^2\tilde{\mathbf{u}}, \tag{1.3}$$

$$\frac{\partial \tilde{T}}{\partial \tilde{t}} + (\tilde{\mathbf{u}} \cdot \nabla')\tilde{T} = \kappa\nabla'^2\tilde{T}, \tag{1.4}$$

where $\tilde{\mathbf{u}}$ is the velocity vector, $\tilde{p}$ is the kinematic pressure deviation from the hydrostatic background, ν is the kinematic viscosity, and κ is the thermal diffusivity. The prime on the gradient operator will be dropped later when we introduce the dimensionless equations for the sake of brevity.

The dynamical state of the flow is governed by two key dimensionless control parameters: the Rayleigh number (Ra) and the Prandtl number (Pr). The Rayleigh number acts as the primary measure of instability, quantifying the ratio of the destabilizing buoyancy force to the stabilizing effects of viscous and thermal dissipation. The Prandtl number describes the intrinsic diffusive properties of the fluid, representing the ratio of momentum diffusivity to thermal diffusivity. These parameters are defined as (Chandrasekhar, 1961; Ahlers et al., 2009; Verma, 2018)

$$\mathrm{Ra} = \frac{\alpha g \Delta T d^3}{\nu\kappa}, \quad \mathrm{Pr} = \frac{\nu}{\kappa}. \tag{1.5}$$

The magnitude of the Rayleigh number varies dramatically across different systems. Most engineering applications and convection phenomena encountered in daily life have modest

Rayleigh numbers (Ra $\sim 10^6$ to 10^{10}). For example, consider a pocket of air trapped between a pair of parallel plates held at 20°C and 220°C (typical of double-pane window insulation or the cooling of electronic components in fan-less enclosures) separated by a gap of 10 cm. Given the fluid properties of air, Ra $\sim 10^7$ for this flow. In contrast, convective flows encountered at atmospheric, geophysical, and astrophysical scales operate at much higher values. For instance, the solar convection zone is estimated to have Ra $\sim 10^{24}$ (Chillà and Schumacher, 2012; Schumacher and Sreenivasan, 2020). Similarly, the Earth's atmosphere is estimated to have Ra $\sim 10^{20}$ (Lohse and Xia, 2010).

To facilitate numerical analysis and uncover universal scaling properties, we cast the governing equations into non-dimensional form. We choose the layer height d as the length scale and the imposed temperature difference ΔT as the temperature scale. For the velocity scale, we employ the free-fall velocity $U_f = \sqrt{\alpha g \Delta T d}$, which balances the buoyancy and inertial forces. The corresponding time scale is the free-fall time $t_f = d/U_f$, and the pressure scale is $\rho_b U_f^2$. We define the non-dimensional temperature T as $T = (\tilde{T} - T_t)/\Delta T$. Substituting these scales into Eqs. (1.2)–(1.4) yields the dimensionless governing equations

$$\nabla \cdot \mathbf{u} = 0, \tag{1.6}$$

$$\frac{\partial \mathbf{u}}{\partial t} + (\mathbf{u} \cdot \nabla)\mathbf{u} = -\nabla p + T\hat{z} + \sqrt{\frac{\mathrm{Pr}}{\mathrm{Ra}}}\nabla^2 \mathbf{u}, \tag{1.7}$$

$$\frac{\partial T}{\partial t} + (\mathbf{u} \cdot \nabla)T = \frac{1}{\sqrt{\mathrm{RaPr}}}\nabla^2 T. \tag{1.8}$$

Under the OB approximation, the RBC system possesses a statistical symmetry about the horizontal mid-plane ($z = 1/2$). The governing equations remain invariant under the transformation $z \to 1 - z$, $T \to 1 - T$, and $u_z \to -u_z$, implying that the flow statistics and thermal structures at the top and bottom boundaries are identical. Furthermore, at high Rayleigh numbers, vigorous turbulent mixing homogenizes the temperature field within the interior of the domain. As a result, the mean vertical temperature profile becomes nearly constant in the bulk, matching the average of the top and bottom plate temperatures (Verma et al., 2017; Verma, 2018). The significant temperature gradients are thus confined to the thin thermal boundary layers adjacent to the walls (Ahlers et al., 2009; Lohse and Xia, 2010).

Turbulence significantly enhances the transport of heat and momentum. This enhancement is quantified by two dimensionless response parameters: the Reynolds number (Re) and the Nusselt number (Nu). The Reynolds number measures the intensity of the turbulent flow, defined as the ratio of inertial forces to viscous forces. In terms of the dimensional root-mean-square velocity $\tilde{U} = \sqrt{\langle \tilde{u}^2 \rangle_V}$, it is given by

$$\mathrm{Re} = \frac{\tilde{U}d}{\nu} = \sqrt{\frac{\mathrm{Ra}}{\mathrm{Pr}}}U, \tag{1.9}$$

where U is the non-dimensional root-mean-square velocity.

The Nusselt number represents the ratio of the total vertical heat flux to the purely conductive heat flux. The total vertical heat flux across any horizontal plane comprises both the convective flux and the local conductive flux. For a specific horizontal plane at height $\tilde{z}$, the local Nusselt number in terms of dimensional variables is defined as

$$\mathrm{Nu}(\tilde{z}) = \frac{\langle \tilde{u}_z \tilde{T} \rangle_{A,t} - \kappa \langle \partial \tilde{T} / \partial \tilde{z} \rangle_{A,t}}{\kappa \Delta T / d}, \tag{1.10}$$

where $\langle \cdot \rangle_{A,t}$ denotes horizontal and temporal averaging. By taking the volume average of this expression over all horizontal planes, the conductive term integrates exactly to $\kappa \Delta T / d$. Dividing this by the denominator yields 1, leading to the global volume-averaged Nusselt number

$$\mathrm{Nu} = 1 + \frac{\langle \tilde{u}_z \tilde{T} \rangle_{V,t}}{\kappa \Delta T / d}, \tag{1.11}$$

where $\langle \cdot \rangle_{V,t}$ denotes volume and time averaging. Using the non-dimensional variables defined above, this expression simplifies to

$$\mathrm{Nu} = 1 + \sqrt{\mathrm{RaPr}} \langle u_z T \rangle_{V,t}. \tag{1.12}$$

In a statistically steady state, the total vertical heat flux is conserved at every height. Consequently, Nu is often computed at the conducting plates (walls) by evaluating the vertical temperature gradient

$$\mathrm{Nu}_{z=0,1} = - \left\langle \left. \frac{\partial T}{\partial z} \right|_{z=0,1} \right\rangle_{A,t}. \tag{1.13}$$

Numerically, the boundary-based calculation is frequently preferred over volume averaging because it exhibits significantly lower temporal fluctuations. The heat transport near the walls is governed by thin thermal boundary layers, where sharp temperature gradients sustain the high heat flux. A detailed discussion on the scaling of Nu and Re with Ra is presented later in Sec. 1.4.

While the RBC framework provides deep insights into turbulent convection, the underlying OB approximation limits its applicability to flows with small density variations. In the

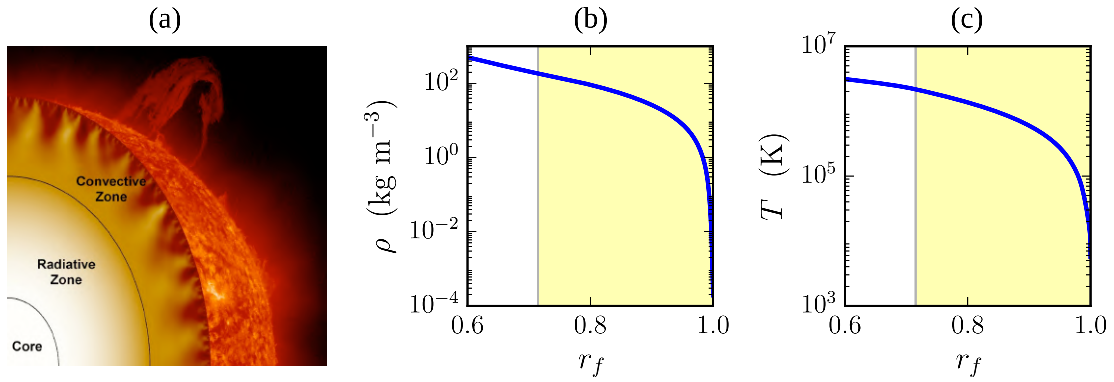

FIGURE 1.2: Stratification in the solar interior. (a) Illustration of the solar convection zone (Image credit: NASA). (b) Radial profile of density ρ versus normalized radius $r_f = r/R_\odot$. (c) Radial profile of temperature T versus r_f. Profiles obtained using Solar Model S (Christensen-Dalsgaard et al., 1996).

next section, we generalize this framework to study compressible convection, which is essential for understanding strongly stratified astrophysical and geophysical flows.

1.2 Compressible convection

The standard RBC model relies on the OB approximation. In laboratory fluids, this assumption is generally robust. For instance, in water at room temperature ($\alpha \approx 3 \times 10^{-4}$ K^{-1}), a temperature difference of $\Delta T = 30$ K results in a relative density change $(\delta\rho)/\rho \approx \alpha\Delta T$ of only 10^{-3} (Verma, 2018). However, density fluctuations in a turbulent star are of the order of unity (Spiegel, 1965). If we assume the star is made of an ideal gas, the thermal expansion coefficient is $\alpha = 1/T$. Consequently, $(\delta\rho)/\rho \approx \alpha(\Delta T) \approx 1$ when the temperature fluctuations are comparable to the background temperature ($\Delta T \approx T$). Therefore, the OB approximation and the RBC equations become invalid for stars and related astrophysical systems (Chandrasekhar, 1961; Spiegel and Veronis, 1960; Hansen et al., 2012; Schumacher and Sreenivasan, 2020). To study such systems, researchers often employ equations for compressible convection or intermediate models that utilize non-Oberbeck-Boussinesq (NOB) effects (Wan et al., 2020; Pandey et al., 2021a,b) or anelastic approximations (Gough, 1969; Verhoeven et al., 2015). In this thesis, we employ the fully compressible equations to study turbulent convection.

The solar convection zone exemplifies the regime where the OB approximation fails. In the Sun, energy generated by nuclear fusion in the core travels through a radiative zone before reaching the outer envelope, where convection becomes the dominant transport mechanism. This convective layer, illustrated in Fig. 1.2(a), extends from approximately $0.7R_\odot$ to the solar surface ($1.0R_\odot$), where $R_\odot$ denotes the solar radius. Across this region, the thermodynamic variables exhibit extreme variations. Figures 1.2(b) and 1.2(c) display the radial profiles of density and temperature, respectively, based on Solar Model S (Christensen-Dalsgaard et al., 1996). The fluid density drops by more than six orders of magnitude, decreasing from approximately 200 kg m^{-3} at the base of the convection zone to 10^{-4} kg m^{-3} at the surface. Concurrently, the temperature falls from approximately 2×10^6 K to 5800 K. These steep gradients indicate that the solar convection zone is a highly stratified medium.

Turbulent compressible convection exhibits fundamental differences from standard RBC (John and Schumacher, 2023b). Unlike the constant bulk temperature observed in RBC, the bulk temperature in compressible convection falls adiabatically (Verhoeven et al., 2015). Furthermore, the background state is characterized by strong density stratification, where the fluid at the bottom is significantly denser than at the top, in sharp contrast to the nearly constant density approximation in RBC. Despite its importance, fully compressible convection has received limited attention compared to its Boussinesq counterpart. Verhoeven et al. (2015) performed a comparative study between the anelastic approximation and fully compressible equations, while John and Schumacher (2023a,b) explored different flow regimes in compressible convection using direct numerical simulations (DNS) up to $\mathrm{Ra} = 10^7$. Other studies have employed inviscid models (Porter and Woodward, 2000), where estimates of the effective Rayleigh number remain uncertain. Consequently, there are no existing studies on fully compressible convection at high Rayleigh numbers. This thesis aims to bridge this gap by performing high-fidelity DNS of fully compressible convection at unprecedented scales, reaching $\mathrm{Ra} = 10^{16}$ in two dimensions and $\mathrm{Ra} = 10^{13}$ in three dimensions.

In the following section, we describe the physical system and present the governing equations for compressible convection.

1.2.1 Physical system and governing equations

We consider a fully compressible fluid confined in a rectangular domain of dimensions $L_x \times L_y \times d$ in 3D and $L_x \times d$ in 2D. The physical configuration is similar to the standard Rayleigh-Bénard system presented in Fig. 1.1. The fluid is assumed to be an ideal gas characterized by its density $\tilde{\rho}$, pressure $\tilde{p}$, and temperature $\tilde{T}$, satisfying the equation of state $\tilde{p} = \tilde{\rho} R_* \tilde{T}$, where R_* is the specific gas constant. A constant downward gravitational acceleration $\mathbf{g} = -g\hat{z}$ acts on the fluid. The flow is driven by a destabilizing temperature difference $\Delta T = T_b - T_t > 0$, imposed by maintaining the bottom and top plates at constant temperatures T_b and T_t, respectively.

The dynamics of the system are governed by the compressible Navier-Stokes equations. In terms of the dimensional primitive variables $(\tilde{\rho}, \tilde{\mathbf{u}}, \tilde{T})$, the evolution equations are (Anderson, 1995)

$$\frac{\partial \tilde{\rho}}{\partial \tilde{t}} + \nabla' \cdot (\tilde{\rho}\tilde{\mathbf{u}}) = 0, \tag{1.14}$$

$$\tilde{\rho}\left[\frac{\partial \tilde{\mathbf{u}}}{\partial \tilde{t}} + (\tilde{\mathbf{u}} \cdot \nabla')\tilde{\mathbf{u}}\right] = -\nabla'\tilde{p} - g\tilde{\rho}\hat{z} + \mu\left[\nabla'^2\tilde{\mathbf{u}} + \frac{1}{3}\nabla'(\nabla' \cdot \tilde{\mathbf{u}})\right], \tag{1.15}$$

$$\tilde{\rho}C_v\left[\frac{\partial \tilde{T}}{\partial \tilde{t}} + (\tilde{\mathbf{u}} \cdot \nabla')\tilde{T}\right] = -\tilde{p}(\nabla' \cdot \tilde{\mathbf{u}}) + K\nabla'^2\tilde{T} + 2\mu\left[\tilde{S}_{ij} - \frac{1}{3}(\nabla' \cdot \tilde{\mathbf{u}})\delta_{ij}\right]^2, \tag{1.16}$$

where $\tilde{\mathbf{u}}$ is the velocity vector, C_v is the specific heat at constant volume, μ is the dynamic viscosity, K is the thermal conductivity, and $\tilde{S}_{ij} = (\tilde{\partial}_i\tilde{u}_j + \tilde{\partial}_j\tilde{u}_i)/2$ is the strain rate tensor. In this study, the dynamic viscosity μ and thermal conductivity K are assumed to be constant. This simplification allows us to isolate the effects of density stratification and compressibility from the complexities arising from temperature-dependent transport properties. Consequently, the kinematic viscosity $\nu = \mu/\tilde{\rho}$ and thermal diffusivity $\kappa = K/(\tilde{\rho}C_p)$ vary spatially solely due to density stratification, where $C_p = C_v + R_*$ is the specific heat at constant pressure. Note that the tilde represents the dimensional variables.

The governing equations can also be expressed in a conservative form, which is particularly useful for analyzing global conservation properties. This form is termed *conservative* because the temporal rate of change of a macroscopic variable (mass, momentum, or energy) is dictated purely by the spatial divergence of its corresponding flux. This formulation ensures that these quantities are globally conserved in the absence of boundary fluxes. The conservative set of equations is given by (Spiegel, 1965; Graham, 1975)

$$\frac{\partial \tilde{\rho}}{\partial \tilde{t}} + \frac{\partial}{\partial \tilde{x}_i}(\tilde{\rho}\tilde{u}_i) = 0, \tag{1.17}$$

$$\frac{\partial}{\partial \tilde{t}}(\tilde{\rho}\tilde{u}_i) + \frac{\partial}{\partial \tilde{x}_j}(\tilde{\rho}\tilde{u}_i\tilde{u}_j + \delta_{ij}\tilde{p} - \tilde{\tau}_{ij}) = -g\tilde{\rho}\delta_{iz}, \tag{1.18}$$

$$\frac{\partial \tilde{E}}{\partial \tilde{t}} + \frac{\partial}{\partial \tilde{x}_i}\left(\tilde{u}_i(\tilde{E} + \tilde{p}) - K\frac{\partial \tilde{T}}{\partial \tilde{x}_i} - \tilde{u}_j\tilde{\tau}_{ij}\right) = 0, \tag{1.19}$$

where $\tilde{u}_i$ are the velocity field components;

$$\tilde{E} = \tilde{\rho}\left(\frac{\tilde{u}^2}{2} + C_v\tilde{T} + g\tilde{z}\right) \tag{1.20}$$

is the total energy density; and

$$\tilde{\tau}_{ij} = \mu\left(\tilde{\partial}_j\tilde{u}_i + \tilde{\partial}_i\tilde{u}_j - \frac{2}{3}\tilde{\partial}_m\tilde{u}_m\delta_{ij}\right) \tag{1.21}$$

is the stress tensor.

Unlike the OB approximation in RBC, which preserves reflectional symmetry about the mid-plane, compressible convection inherently breaks this top-down symmetry. The fundamental cause is the strong stratification of density under gravity; the fluid near the bottom is significantly denser than the fluid near the top. Since local transport coefficients such as kinematic viscosity ($\nu \propto \mu/\tilde{\rho}$) and thermal diffusivity ($\kappa \propto K/\tilde{\rho}$) scale inversely with density, they vary markedly across the domain height. This variation leads to asymmetric boundary layer dynamics: the lower-density top layer tends to be more diffusive and thicker than the high-density bottom layer (Graham, 1975; Hurlburt et al., 1984, 1986). Consequently, the mean temperature and velocity profiles lose their symmetry, and the bulk temperature shifts away from the arithmetic mean of the boundary temperatures.

To understand the energy exchange mechanisms, we write the evolution equations for the kinetic energy density $\tilde{E}_u = \frac{1}{2}\tilde{\rho}\tilde{u}^2$ and the internal energy density $\tilde{I} = \tilde{\rho}C_v\tilde{T}$ explicitly

$$\frac{\partial\tilde{E}_u}{\partial\tilde{t}} + \nabla'\cdot(\tilde{E}_u\tilde{\mathbf{u}}) = -\tilde{\mathbf{u}}\cdot\nabla'\tilde{p} + \tilde{u}_i\tilde{\partial}_j\tilde{\tau}_{ij} - g\tilde{\rho}\tilde{u}_z, \tag{1.22}$$

$$\frac{\partial\tilde{I}}{\partial\tilde{t}} + \nabla'\cdot(\tilde{I}\tilde{\mathbf{u}}) = -\tilde{p}(\nabla'\cdot\tilde{\mathbf{u}}) + \tilde{\tau}_{ij}\tilde{\partial}_i\tilde{u}_j + K\nabla'^2\tilde{T}. \tag{1.23}$$

Integrating these equations over a closed box (with appropriate boundary conditions) reveals the global conservation laws. The total mass $M = \int\tilde{\rho}dV$ and the total energy $E_{tot} = \int\tilde{E}dV$ remain constant in time. We first consider the kinetic energy budget (Eq. 1.22): kinetic energy is generated by buoyancy forces (represented by $-g\tilde{\rho}\tilde{u}_z$) and work done by pressure gradients ($-\tilde{\mathbf{u}}\cdot\nabla'\tilde{p}$). It is dissipated via viscous effects ($\tilde{u}_i\tilde{\partial}_j\tilde{\tau}_{ij}$). Next, we consider the internal energy budget (Eq. 1.23): the pressure work term $-\tilde{p}(\nabla'\cdot\tilde{\mathbf{u}})$ acts as a reversible exchange channel between kinetic and internal energy (compression heats the gas, expansion cools it). The viscous term $\tilde{\tau}_{ij}\tilde{\partial}_i\tilde{u}_j$ represents the irreversible conversion of kinetic energy into heat (viscous dissipation), acting as a source for internal energy. Finally, the thermal diffusion term $K\nabla'^2\tilde{T}$ redistributes heat within the domain.

1.2.2 Equilibrium profiles

To analyze the stability and structure of the flow, we first identify the reference states of the system. In the absence of fluid motion ($\tilde{\mathbf{u}} = 0$) and time evolution ($\partial/\partial\tilde{t} = 0$), the system is in hydrostatic and thermal equilibrium. The heat transport is purely conductive, governed by $\nabla'^2\tilde{T} = 0$. Given the boundary conditions $\tilde{T}(\tilde{z} = 0) = T_b$ and $\tilde{T}(\tilde{z} = d) = T_t$, the conductive temperature profile $\tilde{T}_0(\tilde{z})$ is linear. The corresponding density profile $\tilde{\rho}_0(\tilde{z})$ is determined by the hydrostatic balance condition $\partial\tilde{p}/\partial\tilde{z} = -\tilde{\rho}g$ and the equation of state. These conductive profiles are given by

$$\tilde{T}_0(\tilde{z}) = T_b - \frac{\Delta T}{d}\tilde{z}, \tag{1.24}$$

$$\tilde{\rho}_0(\tilde{z}) = \rho_b \left(\frac{\tilde{T}_0(\tilde{z})}{T_b}\right)^m, \tag{1.25}$$

where ρ_b is the density at the bottom plate and m is the polytropic index of the hydrostatic background, defined as

$$m = \frac{gd}{R_*\Delta T} - 1. \tag{1.26}$$

While the conductive profile represents the initial state, it is physically realized only in subadiabatic or stably stratified fluids. In vigorously turbulent convection, the fluid is efficiently mixed, tending to homogenize entropy in the bulk (Spiegel, 1965; Verhoeven et al., 2015). Consequently, the adiabatic (isentropic) profile provides a more relevant reference state for the turbulent interior. This background state is derived from the hydrostatic balance $\partial\tilde{p}/\partial\tilde{z} = -\tilde{\rho}g$ and the thermodynamic relation for specific entropy s,

$$\tilde{T}ds = C_p d\tilde{T} - \frac{1}{\tilde{\rho}}d\tilde{p}. \tag{1.27}$$

Assuming the bulk flow is adiabatic ($ds = 0$), we obtain $C_p d\tilde{T} = d\tilde{p}/\tilde{\rho}$. Substituting the hydrostatic condition yields the dry adiabatic lapse rate $d\tilde{T}/d\tilde{z} = -g/C_p$. Integrating this relation results in the adiabatic temperature profile $\tilde{T}_A(\tilde{z})$, while the associated density profile $\tilde{\rho}_A(\tilde{z})$ follows a polytropic relation

$$\tilde{T}_A(\tilde{z}) = T_b - \frac{g}{C_p}\tilde{z}, \tag{1.28}$$

$$\tilde{\rho}_A(\tilde{z}) = \rho_b \left(\frac{\tilde{T}_A(\tilde{z})}{T_b}\right)^\beta, \tag{1.29}$$

where $\beta = 1/(\gamma - 1)$ is the adiabatic index and $\gamma = C_p/C_v$ is the ratio of specific heats.

The stability of the fluid layer is governed by the *Schwarzschild criterion*, which states that convection occurs when the magnitude of the conductive temperature gradient exceeds the adiabatic temperature gradient (Carroll, 2006). Explicitly, the condition for instability is given by

$$\frac{\Delta T}{d} > \frac{g}{C_p}. \tag{1.30}$$

This deviation from adiabaticity is quantified by the superadiabaticity parameter ϵ, defined as

$$\epsilon = \frac{d}{T_b}\left(\frac{\Delta T}{d} - \frac{g}{C_p}\right). \tag{1.31}$$

Convection is sustained only when $\epsilon > 0$. In terms of the polytropic indices defined earlier (m for the conductive profile and β for the adiabatic profile), this instability criterion translates to the condition:

$$\beta > m. \tag{1.32}$$

Thus, compressible convection is physically driven by the superadiabatic component of the temperature field, representing the excess thermal energy available to drive buoyancy against the stabilizing effect of stratification.

1.2.3 Non-dimensionalisation

To generalize the governing equations and identify the key non-dimensional parameters characterizing the flow, we non-dimensionalize the system (Eqs. 1.17–1.19). We choose the layer depth d as the length scale, the bottom density ρ_b as the density scale, and the bottom temperature T_b as the temperature scale. For the velocity scale, we employ the free-fall velocity $U_f = \sqrt{\epsilon g d}$, which characterizes the buoyancy-driven motion. The resulting timescale is the free-fall time, $t_f = d/U_f$.

Denoting the non-dimensional variables without tildes (e.g., $x = \tilde{x}/d$, $t = \tilde{t}/t_f$), the governing equations in conservative form are (Verhoeven et al., 2015; John and Schumacher, 2023a)

$$\frac{\partial \rho}{\partial t} + \frac{\partial}{\partial x_i}(\rho u_i) = 0, \tag{1.33}$$

$$\frac{\partial}{\partial t}(\rho u_i) + \frac{\partial}{\partial x_j}(\rho u_i u_j + \delta_{ij} p - \tau_{ij}) = -\frac{1}{\epsilon}\rho \delta_{iz}, \tag{1.34}$$

$$\frac{\partial E}{\partial t} + \frac{\partial}{\partial x_i}\left[u_i(E+p) - \frac{1}{\epsilon D\sqrt{\mathrm{RaPr}}}\frac{\partial T}{\partial x_i} - u_j \tau_{ij}\right] = 0, \tag{1.35}$$

where the non-dimensional pressure p, total energy density E, and viscous stress tensor τ_{ij} are defined respectively as

$$p = \frac{(\gamma - 1)}{\gamma \epsilon D} \rho T, \tag{1.36}$$

$$E = \rho \left(\frac{u^2}{2} + \frac{1}{\gamma \epsilon D} T + \frac{1}{\epsilon} z \right), \tag{1.37}$$

$$\tau_{ij} = \sqrt{\frac{\mathrm{Pr}}{\mathrm{Ra}}} \left(\partial_j u_i + \partial_i u_j - \frac{2}{3} \partial_m u_m \delta_{ij} \right). \tag{1.38}$$

The system behavior is governed by five non-dimensional control parameters: the Rayleigh number (Ra), the Prandtl number (Pr), the dissipation number (D), the superadiabaticity parameter (ϵ), and the ratio of specific heats (γ). These are defined as (Verhoeven et al., 2015; John and Schumacher, 2023b)

$$\epsilon = \frac{d}{T_b} \left(\frac{\Delta T}{d} - \frac{g}{C_p} \right), \quad D = \frac{gd}{C_p T_b}, \tag{1.39}$$

$$\mathrm{Ra} = \frac{\epsilon g d^3}{\nu \kappa}, \quad \mathrm{Pr} = \frac{\nu}{\kappa}, \tag{1.40}$$

where ν and κ are evaluated at the bottom reference density ρ_b. The parameters D and ϵ are unique to compressible convection: D quantifies the background stratification, representing the fractional temperature drop due to the adiabatic lapse rate, while ϵ represents the dimensionless superadiabatic temperature gradient that drives the turbulence. Additionally, the system geometry is characterized by the aspect ratios $\Gamma_x = L_x/d$ and $\Gamma_y = L_y/d$. In the present study, we employ a square horizontal cross-section, setting $\Gamma_x = \Gamma_y = \Gamma$.

Notably, the definition of the Rayleigh number here differs from the standard Boussinesq definition ($\mathrm{Ra}_{\mathrm{OB}} = \alpha g \Delta T d^3/\nu\kappa$). In the Boussinesq approximation, the thermal expansion coefficient α couples temperature fluctuations to density changes. In an ideal gas, however, $\alpha = 1/T$, and the density contrast driving the instability arises specifically from the deviation from the adiabatic profile. Therefore, the factor $\alpha \Delta T$ in $\mathrm{Ra}_{\mathrm{OB}}$ is effectively replaced by the superadiabaticity parameter ϵ. This substitution is necessary because using the total temperature drop ΔT overestimates the buoyant forcing; a significant portion of ΔT is required merely to sustain the background adiabatic stratification. The parameter ϵ correctly isolates only the excess, superadiabatic temperature gradient that actively drives the convective motion.

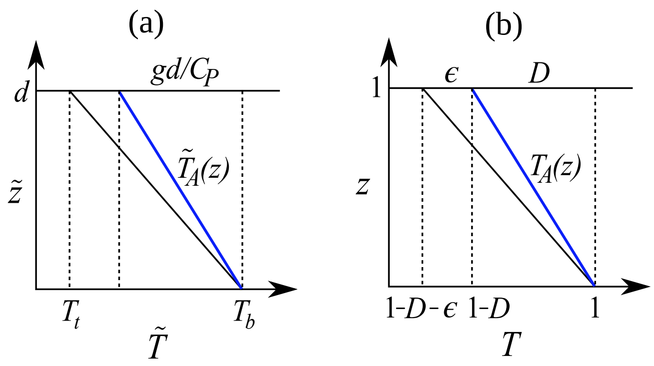

FIGURE 1.3: Vertical profiles of temperature in compressible convection. The adiabatic temperature profile (blue lines) and the conductive temperature profiles (black lines) are shown in (a) dimensional and (b) non-dimensional forms.

In this non-dimensional framework, the adiabatic equilibrium profiles for temperature, density, and pressure are given by (Verhoeven et al., 2015)

$$T_A(z) = 1 - Dz, \tag{1.41}$$

$$\rho_A(z) = (1 - Dz)^{\beta}, \tag{1.42}$$

$$p_A(z) = (1 - Dz)^{\beta+1}. \tag{1.43}$$

The dimensionless temperature is fixed at $T = 1$ at the bottom plate ($z = 0$). At the top plate ($z = 1$), the temperature is fixed at $1 - (\epsilon + D)$, as illustrated in Fig. 1.3. Thus, the total temperature drop across the layer is $\epsilon + D$, where D represents the normalised adiabatic temperature gradient and ϵ represents the superadiabatic contribution that drives the flow.

The adiabatic profiles for temperature, density, and pressure serve as the reference state for our simulations. We fix the control parameters to $\gamma = 1.3$, $\epsilon = 0.1$, and $D = 0.5$ throughout this study. These parameters characterize a moderately stratified fluid. The strength of the stratification is quantified by the density contrast χ_ρ, defined as the ratio of the density at the bottom to that at the top. Following the polytropic relation in Eq. (1.42), the theoretical density contrast is given by (Verhoeven et al., 2015)

$$\chi_\rho = \frac{\rho_A(0)}{\rho_A(1)} = (1 - D)^{-\beta}. \tag{1.44}$$

For our chosen parameters ($D = 0.5, \beta \approx 3.33$), this yields a density contrast of $\chi_\rho \approx 10$. While this is lower than the extreme stratification observed in the solar convection zone ($\chi_\rho \sim 10^6$), it captures the essential physics of compressible flow where density variations

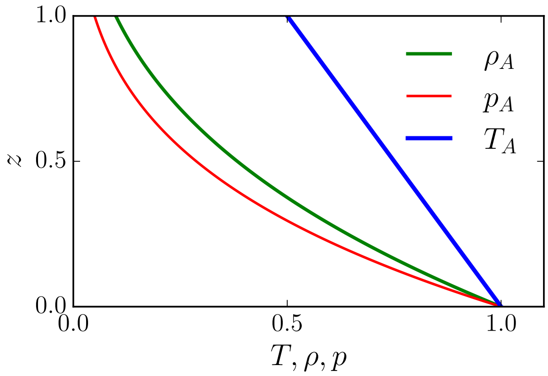

FIGURE 1.4: Dimensionless adiabatic equilibrium profiles of temperature $T_A(z)$ (blue), density $\rho_A(z)$ (green), and pressure $p_A(z)$ (red) as a function of the vertical coordinate z. The profiles correspond to the reference parameters used in this study: $\gamma = 1.3$ and $D = 0.5$, resulting in a density contrast of approximately 10.

are significant ($\mathcal{O}(1)$), unlike in Boussinesq fluids. Figure 1.4 displays the vertical profiles of the thermodynamic variables for this reference state.

1.2.4 Oberbeck-Boussinesq approximation

The Oberbeck-Boussinesq (OB) approximation is the cornerstone of classical convection theory. It assumes that fluid properties are constant, except for the density in the buoyancy term, which depends linearly on temperature. This approximation is valid when the density variations are small, i.e., $|\delta\rho|/\rho \ll 1$. In the context of the compressible equations presented in Sec. 1.2.3, the OB limit is recovered when the stratification is negligible and the superadiabatic driving is weak relative to the background temperature. Mathematically, this corresponds to the double limit

$$D \to 0 \quad \text{and} \quad \epsilon \to 0. \tag{1.45}$$

In this limit, the background adiabatic profiles become uniform ($T_A \to 1, \rho_A \to 1$). We decompose the thermodynamic variables into a constant background and a small perturbation scaled by the superadiabaticity parameter ϵ

$$\rho = 1 + \epsilon\rho', \tag{1.46}$$

$$T = 1 + \epsilon T', \tag{1.47}$$

$$p = p_h + \epsilon p', \tag{1.48}$$

where T' is the non-dimensional temperature fluctuation (scaled by ΔT), p' is the dynamic pressure, and p_h satisfies the hydrostatic balance $\partial_z p_h = -1/\epsilon$.

Applying these limits to the continuity equation (Eq. 1.33), the density time-derivative $\partial_t \rho \sim \mathcal{O}(\epsilon)$ vanishes, and the divergence of mass flux simplifies to the incompressibility condition

$$\nabla \cdot \mathbf{u} = 0. \tag{1.49}$$

Next, we consider the momentum equation (Eq. 1.34). Substituting the linearized equation of state for an ideal gas, $\rho \approx 1 - \epsilon T'$, into the gravitational term $-\frac{1}{\epsilon}\rho\hat{z}$, we obtain

$$-\frac{1}{\epsilon}(1 - \epsilon T')\hat{z} = -\frac{1}{\epsilon}\hat{z} + T'\hat{z}. \tag{1.50}$$

The leading order term $-1/\epsilon$ is balanced by the hydrostatic pressure gradient. The remaining $\mathcal{O}(1)$ term, $T'\hat{z}$, represents the buoyancy force. Consequently, the momentum equation reduces to

$$\frac{\partial \mathbf{u}}{\partial t} + (\mathbf{u} \cdot \nabla)\mathbf{u} = -\nabla p' + T'\hat{z} + \sqrt{\frac{\mathrm{Pr}}{\mathrm{Ra}}}\nabla^2 \mathbf{u}. \tag{1.51}$$

Finally, we examine the energy equation (Eq. 1.35). As $D \to 0$ and $\epsilon \to 0$, the work done by pressure compression ($p\nabla \cdot \mathbf{u}$) vanishes due to incompressibility, and the viscous dissipation term becomes negligible compared to thermal diffusion. The total energy equation reduces to the advection-diffusion equation for temperature

$$\frac{\partial T'}{\partial t} + (\mathbf{u} \cdot \nabla)T' = \frac{1}{\sqrt{\mathrm{RaPr}}}\nabla^2 T'. \tag{1.52}$$

These three reduced equations constitute the standard Rayleigh-Bénard convection system (§ 1.1). They are symmetric with respect to the mid-plane of the layer, a property lost in compressible convection where density stratification breaks the top-down symmetry. This thesis explores the regime where ϵ and D are non-zero, thereby quantifying the deviations from these classical Boussinesq predictions.

1.2.5 Anelastic approximation

While the OB approximation effectively describes flow in laboratory-scale liquids, it fails to capture the significant density variations inherent to large-scale astrophysical and geophysical flows. To bridge this gap, the anelastic approximation is often employed (Gough, 1969; Verhoeven et al., 2015). This approximation filters out acoustic waves—which imposes a stringent time-step constraint in compressible simulations—while retaining the effects of background density stratification.

The anelastic approximation is valid when the flow velocity is much smaller than the speed of sound (low Mach number), yet the background density varies significantly with height. In terms of our non-dimensional parameters, this regime corresponds to the limit where the superadiabaticity vanishes ($\epsilon \to 0$) while the dissipation number remains finite ($D > 0$).

In this limit, the thermodynamic variables are decomposed into a static, height-dependent reference state (the adiabatic profiles defined in § 1.2.3) and small perturbations

$$\rho(\mathbf{x}, t) = \rho_A(z) + \epsilon\rho'(\mathbf{x}, t), \tag{1.53}$$

$$T(\mathbf{x}, t) = T_A(z) + \epsilon T'(\mathbf{x}, t), \tag{1.54}$$

$$p(\mathbf{x}, t) = p_A(z) + \epsilon p'(\mathbf{x}, t). \tag{1.55}$$

Unlike the OB approximation where the background state is constant, here $\rho_A(z)$ and $T_A(z)$ retain their strong vertical variation. Substituting these expansions into the compressible equations and taking the limit $\epsilon \to 0$ yields the anelastic set of equations.

The continuity equation simplifies to the anelastic constraint, which requires the mass flux (momentum density) to be solenoidal, rather than the velocity field itself:

$$\nabla \cdot (\rho_A \mathbf{u}) = 0. \tag{1.56}$$

This constraint effectively filters out sound waves by assuming they propagate instantaneously, necessitating a non-local Poisson solver for the pressure field.

The momentum equation retains the background density in the inertial term, reflecting the variation of fluid inertia with depth. The buoyancy force is modified to account for the stratified background temperature

$$\rho_A \left[\frac{\partial \mathbf{u}}{\partial t} + (\mathbf{u} \cdot \nabla)\mathbf{u} \right] = -\nabla p' + \frac{\rho_A T'}{T_A}\hat{z} + \sqrt{\frac{\mathrm{Pr}}{\mathrm{Ra}}}\nabla^2 \mathbf{u}. \tag{1.57}$$

Here, the buoyancy term $\rho_A(T'/T_A)\hat{z}$ arises from the linearized equation of state, where density perturbations are related to temperature fluctuations via $\rho'/\rho_A \approx -T'/T_A$ (neglecting pressure perturbations in the state equation).

The energy equation governing the potential temperature fluctuation T' becomes

$$\rho_A \left[\frac{\partial T'}{\partial t} + (\mathbf{u} \cdot \nabla) T' \right] - \rho_A u_z \frac{dT_A}{dz} = \frac{1}{\sqrt{\mathrm{RaPr}}} \nabla^2 T'. \tag{1.58}$$

Note that the term $\rho_A u_z (dT_A/dz)$ accounts for the cooling of fluid parcels as they rise and expand adiabatically against the background stratification.

The anelastic equations thus occupy an intermediate complexity: they capture the top-down asymmetry and depth-dependent transport properties characteristic of compressible convection (via $\rho_A(z)$ and $T_A(z)$), but usually neglect the thermodynamic work and viscous heating terms present in the fully compressible energy equation. This thesis employs the fully compressible equations to capture all such thermodynamic effects and to avoid the assumptions inherent in the anelastic formulation.

1.2.6 Strongly heated, unstratified limit

For completeness, we also consider the theoretical regime characterized by finite ϵ and $D \to 0$. Since $D = gd/(C_p T_b) \to 0$, the hydrostatic pressure variations are negligible, and the adiabatic background profiles become effectively uniform ($T_A \to 1, \rho_A \to 1$). This means there is no background stratification. However, because ϵ remains finite ($\epsilon \approx \Delta T/T_b$), the imposed temperature difference is comparable to the absolute reference temperature. Consequently, the fluid experiences order-unity density variations driven entirely by strong thermal expansion ($\rho \propto 1/T$) rather than hydrostatic pressure gradients. This limit effectively isolates the non-Oberbeck-Boussinesq (NOB) effects of strong heating without the complexities of a stratified background (John and Schumacher, 2023a,b). While conceptually important for decoupling these effects, this thesis primarily focuses on regimes where both D and ϵ are finite, capturing the full interplay of strong buoyancy and significant background stratification.

1.3 Energy fluxes and Nusselt number in compressible convection

Quantifying the transport of heat is a central goal of this thesis. In RBC, the efficiency of heat transport is measured by the Nusselt number (Nu), defined as the ratio of total heat flux to the conductive heat flux. To derive a consistent definition of Nu for compressible convection, we rely on the conservation of total energy. In a statistically steady state of turbulent convection, the time derivatives of mean quantities vanish ($\partial_t\langle\cdot\rangle \approx 0$). Consequently, the divergence of the total energy flux must be zero, implying that the vertical energy flux is constant throughout the domain.

The evolution equation for the total energy density $\tilde{E} = \tilde{\rho}(\frac{1}{2}\tilde{u}^2 + C_v\tilde{T} + g\tilde{z})$ is derived by summing the kinetic and internal energy equations. This summation combines the internal energy flux ($\tilde{\rho}\tilde{u}_i C_v\tilde{T}$) and the pressure work ($\tilde{u}_i\tilde{p}$), resulting in the enthalpy flux ($\tilde{\rho}\tilde{u}_i C_p\tilde{T}$). The resulting total energy equation in conservative form is

$$\frac{\partial}{\partial\tilde{t}}\left[\tilde{\rho}\left(\frac{1}{2}\tilde{u}^2 + C_v\tilde{T} + g\tilde{z}\right)\right] + \frac{\partial}{\partial\tilde{x}_i}\left[\tilde{\rho}\tilde{u}_i\left(\frac{1}{2}\tilde{u}^2 + C_p\tilde{T} + g\tilde{z}\right) - K\frac{\partial\tilde{T}}{\partial\tilde{x}_i} - \tilde{u}_j\tilde{\tau}_{ij}\right] = 0. \quad (1.59)$$

Note the appearance of the specific heat at constant pressure, C_p, in the flux term, contrasting with C_v in the energy density term.

To determine the global heat transport, we integrate Eq. (1.59) over the volume V. Under steady-state conditions, the time derivative vanishes. Furthermore, we assume periodic boundary conditions in the horizontal directions, which implies that the horizontal flux contributions integrate to zero. This leaves only the vertical components of the total energy flux $\tilde{F}_T$, which can be expressed as

$$\tilde{F}_T = \left\langle \tilde{\rho}\tilde{u}_z\left(\frac{1}{2}\tilde{u}^2 + C_p\tilde{T} + g\tilde{z}\right) - K\frac{\partial\tilde{T}}{\partial\tilde{z}} - \tilde{u}_i\tilde{\tau}_{iz}\right\rangle_V, \quad (1.60)$$

where $\langle\cdot\rangle_V$ denotes the volume average. The viscous work term $\tilde{u}_i\tilde{\tau}_{iz}$ is negligible in the bulk flow and is omitted in further analysis.

To isolate the convective transport, we expand the temperature field as $\tilde{T}(\mathbf{x},t) = \tilde{T}_A(z) + \tilde{T}_{\mathrm{sa}}(\mathbf{x},t)$, where $\tilde{T}_A(z) = \tilde{T}_b - (g/C_p)\tilde{z}$ is the adiabatic equilibrium profile and $\tilde{T}_{\mathrm{sa}}$ is the superadiabatic temperature fluctuation. Substituting this into the enthalpy and potential energy terms yields

$$C_p\tilde{T} + g\tilde{z} = C_p\left(\tilde{T}_b - \frac{g}{C_p}\tilde{z} + \tilde{T}_{\rm sa}\right) + g\tilde{z} = C_p\tilde{T}_b + C_p\tilde{T}_{\rm sa}. \tag{1.61}$$

Since the system is closed, the total mass is conserved, implying that the volume-averaged vertical mass flux vanishes ($\langle\tilde{\rho}\tilde{u}_z\rangle_V = 0$). Consequently, the constant background term $C_p\tilde{T}_b\langle\tilde{\rho}\tilde{u}_z\rangle_V$ does not contribute to the net energy flux. The total vertical heat flux simplifies to

$$\tilde{F}_T = \left\langle \tilde{\rho}\tilde{u}_z\left(\frac{1}{2}\tilde{u}^2 + C_p\tilde{T}_{\rm sa}\right) - K\frac{\partial\tilde{T}}{\partial\tilde{z}}\right\rangle_V. \tag{1.62}$$

In compressible convection, simply dividing the total heat flux by the conductive heat flux is inappropriate for defining the Nusselt number because a significant portion of the temperature gradient is required just to maintain the adiabatic stratification, which does not drive convection. To compensate for these thermodynamic effects, the heat flux due to the adiabatic gradient, $\tilde{F}_A = Kg/C_p$, must be subtracted from both the total heat flux and the reference conductive heat flux (Spiegel and Veronis, 1960; Graham, 1975; Hurlburt et al., 1984). The Nusselt number is thus defined as

$$\begin{aligned}\mathrm{Nu} &= \frac{\tilde{F}_T - \tilde{F}_A}{\tilde{F}_{\rm cond} - \tilde{F}_A}\\ &= \frac{\left(K\frac{\Delta\tilde{T}}{\tilde{d}} + C_p\langle\tilde{\rho}\tilde{u}_z\tilde{T}_{\rm sa}\rangle_V + \langle\tilde{\rho}\tilde{u}_z\tilde{u}^2/2\rangle_V\right) - K\frac{g}{C_p}}{K\frac{\Delta\tilde{T}}{\tilde{d}} - K\frac{g}{C_p}}\\ &= \frac{K\left(\frac{\Delta\tilde{T}}{\tilde{d}} - \frac{g}{C_p}\right) + C_p\langle\tilde{\rho}\tilde{u}_z\tilde{T}_{\rm sa}\rangle_V + \langle\tilde{\rho}\tilde{u}_z\tilde{u}^2/2\rangle_V}{K\left(\frac{\Delta\tilde{T}}{\tilde{d}} - \frac{g}{C_p}\right)}.\end{aligned} \tag{1.63}$$

Using the definitions of the superadiabaticity parameter $\epsilon = \frac{\tilde{d}}{\tilde{T}_b}(\frac{\Delta\tilde{T}}{\tilde{d}} - \frac{g}{C_p})$ and the non-dimensionalization scales from Sec. 1.2.3, we can express Nu in terms of dimensionless quantities

$$\mathrm{Nu} = 1 + \frac{\sqrt{\mathrm{RaPr}}}{\epsilon}\langle\rho u_z T_{\rm sa}\rangle_{V,t} + \frac{D\sqrt{\mathrm{RaPr}}}{2}\langle\rho u_z u^2\rangle_{V,t}, \tag{1.64}$$

where $\langle\cdot\rangle_{V,t}$ denotes the combined volume and time average. This formulation decomposes the Nusselt number into three contributions

$$\mathrm{Nu} = 1 + \mathrm{Nu}_{\rm conv} + \mathrm{Nu}_K, \tag{1.65}$$

where the first term represents the purely diffusive flux driven by the superadiabatic gradient, $\mathrm{Nu}_{\mathrm{conv}}$ is the convective heat flux carried by enthalpy fluctuations, and Nu_K is the kinetic energy flux. In the Boussinesq limit ($\epsilon, D \to 0$), the kinetic flux Nu_K vanishes, and the expression recovers the standard form $\mathrm{Nu} = 1 + \sqrt{\mathrm{RaPr}}\langle u_z T_{\mathrm{sa}}\rangle$.

The quantity defined in Eq. (1.64) represents the *bulk Nusselt number*. While theoretically robust, it can exhibit significant temporal fluctuations in simulations. A more stable measure is obtained by computing the heat flux at the boundaries ($z = 0$ and $z = 1$). At these rigid walls (no-slip), the velocity field vanishes ($\mathbf{u} = 0$), causing the convective and kinetic fluxes to drop to zero. Consequently, the total vertical flux is purely conductive: $\tilde{F}_{\mathrm{wall}} = -K\partial\tilde{T}/\partial\tilde{z}$. Substituting the decomposition $\tilde{T} = \tilde{T}_A + \tilde{T}_{\mathrm{sa}}$, we find

$$\tilde{F}_{\mathrm{wall}} = -K\frac{\partial}{\partial\tilde{z}}(\tilde{T}_A + \tilde{T}_{\mathrm{sa}}) = -K\left(-\frac{g}{C_p} + \frac{\partial\tilde{T}_{\mathrm{sa}}}{\partial\tilde{z}}\right) = \tilde{F}_A - K\frac{\partial\tilde{T}_{\mathrm{sa}}}{\partial\tilde{z}}. \tag{1.66}$$

Substituting this expression back into the definition of the Nusselt number yields

$$\mathrm{Nu}_{\mathrm{wall}} = \frac{(\tilde{F}_A - K\partial_{\tilde{z}}\tilde{T}_{\mathrm{sa}}) - \tilde{F}_A}{\tilde{F}_{cond} - \tilde{F}_A} = \frac{-K\partial_{\tilde{z}}\tilde{T}_{\mathrm{sa}}}{K\epsilon\tilde{T}_b/\tilde{d}}. \tag{1.67}$$

In non-dimensional terms, this simplifies to (Verhoeven et al., 2015; John and Schumacher, 2023a)

$$\mathrm{Nu}_{z=0,1} = -\frac{1}{\epsilon}\left\langle \left.\frac{dT_{\mathrm{sa}}}{dz}\right|_{z=0,1} \right\rangle_{A,t}, \tag{1.68}$$

where $\langle\cdot\rangle_{A,t}$ represents the horizontal and temporal average. To ensure statistical convergence, the mean Nusselt number is defined as the average over both plates

$$\overline{\mathrm{Nu}} = \frac{\mathrm{Nu}_{z=0} + \mathrm{Nu}_{z=1}}{2}. \tag{1.69}$$

1.4 Turbulent convection

The study of thermal convection begins with the question of stability: under what conditions does a fluid layer become unstable to convective motions? In the classical Boussinesq limit, the fluid remains static for Ra below a critical value Ra_c, and heat is transported solely by conduction. When Ra exceeds Ra_c, the buoyancy force overcomes viscous dissipation, leading to a supercritical pitchfork bifurcation where the fluid organizes into convective rolls (Chandrasekhar, 1961; Verma, 2018). In the context of compressible convection, Spiegel (1965) extended this stability analysis to stratified fluids. He derived that the critical condition is not determined by the absolute temperature gradient, but by the superadiabatic gradient—the excess gradient beyond the adiabatic lapse rate. Thus, even in highly compressible atmospheres, convection initiates only when the Schwarzschild criterion is satisfied (see Eq. 1.30) and $\mathrm{Ra} > \mathrm{Ra}_c$.

Once convection is established, increasing the Rayleigh number drives the flow through a sequence of complex transitions. The initial steady rolls give way to time-periodic oscillations via Hopf bifurcations, eventually transitioning into a chaotic state (Lorenz, 1963; Libchaber et al., 1982; Pal et al., 2009). For fluids with $\mathrm{Pr} \approx 1$, the flow transitions to a chaotic state at relatively low Rayleigh numbers ($\mathrm{Ra} \sim 10^4 - 10^5$) (Libchaber et al., 1982). As the driving increases, it enters a regime of fully developed turbulence for $\mathrm{Ra} \gtrsim 10^8$, characterized by a well-mixed bulk and thin boundary layers (Lohse and Xia, 2010; Chillà and Schumacher, 2012; Verma et al., 2017). However, these values are moderate compared to natural flows. In geophysical and astrophysical systems, such as the Earth's outer core or the solar convection zone, the Rayleigh number reaches extreme values ranging from 10^{20} to 10^{24} (Ahlers et al., 2009; Schumacher and Sreenivasan, 2020).

A central theme in turbulence research is establishing scaling laws that relate these response parameters to the control parameters Ra and Pr. These relationships typically follow power-law forms

$$\mathrm{Nu} \sim \mathrm{Ra}^{a_1}\mathrm{Pr}^{b_1}, \quad \mathrm{Re} \sim \mathrm{Ra}^{a_2}\mathrm{Pr}^{b_2}. \tag{1.70}$$

Determining the exponents (e.g., a_1, a_2) is crucial for understanding the physics of turbulent convection and for extrapolating laboratory findings to the extreme regimes characteristic of natural flows (Ahlers et al., 2009; Lohse and Xia, 2010; Chillà and Schumacher, 2012; Verma et al., 2017).

Crucially, the power-law relations for Nu and Re are not merely empirical curve fits; they are constrained by exact mathematical relations derived from the governing Boussinesq equations. A pivotal theoretical framework was established by Shraiman and Siggia (1990), who emphasized the rigorous connection between global fluxes and dissipation rates in standard RBC. They utilized the exact relationships linking the volume-averaged kinetic energy dissipation rate ϵ_u and the thermal variance dissipation rate ϵ_θ to the global response parameters

$$\epsilon_u \equiv \nu \left\langle (\partial_i u_j)^2 \right\rangle_{V,t} = \frac{\nu^3}{d^4}\frac{\mathrm{Ra}}{\mathrm{Pr}^2}(\mathrm{Nu}-1), \tag{1.71}$$

$$\epsilon_\theta \equiv \kappa \left\langle (\partial_i T)^2 \right\rangle_{V,t} = \kappa \frac{\Delta T^2}{d^2}\mathrm{Nu}. \tag{1.72}$$

These relations demonstrate that the dissipation rates are determined entirely by Nu, Ra, and Pr. However, Shraiman and Siggia (1990) argued that the scaling exponents depend on the spatial distribution of this dissipation—specifically, whether it is dominated by the boundary layers or the bulk flow.

Building on these exact relations, Grossmann and Lohse (2000, 2001) developed the unifying Grossmann-Lohse (GL) theory for RBC. They formally decomposed the total dissipation rates into contributions from the bulk and the boundary layers, i.e., $\epsilon_u = \epsilon_{u,\text{bulk}} + \epsilon_{u,\text{BL}}$ and $\epsilon_\theta = \epsilon_{\theta,\text{bulk}} + \epsilon_{\theta,\text{BL}}$. By modeling the scaling behavior of these contributions in different limits (e.g., laminar boundary layer vs. turbulent bulk), the GL theory maps out a comprehensive phase diagram in the (Ra, Pr) space. The GL theory predicts multiple distinct scaling regimes characterized by unique power-law exponents, successfully reconciling the varying results observed in experiments and simulations. Bhattacharya et al. (2021b) revised the GL theory by using a global *dissipation-based* Reynolds number (Re_ϵ) rather than the traditional wind-based Reynolds number (Re_w). By defining the characteristic velocity scale directly through the kinetic energy dissipation rate, they eliminated the ambiguity associated with the large-scale circulation velocity and derived updated coefficients that offer improved predictive accuracy. The GL relations have been verified by many experiments and numerical simulations (Stevens et al., 2011, 2013). Recently, Bhattacharya et al. (2022) further extended this work by employing machine learning and deep neural networks to discover data-driven closures for Ra and Pr predictions.

In the following sections, we first present a detailed examination of the Nusselt number scaling, followed by a discussion of the Reynolds number scaling.

1.4.1 Nusselt number scaling

The theoretical foundations for heat transport scaling were established in the 1950s through arguments centered on the stability of the thermal boundary layers. Priestley (1954) argued that in the fully turbulent regime, the heat flux q should become independent of the layer height d, as the conducting plates are effectively decoupled by the well-mixed turbulent bulk. Dimensional analysis of this condition requires the heat flux to scale as $q \propto (\alpha g \kappa^2/\nu)^{1/3} (\Delta T)^{4/3}$. In non-dimensional terms, this yields the *classical* scaling law

$$\text{Nu} \sim \text{Ra}^{1/3}. \tag{1.73}$$

Malkus (1954) arrived at a similar result by proposing a *marginal stability* criterion, which was later formalized by Howard (1966) using a bubbling instability model. Howard postulated that heat accumulates in the conduction boundary layer of thickness δ until the local Rayleigh number of the layer, Ra_δ, exceeds a critical value $\mathrm{Ra}_c \sim 10^3$

$$\mathrm{Ra}_\delta = \frac{g\alpha(\Delta T/2)\delta^3}{\nu\kappa} \approx \mathrm{Ra}_c. \tag{1.74}$$

Assuming the heat transport is dominated by conduction across these marginal layers ($\mathrm{Nu} \approx d/2\delta$), substituting for δ recovers the scaling $\mathrm{Nu} \sim (\mathrm{Ra}/\mathrm{Ra}_c)^{1/3} \sim \mathrm{Ra}^{1/3}$. Physically, this implies that transport is limited solely by the thermal resistance of the laminar boundary layers, while the bulk remains isothermal.

Kraichnan (1962) challenged the universality of the classical regime. He proposed that at extremely high Rayleigh numbers, the strong shear generated by the large-scale wind would render the boundary layers turbulent. Under these conditions, the laminar sublayer thickness would vanish relative to the thermal boundary layer, removing the conduction bottleneck. Using mixing-length theory, where the eddy diffusivity scales with the distance from the wall, Kraichnan derived the *ultimate* regime scaling with a logarithmic correction

$$\mathrm{Nu} \sim \mathrm{Pr}^{1/2}\mathrm{Ra}^{1/2}(\ln \mathrm{Ra})^{-3/2}. \tag{1.75}$$

Note that the Prandtl number exponent in Kraichnan's derivation is regime-dependent; he predicted a scaling of $\mathrm{Pr}^{1/2}$ for low Prandtl numbers (specifically $\mathrm{Pr} \lesssim 0.15$, relevant to stellar interiors) and $\mathrm{Pr}^{-1/4}$ for moderate Prandtl numbers ($\mathrm{Pr} \gtrsim 0.15$, such as air or water). The form presented in Eq. 1.75 corresponds to the low-Pr limit. Asymptotically, as $\mathrm{Ra} \to \infty$, the logarithmic term becomes negligible, approaching the pure $\mathrm{Ra}^{1/2}$ scaling.

Spiegel (1963, 1971) derived a similar dependence $\mathrm{Ra}^{1/2}$ specifically for astrophysical fluids arguing that, in the limit of very large spatial scales, the heat flux must be independent of the microscopic fluid properties (ν and κ). The flux is instead determined by the free-fall velocity $U_f \sim \sqrt{g\alpha\Delta T d}$, leading to $q \sim \rho c_p U_f \Delta T$, or $\mathrm{Nu} \sim \sqrt{\mathrm{RaPr}}$. Complementing these phenomenological arguments, Howard (1963) employed a variational calculus to maximize the heat flux subject to the integral constraints of energy power. He established a rigorous upper bound on the heat transport, valid for arbitrary Ra

$$\mathrm{Nu} \leq \left(\frac{3}{64}\mathrm{Ra}\right)^{1/2}. \tag{1.76}$$

This bound confirmed that the transport cannot exceed the ultimate scaling limit. See also Doering et al. (2006) for later applications of variational principles for computing upper bounds on the Nusselt number and Doering (2020b) for a concise historical perspective.

The quest to observe this ultimate regime has driven decades of experimental research. Castaing et al. (1989) performed seminal experiments with helium gas over the range $4 \times 10^7 \lesssim \mathrm{Ra} \lesssim 6 \times 10^{12}$, identifying a *hard turbulence* regime characterized by a scaling exponent of $2/7 \approx 0.29$. This 2/7 scaling was theoretically rationalized by Shraiman and Siggia (1990), who accounted for the coupling between the thermal and viscous boundary layers. Further high-precision experiments by Niemela et al. (2000) in a large cryogenic helium tank reached $\mathrm{Ra} \sim 10^{17}$ but found a robust scaling of $\mathrm{Nu} \sim \mathrm{Ra}^{0.31}$ with no evidence of a transition to the 1/2 regime. Similarly, Urban et al. (2012) reported consistent classical behavior up to $\mathrm{Ra} \approx 10^{15}$.

In contrast, other experimental groups have reported evidence supporting the transition. Chavanne et al. (2001), and later Roche et al. (2001), observed a steepening of the Nu-Ra slope to an exponent of $\gamma \approx 0.38$ around $\mathrm{Ra} \approx 10^{11}$ to 10^{12} (depending on aspect ratio and Pr), interpreting this as the onset of the ultimate regime. He et al. (2012) performed high-precision experiments with sulfur hexafluoride (SF_6) and reported a similar transition to ultimate scaling at $\mathrm{Ra} \approx 10^{14}$. The discrepancies between these various high-Ra experiments have been attributed to subtle experimental factors, including differences in cell geometry, aspect ratio, sidewall leakage corrections, and finite plate conductivity effects (Ahlers et al., 2009; Chillà and Schumacher, 2012), leaving the experimental status of the ultimate regime inconclusive.

Numerical simulations have provided complementary insights, although 3D simulations are generally constrained to lower Ra than experiments. Direct numerical simulations (DNS) of RBC in three dimensions (3D) consistently support the classical scaling picture. Stevens et al. (2011) performed DNS in a cylindrical cell of aspect ratio $\Gamma = 0.5$ up to $\mathrm{Ra} = 2 \times 10^{12}$ and reported a scaling of $\mathrm{Nu} \sim \mathrm{Ra}^{0.31}$. Pushing to higher regimes, Iyer et al. (2020) employed a slender cylindrical domain with $\Gamma = 0.1$ to reach $\mathrm{Ra} = 10^{15}$. They recovered a classical scaling of $\mathrm{Nu} \sim \mathrm{Ra}^{0.331}$, finding no evidence of a transition to the ultimate regime. Recently, Samuel et al. (2024) and Shevkar et al. (2025) performed DNS in a $\Gamma = 4$ Cartesian box up to $\mathrm{Ra} = 10^{11}$, revealing that the boundary layers are in fact *fluctuation-dominated*, characterized by strong shear and intermittent plume detachments. They argue that despite these intense fluctuations, the boundary layers are marginally stable and do not undergo the shear instability envisioned by Kraichnan, thereby maintaining the classical heat transport bottleneck.

In the realm of two-dimensional (2D) RBC, Zhu et al. (2018) reported a distinct transition to the ultimate regime around $\mathrm{Ra} \approx 10^{13}$, observing a scaling of $\mathrm{Nu} \sim \mathrm{Ra}^{0.38}$ and the development of logarithmic mean temperature profiles. This result, however, has sparked significant controversy. Critics, such as Doering (2020a) and Lindborg (2023), have challenged these findings, attributing the apparent transition to insufficient statistical convergence and finite-time effects rather than a fundamental change in transport physics. The discrepancy between 2D and 3D RBC behaviors remains an active area of debate, highlighting the sensitivity of the ultimate regime to dimensionality and boundary conditions.

To decouple the effects of the boundary layer from the bulk, researchers have studied alternative convective systems. Lohse and Toschi (2003) introduced the concept of *periodic convection*, where the top and bottom walls are removed and replaced with periodic boundary conditions (while maintaining the destabilizing temperature gradient). In the absence of viscous boundary layers, these simulations exhibit clear ultimate scaling $\mathrm{Nu} \sim \mathrm{Ra}^{1/2}$ (Verma et al., 2012; Winchester et al., 2024). Similarly, systems with rough walls (Zhu et al., 2017) or internal heating (Lepot et al., 2014) have been shown to enhance heat transport efficiency, occasionally approaching the ultimate limit.

Finally, the context of compressible convection remains less explored. While the Boussinesq approximation is valid for the laboratory experiments discussed above, astrophysical flows involve strong density stratification. Early numerical works by John and Schumacher (2023a,b) simulated compressible convection up to $\mathrm{Ra} \approx 10^{7}$ and observed flow regimes distinct from RBC. Although theoretical arguments suggest that stratification might alter the boundary layer dynamics or the bulk mixing efficiency, there is a scarcity of data on heat transport scaling in stratified, fully compressible fluids at high Rayleigh numbers. In this thesis, we address this gap by performing direct numerical simulations (DNS) of compressible convection up to $\mathrm{Ra} = 10^{16}$ in two dimensions and $\mathrm{Ra} = 10^{13}$ in three dimensions. Our results conclusively demonstrate that the classical $\mathrm{Nu} \sim \mathrm{Ra}^{1/3}$ scaling persists even in these stratified regimes, ruling out a transition to the ultimate regime within the explored parameter space.

1.4.2 Reynolds number scaling

The Reynolds number, defined as $\mathrm{Re} = \tilde{U}d/\nu$, quantifies the intensity of flow turbulence, where $\tilde{U}$ is the characteristic root-mean-square velocity. In 3D RBC, a fundamental balance between the buoyancy force and non-linear inertial acceleration suggests a free-fall scaling of $\mathrm{Re} \sim \mathrm{Ra}^{1/2}$. However, for moderate Prandtl numbers ($\mathrm{Pr} \approx 1$), experimental and numerical studies typically report a lower exponent in the range of $0.42 - 0.46$ (Ahlers et al., 2009; Chillà and Schumacher, 2012). The GL theory explains this deviation by accounting for the dissipation in the boundary layers. As Ra increases and the flow becomes fully turbulent, the bulk drag is expected to dominate, and the scaling is predicted to asymptotically approach the free-fall limit of $\mathrm{Re} \sim \mathrm{Ra}^{1/2}$ (Grossmann and Lohse, 2001).

The scaling behavior changes drastically in 2D RBC due to fundamental differences in turbulence phenomenology. In 2D, the inverse energy cascade causes kinetic energy to accumulate at the largest scales, resulting in much stronger flow velocities than in 3D. Consequently, 2D simulations exhibit significantly steeper scaling exponents, typically $\mathrm{Re} \sim \mathrm{Ra}^{0.60}$ for no-slip boundaries (Schmalzl et al., 2004; van der Poel et al., 2013). For stress-free boundaries, Lindborg (2025) derived a rigorous theoretical scaling of $\mathrm{Re} \sim \mathrm{Ra}^{2/3}\mathrm{Pr}^{-1}$ based on the enstrophy budget, a result that has been confirmed by high-resolution numerical studies.

The extreme vigor of the 2D RBC at high Ra also introduces complex temporal dynamics. Pandey and Sreenivasan (2025) demonstrated that 2D RBC is characterized by exceedingly long transient times, where the flow can exhibit persistent oscillations or violent bursting events long after the initial saturation. They showed that the time required to reach a true statistically stationary state scales as $\tau \sim \mathrm{Ra}^{0.59}$ (for $\mathrm{Pr} = 0.1$) to $\tau \sim \mathrm{Ra}^{0.71}$ (for $\mathrm{Pr} = 1$). This implies that many reported high-Ra results in 2D RBC might suffer from insufficient time-averaging.

In summary, while the scaling laws for standard RBC are well-constrained by the GL theory and extensive DNS, the behavior in the limit of extreme driving and strong stratification remains an open frontier. The interplay between density stratification, compressibility, and turbulence presents a unique set of challenges that classical Boussinesq theories may not fully capture. Addressing these gaps requires a systematic investigation that extends the scaling analysis into the fully compressible regime, a task that demands both rigorous theoretical frameworks and high-performance numerical tools.

1.5 Goals of the thesis

This thesis presents three major contributions to the study of compressible turbulent convection and high-performance computational fluid dynamics:

- **Development of the high-performance solver DHARA:** Performing simulations of compressible convection at extreme Rayleigh numbers requires highly parallel solvers capable of handling stiff acoustic timescales. To this end, we present the solver DHARA, which was used to generate all the simulation data presented in this thesis. Built using a Python interface with custom CUDA kernels for computation and MPI for parallel communication, DHARA facilitates rapid prototyping while maintaining the high throughput required for DNS. All the simulations reported in this work were performed on GPUs using this solver. Beyond the central results of this thesis, the code was extensively used to investigate the Prandtl number dependence in compressible convection (Sharma et al., 2025; Pathak et al., 2025) and to study energy transfers in compressible turbulence (Singh et al., 2025). During the course of this work, the code was also significantly extended to include high-order finite volume methods, broadening its scope to shock-dominated flows. We demonstrate this new capability through high-resolution DNS of supersonic turbulence (turbulent Mach number, $M_t = 3.0$), establishing a robust computational framework for future investigations into energy scaling laws and shock dynamics. Considering its versatility and application across diverse flow regimes, the development of this code is a major outcome of this thesis.
- **Scaling laws in compressible convection at extreme Rayleigh numbers:** A central open question in thermal convection is whether compressibility alters the scaling laws of heat and momentum transport observed in RBC. In this thesis, we perform DNS of compressible convection (density contrast ≈ 10) up to $\mathrm{Ra} = 10^{16}$ in 2D and $\mathrm{Ra} = 10^{13}$ in 3D. A major outcome of this study is the confirmation of classical scaling in the compressible regime. We demonstrate that despite significant density variations, the bulk region remains effectively adiabatic. Consequently, we observe that the Nusselt number follows the classical scaling $\mathrm{Nu} \sim \mathrm{Ra}^{1/3}$, and the Reynolds number scales as $\mathrm{Re} \sim \mathrm{Ra}^{1/2}$ in both 2D and 3D. These results conclusively rule out a transition to the ultimate regime within the explored parameter space.
- **Comparative analysis of heat flux mechanisms:** This thesis also provides a mechanistic explanation for the observed scaling laws by performing a comparative analysis of compressible convection, RBC, and periodic convection (Lohse and

Toschi, 2003). To isolate the physical mechanism, we decompose the vertical heat flux into positive (upward) and negative (downward) contributions. We find that periodic convection, which lacks thermal plates, exhibits predominantly positive flux and follows the ultimate scaling $\mathrm{Nu} \sim \mathrm{Ra}^{1/2}$. In contrast, in RBC and compressible convection, the presence of thermal plates induces significant negative heat fluxes (e.g., by deflecting hot plumes downward). We demonstrate that the asymmetry between these positive and negative fluxes scales as $\mathrm{Ra}^{-0.20}$, which corrects the $\mathrm{Ra}^{1/2}$ dependence to the classical scaling $\mathrm{Nu} \sim \mathrm{Ra}^{0.30}$. This analysis reveals that the robustness of the classical regime arises from wall-induced flux cancellation in the bulk flow, challenging the prevailing view that the transition to the ultimate regime is dictated solely by boundary layer shear transitions.

1.6 Outline of the thesis

The outline of the rest of the thesis is as follows.

- In Chapter 2, we discuss the numerical formulation and software architecture of the solver DHARA, which uses a MacCormack-TVD (total variation diminishing) scheme to handle compressible flows. We describe the Python-based design utilizing CuPy for GPU acceleration, ensuring portability and high throughput. We demonstrate the code's performance, highlighting super-linear scaling on the CPU-based Shaheen III and robust scalability on the GPU-accelerated Frontier and Polaris supercomputers. Finally, we validate the solver against established benchmarks for compressible convection and turbulence.

- In Chapter 3, we present numerical simulations of compressible convection in box of aspect ratio $\Gamma = 4$, reaching $\mathrm{Ra} = 10^{15}$ in 2D and 10^{11} in 3D. We demonstrate that the bulk flow remains adiabatic, satisfying the Schwarzschild criterion. We observe significant flow asymmetry, where the bottom boundary layer is thinner and the turbulence is more vigorous than at the top due to density stratification. Despite these effects, we find that the heat transport follows near classical scaling ($\mathrm{Nu} \sim \mathrm{Ra}^{0.30}$) and the Reynolds number scales as $\mathrm{Re} \sim \mathrm{Ra}^{0.50}$, driven by a residual imbalance between pressure and buoyancy forces.

- In Chapter 4, we focus on the contributions of positive and negative heat fluxes to the total heat transport and their relation to the Nusselt number scaling. We compare our DNS of compressible and periodic convection (Lohse and Toschi, 2003) with high-fidelity RBC datasets from Samuel and Verma (2024) and Samuel (2023) for 2D, and Bhattacharya et al. (2021a) for 3D. We find that while periodic convection exhibits predominantly positive heat flux, RBC and compressible convection display nearly equal positive and negative fluxes up to $\mathrm{Ra} = 10^{16}$ (2D) and 10^{13} (3D). Analysis of the flux distributions reveals that positive fluxes possess longer tails; their difference scales as $\mathrm{Ra}^{-0.20}$, yielding the near classical $\mathrm{Nu} \sim \mathrm{Ra}^{0.30}$ scaling. These results indicate the likely absence of the ultimate regime, even in the presence of logarithmic boundary layers in 2D compressible convection.

- In Chapter 5, we extend the DHARA framework with a general-purpose, high-order finite volume module for compressible flows. We implement the Riemann-solver-free Kurganov-Tadmor scheme (Kurganov and Tadmor, 2000) integrated with weighted (WENO) (Borges et al., 2008) and targeted essentially non-oscillatory (TENO) reconstructions (Fu et al., 2016). Following validation against canonical benchmarks—such as the isentropic vortex, Kelvin-Helmholtz instability, and supersonic Taylor-Green vortex—we demonstrate the superior low-dissipation properties of the TENO schemes. Finally, we establish the solver's robustness in the high-Mach number regime through a high-resolution (1024^3) direct numerical simulation of supersonic turbulence at $M_t = 3.0$. This qualitative analysis demonstrates the code's capability to resolve complex shock structures, paving the way for future comprehensive studies on scaling laws and inter-scale energy transfers.

- In Chapter 6, we conclude the present study. We also outline the scope for future work building upon the findings of this thesis.

Chapter 2

Numerical method and DHARA fluid solver

The theoretical framework governing compressible convection, established in the previous chapter, comprises a system of coupled non-linear partial differential equations (see Eqs. 1.33–1.35). Due to the inherent non-linearity and the strong coupling between the momentum and energy equations, analytical solutions are intractable for the turbulent regimes of interest. Consequently, we must rely on high-fidelity numerical simulations to investigate the system dynamics.

In this chapter, we detail the numerical methodology employed to solve these equations. We begin by reviewing the historical evolution of numerical schemes for compressible convection, highlighting the specific challenges posed by acoustic waves and shock-like structures. This motivates our choice of the MacCormack-TVD scheme, which effectively balances accuracy and stability. Subsequently, we describe the architecture of our in-house solver, DHARA (derived from the Hindi word *dhara*, meaning 'flow' or 'stream'), focusing on its object-oriented design and optimization for GPU-accelerated supercomputers. This design philosophy aligns with the principle of *co-evolution* described by Dongarra and Keyes (2024), where the development of computational physics software is inextricably linked to the architectural constraints of high-performance computing hardware. Finally, we present extensive scaling results and rigorous validation tests against established benchmarks to demonstrate the solver's reliability.

2.1 Numerical approaches for compressible convection

The numerical solution of the compressible Navier-Stokes equations presents distinct challenges compared to its incompressible counterpart. While incompressible flows are governed by elliptic-parabolic equations requiring a Poisson solver for pressure, compressible flows are described by a coupled system of hyperbolic-parabolic equations (Anderson, 1992, 1995). In regimes characterized by high Reynolds (Re) and Rayleigh (Ra) numbers, the advective transport dominates over diffusion. Consequently, the system exhibits strong hyperbolic characteristics, admitting wave-like solutions (sound waves) and allowing for the formation of steep gradients or shock-like structures that require robust numerical treatment (Chorin and Marsden, 1993).

The simulation of compressible convection has a rich history, driven largely by the need to understand stellar and planetary interiors. Early efforts were constrained by the limited computational power of the time. Graham (1975) conducted one of the first numerical studies of two-dimensional compressible convection in a polytropic atmosphere. He employed the Lax-Wendroff finite difference scheme, a second-order accurate method capable of capturing the basic dynamics of the flow (Lax and Wendroff, 1960). His work highlighted the asymmetry between broad, slow upflows and narrow, fast downflows, establishing a foundational feature of stratified convection.

Subsequently, the field was significantly advanced by the work of the Toomre group. Hurlburt et al. (1984) performed high-resolution 2D simulations to study compressible convection. Using explicit finite difference schemes similar to Graham's, they elucidated the crucial role of downward-directed plumes and analyzed the resulting heat and kinetic energy fluxes. These studies, along with subsequent 3D work (Hurlburt et al., 1986), demonstrated that compressibility leads to a strong asymmetry between upflows and downflows, contrasting with the Boussinesq limit.

As computational capabilities expanded, researchers sought higher-order accuracy to resolve finer turbulent structures. The piecewise parabolic method (PPM), developed by Colella and Woodward (1984) and Woodward and Colella (1984), became a popular choice in the astrophysical community. This method is a higher-order extension of Godunov's scheme that reconstructs flow variables as parabolas within each grid cell. Porter and Woodward (2000) utilized PPM to study compressible convection at much higher resolutions, benefiting from the method's ability to capture sharp discontinuities with minimal numerical dissipation.

However, a distinct divergence exists in the methodology applied to astrophysical problems versus fundamental fluid dynamics. In astrophysical settings, such as the solar convection zone, the Rayleigh number is astronomical (Ra $\sim 10^{24}$), and the viscous dissipation scales are microscopically small. Resolving these scales directly is impossible. Therefore, many astrophysical simulations effectively solve the inviscid Euler equations or employ large-eddy simulation (LES) methods (Porter and Woodward, 2000; Miesch et al., 2000). In these models, the explicit viscosity μ and thermal conductivity K are often neglected, and the simulation relies on the inherent numerical viscosity of the scheme to dissipate energy at the grid scale (Porter and Woodward, 2000). While effective for modeling large-scale stellar dynamics, this approach makes the definition of an effective Rayleigh number ambiguous and grid-dependent.

In contrast, the objective of this thesis is to perform direct numerical simulations (DNS) where all relevant spatial and temporal scales are resolved. We aim to study the fundamental scaling laws of heat and mass transport. To do so precisely, we must retain the explicit viscous stress tensor and heat conduction terms in the governing equations. This allows us to simulate the flow using the exact specified control parameters, Ra and Pr, without relying on subgrid-scale models that artificially alter the fluid's effective viscosity or thermal diffusivity. This exact correspondence holds true provided the numerical grid is fine enough to resolve the smallest dissipative scales of the flow (Pope, 2000; Moin and Mahesh, 1998; Grötzbach, 1983).

Simulating these resolved viscous compressible flows requires a numerical scheme that balances accuracy, stability, and computational efficiency. Standard central-difference schemes, while non-dissipative, suffer from severe dispersion errors (Gibbs phenomenon) when handling sharp gradients inherent to high-speed compressible flows (Hirsch, 2007; Tannehill et al., 1997). Conversely, first-order upwind schemes are strictly stable but introduce excessive numerical diffusion, which can artificially dampen the turbulence and distort the effective Reynolds number (LeVeque, 2002; Anderson, 1995).

To address these challenges, we employ the MacCormack finite difference scheme combined with a total variation diminishing (TVD) mechanism. The standard MacCormack scheme is a widely used predictor-corrector method that is second-order accurate in both space and time (MacCormack, 1969). It is essentially a two-step variation of the Lax-Wendroff scheme but is significantly easier to implement as it does not require the computation of the Jacobian matrix. However, like all second-order linear schemes, it can generate spurious oscillations near steep gradients.

The TVD property, introduced by Harten (1983), ensures that the total variation of the solution does not increase over time, thereby preventing the generation of new numerical extrema. By adding a TVD flux-limiter correction to the standard MacCormack steps, we can suppress these oscillations without degrading the accuracy in smooth regions of the flow. This hybrid approach—MacCormack-TVD—was successfully applied to shallow water equations by Liang et al. (2007) and Ouyang et al. (2013), proving to be both robust and accurate.

In this thesis, we adapt the MacCormack-TVD scheme for the compressible Navier-Stokes equations with explicit diffusion terms. This method offers several advantages: (1) it is strictly stable and eliminates numerical oscillations; (2) it utilizes a collocated grid arrangement, simplifying the implementation compared to staggered grids; and (3) its explicit nature makes it highly suitable for massive parallelization on Graphics Processing Units (GPUs). We have implemented this scheme in our in-house solver, DHARA, which is described in detail in the following sections.

2.2 MacCormack-TVD scheme

We solve the nondimensional compressible Navier-Stokes equations [Eqs. (1.33)-(1.35)] using the MacCormack-TVD finite-difference scheme on a collocated grid (Ouyang et al., 2013; Yee, 1987; Liang et al., 2007). The scheme is explicit and second-order accurate in both space and time. We employ a non-uniform tangent-hyperbolic grid in the z-direction to increase resolution near the boundary layers, and uniform grids along the x and y directions.

All the governing equations are written in vectorial notation in the following conservative form (Ouyang et al., 2013):

$$\frac{\partial \mathbf{X}}{\partial t} + \sum_{\alpha} \frac{\partial \mathbf{F}_\alpha}{\partial x_\alpha} = \sum_{\alpha} \mathbf{S}_\alpha, \tag{2.1}$$

where $\alpha = 1, 2, 3$ represent the x, y, and z directions respectively. $\mathbf{X}$ is a column vector that contains the conservative variables: density ρ, momentum density ρu_α, and total energy density E. $\mathbf{F}_\alpha$ and $\mathbf{S}_\alpha$ are the respective flux vectors and source term vectors

(Anderson, 1992). They are defined as

$$\mathbf{X} = \begin{bmatrix} \rho \\ \rho u_x \\ \rho u_y \\ \rho u_z \\ E \end{bmatrix}; \quad \mathbf{S}_1 = \begin{bmatrix} 0 \\ f_1 \\ 0 \\ 0 \\ 0 \end{bmatrix}; \quad \mathbf{S}_2 = \begin{bmatrix} 0 \\ 0 \\ f_2 \\ 0 \\ 0 \end{bmatrix}; \quad \mathbf{S}_3 = \begin{bmatrix} 0 \\ 0 \\ 0 \\ f_3 \\ 0 \end{bmatrix}, \tag{2.2}$$

and the flux vectors in the three spatial directions are

$$\mathbf{F}_\alpha = \begin{bmatrix} \rho u_\alpha \\ \rho u_x u_\alpha - \tau_{x\alpha} \\ \rho u_y u_\alpha - \tau_{y\alpha} \\ \rho u_z u_\alpha - \tau_{z\alpha} + \delta_{3\alpha} p \\ u_\alpha (E + p) - \frac{1}{\epsilon D \sqrt{\mathrm{Ra} Pr}} \frac{\partial T}{\partial x_\alpha} - \sum_\beta u_\beta \tau_{\beta\alpha} \end{bmatrix}. \tag{2.3}$$

For natural convection with gravity acting in the $-\hat{z}$ direction, the body force components are $f_1 = 0$, $f_2 = 0$, and $f_3 = -\rho/\epsilon$.

To evolve the system in time, we employ the Strang operator-splitting method. This technique splits the three-dimensional problem into a sequence of one-dimensional problems. While computationally more expensive than a direct 3D update due to the increased number of intermediate steps, this splitting is essential for numerical stability. It allows the scheme to be governed by the less restrictive one-dimensional Courant-Friedrichs-Lewy (CFL) condition ($Co \leq 1$) rather than the stricter multidimensional stability limit (Strang, 1968; LeVeque, 2002). By applying the operators in a symmetric sequence, we maintain second-order accuracy in time. The split equations are

$$\frac{\partial \mathbf{X}}{\partial t} + \frac{\partial \mathbf{F}_1}{\partial x_1} = \mathbf{S}_1; \quad \frac{\partial \mathbf{X}}{\partial t} + \frac{\partial \mathbf{F}_2}{\partial x_2} = \mathbf{S}_2; \quad \frac{\partial \mathbf{X}}{\partial t} + \frac{\partial \mathbf{F}_3}{\partial x_3} = \mathbf{S}_3. \tag{2.4}$$

The fields in $\mathbf{X}$ are discretized in space, where the value at grid point (i, j, k) is denoted by $\mathbf{X}_{ijk}$. The time step is denoted by the superscript (n). The full time-stepping of $\mathbf{X}_{ijk}$ from step (n) to $(n + 1)$ is achieved by the symmetric sequence (Ouyang et al., 2013)

$$\mathbf{X}_{ijk}^{(n+1)} = \mathbf{L}_x \left(\frac{\delta t}{2}\right) \mathbf{L}_y \left(\frac{\delta t}{2}\right) \mathbf{L}_z \left(\frac{\delta t}{2}\right) \mathbf{L}_z \left(\frac{\delta t}{2}\right) \mathbf{L}_y \left(\frac{\delta t}{2}\right) \mathbf{L}_x \left(\frac{\delta t}{2}\right) \mathbf{X}_{ijk}^{(n)}, \tag{2.5}$$

where δt is the global time-step, and $\mathbf{L}_\alpha(\Delta t)$ represents the one-dimensional difference operator in the α-direction for a duration Δt.

Each operator $\mathbf{L}_\alpha$ consists of a predictor step, a corrector step, and a TVD regularization step. For example, the operator in the z-direction ($\alpha = 3$) is evaluated as follows

1. Predictor Step: A provisional value $\mathbf{X}^P$ is computed using a backward finite difference approximation for the flux derivatives

$$\mathbf{X}^P_{ijk} = \mathbf{X}^{(n)}_{ijk} - \frac{\delta t}{2}\left(\frac{\mathbf{F}^{(n)}_{\alpha,ijk} - \mathbf{F}^{(n)}_{\alpha,ij(k-1)}}{\delta x_\alpha}\right) + \frac{\delta t}{2}\mathbf{S}^{(n)}_{\alpha,ijk}. \tag{2.6}$$

2. Corrector Step: Using the predicted values, a corrector value $\mathbf{X}^C$ is computed using a forward finite difference approximation

$$\mathbf{X}^C_{ijk} = \mathbf{X}^{(n)}_{ijk} - \frac{\delta t}{2}\left(\frac{\mathbf{F}^P_{\alpha,ij(k+1)} - \mathbf{F}^P_{ijk}}{\delta x_\alpha}\right) + \frac{\delta t}{2}\mathbf{S}^P_{\alpha,ijk}. \tag{2.7}$$

Treatment of Viscous Terms: A critical aspect of applying the MacCormack scheme to the Navier-Stokes equations is the discretization of the second-order diffusion terms (viscous stresses and heat conduction) inside the flux vectors. When applying the operator in a specific direction (e.g., the z-direction sweep $\mathbf{L}_z$), the derivatives inside the flux vector $\mathbf{F}_3$ are treated as follows to ensure stability.

i) Normal Derivatives: The derivatives with respect to the sweep direction (e.g., $\partial_z u_z$, $\partial_z T$) are approximated using one-sided differences opposing the flux divergence. Specifically, in the predictor step where the flux divergence $\partial_z \mathbf{F}_3$ is approximated using a backward difference, the internal normal derivatives are computed using a forward difference. Conversely, in the corrector step where the flux divergence is forward, the internal normal derivatives use a backward difference. This alternating pattern prevents the odd-even decoupling of the grid solution (Tannehill et al., 1997; Anderson, 1995).

ii) Transverse and Mixed Derivatives: The derivatives with respect to the transverse directions (e.g., $\partial_x u_x$, $\partial_y u_y$) and the mixed derivative terms (e.g., $\partial_x u_z$) appearing within $\mathbf{F}_3$ are computed using standard central difference approximations in both steps.

3. Averaging and TVD Correction: The standard MacCormack solution is the average of the predictor and corrector steps. To prevent numerical oscillations, a TVD term

$\mathbf{T}_{ijk}$ is added

$$\mathbf{X}_{ijk}^{(n+1/2)} = \frac{\mathbf{X}_{ijk}^{P} + \mathbf{X}_{ijk}^{C}}{2} + \mathbf{T}_{ijk}^{n+1/2}. \tag{2.8}$$

The TVD correction term is defined based on the flux limiter theory (Yee, 1987; Ouyang et al., 2013)

$$\begin{aligned} \mathbf{T}_{ijk}^{n+1/2} &= G(r_{ijk}^{+} + r_{ij(k+1)}^{-})\ \delta\mathbf{X}_{ij(k+1/2)}^{n} - \\ &\quad G(r_{ij(k-1)}^{+} + r_{ijk}^{-})\ \delta\mathbf{X}_{ij(k-1/2)}^{n}, \end{aligned} \tag{2.9}$$

where the local solution differences are

$$\delta\mathbf{X}_{ij(k+1/2)}^{n} = \mathbf{X}_{ij(k+1)}^{n} - \mathbf{X}_{ijk}^{n}, \tag{2.10}$$

$$\delta\mathbf{X}_{ij(k-1/2)}^{n} = \mathbf{X}_{ijk}^{n} - \mathbf{X}_{ij(k-1)}^{n}. \tag{2.11}$$

The sensor functions $r_{ijk}^{\pm}$ monitor the smoothness of the solution by comparing gradients

$$r_{ijk}^{\pm} = \frac{\left(\delta\mathbf{X}_{ij(k-1/2)}^{n}, \delta\mathbf{X}_{ij(k+1/2)}^{n}\right)}{\left(\delta\mathbf{X}_{ij(k\pm1/2)}^{n}, \delta\mathbf{X}_{ij(k\pm1/2)}^{n}\right)}. \tag{2.12}$$

Here, the bracket $(\mathbf{A}, \mathbf{B})$ indicates the dot product between vectors $\mathbf{A}$ and $\mathbf{B}$. The function $G(x)$ determines the strength of the artificial dissipation added to smooth out oscillations

$$G(x) = 0.5C(1 - \phi(x)), \tag{2.13}$$

where $\phi(x) = \max(0, \min(2x, 1))$ is the *minmod flux limiter function*. The coefficient C depends on the local Courant number $\mathrm{Co}_\alpha = (|u_\alpha| + c_s)\delta t/\delta x_\alpha$ (where $c_s = \sqrt{\gamma p/\rho}$ is the sound speed)

$$C = \begin{cases} \mathrm{Co}_\alpha(1 - \mathrm{Co}_\alpha), & \mathrm{Co}_\alpha \le 0.5 \\ 0.25, & \mathrm{Co}_\alpha > 0.5 \end{cases}. \tag{2.14}$$

Identical procedures are applied for the $\mathbf{L}_x$ and $\mathbf{L}_y$ operators. The TVD correction acts as a smart artificial viscosity: in smooth regions where the limiter $\phi(x) \approx 1$, the correction term vanishes, preserving second-order accuracy. In regions with steep gradients or discontinuities, the limiter activates, adding just enough dissipation to enforce the TVD property and prevent non-physical oscillations.

With the numerical integration scheme established, we now define the specific initial configurations and boundary conditions required to close the problem.

2.3 Initial values and boundary conditions

To initialize the simulation, we superimpose small velocity perturbations onto a static, conductive background state. The reference conductive state corresponds to the hydrostatic and thermal equilibrium solution derived in Chapter 1 (see Eq. 1.24 and 1.25). The nondimensional temperature profile $T_0(z)$ decreases linearly from the bottom to the top plate

$$T_0(z) = 1 - (\epsilon + D)z, \tag{2.15}$$

where ϵ is the superadiabaticity parameter and D is the dissipation number. The corresponding density profile $\rho_0(z)$ follows the polytropic relation determined by the hydrostatic balance

$$\rho_0(z) = [T_0(z)]^m, \tag{2.16}$$

where m is the polytropic index of the background state (see Sec. 1.2.2 and Eq. 1.26), defined as

$$m = \frac{\gamma D}{(\gamma - 1)(\epsilon + D)} - 1. \tag{2.17}$$

The static pressure profile is determined by the equation of state

$$p_0(z) = \frac{(\gamma - 1)}{\gamma \epsilon D}\rho_0(z)T_0(z) = \frac{(\gamma - 1)}{\gamma \epsilon D}[T_0(z)]^{m+1}. \tag{2.18}$$

To trigger convective instability, we introduce small-amplitude velocity perturbations to this static background. The initial velocity components are set as

$$u_x = A \sin\left(\frac{2\pi x}{\Gamma_x}\right) \sin\left(\frac{2\pi y}{\Gamma_y}\right) \sin(\pi z), \tag{2.19}$$

$$u_y = A \sin\left(\frac{2\pi x}{\Gamma_x}\right) \sin\left(\frac{2\pi y}{\Gamma_y}\right) \sin(\pi z), \tag{2.20}$$

$$u_z = A \cos\left(\frac{2\pi x}{\Gamma_x}\right) \cos\left(\frac{2\pi y}{\Gamma_y}\right) \sin(\pi z), \tag{2.21}$$

where A is the perturbation amplitude (typically 10^{-4}), and Γ_x, Γ_y are the horizontal aspect ratios of the rectangular box.

The boundary conditions are crucial for the stability and physical accuracy of the simulation. We take periodic boundary conditions for all variables in the horizontal directions (x and y). For the temperature field, we impose fixed isothermal conditions at the top and bottom plates

$$T(x, y, z = 0) = 1, \quad T(x, y, z = 1) = 1 - (\epsilon + D). \tag{2.22}$$

For the velocity field, we enforce no-slip conditions at the top and bottom plates

$$\mathbf{u}(x, y, z = 0) = \mathbf{u}(x, y, z = 1) = 0. \tag{2.23}$$

The boundary condition for density is more complex because it is coupled to the momentum conservation equation. Unlike in incompressible flows where density is effectively constant, here the density at the wall must satisfy the vertical momentum balance. At the boundaries ($z = 0$ and $z = 1$), the no-slip condition ($\mathbf{u} = 0$) implies that the advective and time-derivative terms vanish. Thus, the vertical momentum equation simplifies to a balance between the pressure gradient, gravity, and the viscous stress gradient

$$\frac{\partial p}{\partial z} = -\frac{\rho}{\epsilon} + \frac{\partial \tau_{zz}}{\partial z}. \tag{2.24}$$

Using the equation of state $p = (\gamma - 1)\rho T/(\gamma \epsilon D)$, we can express $\partial p/\partial z$ in terms of ρ and T. We substitute this into Eq. (2.24) and discretize the resulting expression to update the density at the boundaries. To maintain numerical stability consistent with the MacCormack scheme, we utilize second-order forward and backward difference approximations at the bottom ($z = 0$) and top ($z = 1$) boundaries, respectively, to compute these vertical gradients.

Since we employ periodic boundary conditions in the horizontal directions and no-slip conditions at the vertical boundaries, there is zero net mass flux into or out of the domain ($\oint \rho \mathbf{u} \cdot \mathbf{n} \, dA = 0$). Consequently, the total mass of the fluid in the domain is strictly conserved throughout the simulation. It is therefore critical to initialize the simulation with the correct equilibrium density profile, ρ_0. The initial total mass M is then determined by integrating the background density profile $\rho_0(z)$ [Eq. (2.16)] over the domain volume V

$$M = \int_V \rho_0(z) \, dV = \Gamma_x \Gamma_y \int_0^1 [1 - (\epsilon + D)z]^m \, dz. \tag{2.25}$$

Evaluating this integral yields the conserved total mass of the system

$$M = \Gamma_x \Gamma_y \frac{1 - (1 - \epsilon - D)^{m+1}}{(m + 1)(\epsilon + D)}. \tag{2.26}$$

With the numerical framework and problem configuration fully established, we now turn to the computational implementation of these methods in our high-performance fluid solver.

2.4 DHARA code for compressible convection

We have developed DHARA, a modular and object-oriented fluid solver written in Python, to simulate the compressible Navier-Stokes equations. While Python is traditionally viewed as a high-level scripting language, DHARA leverages the modern scientific Python ecosystem to combine rapid prototyping capabilities with the raw performance of compiled C++/CUDA kernels. This hybrid approach, often termed *scripting-based HPC*, balances developer productivity with hardware performance and has been successfully validated for GPU computing by Klöckner et al. (2012) The solver is built with a strong emphasis on vectorized operations and memory efficiency to handle large-scale simulations effectively.

2.4.1 Code structure and libraries

DHARA is built upon a stack of open-source scientific computing libraries that encapsulate complex hardware details while delivering high performance. For mathematical operations on standard CPUs, it utilizes `NumPy` (Harris et al., 2020). Although Python is an interpreted language, `NumPy` achieves near-native C/Fortran speeds for array operations by leveraging highly optimized, pre-compiled BLAS (Basic Linear Algebra Subprograms) and LAPACK libraries under the hood. For GPU acceleration, the solver employs the `CuPy` library (Okuta et al., 2017), which provides a GPU-optimized drop-in replacement for `NumPy`. While `CuPy` natively targets NVIDIA GPUs via the CUDA toolkit, it also supports AMD GPUs through the ROCm (Radeon Open Compute) platform. This versatile dual-backend design allows the exact same codebase to execute efficiently on workstation CPUs, NVIDIA-based clusters (like Polaris), and AMD-based exascale systems (like Frontier) with minimal modification.

For high-performance input/output operations, the solver utilizes `h5py`, which provides a Pythonic interface to the HDF5 (Hierarchical Data Format version 5) library. HDF5 is the standard for high-performance computing data storage, allowing for the efficient, parallel reading and writing of massive, complex datasets in a self-describing binary format.

The code follows a strict object-oriented design to enforce separation of concerns and modularity. This architectural strategy addresses the software engineering challenges inherent in modern multiphysics simulations, where managing complexity is as critical as algorithmic performance (Keyes et al., 2013). The core functionalities are encapsulated in the following classes.

- **Grid Class:** Manages the computational mesh, coordinates domain decomposition, and establishes the MPI topology for parallel execution.
- **Library Module:** Serves as the mathematical engine of the solver. It contains highly optimized finite-difference operators for computing spatial derivatives (first and second order), as well as the implementation of the TVD flux limiters. These operators are designed to be generic, allowing them to be reused across different physics solvers.
- **Solver Class:** Contains the physics kernels specific to compressible convection. It orchestrates the simulation by calling the library operators to implement the time-integration loops, the MacCormack-TVD predictor-corrector steps, and the calculation of fluxes and source terms.
- **IO Class:** Handles all data management tasks. This includes loading initial conditions and saving full 3D flow fields in the HDF5 format for checkpoints and restart capabilities. Crucially, it manages *in situ* analysis to mitigate storage bottlenecks. This involves computing and saving global time series diagnostics (e.g., Nusselt number, Reynolds number, kinetic energy), surface fluxes, and coarse-grained 2D slices or downsampled 3D volumes specifically for visualization plots and movie generation.

2.4.2 Parallelization strategy

To enable simulations at the scale of 1024^3 grid points and beyond, DHARA employs a robust distributed parallelization strategy utilizing `mpi4py` (Dalcín et al., 2008) for efficient MPI communications. The domain decomposition strategy is adapted based on the hardware architecture to balance communication overhead with memory access efficiency.

For CPU-based executions, which often involve hundreds of thousands of cores, we employ a *pencil decomposition* (2D decomposition). In this approach, the domain is partitioned along two spatial directions (typically y and z), resulting in long, thin data pencils aligned with the x-axis. This prevents the subdomains from becoming too thin for the numerical stencil, a common limitation of 1D decomposition at this scale.

In contrast, for GPU-based executions, we utilize a *slab decomposition* (1D decomposition) along the x-direction. Since the number of GPU ranks (e.g., thousands) is typically orders of magnitude lower than the number of CPU cores for a comparable problem size, slab decomposition remains viable and efficient. This strategy simplifies the communication topology, as each rank only exchanges data with two neighbors (left and right). Furthermore, it ensures that large contiguous blocks of memory are processed, maximizing the throughput of the GPU's high-bandwidth memory (HBM).

At each time step, ghost cells (halos) at the subdomain boundaries are exchanged between neighboring ranks to maintain the stencil connectivity required by the high-order finite-difference scheme. For high-performance I/O, we utilize the `h5py-parallel` library, which interfaces with the HDF5 binary data format. This setup allows for parallel file writing, where multiple MPI ranks write to a single shared file simultaneously using independent pointers, significantly reducing the wall-clock time spent on checkpointing large terabyte-scale datasets.

2.4.3 Optimization strategies

While DHARA is designed to be portable across hardware architectures, it is important to note that all production simulations presented in this thesis were conducted exclusively on GPU-accelerated clusters. Consequently, the optimization strategies discussed here focus primarily on maximizing throughput on modern GPU architectures (NVIDIA A100 and AMD MI250X), although the underlying principles apply equally to high-performance CPU clusters.

Achieving peak performance on these devices requires minimizing data movement, as finite-difference solvers are typically bound by memory bandwidth rather than compute capability. This optimization is driven by the widening gap between processor speed and memory access latency, classically referred to as the *Memory Wall* (Wulf and McKee, 1995). In the exascale era, the primary energy and time cost in a simulation is often not the floating-point arithmetic, but the movement of data (Dongarra et al., 2011). In a standard Python/NumPy style implementation, an arithmetic operation like `A = B * C + D` triggers the creation of temporary intermediate arrays for each binary operation (e.g., one temporary array for `B * C` and another for the addition). This leads to excessive memory allocation overhead and redundant read/write cycles to the global memory.

This performance penalty is particularly severe in GPU environments using libraries like CuPy. In such a framework, every individual arithmetic operator in a high-level expression triggers a separate CUDA kernel launch. For a composite operation like `A = B * C + D`, the system must launch a multiplication kernel followed by an addition kernel. This fragmentation introduces a two-fold overhead: first, the latency associated with scheduling and launching multiple kernels; and second, the inability to perform *kernel fusion*. Without fusion, the GPU is forced to repeatedly fetch operands from the slow global memory into registers and write intermediate results back to memory for every step, rather than keeping the data in the fast registers to compute the entire expression in a single pass.

A critical optimization in DHARA is the use of kernel fusion to mitigate this bottleneck. We employ `cupy.ElementwiseKernel`, which compiles complex, element-wise algebraic expressions into a single optimized CUDA/ROCm kernel at runtime. This allows the operation to be evaluated in a single pass over the data residing in memory, keeping intermediate results in fast registers rather than writing them back to global memory.

For example, the calculation of the vertical convective flux for 2D convection involves mixing momentum, energy, and density terms. We implement this as a fused kernel, `compute_vertical_flux_2d`, which computes the flux components for the continuity, momentum, and energy equations simultaneously.

```
compute_vertical_flux_2d = ncp.ElementwiseKernel(
    'T rho, T ux, T uz, T temp, T z, float64 a1, float64 a2, float64 a3',
    'T flux_rho, T flux_mom_x, T flux_mom_z, T flux_eng',
    '''
    // Continuity flux: rho * uz
    flux_rho = rho * uz;

    // Horizontal momentum flux: rho * uz * ux
    flux_mom_x = rho * uz * ux;

    // Vertical momentum flux: rho * (uz^2 + p), where p ~ temp
    flux_mom_z = rho * (uz * uz + a1 * temp);

    // Energy flux: rho * uz * H, where H is enthalpy
    flux_eng = rho * uz * (0.5 * (ux * ux + uz * uz) + a2 * temp + a3 * z);
    ''',
    'compute_vertical_flux_2d'
)
```

LISTING 2.1: Fused kernel for vertical convective flux computation in 2D.

In this kernel, `flux_rho` through `flux_eng` represent the flux components for density, x-momentum, z-momentum, and energy, respectively. By fusing these operations, we achieve significant performance gains. Benchmarking on an NVIDIA A100 GPU demonstrates a 200× speedup compared to a single-core execution on an AMD EPYC 7543 processor.

Beyond memory optimization, efficient parallelization on thousands of processors (CPUs or GPUs) requires not just distributing the data, but also hiding the latency of communication behind useful computation. We employ `mpi4py` for distributed parallelism, utilizing *non-blocking* MPI primitives (`Isend` and `Irecv`) to overlap the exchange of ghost cells (halos) with the computation of the internal domain.

The strategy relies on splitting the computational domain into boundary points (which depend on ghost data from neighbors) and interior points (which do not). At the beginning of a timestep, we initiate the non-blocking transfer of boundary data. While the data is traveling through the interconnect, the compute device immediately proceeds to calculate derivatives for the vast majority of grid points located in the interior of the subdomain. By the time the interior computation finishes, the communication is typically complete, allowing us to finalize the timestep by computing the boundaries. This overlap is illustrated in the following pseudo-code:

```
# 1. Initiate non-blocking communication for ghost cells
req_send = comm.Isend(send_buffer, dest=neighbor_rank)
req_recv = comm.Irecv(recv_buffer, source=neighbor_rank)

# 2. Compute interior points (Independent of ghost cells)
# The CPU/GPU is kept busy here while data travels through the network
compute_derivatives(domain_interior)

# 3. Wait for communication to complete (Latency hidden by step 2)
MPI.Wait(req_send)
MPI.Wait(req_recv)

# 4. Update ghost cells and compute boundary points
update_ghost_cells(recv_buffer)
compute_derivatives(domain_boundary)
```

LISTING 2.2: Pseudo-code demonstrating communication-computation overlap strategy.

This latency-hiding technique is critical for maintaining strong scaling efficiency on leadership-class systems, as it ensures that the compute units are rarely idling while waiting for network transfers.

2.5 Computational performance

To validate the capability of DHARA to handle extreme-scale simulations, we performed extensive scaling studies on leadership-class computing facilities. Before discussing the scalability on thousands of nodes, it is instructive to quantify the baseline performance gain offered by modern accelerators.

In single-device benchmarks, we compared the performance of a single NVIDIA A100 GPU against a single core of an AMD EPYC 7543 processor. For sufficiently large grid sizes that saturate the GPU memory bandwidth (typically 128^3 for 3D or 1024^2 for 2D configurations), DHARA achieves a speedup of approximately 200× on the GPU. This massive throughput advantage justifies our primary focus on GPU-based production runs. However, ensuring efficient scaling on traditional CPU architectures remains vital for code portability and validation on general-purpose clusters.

2.5.1 CPUs performance

We benchmarked the code on the Shaheen III supercomputer at King Abdullah University of Science and Technology (KAUST). Shaheen III is a Cray EX system where each node is equipped with dual AMD EPYC 9654 “Genoa” processors, providing a total of 192 physical cores and 384 GB of DDR5 memory per node.

The scaling tests were pushed to extreme limits, varying the grid size from 576^3 to 9216^3. We utilized resources ranging from a single node up to 4,096 nodes, effectively scaling the application to 786,432 CPU cores. This configuration encompasses approximately 90% of the total computing resources of Shaheen III. Notably, DHARA holds the distinction of being the first code to successfully scale across the full machine, thereby serving as a benchmark for the supercomputer’s operational performance at the system limit. For these runs, we employed a pencil decomposition strategy where the global domain is partitioned into uniformly sized pencils. To accommodate the high core count per node, the processor grid dimensions (P_x, P_y) were set as factors of 192 to ensure optimal load balancing.

The scaling results are presented in Fig. 2.1, which evaluates performance in two distinct regimes: strong scaling and weak scaling. First, we examined strong scaling (solid lines), where the global problem size remains fixed while the number of computing cores increases. In the ideal scenario, the wall-clock time per timestep, t, decreases linearly with the number of cores n (i.e., $t \propto n^{-1}$). However, we consistently observed *super-linear scaling*,

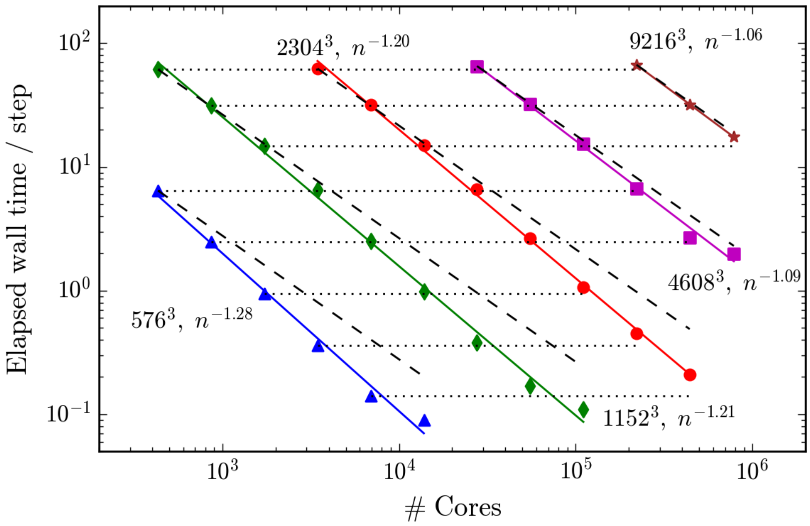

FIGURE 2.1: Scaling performance of DHARA on Shaheen III for grid sizes ranging from 576^3 to 9216^3. The figure demonstrates both strong and weak scaling regimes. The dashed lines indicate ideal linear strong scaling ($t \propto n^{-1}$), while dotted lines represent the weak scaling trends. Solid lines with markers show the observed performance, which exhibits super-linear scaling (e.g., $n^{-1.20}$ for 2304^3).

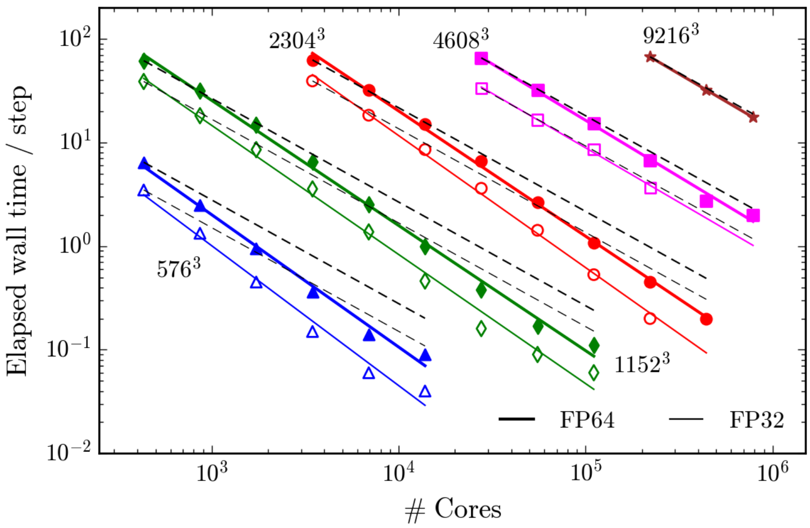

FIGURE 2.2: Comparison of strong scaling performance between double precision (FP64) and single precision (FP32) on Shaheen III. Both precisions exhibit super-linear scaling, with FP32 computations completing approximately twice as fast as their FP64 counterparts.

where the performance gains exceed the theoretical linear baseline. This phenomenon is frequently observed in explicit finite-difference and stencil-based applications (Hager and Wellein, 2010). It arises when the domain decomposition reduces the local subdomain size sufficiently such that the working set fits entirely within the processor's high-speed cache hierarchy (L2/L3), thereby mitigating the memory bandwidth bottleneck. This mechanism is rigorously verified through cache-miss profiling in the subsequent analysis.

As shown in the Fig. 2.1, the scaling exponents are significantly steeper than -1; for instance, the 2304^3 case scaled as $n^{-1.20}$, and the 1152^3 case as $n^{-1.21}$. Second, we assessed weak scaling (dotted lines), where the workload per core is held constant while the global problem size increases proportionally with the core count. In an ideal weak-scaling regime, the time-to-solution should remain constant regardless of the scale. The dotted lines in Fig. 2.1 illustrate that DHARA maintains a nearly constant time-per-step as the simulation scales up, demonstrating excellent parallel efficiency and the capability to handle massive domain sizes without incurring prohibitive communication penalties.

We further evaluated the impact of floating-point precision on performance, as shown in Fig. 2.2. The solver maintains its super-linear scaling characteristics in both double (FP64) and single (FP32) precision. Notably, the wall-clock time for the FP32 simulations is approximately half that of the FP64 runs. In turbulent flow simulations, the numerical round-off errors introduced by single-precision arithmetic are typically orders of magnitude smaller than the physical chaotic fluctuations being resolved. Consequently, the global statistical quantities of interest (such as mean Nusselt and Reynolds numbers) remain practically indistinguishable between FP32 and FP64 computations. The reliability of FP32 in preserving the statistical fidelity of fully developed turbulence has been well documented and validated in previous finite-difference and spectral DNS studies (Homann et al., 2007; Costa, 2018). This allows us to leverage the 2× throughput advantage of single precision for efficient data generation while maintaining statistical fidelity.

To rigorously identify the source of the super-linear performance boost, we profiled the code utilizing the TAU (Tuning and Analysis Utilities) performance system. We tracked the performance metrics for a fixed 1152^3 grid scaling from 9 nodes (1,728 cores) to 288 nodes (55,296 cores).

To analyze the scaling performance, we decompose the total execution time per time step into pure computation time (t_{comp}) and communication overhead (t_{comm}). Figure 2.3(a) presents this breakdown. We observe that t_{comp} exhibits excellent strong scaling, dropping

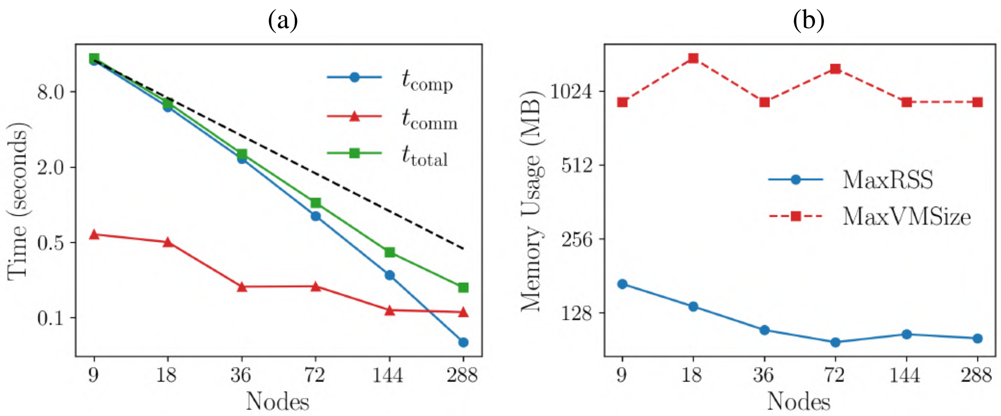

FIGURE 2.3: Profiling metrics for the 1152^3 case on Shaheen III. (a) Breakdown of wall time into computation (t_{comp}) and communication (t_{comm}) per timestep. (b) Memory usage per core (MaxRSS and MaxVMSize) as a function of node count.

drastically from 14.21 seconds at 9 nodes to just 0.08 seconds at 288 nodes. The communication cost remains sub-dominant throughout most of the scaling range; however, it inevitably becomes comparable to computation at the highest node counts, as evidenced by the ratio $t_{\mathrm{comp}}/t_{\mathrm{comm}}$ decreasing from 24.50 to 0.57.

To distinguish between architectural efficiency and memory capacity effects, we track two key metrics: Maximum Resident Set Size (`MaxRSS`), which represents the peak physical RAM used by a process, and Virtual Memory Size (`MaxVMSize`), which denotes the total reserved virtual address space. Figure 2.3(b) illustrates the behavior of these metrics during the scaling test. As the node count increases, the local grid size per core shrinks drastically from $24 \times 32 \times 1152$ (approx. 337.5 MB, 9 nodes) to $4 \times 6 \times 1152$ (10.5 MB, 288 nodes). Despite this reduction in local data volume, the `MaxRSS` per core remains stable across all runs, hovering approximately around 100 MB. This value is orders of magnitude lower than the available 384 GB of DDR5 memory per node, confirming that the simulation is far from being capacity-bound. The stability of `MaxRSS` confirms that the observed performance gains are not driven by the alleviation of memory bottlenecks or the avoidance of page swapping, but are rather attributable to the algorithmic efficiency of the decomposition strategy.

The root cause of the super-linear scaling is revealed in Fig. 2.4, which plots the L1 and L2 cache misses. The profiling data confirms that the speedup is driven by the hierarchical memory architecture of the AMD EPYC processors.

At 288 nodes, the local data footprint per core (10.5 MB) is still larger than the L2 cache (1 MB/core). However, the working set for individual kernels becomes small enough to

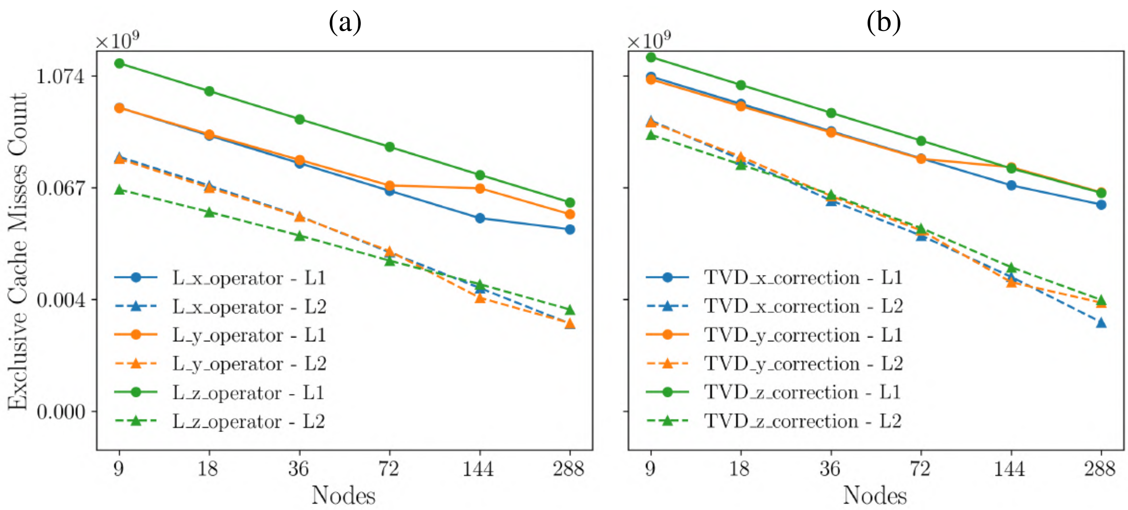

FIGURE 2.4: Exclusive L1 and L2 cache misses for key kernels (Solid: L1, Dashed: L2) as a function of node count. Panel (a) shows cache misses for the finite-difference derivative operators (`L_operator`) in all directions. Panel (b) shows cache misses for the TVD flux correction operators (`TVD_correction`). The significant reduction in misses correlates directly with the super-linear speedup.

fit entirely within the fast L1 (64 KB) or L2 caches. Panel (a) of Fig. 2.4 demonstrates a sharp decline in exclusive L1 and L2 cache misses for the derivative operators (`L_x`, `L_y`, `L_z`), while Panel (b) shows a similar trend for the TVD correction steps. This improved cache locality drastically reduces the latency of fetching data from main DRAM, resulting in computational throughput exceeding the theoretical linear baseline. This behavior is consistent with established performance models for stencil computations (Datta et al., 2008; Hager and Wellein, 2010), where fitting the working set into higher levels of the cache hierarchy significantly mitigates the bandwidth bottleneck.

2.5.2 GPUs performance

The GPU scalability of DHARA was evaluated on Frontier at the Oak Ridge National Laboratory (OLCF) and Polaris at the Argonne Leadership Computing Facility (ALCF). Frontier is a Cray EX system where each node contains four AMD MI250X GPUs, each consisting of two Graphics Compute Dies (GCDs), effectively providing 8 accelerators per node. At the time these scaling runs were conducted, Frontier was the fastest supercomputer in the world (currently ranked second), representing the pinnacle of exascale computing. In contrast, Polaris is an HPE Apollo system equipped with four NVIDIA A100 GPUs per node.

For the benchmarking on Frontier, we scaled the code from 8 nodes (64 GCDs) to 1024 nodes (8192 GCDs), varying the grid size from 2048^3 to $16384^2 \times 2048$. On Polaris, we varied the grid size from 1024^3 to 4096^3 and scaled the resource usage from 2 nodes (8 GPUs) to 128 nodes (512 GPUs).

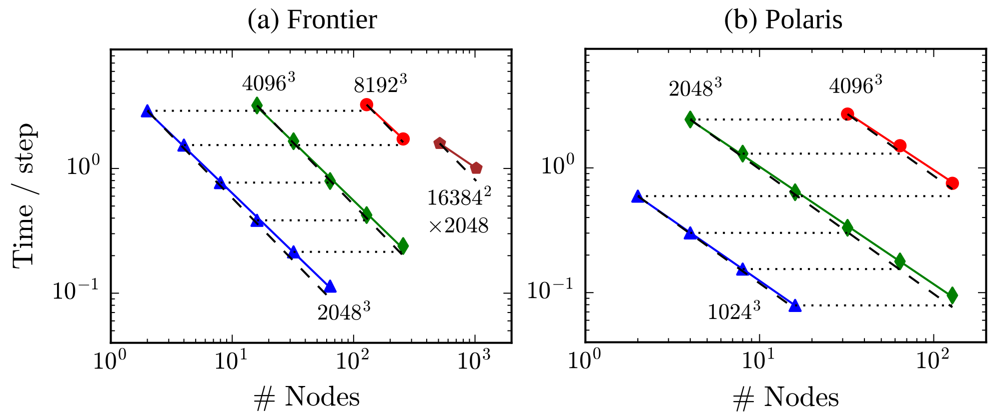

FIGURE 2.5: Scalability of DHARA on leadership-class GPU systems. Panel (a) shows performance on Frontier (AMD MI250X) and Panel (b) shows performance on Polaris (NVIDIA A100). The figure plots the wall-clock time per timestep versus the number of nodes, demonstrating both strong and weak scaling regimes.

The scaling results are illustrated in Fig. 2.5. We evaluated performance in two regimes: strong scaling, where the global problem size is fixed, and weak scaling, where the problem size grows proportionally with the core count. As shown in both panels, the time per timestep t decreases inversely with the number of nodes n in the strong scaling regime ($t \propto n^{-1}$), indicating excellent efficiency even as the local workload decreases. Furthermore, the solver demonstrates near-ideal weak scaling, evident from the flat trend lines where the time-to-solution remains constant despite the massive increase in problem size.

These results highlight that DHARA scales efficiently on both NVIDIA and AMD architectures, adapting seamlessly to the underlying hardware. Whether running on the established CUDA ecosystem of Polaris or the newer ROCm environment of Frontier, the solver maintains high throughput and strong parallel efficiency, confirming its readiness for production runs at the exascale.

2.6 Validation

Before conducting production runs, we subjected DHARA to a series of rigorous validation tests to ensure the accuracy and reliability of the solver. As a primary verification step, we assessed the conservation properties of the code in an unforced, periodic domain. We confirmed that the solver conserves total mass and total energy with an accuracy consistent with the second-order numerical scheme, verifying the correct implementation of the governing conservation laws. Following these fundamental checks, we validated the solver against established benchmarks in the literature for both compressible convection and turbulence.

2.6.1 Compressible convection

We validate our code by comparing our numerical Nusselt (Nu) and Reynolds (Re) numbers with established results from John and Schumacher (2023a) and Verhoeven et al. (2015). The Nusselt number is computed using Eq. (1.69).

Table 2.1: Comparison of Nu and Re computed by DHARA against reference data $(\mathrm{Nu}_1, \mathrm{Re}_1)$ from John and Schumacher (2023a). Parameters: $\mathrm{Ra} = 10^6$, $\mathrm{Pr} = 0.7$, $\Gamma = 4$, $\gamma = 1.4$, $\epsilon = 0.1$.

Case	D	Nu_1	Nu (Present)	$\mathrm{Error}_{\mathrm{Nu}}$ (%)	Re_1	Re (Present)	$\mathrm{Error}_{\mathrm{Re}}$ (%)
1	0.1	7.94	7.90 ± 0.06	0.7	424	425 ± 3	0.7
2	0.34	7.64	7.67 ± 0.08	1.0	414	414 ± 4	0.9
3	0.5	6.93	6.89 ± 0.05	0.7	407	406 ± 3	0.7
4	0.6	6.24	6.18 ± 0.09	1.4	370	368 ± 5	1.3

First, we simulate the governing equations for fixed $\mathrm{Ra} = 10^6$, $\mathrm{Pr} = 0.7$, $\Gamma = 4$, $\gamma = 1.4$, and $\epsilon = 0.1$. We vary D across the values $0.1, 0.34, 0.5$, and 0.6. The resulting Nu and Re are compared with the reference values $(\mathrm{Nu}_1, \mathrm{Re}_1)$ from John and Schumacher (2023a) in Table 2.1. Next, we validate the scaling behavior by varying Ra while fixing $D = 0.49$, $\Gamma = 2$, $\gamma = 5/3$, $\epsilon = 0.1$, and $\mathrm{Pr} = 0.7$. We compare our results with the reference values $(\mathrm{Nu}_2, \mathrm{Re}_2)$ reported by Verhoeven et al. (2015) in Table 2.2. In all cases, our results show good agreement with the reference data. The computed Nu and Re values differ from the previous works by less than 3%. While the relative error slightly increases

Table 2.2: Comparison of Nu and Re computed by DHARA against reference data $(\mathrm{Nu}_2, \mathrm{Re}_2)$ from Verhoeven et al. (2015). Parameters: $D = 0.49$, $\epsilon = 0.1$, $\mathrm{Pr} = 0.7$, $\Gamma = 2$, $\gamma = 5/3$.

Case	Ra	Nu_2	Nu (Present)	$\mathrm{Error}_{\mathrm{Nu}}$ (%)	Re_2	Re (Present)	$\mathrm{Error}_{\mathrm{Re}}$ (%)
1	10^4	2.1	2.175 ± 0.005	0.2	26.3	26.98 ± 0.05	0.2
2	10^5	3.9	4.0 ± 0.1	2.5	102	100 ± 3	3.3
3	10^6	7.1	7.3 ± 0.2	2.7	322	330 ± 7	2.0
4	10^7	13.4	14.1 ± 0.4	2.8	973	970 ± 20	2.4

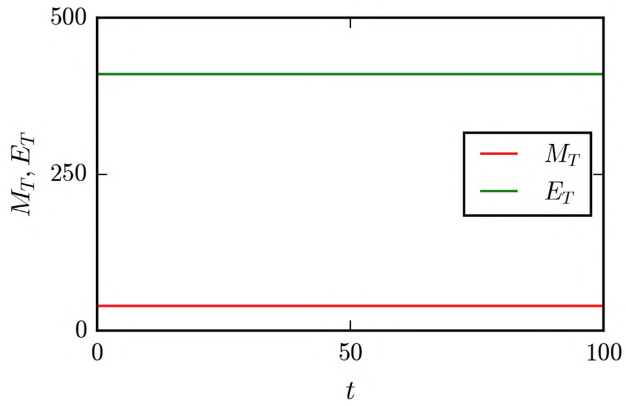

FIGURE 2.6: Accuracy test of the 2D solver without external forcing: Time series of the total mass and total energy, demonstrating the constancy of these conserved quantities over the simulation duration.

at Ra $= 10^7$, it remains well within the acceptable bounds for high-order finite difference schemes. These minor deviations at higher Ra are primarily attributed to slight differences in the exact numerical implementation of the wall boundary conditions between different solvers, but the overall scaling trends remain robustly captured. This confirms the stability and accuracy of DHARA for compressible convection problems even as the driving forces increase.

2.6.2 Compressible turbulence

We begin by assessing the fundamental conservation properties of the solver in an unforced setup. To test the accuracy of our code, we performed a 2D simulation on a 512^2 grid without external forcing using the MacCormack scheme (Yee, 1987). The simulation parameters were set to $\mathrm{Re}_0 = 10^3$, $\mathrm{Pr} = 1$, $M_0 = 0.5$, and $\gamma = 1.3$, where Re_0 is the reference Reynolds number and M_0 is the reference Mach number (see Singh et al. (2025) for parameters definition). From the code output, we compute the total mass and the total energy of the system. As shown in Fig. 2.6, both quantities are conserved. The relative errors in energy are of the order of 10^{-5}, demonstrating that the numerical dissipation is much smaller compared to the viscous dissipation (which is of the order of 10^{-2}).

Following this conservation check, we validate the solver for forced compressible turbulence by comparing our results with the spectral simulations of Kida and Orszag (1990). We simulate the system under identical forcing conditions and compare the time-averaged statistics for the pressure-dilatation (PD) and viscous-dissipation (VD) terms. These

TABLE 2.3: Comparison of time-averaged viscous dissipation ($\langle VD \rangle$) and pressure dilatation ($\langle PD \rangle$) with the forced turbulence study of Kida and Orszag (1990). The averaging intervals correspond to $70 \leq t \leq 150$ (Case I), $15 \leq t \leq 30$ (Case II), and $60 \leq t \leq 80$ (Case III).

	$\langle VD \rangle$		$\langle PD \rangle$	
Case	Kida & Orszag	Present	Kida & Orszag	Present
I	-0.0016	-0.00158	5.6×10^{-5}	5.7×10^{-5}
II	-0.068	-0.066	-0.005	-0.0047
III	-5.4×10^{-4}	-5.5×10^{-4}	-5.1×10^{-4}	-5.2×10^{-4}

quantities are defined as:

$$(PD) = -u_i \frac{\partial p}{\partial x_i}, \quad (VD) = u_j \frac{\partial \tau_{ij}}{\partial x_i}. \tag{2.27}$$

Table 2.3 presents the comparison of the spatial averages $\langle VD \rangle$ and $\langle PD \rangle$. Our finite-difference results match the spectral benchmark of Kida and Orszag within 5% for both viscous dissipation and pressure dilatation, confirming that DHARA accurately resolves the dissipative scales and thermodynamic exchanges in forced compressible turbulence.

2.7 Summary

In this chapter, we have established the numerical foundation for simulating high-Rayleigh-number compressible convection. We detailed the implementation of the MacCormack-TVD finite difference scheme within our in-house solver, DHARA. By leveraging a modular, object-oriented architecture built on the Python-CuPy ecosystem, we successfully bridged the gap between high-level code flexibility and low-level hardware performance. Extensive benchmarking on leadership-class systems, including Shaheen III and Frontier, demonstrated the solver's exceptional scalability, achieving super-linear performance through efficient cache utilization and latency hiding. Furthermore, rigorous validation against standard results for both convection and forced turbulence confirms the code's accuracy in resolving the thermodynamic fluctuations and dissipative scales essential for this study.

The computational efficiency and massive scalability established here are the critical enablers for the central research presented in the subsequent chapters. In Chapters 3 and 4, we deploy this optimized MacCormack-based framework to perform DNS of compressible convection at extreme Rayleigh numbers. The low memory footprint and high throughput of the MacCormack solver allow us to conduct these computationally demanding parameter sweeps, providing the high-fidelity data needed to investigate the scaling laws of global heat and momentum transport in stratified interiors.

Beyond the specific application to convection, the modular design of DHARA facilitates its evolution into a general-purpose compressible flow solver. Recognizing the limitations of second-order difference schemes in regimes dominated by strong discontinuities, we have extended the framework to include high-order finite volume capabilities. As will be detailed in Chapter 5, we have integrated advanced reconstruction algorithms, such as weighted and targeted essentially non-oscillatory (WENO/TENO) schemes, to robustly capture shock structures in supersonic turbulence. This extensibility ensures that DHARA remains a versatile tool, capable of tackling a broad spectrum of astrophysical and geophysical flow problems ranging from sub-adiabatic convection to high-Mach-number shock dynamics.

Chapter 3

Compressible turbulent convection at very high Rayleigh numbers

Turbulent thermal convection is a dominant transport mechanism in astrophysical bodies, such as the solar convection zone and the interiors of giant planets. While Rayleigh-Bénard convection (RBC) under the Oberbeck-Boussinesq (OB) approximation has been extensively studied, it fails to capture the strong density stratification inherent to these large-scale natural flows. In stars, density fluctuations are of the order of unity, rendering the OB approximation invalid. To address this, we investigate fully compressible convection, which accounts for significant variations in density and temperature, providing a more realistic model for astrophysical turbulence.

In the work presented in this chapter, we perform extensive numerical simulations of compressible turbulent convection in a rectangular domain with an aspect ratio of $\Gamma = 4$. We utilize the solver DHARA, which supports both finite difference and finite volume architectures (see Chapter 5). For the current study, we employ the computationally efficient MacCormack-TVD (Total Variation Diminishing) finite-difference scheme. This method is particularly robust for compressible flows as it eliminates spurious numerical oscillations. The simulations are accelerated using single and multi-GPU configurations, allowing us to access unprecedented parameter regimes.

We achieve extremely high Rayleigh numbers, reaching up to $\mathrm{Ra} = 10^{15}$ in two dimensions (2D) and $\mathrm{Ra} = 10^{11}$ in three dimensions (3D). The simulations are conducted for fixed ratio of heat capacities $\gamma = 1.3$, Prandtl number $\mathrm{Pr} = 0.7$, superadiabaticity $\epsilon = 0.1$, and dissipation number $D = 0.5$. By spanning such a wide range of Ra, we are able to robustly quantify the scaling laws of heat and momentum transport and perform a detailed comparison with the available literature, including standard RBC.

A fundamental observation from our simulations is that the bulk flow maintains a nearly adiabatic profile, similar to the Schwarzschild criterion. Unlike RBC, where the bulk temperature is constant, the temperature in compressible convection drops linearly with height at the adiabatic gradient g/C_p. Similarly, the density decreases with height, following a polytropic profile. This adiabaticity persists even at the highest Rayleigh number simulated. We observe that the internal energy of the fluid dominates the kinetic energy by several orders of magnitude. Consequently, the local Mach number remains small, and the flow velocities are much lower than the sound speed. This dominance of internal energy ensures that the deviations from the static adiabatic background remain small, driven only by the weak superadiabatic temperature gradients.

The strong density stratification leads to significant asymmetries in the flow structure, distinguishing it from the top-bottom symmetry observed in RBC. We observe that the fluid is significantly denser at the bottom than at the top. Since the dynamic viscosity is constant, the kinematic viscosity $\nu = \mu/\rho$ is lower at the bottom, leading to more vigorous turbulence and finer flow structures near the bottom plate compared to the top.

This asymmetry extends to the thermal boundary layers. We find that the top boundary layer is consistently thicker than the bottom boundary layer. Furthermore, the scaling of the boundary layer thickness λ with Rayleigh number deviates from the standard RBC prediction. While RBC typically exhibits $\lambda \sim \mathrm{Ra}^{-0.3}$, our compressible simulations yield $\lambda \sim \mathrm{Ra}^{-0.18}$ in 2D and $\lambda \sim \mathrm{Ra}^{-0.20}$ in 3D. This suggests that the boundary layer dynamics in compressible convection are fundamentally different from those in the Boussinesq limit.

We also analyze the force balance in the vertical momentum equation. The results show that the vertical pressure gradient ∇p nearly balances the buoyancy force $-\rho g$ across the entire domain. However, they do not cancel exactly. The small residual between these two dominant terms balances the nonlinear advection term $\rho(\mathbf{u} \cdot \nabla)u_z$. This balance is crucial for understanding the momentum transport in the system.

Based on this force balance, we derive a theoretical scaling for the Reynolds number, predicting $\mathrm{Re} \sim \mathrm{Ra}^{1/2}$. Our numerical data strongly supports this prediction, yielding scaling exponents of approximately 0.49 for 2D and 0.47 for 3D flows. This confirms that the residual imbalance between pressure and buoyancy forces drives the intensity of turbulence in compressible convection.

Regarding heat transport, we compute the Nusselt number (Nu) by subtracting the adiabatic heat flux. We observe that the Nusselt number follows the *classical* scaling law, $\mathrm{Nu} \sim \mathrm{Ra}^{0.30}$, for both 2D and 3D simulations. The convective contribution dominates the heat transport, while the kinetic energy flux makes a negligible (and negative) contribution.

Crucially, despite reaching $\mathrm{Ra} = 10^{15}$ in 2D, we do not observe a transition to the *ultimate regime* of convection, where Nu is predicted to scale as $\mathrm{Ra}^{1/2}$. The scaling exponent remains robustly near 0.30. We attribute this to the scaling of the correlation between density-velocity fluctuations and superadiabatic temperature, which scales as $\mathrm{Ra}^{-0.20}$, effectively correcting the $\mathrm{Ra}^{1/2}$ dependence of the free-fall velocity down to the observed $\mathrm{Ra}^{0.30}$ for the heat flux. We revisit this issue in the next chapter, where we offer an alternative perspective, attributing the near-classical scaling to the imbalance between the positive and negative contributions to the local heat flux.

In summary, this study provides a comprehensive characterization of fully compressible convection at extreme Rayleigh numbers. While the heat and momentum transport scaling laws ($\mathrm{Nu} \sim \mathrm{Ra}^{0.3}$ and $\mathrm{Re} \sim \mathrm{Ra}^{0.5}$) bear a resemblance to those in RBC, the underlying physics—characterized by adiabatic bulk profiles, flow asymmetries, and distinct boundary layer scaling—is fundamentally different. The following paper details these findings.

International Journal of Heat and Mass Transfer 242 (2025) 126821

Contents lists available at ScienceDirect

International Journal of Heat and Mass Transfer

journal homepage: www.elsevier.com/locate/hmt

Compressible turbulent convection at very high Rayleigh numbers

Harshit Tiwari, Lekha Sharma, Mahendra K. Verma *

Department of Physics, Indian Institute of Technology Kanpur, Kanpur 208016, India

ARTICLE INFO

Keywords:
Compressible thermal convection
Turbulent thermal convection
Solar convection

ABSTRACT

Heat transport in highly turbulent convection is not well understood. In this paper, we simulate compressible convection in a box of aspect ratio 4 using computationally-efficient MacCormack-TVD finite difference method on single and multi-GPUs, and reach very high Rayleigh number (Ra)— 10^{15} in two dimensions and 10^{11} in three dimensions. We show that the Nusselt number $\mathrm{Nu} \propto \mathrm{Ra}^{0.3}$ (classical scaling) that differs strongly from the ultimate-regime scaling, which is $\mathrm{Nu} \propto \mathrm{Ra}^{1/2}$. The bulk temperature drops adiabatically along the vertical even for high Ra, which is in contrast to the constant bulk temperature in Rayleigh–Bénard convection (RBC). Unlike RBC, the density decreases with height. In addition, the vertical pressure-gradient ($-dp/dz$) nearly matches the buoyancy term (ρg). But, the difference, $-dp/dz - \rho g$, is equal to the nonlinear term that leads to Reynolds number $\mathrm{Re} \propto \mathrm{Ra}^{1/2}$.

1. Introduction

Turbulent thermal convection occurs in a wide range of geophysical and astrophysical flows, as well as in many natural and industrial processes [1–8]. There are various models of turbulent convection, the leading one being Rayleigh–Bénard convection (RBC) [1–5] that follows Oberbeck–Boussinesq (OB) approximation. In RBC, a horizontal layer of fluid confined between two parallel plates is heated from below and cooled from above. In the OB approximation, the density of the fluid is nearly constant, except for a small variation in the buoyancy term. For example, for water, whose thermal expansion coefficient $\alpha \approx 3 \times 10^{-4}$ K^{-1} at room temperature, the relative change in density $(\delta\rho)/\rho \approx \alpha(\Delta T) \approx 10^{-3}$ when the temperature difference between the two plates is around 30 K [5].

However, $(\delta\rho)/\rho$ in a turbulent star is of the order of unity [9]. Let us assume that the star is made of ideal gas, whose thermal expansion coefficient is $1/T$, where T is the gas temperature. Hence, $(\delta\rho)/\rho \approx \alpha(\Delta T) \approx 1$ when $(\Delta T) \approx T$. Therefore, the OB approximation and the RBC equations become invalid for stars and related astrophysical systems [6,10–12]. To study such systems, researchers often employ equations for compressible convection or intermediate models that employ non-Oberbeck–Boussinesq (NOB) effects [13–15] or anelastic approximations [16,17]. In this paper, we employ fully compressible equations to study turbulent convection at very large Rayleigh numbers (Ra)—up to 10^{15} for two-dimensions (2D), and 10^{11} for three-dimension (3D). Note, however, that the solar convection has even larger Ra ($\sim 10^{24}$) than the above [6].

Many aspects of turbulent convection, which is more complex than hydrodynamic turbulence, are understood quite well, in particular for RBC systems. Grossmann and Lohse (GL in short) [18,19] modeled the Reynolds number (Re) and Nusselt number (Nu) scaling using the relations for viscous and thermal dissipation rates [20,21]. The GL relations have been verified by many experiments and numerical simulations [22]. Recently, Bhattacharya and Verma [23] employed machine learning, artificial intelligence, and more accurate dissipation rates for Ra and Pr predictions. In addition, it has been shown that for small and moderate Prandtl numbers ($\mathrm{Pr} \lesssim 1$), turbulent convection has properties similar to hydrodynamic turbulence [5,24]. For example, the energy spectrum for turbulent convection follows Kolmogorov's 5/3 spectrum.

For the RBC setup, while the Reynolds number scaling is reasonably well established, the properties of velocity fluctuations remains to be quantified [25]. Additionally, accurate characterization of the Nusselt number scaling remains a challenge. Two main theories describe the dependence of Nu on Ra. In the extreme turbulent regime, known as *ultimate regime*, Kraichnan argued that Nu scales as $\mathrm{Ra}^{1/2}$ [26,27]. On the contrary, Malkus [28] proposed that Nu is proportional to $\mathrm{Ra}^{1/3}$, referred to as the *classical scaling* [1–4,18,27]. It is reported both in experiments and numerical simulations that up to $\mathrm{Ra} = 10^{12}$, the Nu scaling exponent is near 0.30. However, Chavanne et al. [29], He et al. [30], Zhu et al. [31] and some others argued that the Nu exponent gradually increases to about 0.38 near $\mathrm{Ra} = 10^{15}$. Therefore, some researchers believe that the exponent might reach the value 1/2 at extreme Ra's [27]. But, some others, based on different experiments and related simulations, argue that the classical scaling will remain valid for all Ra's [6,32–34]. The scaling of Nu is discussed in detail in recent

* Corresponding author.
E-mail addresses: tharshit@iitk.ac.in (H. Tiwari), lekhas@iitk.ac.in (L. Sharma), mkv@iitk.ac.in (M.K. Verma).

https://doi.org/10.1016/j.ijheatmasstransfer.2025.126821
Received 27 August 2024; Received in revised form 9 January 2025; Accepted 10 February 2025
Available online 19 February 2025

articles [27,35].

Turbulent compressible convection behaves very differently than RBC turbulence [36]. Unlike the constant bulk temperature in RBC, the bulk temperature in compressible convection falls adiabatically [17]. In compressible convection, the fluid at the bottom is heavier than that at the top, which is in sharp contrast to that in RBC. Unfortunately, compressible convection has not been studied extensively. In recent times, Verhoeven et al. [17], and John and Schumacher [36–38] analyzed turbulent compressible convection. Verhoeven et al. [17] performed a comparative study of the anelastic approximation and fully compressible turbulent convection. John and Schumacher [36,37] performed numerical simulations of fully compressible convection up to $\mathrm{Ra} = 10^7$ and explored different regimes of compressible convection. Some compressible simulations use inviscid flows [39] whose Ra estimates are somewhat uncertain. We find that there are no existing studies on fully compressible convection at very high Rayleigh numbers. The present paper aims to fill this gap.

In this paper, we simulate turbulent compressible convection using a computationally-efficient MacCormack-TVD (total variation diminishing) finite difference method that eliminates numerical oscillations [40]. Our method is an extension of the novel and stable numerical scheme proposed by Ouyang et al. [40], Yee [41], and Liang et al. [42] for shallow water equations to compressible turbulent convection. Our stable numerical scheme enabled us to perform convection simulations at very large Ra's, e.g., 10^{15} for 2D flows, and 10^{11} for 3D flows.

We quantify various quantities using the data generated by our numerical simulations. Our numerical data show that the internal energy dominates the fluid kinetic energy even at very large Ra. We attribute adiabaticity to this effect. In addition, we study the superadiabatic temperature and density of the flow. Based on numerical data, we report that $\mathrm{Nu} \sim \mathrm{Ra}^{0.3}$ up to $\mathrm{Ra} = 10^{15}$ in 2D and up to 10^{11} in 3D. We caution that our results differ significantly from those for RBC, which is very different from compressible convection. Among the two, compressible equations model the astrophysical systems better.

Simulations of 3D turbulent convection at extreme Ra's are very expensive. Fortunately, in the RBC framework, the scaling of Nu and Re for 2D and 3D flows are reasonably similar for $\mathrm{Pr} \gtrapprox 1$ [43–45]. Motivated by these observations, we examine the Nu and Re scaling for extreme Ra in 2D, and for moderate Ra in 3D. We believe that these important findings will improve the models of stellar and planetary convection.

We have organized the paper as follows. In Section 2, we describe the physical system along with the governing equations. Section 3 discusses the numerical scheme along with the simulation parameters. In Sections 4 and 5, we describe the adiabaticity and boundary layers in turbulent convection. Section 6 contains discussions on Nu and Re scaling. We conclude in Section 7.

2. Physical system and governing equations

We consider a fully compressible fluid confined in a rectangular box of dimension (L, L, d) in 3D and (L, d) in 2D, with the bottom and top plates at temperatures T_b and T_t respectively ($T_b > T_t$). Note that the adverse temperature gradient $\Delta = (T_b - T_t)/d > 0$. We employ periodic boundary condition for the vertical sideways walls. However, for the top and bottom plates, we employ no-slip boundary conditions for the velocity field, and perfectly conducting boundary conditions for the temperature field [17,37]. Note that a perfectly conducting plate maintains constant temperatures.

We assume that the fluid has constant dynamic viscosity μ and thermal conductivity K. We also assume that the fluid follows ideal gas law, $\tilde{p} = \tilde{\rho} R_* \tilde{T}$, where $\tilde{p}$ is the pressure; $\tilde{\rho}$ is the density of fluid; $R_* = C_p - C_v$ is the gas constant; C_p, C_v are the specific heat capacities at constant pressure and volume respectively; and $\tilde{T}$ is the temperature field. The following conservative set of equations govern

Nomenclature

d	Height of rectangular box
L	Length and width of rectangular box
g	Gravitational acceleration
K	Thermal conductivity
T_b	Temperature at the bottom plate
T_t	Temperature at the top plate
C_p	Specific heat capacity at constant pressure
C_v	Specific heat capacity at constant volume
R_*	Gas constant
$\tilde{\mathbf{r}} = (\tilde{x}, \tilde{y}, \tilde{z})$	Dimensional position vector
$\mathbf{r} = (x, y, z)$	Nondimensional position vector
$\tilde{\mathbf{u}}$	Dimensional velocity
$\mathbf{u}$	Nondimensional velocity
$\tilde{t}$	Dimensional time
t	Nondimensional time
$\tilde{T}$	Dimensional temperature
T	Nondimensional temperature
$\tilde{p}$	Dimensional pressure
p	Nondimensional pressure
$\tilde{E}$	Dimensional total energy density
E	Nondimensional total energy density
$\tilde{T}_A$	Dimensional adiabatic temperature
T_A	Nondimensional adiabatic temperature
$\tilde{p}_A$	Dimensional adiabatic pressure
p_A	Nondimensional adiabatic pressure
$\tilde{T}_{\mathrm{sa}}$	Dimensional superadiabatic temperature
T_{sa}	Nondimensional superadiabatic temperature
Pr	Prandtl number
Ra	Rayleigh number
Re	Reynolds number
D	Dissipation number
$r = K_e/I_e$	Ratio of kinetic energy and internal energy
$\tilde{H}_T$	Dimensional total heat flux
$\tilde{H}_A$	Dimensional adiabatic heat flux
$\tilde{H}_{\mathrm{cond}}$	Dimensional conductive heat flux
$\tilde{H}_{\mathrm{conv}}$	Dimensional convective heat flux
$\overline{\mathrm{Nu}}$	Mean Nusselt number
Nu	Bulk Nusselt number
$\mathrm{Nu}_{\mathrm{conv}}$	Convective Nusselt number
Nu_K	u_z-induced kinetic Nusselt number
$\tilde{U}$	Dimensional root-mean square velocity
U	Nondimensional root-mean square velocity
$\mathbf{X}$	Column vector containing ρ, ρu_α, and E
$\mathbf{F}_\alpha$	Fluxes in α-direction
$\mathbf{S}_\alpha$	Sources in α-direction
$\mathbf{L}_\alpha$	Predictor–corrector operator in α-direction
Co_α	Local Courant number in α-direction
$C(\mathrm{Ra})$	Correlation between ρu_z and T_{sa}
Greek:	
Γ	Aspect ratio of computational domain
Δ	Temperature gradient in z-direction
γ	Ratio of specific heats
μ	Dynamic viscosity
ν	Kinematic viscosity
κ	Thermal diffusivity
$\tilde{\rho}$	Dimensional fluid density
ρ	Nondimensional fluid density
$\tilde{\rho}_A$	Dimensional adiabatic density field
ρ_A	Nondimensional adiabatic density field
β	Adiabatic index
ϵ	Superadiabaticity
$\tilde{\boldsymbol{\tau}}$	Dimensional stress tensor
$\boldsymbol{\tau}$	Nondimensional stress tensor

the system [9,46]:

$$\frac{\partial \tilde{\rho}}{\partial \tilde{t}} + \frac{\partial}{\partial \tilde{x}_i}(\tilde{\rho}\tilde{u}_i) = 0, \tag{1}$$

$$\frac{\partial}{\partial \tilde{t}}(\tilde{\rho}\tilde{u}_i) + \frac{\partial}{\partial \tilde{x}_j}(\tilde{\rho}\tilde{u}_i\tilde{u}_j + \delta_{ij}\tilde{p} - \tilde{\tau}_{ij}) = -g\tilde{\rho}\delta_{iz}, \tag{2}$$

$$\frac{\partial \tilde{E}}{\partial \tilde{t}} + \frac{\partial}{\partial \tilde{x}_i}\left(\tilde{u}_i(\tilde{E}+\tilde{p}) - K\frac{\partial \tilde{T}}{\partial \tilde{x}_i} - \tilde{u}_j\tilde{\tau}_{ij}\right) = 0, \tag{3}$$

where $\tilde{u}_i$ are the velocity field components; g is the acceleration due to gravity along $-\hat{z}$ direction;

$$\tilde{E} = \tilde{\rho}\left(\frac{\tilde{u}^2}{2} + C_v\tilde{T} + g\tilde{z}\right) \tag{4}$$

is the total energy density; and

$$\tilde{\tau}_{ij} = \mu\left(\tilde{\partial}_j\tilde{u}_i + \tilde{\partial}_i\tilde{u}_j + \frac{2}{3}\tilde{\partial}_m\tilde{u}_m\delta_{ij}\right) \tag{5}$$

is the stress tensor. Another important parameter is the aspect ratio Γ, which is the ratio of the length (L) and the height (d) of the rectangular box. All tilde variables have their respective dimensions.

The bulk flow is nearly adiabatic (or isentropic) because the convection time scale is faster than the conduction time scale (estimates in Section 4). Therefore, the vertical profiles of the adiabatic temperature $\tilde{T}_A(\tilde{z})$, adiabatic density $\tilde{\rho}_A(\tilde{z})$, and adiabatic pressure $\tilde{p}_A(\tilde{z})$ are [9,17]

$$\tilde{T}_A(\tilde{z}) = \left(T_b - \frac{g}{C_p}\tilde{z}\right), \tag{6}$$

$$\tilde{\rho}_A(\tilde{z}) = \frac{\rho_b}{T_b^{\beta}}(\tilde{T}_A(\tilde{z}))^{\beta}, \tag{7}$$

$$\tilde{p}_A(\tilde{z}) = (C_p - C_v)\tilde{\rho}_A(\tilde{z})\tilde{T}_A(\tilde{z}), \tag{8}$$

where T_b and ρ_b are respectively the temperature and fluid density at the bottom plate; and $\beta = 1/(\gamma-1)$ is the adiabatic index with $\gamma = C_p/C_v$. Later in the paper we will show the bulk temperature nearly follows the adiabatic profile [Eq. (6)]. The difference between the real temperature and the adiabatic profile is called *superadiabatic temperature*: $\tilde{T}_{\mathrm{sa}}(\tilde{\mathbf{r}},\tilde{t}) = \tilde{T}(\tilde{\mathbf{r}},\tilde{t}) - \tilde{T}_A(\tilde{z})$.

Compressible convection has several important nondimensional parameters, which are [17,36]

$$\text{superadiabaticity } \epsilon = \frac{d}{T_b}\left(\frac{\Delta}{d} - \frac{g}{C_p}\right), \tag{9}$$

$$\text{dissipation number } D = \frac{gd}{T_bC_p} = \frac{T_b - \tilde{T}_A(d)}{T_b}, \tag{10}$$

$$\text{Rayleigh number Ra} = \frac{\epsilon g d^3}{\nu\kappa}, \tag{11}$$

$$\text{Prandtl number Pr} = \frac{\nu}{\kappa}, \tag{12}$$

where $\nu = \mu/\rho$ is the kinematic viscosity, and $\kappa = K/(C_p\rho)$ is the thermal diffusivity of fluid. The parameters Ra and Pr are common with RBC, except that the temperature gradient has an adiabatic correction via ϵ. The parameters D and ϵ are unique to compressible convection: D represents the nondimensional adiabatic temperature drop, whereas ϵ represents the excess temperature gradient relative to the adiabatic profile [17,36]. In Fig. 1(A,B), we plot the total temperature gradient and the adiabatic temperature gradient in dimensional and nondimensional forms respectively.

In Section 4, we will show that the bulk temperature nearly follows the adiabatic temperature profile $\tilde{T}_A(\tilde{z})$, which is in sharp contrast to RBC where the bulk temperature is constant. Additionally, the density at the bottom is larger than that at the top, which is opposite to that in RBC. Therefore, compressible convection exhibits behavior that is markedly different from that of RBC.

We non-dimensionalize Eqs. (1)–(3) using d as the length scale, free-fall velocity $\sqrt{\epsilon g d}$ as the velocity scale, ρ_b as the density scale, and T_b as the temperature scale. The governing equations in dimensionless form are [17,37]

$$\frac{\partial \rho}{\partial t} + \frac{\partial}{\partial x_i}(\rho u_i) = 0, \tag{13}$$

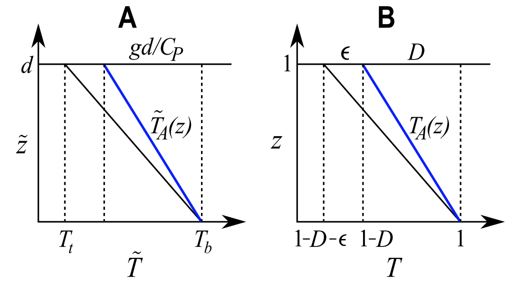

Fig. 1. The adiabatic temperature gradient (blue lines) and the total temperature gradients (black lines) in (A) dimensional and (B) non-dimensional forms.

$$\frac{\partial}{\partial t}(\rho u_i) + \frac{\partial}{\partial x_j}(\rho u_i u_j + \delta_{ij}p - \tau_{ij}) = -\frac{1}{\epsilon}\rho\delta_{iz}, \tag{14}$$

$$\frac{\partial E}{\partial t} + \frac{\partial}{\partial x_i}\left(u_i(E+p) - \frac{1}{\epsilon D\sqrt{\mathrm{Ra}Pr}}\frac{\partial T}{\partial x_i} - u_j\tau_{ij}\right) = 0, \tag{15}$$

where the nondimensionalized pressure, total energy density, and stress tensor are defined respectively as:

$$p = \frac{(\gamma-1)}{\gamma\epsilon D}\rho T, \tag{16}$$

$$E = \rho\left(\frac{u^2}{2} + \frac{1}{\gamma\epsilon D}T + \frac{1}{\epsilon}z\right), \tag{17}$$

$$\tau_{ij} = \sqrt{\frac{\mathrm{Pr}}{\mathrm{Ra}}}\left(\partial_j u_i + \partial_i u_j + \frac{2}{3}\partial_m u_m\delta_{ij}\right). \tag{18}$$

Note that the tilde variables are dimensionful, whereas those without tilde are dimensionless. The nondimensional adiabatic profiles are [17]

$$T_A(z) = (1 - Dz), \tag{19}$$

$$\rho_A(z) = (1 - Dz)^{\beta}, \tag{20}$$

$$p_A(z) = (1 - Dz)^{(\beta+1)}. \tag{21}$$

The nondimensional temperature is 1 at the bottom plate, and $1-\epsilon-D$ at the top plate (see Fig. 1).

In this paper, we study heat transport as a function of Ra for a fixed Pr, ϵ, and D. In the RBC framework, Nu is the ratio of total heat flux ($\tilde{H}_T$) and conductive heat flux ($\tilde{H}_{\mathrm{cond}}$). In compressible convection, the heat flux due to adiabatic cooling ($\tilde{H}_A$) must be subtracted from both $\tilde{H}_T$ and $\tilde{H}_{\mathrm{cond}}$ to compensate the thermodynamic effects [11,46,47]. Here, the total heat flux is a sum of $\tilde{H}_{\mathrm{cond}} = K\Delta$, convective heat flux $\tilde{H}_{\mathrm{conv}} = C_p\langle\tilde{\rho}\tilde{u}_z\tilde{T}_{\mathrm{sa}}\rangle_{V,t}$, and u_z-induced kinetic heat flux $\tilde{H}_K = \langle\rho\tilde{u}_z\tilde{u}^2/2\rangle_{V,t}$. The adiabatic heat flux is given by $\tilde{H}_A = Kg/C_p$. Hence, the Nusselt number is [46,47]

$$\begin{aligned}\mathrm{Nu} &= \frac{\tilde{H}_T - \tilde{H}_A}{\tilde{H}_{\mathrm{cond}} - \tilde{H}_A} \\ &= \frac{K\Delta + C_p\langle\tilde{\rho}\tilde{u}_z\tilde{T}_{\mathrm{sa}}\rangle_{V,t} + \langle\rho\tilde{u}_z\tilde{u}^2/2\rangle_{V,t} - Kg/C_p}{K\left(\Delta - \frac{g}{C_p}\right)} \\ &= 1 + \frac{\sqrt{\mathrm{RaPr}}}{\epsilon}\langle\rho u_z T_{\mathrm{sa}}\rangle_{V,t} + \frac{D\sqrt{\mathrm{RaPr}}}{2}\langle\rho u_z u^2\rangle_{V,t} \\ &= 1 + \mathrm{Nu}_{\mathrm{conv}} + \mathrm{Nu}_K.\end{aligned} \tag{22}$$

We report the volume and temporal averages of the above quantities and denote them by $\langle.\rangle_{V,t}$.

The above Nu, called *bulk Nusselt number*, fluctuates significantly. In contrast, the Nusselt number computed near the bottom plate ($z = 0$) and top plate ($z = 1$) [17,37]

$$\mathrm{Nu}_{z=0,1} = -\frac{1}{\epsilon}\left.\frac{d\langle T_{\mathrm{sa}}\rangle_{A,t}}{dz}\right|_{z=0,1}, \tag{23}$$

have much less fluctuations. Here $\langle.\rangle_{A,t}$ represents the horizontal and temporal averages. Consequently, the mean Nusselt number at the boundaries is given by

$$\overline{\mathrm{Nu}} = \frac{\mathrm{Nu}_{z=0} + \mathrm{Nu}_{z=1}}{2}. \tag{24}$$

In this paper, we report Nu and $\overline{\mathrm{Nu}}$, as well as $\mathrm{Nu}_{\mathrm{conv}}$ and Nu_K. In addition to Nu, we also report the Reynolds number Re, which is defined as [5]

$$\mathrm{Re} = \frac{\tilde{U} d}{\nu}, \tag{25}$$

where $\tilde{U}$ is the root-mean-square (rms) velocity. After non-dimensionalization [17],

$$\mathrm{Re} = \sqrt{\frac{\mathrm{Ra}}{\mathrm{Pr}}} U = \sqrt{\frac{\mathrm{Ra}}{\mathrm{Pr}}} \langle \sqrt{\langle u^2 \rangle_V} \rangle_t. \tag{26}$$

where U is the dimensionless velocity.

In Section 3, we solve Eqs. (13)–(15) numerically.

3. Numerical method, validation, and simulation parameters

In this section, we describe our numerical method, its validation, and the simulation parameters.

3.1. Numerical method

We solve Eqs. (13)–(15) using MacCormack-TVD (total variation diminishing) finite-difference scheme on a collocated grid [40–42]. We employ a non-uniform tangent-hyperbolic grid in the z-direction to increase resolution near the boundaries, and uniform grids along the x and y directions.

All the equations are written in vectorial notation in the following conservative form [40]:

$$\frac{\partial \mathbf{X}}{\partial t} + \sum_\alpha \frac{\partial \mathbf{F}_\alpha}{\partial x_\alpha} = \sum_\alpha \mathbf{S}_\alpha, \tag{27}$$

where $\alpha = 1, 2, 3$ represent the x, y, and z directions respectively. $\mathbf{X}$ is a column vector that contains the variables ρ, ρu_α, and E; $\mathbf{F}_\alpha$ and $\mathbf{S}_\alpha$ are the respective fluxes and sources [48]. Hence,

$$\mathbf{X} = \begin{bmatrix} \rho \\ \rho u_x \\ \rho u_y \\ \rho u_z \\ E \end{bmatrix}; \quad \mathbf{S}_1 = \begin{bmatrix} 0 \\ f_1 \\ 0 \\ 0 \\ 0 \end{bmatrix}; \quad \mathbf{S}_2 = \begin{bmatrix} 0 \\ 0 \\ f_2 \\ 0 \\ 0 \end{bmatrix}; \quad \mathbf{S}_3 = \begin{bmatrix} 0 \\ 0 \\ 0 \\ f_3 \\ 0 \end{bmatrix};$$

$$\mathbf{F}_\alpha = \begin{bmatrix} \rho u_\alpha \\ \rho u_x u_\alpha - \tau_{x\alpha} \\ \rho u_y u_\alpha - \tau_{y\alpha} \\ \rho u_z u_\alpha - \tau_{z\alpha} + p \\ u_\alpha (E + p) - K \frac{\partial T}{\partial x_\alpha} - \sum_\beta u_\beta \tau_{\beta\alpha} \end{bmatrix}. \tag{28}$$

For natural convection, $f_1 = 0$, $f_2 = 0$, and $f_3 = -\rho g$. Using operator-splitting method, we separate the Eq. (27) into three one-dimensional equations:

$$\frac{\partial \mathbf{X}}{\partial t} + \frac{\partial \mathbf{F}_1}{\partial x_1} = \mathbf{S}_1, \; \frac{\partial \mathbf{X}}{\partial t} + \frac{\partial \mathbf{F}_2}{\partial x_2} = \mathbf{S}_2, \; \frac{\partial \mathbf{X}}{\partial t} + \frac{\partial \mathbf{F}_3}{\partial x_3} = \mathbf{S}_3. \tag{29}$$

The fields in $\mathbf{X}$ are discretized in space, whose value at the site (i, j, k) is $\mathbf{X}_{ijk}$. We denote the time step using superscript (n). The time stepping of $\mathbf{X}_{ijk}$ from (n) to $(n+1)$ is [40]

$$\mathbf{X}^{(n+1)}_{ijk} = \mathbf{L}_x\left(\frac{\delta t}{2}\right)\mathbf{L}_y\left(\frac{\delta t}{2}\right)\mathbf{L}_z\left(\frac{\delta t}{2}\right)\times \mathbf{L}_x\left(\frac{\delta t}{2}\right)\mathbf{L}_y\left(\frac{\delta t}{2}\right)\mathbf{L}_z\left(\frac{\delta t}{2}\right)\mathbf{X}^{(n)}_{ijk}, \tag{30}$$

where δt is the time-step; and $\mathbf{L}_\alpha$ is predictor–corrector operator in α-direction. The last three terms of Eq. (30) carry forward $\mathbf{X}$ from (n) to $(n+1/2)$, whereas the first three terms take from $(n+1/2)$ to $(n+1)$, each of which involves several sub-steps.

Along the z-direction ($\alpha = 3$), a predictor step from (n) to $(n+1/2)$ using backward difference is [40]

$$\mathbf{X}^P_{ijk} = \mathbf{X}^{(n)}_{ijk} - \frac{\delta t}{2}\left(\frac{\mathbf{F}^{(n)}_{\alpha,ijk} - \mathbf{F}^{(n)}_{\alpha,ij(k-1)}}{\delta x_\alpha}\right) + \frac{\delta t}{2}\mathbf{S}^{(n)}_{\alpha,ijk}. \tag{31}$$

After this step, we perform the corrector step [40]

$$\mathbf{X}^C_{ijk} = \mathbf{X}^{(n)}_{ijk} - \frac{\delta t}{2}\left(\frac{\mathbf{F}^{(n)}_{\alpha,ij(k+1)} - \mathbf{F}^P_{ijk}}{\delta x_\alpha}\right) + \frac{\delta t}{2}\mathbf{S}^P_{\alpha,ijk}. \tag{32}$$

We take an average of the above steps and add the TVD correction term $\mathbf{T}^{(n+1/2)}_{ijk}$, which yields [40]

$$\mathbf{X}^{(n+1/2)}_{ijk} = \frac{\mathbf{X}^P_{ijk} + \mathbf{X}^C_{ijk}}{2} + \mathbf{T}^{n+1/2}_{ijk}, \tag{33}$$

where

$$\mathbf{T}^{n+1/2}_{ijk} = G(r^+_{ijk} + r^-_{ij(k+1)})\, \delta\mathbf{X}^n_{ij(k+1/2)} - G(r^+_{ij(k-1)} + r^-_{ijk})\, \delta\mathbf{X}^n_{ij(k-1/2)}, \tag{34}$$

$$\delta\mathbf{X}^n_{ij(k+1/2)} = \mathbf{X}^n_{ij(k+1)} - \mathbf{X}^n_{ijk}, \tag{35}$$

$$\delta\mathbf{X}^n_{ij(k-1/2)} = \mathbf{X}^n_{ijk} - \mathbf{X}^n_{ij(k-1)}, \tag{36}$$

$$r^\pm_{ijk} = \frac{\left(\delta\mathbf{X}^n_{ij(k-1/2)}, \delta\mathbf{X}^n_{ij(k+1/2)}\right)}{\left(\delta\mathbf{X}^n_{ij(k\pm1/2)}, \delta\mathbf{X}^n_{ij(k\pm1/2)}\right)}. \tag{37}$$

The bracket $(\mathbf{A}, \mathbf{B})$ indicates the dot product between $\mathbf{A}$ and $\mathbf{B}$, and

$$G(x) = 0.5C(1 - \phi(x)), \tag{38}$$

where $\phi(x) = \max(0, \min(2x, 1))$ is the *minmod flux limiter function*, and

$$C = \begin{cases} \mathrm{Co}_\alpha(1 - \mathrm{Co}_\alpha), & \mathrm{Co}_\alpha \le 0.5 \\ 0.25, & \mathrm{Co}_\alpha > 0.5 \end{cases} \tag{39}$$

with Co_α representing the local Courant number in α-direction [40,41]. Identical processes are also adopted for the x- and y-directions.

The TVD correction preserves monotonicity and prevents spurious oscillations in the solution [41]. The MacCormack-TVD scheme is second-order accurate in space and time. For computing the boundary points, we use second-order forward and backward differences at the bottom and top plates, respectively.

3.2. Programming tools

We developed an object-oriented Python solver, DHARA, for simulating fully compressible equations on many GPUs and CPUs. The solver employs CuPy library [49] for GPU acceleration, and mpi4py [50] for multi-GPU communications. Note that CuPy provides a GPU-optimized alternative to NumPy [51]. We enhanced the code performance using `cupy.ElementwiseKernel()`, leading to 200X speedup on NVIDIA A100 GPU in comparison to a single-core AMD EPYC 7543 processor. For scaling studies, we ran DHARA on 128 nodes (512 A100 GPUs) of Polaris (Argonne National Laboratory) and on 1024 nodes (8192 AMD MI250X GPUs) of Frontier (Oak Ridge National Laboratory) and demonstrated near ideal scaling (see Appendix).

We performed the majority of our convection simulations on Polaris. Some simulations with smaller grids were performed on the Param Sanganak supercomputer of IIT Kanpur and on our laboratory clusters.

3.3. Validation

We validate our code by comparing our numerical Nusselt and Reynolds numbers with those computed by John and Schumacher [37] and Verhoeven et al. [17]. We compute Nu using Eq. (24). In particular, we simulate Eqs. (13)–(15) for $\mathrm{Ra} = 10^6$, $\epsilon = 0.1$, $\Gamma = 4$, $\gamma = 1.4$, Pr =

Table 1
Comparison between our Nu and Re and those of John and Schumacher [37] for Ra = 10^6, Pr = 0.7, $\Gamma = 4$, $\gamma = 1.4$, $\epsilon = 0.1$, and various D's.

Case	D	Nu [37]	Nu (our simulations)	$\mathrm{Error_{Nu}}$ (in %)	Re [37]	Re (our simulations)	$\mathrm{Error_{Re}}$ (in %)
1	0.1	7.94	7.90 ± 0.06	0.7	424	425 ± 3	0.7
2	0.34	7.64	7.67 ± 0.08	1.0	414	414 ± 4	0.9
3	0.5	6.93	6.89 ± 0.05	0.7	407	406 ± 3	0.7
4	0.6	6.24	6.18 ± 0.09	1.4	370	368 ± 5	1.3

Table 2
Comparison between our Nu and Re and those of Verhoeven et al. [17] for D = 0.49, $\epsilon = 0.1$, Pr = 0.7, $\Gamma = 2$, $\gamma = \frac{5}{3}$, and various Ra's.

Case	Ra	Nu [17]	Nu (our simulations)	$\mathrm{Error_{Nu}}$ (in %)	Re [17]	Re (our simulations)	$\mathrm{Error_{Re}}$ (in %)
1	10^4	2.1	2.175 ± 0.005	0.2	26.3	26.98 ± 0.05	0.2
2	10^5	3.9	4.0 ± 0.1	2.5	102	100 ± 3	3.3
3	10^6	7.1	7.3 ± 0.2	2.7	322	330 ± 7	2.0
4	10^7	13.4	14.1 ± 0.4	2.8	973	970 ± 20	2.4

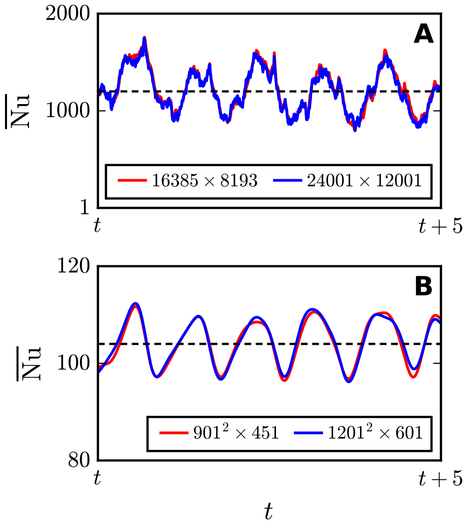

Fig. 2. For $\epsilon = 0.1, D = 0.5, \gamma = 1.3, \Gamma = 4$, and Pr = 0.7, the time series of $\overline{\mathrm{Nu}}$ computed using Eq. (24) for (A) 2D convection at Ra = 10^{15} on grids 16 385 × 8193 (red) and 24 001 × 12 001 (blue), and for (B) 3D convection at Ra = 10^{11} on grids $901^2 \times 451$ (red) and $1201^2 \times 601$ (blue).

0.7, and $D = 0.1, 0.34, 0.5, 0.6$. The Nu and Re computed by our code and those by John and Schumacher [37] are listed in Table 1. Next, we compute Re and Nu by varying Ra for a fixed $D = 0.49$, $\Gamma = 2$, $\gamma = \frac{5}{3}$, $\epsilon = 0.1$, Pr = 0.7, and compare our results with Verhoeven et al. [17] (see Table 2). Our results show good agreement with those reported by John and Schumacher [37] and Verhoeven et al. [17]. Our Nu and Re differ from the previous works by less than 3%.

We also perform grid independence test by comparing Nu for 2D convection at Ra = 10^{15} on grids 16 385 × 8193 and 24 001 × 12 001, and for 3D convection at Ra = 10^{11} on grids $901^2 \times 451$ and $1201^2 \times 601$. We compute $\overline{\mathrm{Nu}}$ for the steady states using Eq. (24) and plot the time series in Fig. 2(A, B) for 2D and 3D, respectively. The respective $\overline{\mathrm{Nu}}$ for 2D at Ra = 10^{15} are 1218 and 1204, and for 3D at Ra = 10^{11} are 103 and 104, which are within 1% of each other. The near similarity of Nu time series and their averages indicate that our results are grid independent, as long as the flow is well resolved.

3.4. Simulation parameters

We simulate Eqs. (13)–(15) in 2D and 3D using the numerical scheme described in Section 3.1. For the horizontal plates, we employ no-slip boundary condition for the velocity field and conducting boundary condition for the temperature field. The fields at the side walls satisfy periodic boundary condition.

For our simulations, we fix $\Gamma = 4$, $\gamma = 1.3$, $\epsilon = 0.1$, $D = 0.5$, Pr = 0.7 and vary Ra. The Rayleigh number Ra ranges from 10^9 to 10^{15} for 2D, and from 10^8 to 10^{11} for 3D. In Table 3, we list the grid sizes, Ra, $\overline{\mathrm{Nu}}$, Re, number of points in the top and bottom boundary layers (N_t^{BL} and N_b^{BL} respectively), and thicknesses of the top and bottom boundary layers (λ_t and λ_b respectively).

We compute $\overline{\mathrm{Nu}}$ and Re using Eqs. (24) and (26) respectively. However, $\overline{\mathrm{Nu}}$ and Re exhibit significant fluctuations, hence we average them over 50 time units in the steady state, except that we average over 30 and 20 time units for Ra = 10^{14} and 10^{15} respectively. We list these values in Table 3. Note that $\overline{\mathrm{Nu}}$ has around 10% errors for the 2D runs, but has maximum of 4% error for the 3D runs. The errors in Re range from 1% to 15% for 2D flows, and from 0.5% to 2% for 3D flows.

The highest grid resolutions are 16 385 × 8193 for 2D, and $901^2 \times 451$ for 3D. For all our runs, the number of grid points in the boundary layers exceeds 5, hence they satisfy the Grötzbach resolution criteria [27,52–54]. These observations indicate that our simulations are well resolved. For faster execution, we employ a single or multiple GPUs: a single GPU for Runs 1–5 and 8; and 4 GPUs for Runs 6, 7 and 9–11 of Table 3. Our largest 3D run with $901^2 \times 451$ grid required 7 days to complete on a Polaris node with four NVIDIA A100 GPUs.

In the following three sections, we will discuss various properties of compressible convection. We start with adiabatic profile and flow structures of the flow.

4. Adiabatic profile and flow structures

According to *Schwarzschild criterion*, at the onset of convection, the temperature in compressible convection decreases vertically with the rate g/C_p, which is the adiabatic temperature profile [55]. This result is derived using equilibrium thermodynamics. Interestingly, the atmospheres of the Earth and Sun too exhibit adiabatic temperature drop even though these systems are turbulent [6]. As we show below, we observe adiabatic cooling in our high Ra simulations, consistent with solar and Earth convection.

We compute horizontally and temporally averaged temperature $\langle T\rangle_{A,t}(z)$ for 2D and 3D runs. For a 2D flow, we average T along the horizontal axis and over time during a steady state. In 3D, the corresponding averaging is performed over horizontal planes and over time. In Fig. 3(A, B), we plot $\langle T\rangle_{A,t}(z)$ for the 2D and 3D flows respectively. Interestingly, $dT(z)/dz = -g/C_p$ in the bulk, thus verifying adiabatic cooling. The reason for this observation is as follows. We compute the ratio of the fluid kinetic energy and internal energy, $r = K_e/I_e = (\rho u^2/2)/(\rho C_v T)$, at every grid point. For 2D simulation with Ra = $10^9, 10^{12}, 10^{15}$, Fig. 4 illustrates the density plot of r. Fig. 5 illustrates the probability distribution function of r for 2D and 3D convection. As shown in the figures, $r \to 0$, implying that the internal energy dominates the fluid kinetic energy, or $u \ll c_s$ (c_s is the sound speed). The local Mach number of the flow is predominantly very small, but it reaches a maximum value of 0.9 at some isolated locations. The time

Table 3
For our 2D convection Runs 1 to 7, and 3D Runs 8 to 11: the Rayleigh number Ra, the grid size, the Reynolds number Re, the mean Nusselt number $\overline{\mathrm{Nu}}$, the number of grid points in the top and bottom boundary layers (N_t^{BL}, N_b^{BL}), and the thicknesses of top and bottom thermal boundary layers (λ_t, λ_b). Also, the polytropic index $\gamma = 1.3$, Prandtl number $\mathrm{Pr} = 0.7$, dissipation number $D = 0.5$, superadiabaticity $\epsilon = 0.1$, and the aspect ratio $\Gamma = 4$.

Run	Ra	Grid size	Re	$\overline{\mathrm{Nu}}$	N_t^{BL}	N_b^{BL}	λ_t	λ_b
1	10^9	3001 × 1501	$(1.35 \pm 0.01) \times 10^4$	22 ± 3	133	34	0.055	0.013
2	10^{10}	5001 × 2501	$(4.23 \pm 0.01) \times 10^4$	42 ± 5	180	54	0.036	0.010
3	10^{11}	5601 × 2801	$(1.28 \pm 0.03) \times 10^5$	90 ± 10	120	38	0.020	0.0062
4	10^{12}	6001 × 3001	$(4.04 \pm 0.07) \times 10^5$	180 ± 20	95	32	0.015	0.0047
5	10^{13}	8193 × 4097	$(1.3 \pm 0.1) \times 10^6$	360 ± 50	70	23	0.010	0.0031
6	10^{14}	12 001 × 6001	$(4.0 \pm 0.2) \times 10^6$	570 ± 70	72	21	0.0066	0.002
7	10^{15}	16 385 × 8193	$(1.3 \pm 0.2) \times 10^7$	1200 ± 200	62	18	0.0042	0.0012
8	10^8	513^2 × 257	$(2.21 \pm 0.01) \times 10^3$	14.0 ± 0.2	35	12	0.076	0.0226
9	10^9	801^2 × 401	$(6.86 \pm 0.02) \times 10^3$	28.6 ± 0.5	32	11	0.047	0.0158
10	10^{10}	801^2 × 401	$(2.03 \pm 0.04) \times 10^4$	53.9 ± 0.5	20	7	0.028	0.010
11	10^{11}	901^2 × 451	$(5.86 \pm 0.08) \times 10^4$	103 ± 4	13	5	0.017	0.0061

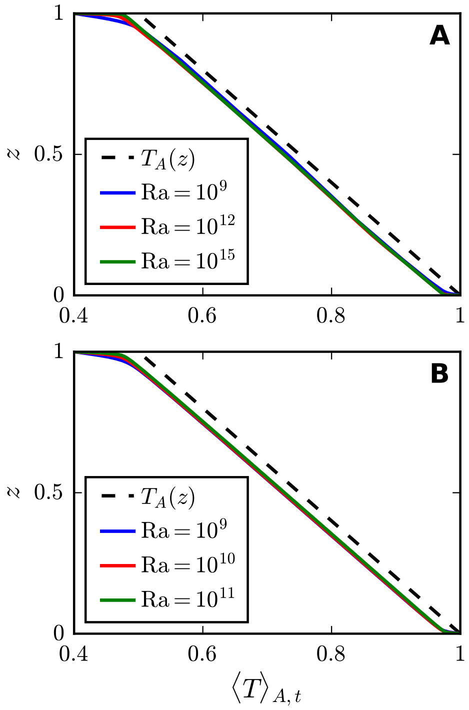

Fig. 3. Profiles of horizontally and temporally averaged $\langle T \rangle_{A,t}(z)$ for (A) 2D convection for $\mathrm{Ra} = 10^9$ (blue), $\mathrm{Ra} = 10^{12}$ (red), and $\mathrm{Ra} = 10^{15}$ (green); and (B) 3D convection for $\mathrm{Ra} = 10^9$ (blue), $\mathrm{Ra} = 10^{10}$ (red), and $\mathrm{Ra} = 10^{11}$ (green). The black dashed line represents the adiabatic temperature ($T_A(z)$). (For interpretation of the references to color in this figure legend, the reader is referred to the web version of this article.)

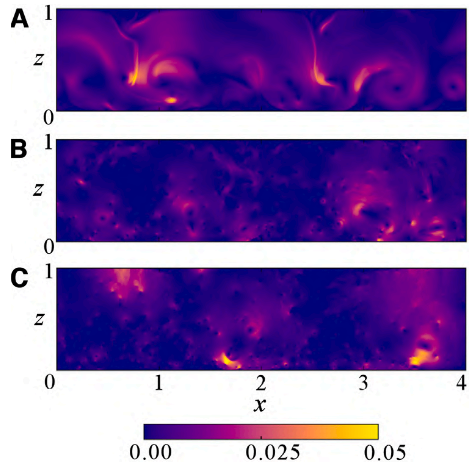

Fig. 4. For 2D compressible convection with (A) $\mathrm{Ra} = 10^9$, (B) 10^{12}, and (C) 10^{15}, the density plots of the ratio of fluid kinetic energy and internal energy, $r = (\rho u^2/2)/(\rho C_v T)$.

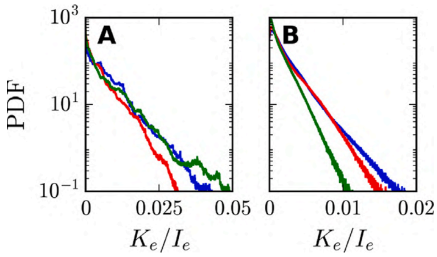

Fig. 5. Normalized probability distribution function (PDF) of the ratio of the kinetic energy density, $K_e = \rho u^2/2$, and the internal energy density, $I_e = \rho C_v T$ for (A) 2D and (B) 3D convection during respective steady states. Color convention is the same as Fig. 3. (For interpretation of the references to color in this figure legend, the reader is referred to the web version of this article.)

average of maximum turbulent Mach number for all Ra's vary from 0.5 to 0.6. This feature implies that the system is near thermodynamic equilibrium in the bulk. This is the reason why compressible convection exhibits adiabaticity in the bulk even for large Ra's [6,12]. These results are consistent with the fact that the convective time scale, $t_{\mathrm{conv}} = \sqrt{d/(\epsilon g)}$, is smaller than conductive time scale, $t_{\mathrm{cond}} = d^2/\kappa$. Their ratio $t_{\mathrm{conv}}/t_{\mathrm{cond}} = 1/\sqrt{\mathrm{RaPr}} \ll 1$. Note, however, that the Schwarzschild criterion does hold in the boundary layers, where the flow is dynamic.

Next, we discuss the flow structures of compressible convection. Since the temperature is dominated by $T_A(z)$, we subtract it from the total temperature and plot the superadiabatic temperature $T_{\mathrm{sa}}(\mathbf{r}) = T(\mathbf{r}) - T_A(z)$, along with the vector plots of the velocity field. These plots are illustrated in Figs. 6 and 7 for 2D and 3D flows respectively. For movies, refer to [56]. The figures and movies exhibit flow activities at the bottom and the top of the box, where the thermal plumes are generated. Note, however, that the flow velocity of the plumes is much smaller than the sound speed.

As shown in Fig. 3, the bulk temperature is nearly adiabatic, in contrast to the constant bulk temperature in RBC. Interestingly, $T_{\mathrm{sa}} \ll T_A$ (see Figs. 6 and 7) indicating the dominance of T_A. As shown in Figs. 6 and 7), turbulent convection is more prominent near the bottom than the top, consistent with earlier findings [37,57]. As argued by John and Schumacher [37], and Wu and Libchaber [57], the fluid is denser at the bottom than the top. Hence, using $\mu = \nu\rho = \mathrm{const.}$, we deduce that ν and κ at the bottom are smaller than those at the top. Therefore, the bottom region has stronger turbulence with relatively thin and easily-detachable plumes than the top region [36,57]. In the following, we discuss these boundary layer features.

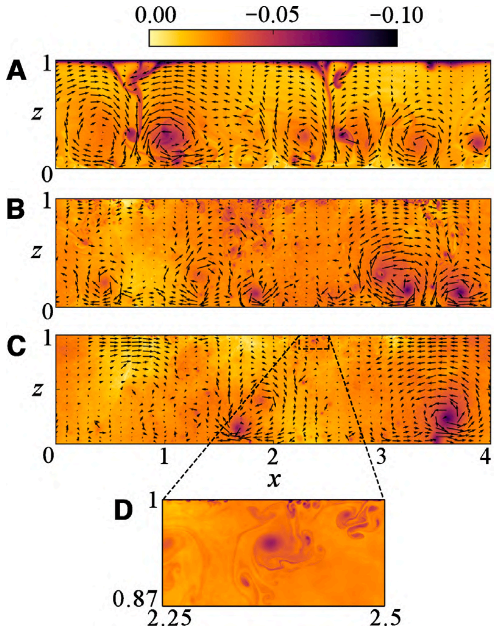

Fig. 6. Plots of the velocity field **u** and superadiabatic temperature $T_{sa}(\mathbf{r})$ for 2D convection with (A) Ra = 10^9, (B) Ra = 10^{12}, and (C) Ra = 10^{15}. (D) The magnified view near the top boundary for Ra = 10^{15}.

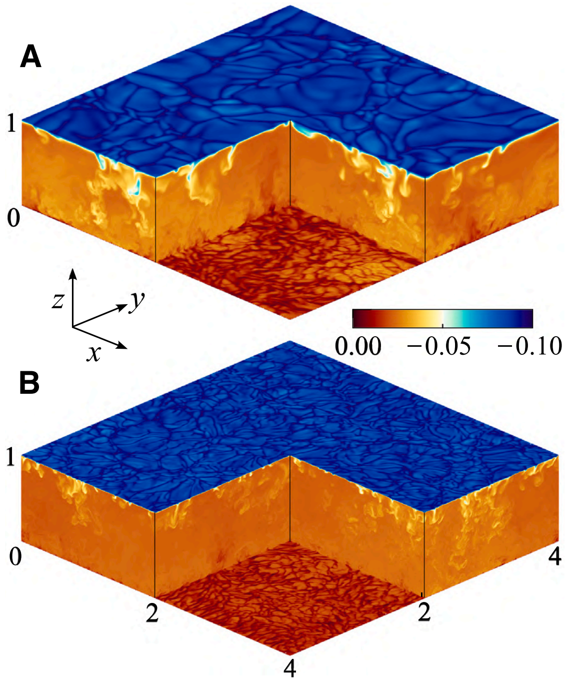

Fig. 7. Plots of superadiabatic temperature $T_{sa}(\mathbf{r})$ for 3D convection at (A) Ra = 10^9 and (B) Ra = 10^{11}.

5. Boundary layers of compressible convection

The planar-averaged temperature $\langle T\rangle_{A,t}(z)$, exhibited in Fig. 3, shows that the temperature drops rather sharply at the top and bottom boundary layers. In Figs. 8 and 9, we plot the zoomed-view of the 2D

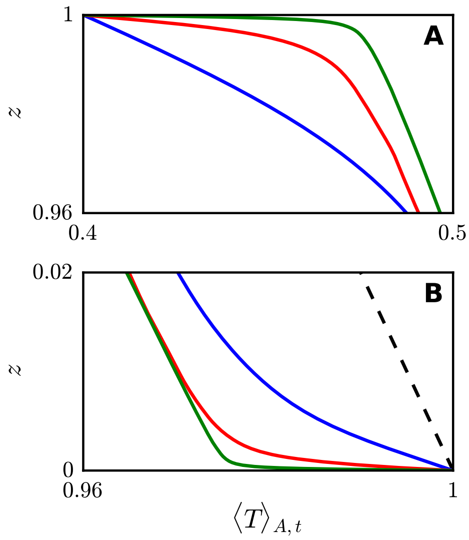

Fig. 8. Boundary layers in 2D convection: The horizontally and temporally averaged $\langle T\rangle_{A,t}(z)$ in the (A) top boundary layer and (B) bottom boundary layer. Color convention is the same as Fig. 3. (For interpretation of the references to color in this figure legend, the reader is referred to the web version of this article.)

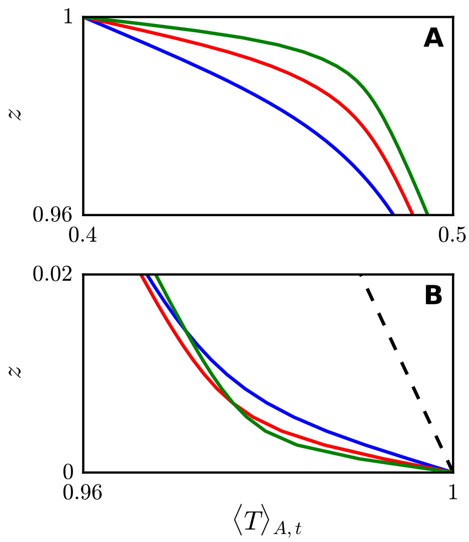

Fig. 9. Boundary layers in 3D convection: $\langle T\rangle_{A,t}(z)$ in the (A) top boundary layer and (B) bottom boundary layer. Color convention is the same as Fig. 3. (For interpretation of the references to color in this figure legend, the reader is referred to the web version of this article.)

and 3D boundary layers.

Unlike RBC, in compressible convection, the top boundary layer is thicker than the bottom one. At the bottom boundary layers of the 2D flows, the nondimensional temperature drops from 1 to 0.96 (approximately) as z increases from 0 to 0.02. However, at the top boundary layer, the temperature drops more rapidly—from 0.5 to 0.4 as z varies from 0.96 to 1. A similar temperature drop is observed in 3D flows, albeit at low Ra's. These abrupt temperature drops at the top are due to higher κ at the top than the bottom because of the density profile [37,57]. Also note that at the top boundary layer, the rate of temperature drop increases with Ra. The above results are consistent with those of John and Schumacher [36,37].

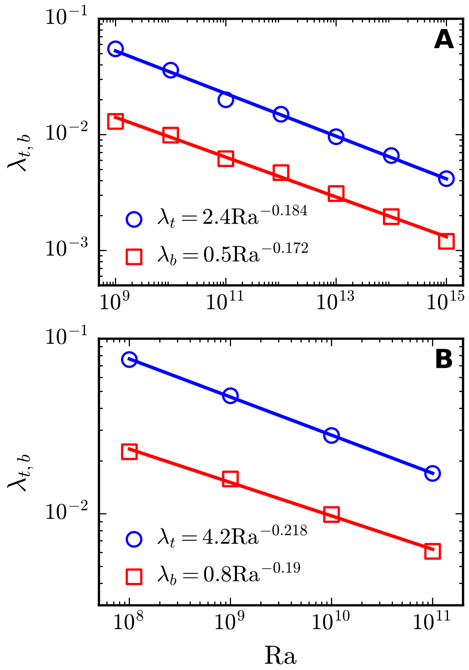

Fig. 10. Plots of thermal boundary layer thicknesses $\lambda_{t,b}$ vs. Ra for (A) 2D and (B) 3D flows. The blue and red symbols depict the thicknesses of the top and bottom boundary layers for various Ra's.

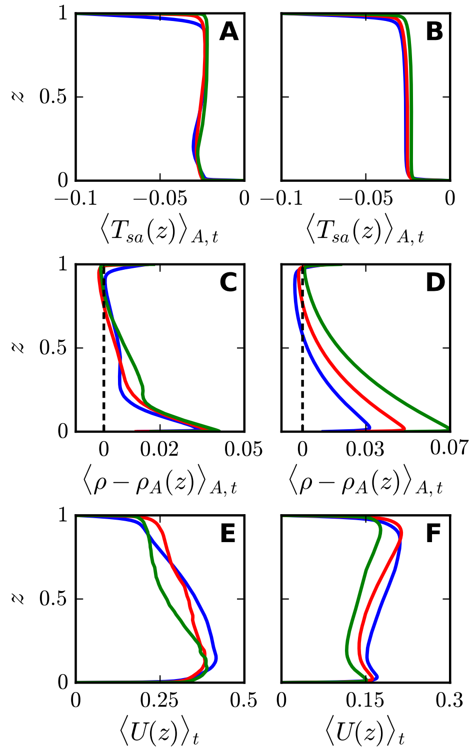

Fig. 11. The planar and temporal averaged $T_{sa}(z) = T(z) - T_A(z)$ (A,B), $\rho - \rho_A(z)$ (C,D), and rms velocity $U(z)$ (E,F). The left column represents 2D flows, whereas the right column represents 3D flows. The black dashed lines in (C, D) denote adiabatic profile. Color convention is the same as Fig. 3. (For interpretation of the references to color in this figure legend, the reader is referred to the web version of this article.)

We compute the thicknesses of the top and bottom boundary layers. For the same, we identify $z = \lambda_{t,b}$ where the slope of $\langle T\rangle_{A,t}$ approximates the adiabatic temperature gradient $-D$ near the top and bottom boundaries, respectively. The variation of $\lambda_{t,b}$ as a function of Ra is plotted in Fig. 10(A, B) for 2D and 3D flows. The red squares and blue circles represent the bottom and top boundary layers, respectively. It is evident that the top boundary layer is wider than the bottom boundary layer, and that the thickness of both boundary layers decrease with the increase of Ra. Interestingly, the boundary layer thickness follows a power law with Ra: $\lambda_t = (2.4 \pm 0.4)\text{Ra}^{(-0.184\pm0.005)}$, $\lambda_b = (0.5 \pm 0.1)\text{Ra}^{(-0.172\pm0.006)}$ for 2D, and $\lambda_t = (4.2 \pm 0.2)\text{Ra}^{(-0.218\pm0.003)}$, $\lambda_b = (0.8 \pm 0.2)\text{Ra}^{-0.19\pm0.01}$ for 3D. Note that the prefactor of λ_t is larger than that of λ_b because the top boundary layer is thicker than the bottom one. In contrast, the top and bottom boundary layers in RBC scale identically, e.g., $\lambda_t \sim \lambda_b \sim \text{Ra}^{-0.30}$ for Pr = 1 [58]. Thus, boundary layers of RBC and compressible convection behave very differently.

In Fig. 11 we plot the temporal and planar averaged superadiabatic temperature $T_{sa}(z) = T(z) - T_A(z)$, $\rho - \rho_A(z)$, and rms velocity $U(z)$. We observe that in the bulk, $T_{sa}(z) \approx 0$ for both 2D and 3D because the bulk temperature nearly follows adiabatic profile (see Fig. 11(A, B)). The additional temperature gradients, $dT_{sa}(z)/dz$, near the top and bottom boundary layers drive the flow. As shown in Fig. 11(A, B), $T_{sa}(z)$ nearly collapses over each other, apart from some fluctuations. As described earlier in this section, $T_{sa}(z)$ drop is greater at the top than the bottom. Figs. 11(C, D) illustrate that the density is closer to the adiabatic profile in the upper box than in the lower box. The density variations from the adiabatic profile are greater near the bottom boundary than the top one. Note that the deviation from adiabaticity for density ($\rho - \rho_A(z)$) increases with Ra, both for 2D and 3D. Figs. 11(E, F) illustrate $\langle U(z)\rangle_t$ arising due to the turbulent activities. Note that $\langle U(z)\rangle_t$ decreases with increase in Ra for both 2D and 3D flows. Also, for 2D convection, $\langle U(z)\rangle_t$ at the bottom is larger than that near the top. However, it is nearly reversed in 3D. Thus, $\langle U(z)\rangle_t$ exhibits asymmetry around the mid-plane, which is unlike nearly symmetric $\langle U(z)\rangle_t$ in RBC [59]. Compared to the 3D plots, 2D plots exhibit stronger fluctuations probably because of dimensionality. We need averaging over longer times to achieve the same statistical convergence as in 3D.

In the next section, we will discuss Nu and Re scaling for turbulent compressible convection.

6. Nu and Re scaling for compressible convection

In this section, we compute the global measures, Re and Nu, for 2D and 3D compressible convection.

6.1. Re *Scaling*

We analyze the relative strengths of various terms of the momentum equation along $\hat{z}$ [Eq. (2)]. The different terms of the equation along $\hat{z}$ are

$$\text{Nonlinear term}: \mathrm{F}_n = \rho(\mathbf{u}\cdot\nabla)u_z, \tag{40}$$

$$\text{Pressure gradient}: \mathrm{F}_p = -\frac{\partial p}{\partial z}, \tag{41}$$

$$\text{Buoyancy}: \mathrm{F}_b = \rho g, \tag{42}$$

$$\text{Viscous force}: \mathrm{F}_v = \partial_i \tau_{iz}. \tag{43}$$

We compute the volume averages of the above four terms, along with $\langle \mathrm{F}_b\rangle - \langle \mathrm{F}_p\rangle$. These quantities are plotted in (Figs. 12A, 13A) for 2D and

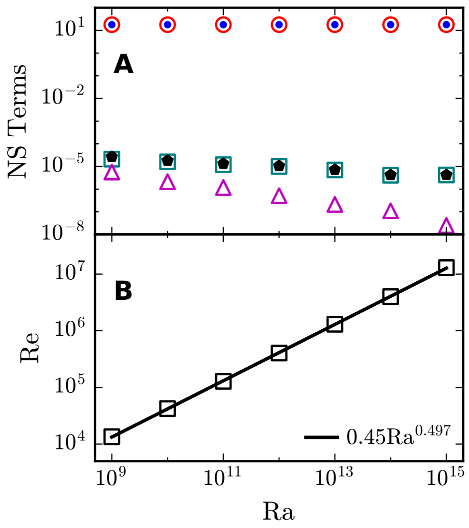

Fig. 12. For 2D convection, along the z direction of the momentum equation: (A) the volume averaged $\langle F_p \rangle$ (red unfilled circles), $\langle F_b \rangle$ (blue dots), $\langle F_n \rangle$ (teal unfilled squares), $\langle F_v \rangle$ (magenta unfilled triangles), and $\langle F_b \rangle - \langle F_p \rangle$ (black pentagons); (B) the Re scaling, which is $\mathrm{Re} \sim \mathrm{Ra}^{0.497}$.

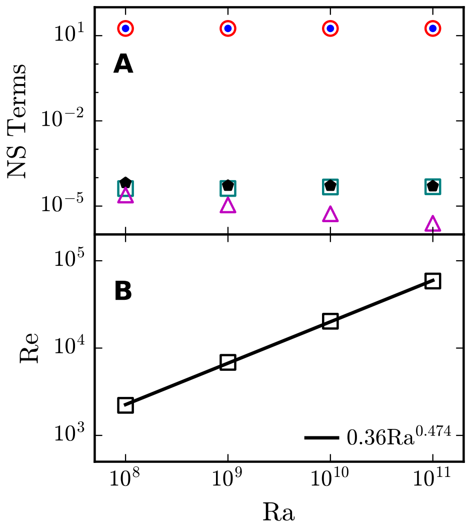

Fig. 13. For 3D convection, along the z direction of the momentum equation: (A) the volume averaged $\langle F_p \rangle$ (red unfilled circles), $\langle F_b \rangle$ (blue dots), $\langle F_n \rangle$ (teal unfilled squares), $\langle F_v \rangle$ (magenta unfilled triangles), and $\langle F_b \rangle - \langle F_p \rangle$ (black pentagons); (B) the Re scaling, which is $\mathrm{Re} \sim \mathrm{Ra}^{0.474}$.

3D flows respectively. The plots clearly show that

$$\langle F_p \rangle \approx \langle F_b \rangle. \tag{44}$$

This balance is a key feature of *Schwarzschild criterion* [55] (see Section 4). Interestingly, Eq. (44) is satisfied for larger Ra's as well. This is the reason why bulk flow of compressible convection is nearly adiabatic for high Ra's as well.

It turns out that $\langle F_p \rangle$ and $\langle F_b \rangle$ do not cancel precisely, and the difference between the two terms nearly equals the nonlinear term, i.e.,

$$\langle F_n \rangle \approx \langle F_b \rangle - \langle F_p \rangle. \tag{45}$$

Table 4
The volume- and time-averaged (over 10 free-fall times) Nu, $\mathrm{Nu_{conv}}$ and Nu_K of Eq. (22) for 2D and 3D runs. These quantities have significant fluctuations, especially in 2D convection. Nu_K is relatively small with large fluctuations. In the table, we do not report Nu_K for runs 2 to 5 because of large fluctuations.

Run	Ra	Nu	$\mathrm{Nu_{conv}}$	Nu_K
1	10^9	21 ± 2	28 ± 2	−6 ± 2
2	10^{10}	39 ± 7	52 ± 4	–
3	10^{11}	80 ± 23	114 ± 8	–
4	10^{12}	160 ± 50	250 ± 30	–
5	10^{13}	300 ± 150	500 ± 100	–
6	10^8	13.9 ± 0.4	16.1 ± 0.5	−1.9 ± 0.7
9	10^9	27 ± 2	32 ± 2	−4 ± 1
7	10^{10}	55 ± 2	64 ± 3	−9 ± 1
8	10^{11}	110 ± 14	130 ± 15	−18 ± 2

The viscous term, which is $\lessapprox 10^{-5}$ for all Ra's, is much less than the other three terms. Using Eq. (45) we derive that

$$\frac{\tilde{\rho}\tilde{U}^2}{d} \sim \epsilon \tilde{\rho} g, \tag{46}$$

where ϵ is superadiabaticity, a small constant. Using Eqs. (11) and (12), we derive that

$$\mathrm{Re} = \frac{\tilde{U}d}{\nu} \approx \sqrt{\frac{\mathrm{Ra}}{\mathrm{Pr}}}. \tag{47}$$

Therefore, $\mathrm{Re} \propto \mathrm{Ra}^{1/2}$. We remark that the momentum equation of RBC exhibits a different balance among various terms, with significant weight for the nonlinear term [5,60]. Consequently, the Re scaling for the two systems are somewhat different. The relation $\mathrm{Re} \propto \mathrm{Ra}^{1/2}$ remains the dominant scaling for RBC as well [18], but the exponent correction may reach 0.05 for large Ra's [5,18].

Using the 2D and 3D numerical data, we compute Re for various Ra's in the respective steady states, and list them in Table 3 (see Section 3.4). The listed Re's have errors ranging from 1% to 15% for the 2D flows, and from 0.5% to 2% for the 3D flows. We exhibit the Re vs. Ra plots for the 2D and 3D flows in (Figs. 12B, 13B). We observe that $\mathrm{Re} = (0.45 \pm 0.02)\mathrm{Ra}^{(0.497 \pm 0.002)}$ for 2D, and $\mathrm{Re} = (0.36 \pm 0.04)\mathrm{Ra}^{(0.474 \pm 0.005)}$ for 3D. These numerical results are consistent with the prediction that $\mathrm{Re} \propto \mathrm{Ra}^{1/2}$.

6.2. Nu *Scaling*

Here, we discuss the Nu scaling. We compute the volume- and time-averaged Nu, convection-induced $\mathrm{Nu_{conv}}$, and u_z-induced Nu_K using Eq. (22), as well as boundary-layer $\overline{\mathrm{Nu}}$ using Eq. (24) for 2D and 3D runs. We employ a moving average over 10 free-fall times. The bulk Nu's, the first three quantities of the above, are listed in Table 4, whereas $\overline{\mathrm{Nu}}$ is listed in Table 3. Note that $\overline{\mathrm{Nu}}$, averaged over nearly 50 time units, has a maximum of 17% error for the 2D runs, but a maximum of 4% errors for the 3D runs (see Table 3 and Section 3.4).

The bulk Nu fluctuates significantly for 2D convection [61], hence we time average them over approximately 10 time units. The total Nu's have large errors, especially for large Ra's. We exclude the bulk Nu's for 2D at $\mathrm{Ra} = 10^{14}$ and $\mathrm{Ra} = 10^{15}$ as they exhibit more than 100% error. The errors in Nu for the 2D flows range from 10% up to 50%, but they are within 10% for the 3D flows. We observe that $\mathrm{Nu_{conv}}$ has similar errors as Nu, but Nu_K has relatively large errors for 2D convection. We do not list Nu_K for Runs 2 to 5 due to large errors. Fortunately, $\mathrm{Nu}_K \ll \mathrm{Nu_{conv}}$, hence we can ignore Nu_K safely.

In Figs. 14(A, B), we plot the averaged Nu, $\mathrm{Nu_{conv}}$, and $\overline{\mathrm{Nu}}$ for 2D and 3D flows. We also plot Nu_K for 3D flows. Interestingly, $\overline{\mathrm{Nu}} \approx \mathrm{Nu}$, but Nu has much larger fluctuations than $\overline{\mathrm{Nu}}$. Also, $\mathrm{Nu}_K \ll \mathrm{Nu_{conv}}$ up to $\mathrm{Ra} = 10^{13}$. Hence, in Eq. (22), the maximal contribution to Nu comes from $\mathrm{Nu_{conv}}$. The fluid is denser at the bottom than near the top, which leads to $\rho u_z u^2$ being more negative than positive. Hence, $\mathrm{Nu}_K \sim \langle \rho u_z u^2 \rangle < 0$

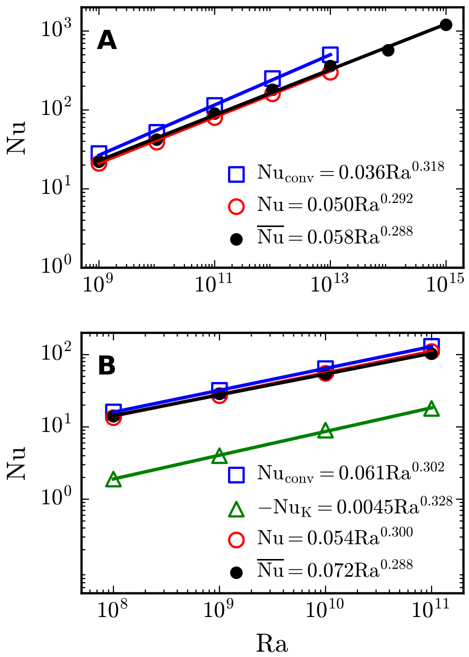

Fig. 14. Nu Scaling for (A) 2D and (B) 3D convection. The figure exhibits $\mathrm{Nu_{conv}}$, Nu_K, Nu, and $\overline{\mathrm{Nu}}$ [see Eqs. ((22), (24))]. Note that Nu follows near classical scaling in both 2D and 3D.

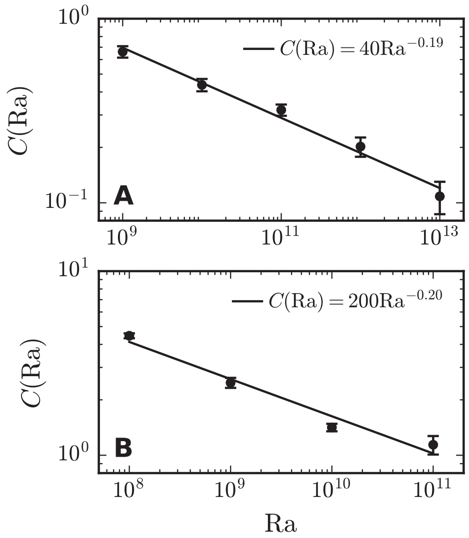

Fig. 15. Plots of correlation $C(\mathrm{Ra})$ [Eq. (49)] for (A) 2D and (B) 3D convection. These correlations bring down the Nu scaling from 1/2 to near 0.3.

in compressible convection. This is unlike RBC where u_z is symmetric around the mid-plane, leading to $\langle \rho u_z u^2 \rangle = 0$ [1,2].

Quantitatively, $\mathrm{Nu_{conv}} = (0.036 \pm 0.007)\mathrm{Ra}^{(0.318\pm0.007)}$ for 2D convection, and $(0.061 \pm 0.002)\mathrm{Ra}^{(0.302\pm0.002)}$ for 3D convection. The volume-averaged Nu scales as $(0.050 \pm 0.005)\mathrm{Ra}^{(0.292\pm0.004)}$ for 2D, and $(0.054 \pm 0.003)\mathrm{Ra}^{(0.300\pm0.003)}$ for 3D. We observe that $\overline{\mathrm{Nu}}$ follows a similar scaling as Nu. Thus, turbulent compressible convection follows *classical scaling*, rather than *ultimate-regime scaling*.

The above results lead to [see Eq. (22)]

$$\mathrm{Nu} \approx \mathrm{Nu_{conv}} \approx \left\langle \tilde{\rho}\tilde{u}_z \tilde{T}_{\mathrm{sa}} \right\rangle \approx C(\mathrm{Ra}) \sqrt{\left\langle (\tilde{\rho}\tilde{u}_z)^2 \right\rangle \left\langle \tilde{T}_{\mathrm{sa}}^2 \right\rangle}, \tag{48}$$

where

$$C(\mathrm{Ra}) = \frac{\left\langle \tilde{\rho}\tilde{u}_z \tilde{T}_{\mathrm{sa}} \right\rangle}{\sqrt{\left\langle (\tilde{\rho}\tilde{u}_z)^2 \right\rangle \left\langle \tilde{T}_{\mathrm{sa}}^2 \right\rangle}} \tag{49}$$

is the normalized correlation between $\tilde{\rho}\tilde{u}_z$ and $\tilde{T}_{\mathrm{sa}}$. Note that $\sqrt{\left\langle (\tilde{\rho}\tilde{u}_z)^2 \right\rangle \left\langle \tilde{T}_{\mathrm{sa}}^2 \right\rangle} \sim U \sim \sqrt{\mathrm{RaPr}}$. The correlation $C(\mathrm{Ra})$ plotted in Fig. 15 reveals that $C(\mathrm{Ra}) = (40 \pm 10)\mathrm{Ra}^{(-0.19\pm0.01)}$ for 2D, and $C(\mathrm{Ra}) = (200 \pm 100)\mathrm{Ra}^{(-0.20\pm0.03)}$ for 3D. Hence, $C(\mathrm{Ra})$ corrects the Nu exponent from 1/2 to near 0.3. This feature is similar to those observed by Verma et al. [62] for RBC. However, the component Nu_K present in compressible convection, which is negative, further suppresses the Nu exponent to 0.29 in 2D and 0.3 in 3D.

Even though the dynamics of RBC and compressible convection are significantly different, the classical Re and Nu scaling are very similar. This feature is possibly due to similar $C(\mathrm{Ra})$ scaling in both the systems, an issue that needs a closer examination.

7. Summary

In this paper, we present simulation results of compressible convection for very high Ra's. We simulated 2D and 3D convective flows for $\mathrm{Pr} = 0.7$, superadiabaticity parameter $\epsilon = 0.1$, and dissipation number $D = 0.5$. We choose Ra's in the range of 10^9 to 10^{15} in 2D, but $\mathrm{Ra} = 10^8$, 10^9, 10^{10} and 10^{11} in 3D. The main results reported in the paper are as follows:

1. For all our runs, the pressure gradient nearly matches with the buoyancy, thus satisfying the adiabaticity condition or Schwarzschild criterion, even for very large Ra. The density too is nearly adiabatic with the fluid density decreasing with height. We show that the adiabaticity arises because the internal energy is much stronger than the fluid kinetic energy. Hence, the flow is in quasi thermodynamic equilibrium, except near the bottom and top plates where the temperature gradients exceed g/C_P.
2. Unlike RBC, the flow and the boundary layers of compressible convection are asymmetric along the vertical. For example, the top boundary layer is thicker than the bottom boundary. With the increase in Ra, the thicknesses of both the thermal boundary layers decrease with Ra as $\sim \mathrm{Ra}^{-0.178}$ in 2D and as $\sim \mathrm{Ra}^{-0.2}$ in 3D.
3. For high Ra's, the pressure gradient and buoyancy do not cancel each other exactly. The difference between the two terms nearly equals the nonlinear term. Using this feature, we derive that $\mathrm{Re} \sim \mathrm{Ra}^{1/2}$. Our numerical results nearly follow the above scaling.
4. We show that the Nusselt number for compressible convection exhibits near classical scaling ($\mathrm{Ra}^{0.30}$) up to $\mathrm{Ra} = 10^{15}$ in 2D and up to 10^{11} in 3D. Note that for RBC, several researchers [27,30] have reported a gradual transition to the ultimate regime, which appears to be absent in compressible convection, at least up to $\mathrm{Ra} = 10^{15}$ for 2D convection.
5. Many features of compressible convection deviate from RBC, where the temperature and the density in the bulk are nearly constant. Despite these differences, the Re and Nu scaling for compressible convection and RBC are quite similar.

Our results on compressible convection are of major importance to the atmospheres of the Earth and the Sun, both of which exhibit near adiabatic temperature profile while being turbulent. We plan to perform somewhat realistic simulations of the Earth and the Sun in near future; the latter simulation would require higher Rayleigh numbers (10^{22} to 10^{24}) and inclusion of the magnetic field. These studies would provide us valuable insights into the energetics, heat transport, and magnetic field dynamics in the Sun.

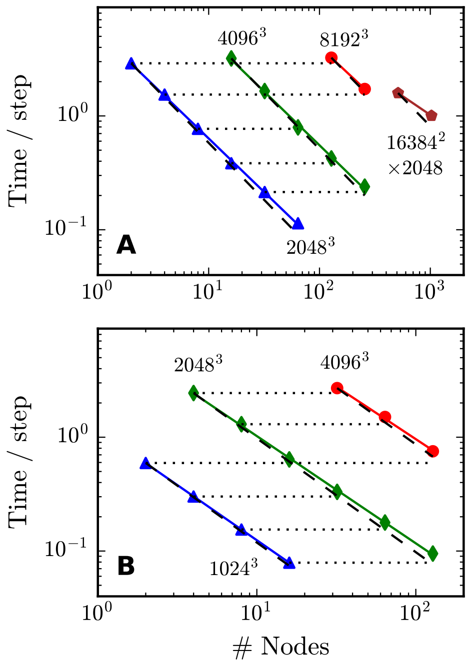

Fig. A.16. Scalability of DHARA on GPUs of (A) Frontier and (B) Polaris. The figure shows the time taken per timestep vs. the number of nodes, demonstrating strong and weak scaling.

CRediT authorship contribution statement

Harshit Tiwari: Writing – review & editing, Visualization, Validation, Software, Methodology, Investigation, Formal analysis, Data curation, Conceptualization. **Lekha Sharma:** Writing – review & editing, Writing – original draft, Visualization, Validation, Software, Methodology, Investigation, Formal analysis, Data curation, Conceptualization. **Mahendra K. Verma:** Writing – review & editing, Supervision, Resources, Project administration, Funding acquisition, Conceptualization.

Declaration of competing interest

The authors declare the following financial interests/personal relationships which may be considered as potential competing interests: Mahendra K. Verma reports financial support was provided by Science and Engineering Research Board. If there are other authors, they declare that they have no known competing financial interests or personal relationships that could have appeared to influence the work reported in this paper.

Acknowledgments

The authors thank K. R. Sreenivasan and Jörg Schumacher for useful discussions. We also thank Argonne Leadership Computing Facility (ALCF) and Oak Ridge National Laboratory (ORNL) for the computer time through the Director's Discretionary Program. Simulations were performed on Polaris, Frontier, Param Sanganak, and our laboratory GPUs. We acknowledge Manthan Verma for his assistance in configuring the computing environments. LS acknowledges the Institute Postdoctoral Fellowship of IITK. Part of this work was supported by the Science and Engineering Research Board, India (Grant Nos. SERB/PHY/2021522 and SERB/PHY/2021473), and the J. C. Bose Fellowship (SERB /PHY/2023488).

Appendix. Scalability of DHARA

We performed scaling analysis of DHARA (finite-difference solver) on Frontier of Oak Ridge National Laboratory (ORNL) and on Polaris of Argonne Leadership Computing Facility (ALCF). Each node of Frontier contains four AMD MI250X, each with 2 Graphics Compute Dies (GCDs), whereas each node of Polaris contains four NVIDIA A100 GPUs. On Frontier, we vary grids from 2048^3 to $16384^2 \times 2048$ and nodes from 8 to 1024. On Polaris, the corresponding grids were varied from 1024^3 to 4096^3, and the nodes from 2 to 128.

Fig. A.16(A, B) illustrate the time taken for a timestep as a function of number of nodes on Frontier and Polaris respectively. The reported time is averaged over several timesteps. We observe that the time taken $T \propto n^{-1}$, where n is the number of nodes, thus indicating strong scaling for DHARA in both systems. In addition, DHARA shows good weak scaling because the time taken remains unchanged when the grid size and number of nodes are increased proportionally.

Data availability

Data will be made available on request.

References

[1] E.D. Siggia, High Rayleigh number convection, Annu. Rev. Fluid Mech. 26 (1) (1994) 137–168.
[2] G. Ahlers, S. Grossmann, D. Lohse, Heat transfer and large scale dynamics in turbulent Rayleigh-Bénard convection, Rev. Modern Phys. 81 (2009) 503–537.
[3] D. Lohse, K.-Q. Xia, Small-scale properties of turbulent Rayleigh–Bénard convection, Annu. Rev. Fluid Mech. 42 (1) (2010) 335–364.
[4] F. Chillà, J. Schumacher, New perspectives in turbulent Rayleigh-Bénard convection, Eur. Phys. J. E 35 (7) (2012) 58.
[5] M.K. Verma, Physics of Buoyant Flows: From Instabilities to Turbulence, World Scientific, Singapore, 2018.
[6] J. Schumacher, K.R. Sreenivasan, Colloquium: Unusual dynamics of convection in the sun, Rev. Modern Phys. 92 (4) (2020) 041001.
[7] H.C. Spruit, A. Nordlund, A.M. Title, Solar convection, Annu. Rev. Astron. Astrophys. 28 (1) (1990) 263–303.
[8] C.A. Jones, K.M. Kuzanyan, Compressible convection in the deep atmospheres of giant planets, Icarus 204 (1) (2009) 227–238.
[9] E.A. Spiegel, Convective instability in a compressible atmosphere. I., Astrophys. J. 141 (1965) 1068–1090.
[10] S. Chandrasekhar, Hydrodynamic and Hydromagnetic Stability, Oxford University Press, Clarendon, 1961.
[11] E.A. Spiegel, G. Veronis, On the Boussinesq approximation for a compressible fluid, Astrophys. J. 131 (1960) 442.
[12] C.J. Hansen, S.D. Kawaler, V. Trimble, Stellar Interiors: Physical Principles, Structure, and Evolution, Springer-Verlag, New York, 2012.
[13] Z.-H. Wan, Q. Wang, B. Wang, S. Xia, Q. Zhou, D.-J. Sun, On non-Oberbeck–Boussinesq effects in Rayleigh–Bénard convection of air for large temperature differences, J. Fluid Mech. 889 (2020) A10.
[14] A. Pandey, J. Schumacher, K.R. Sreenivasan, Non-Boussinesq convection at low Prandtl numbers relevant to the sun, Phys. Rev. Fluids 6 (10) (2021) 100503.
[15] A. Pandey, J. Schumacher, K.R. Sreenivasan, Non-Boussinesq low-Prandtl-number convection with a temperature-dependent thermal diffusivity, Astrophys. J. 907 (1) (2021) 56.
[16] D.O. Gough, The anelastic approximation for thermal convection, J. Atmos. Sci. 26 (1969) 448–456.
[17] J. Verhoeven, T. Wiesehöfer, S. Stellmach, Anelastic versus fully compressible turbulent Rayleigh–Bénard convection, Astrophys. J. 805 (1) (2015) 62.
[18] S. Grossmann, D. Lohse, Scaling in thermal convection: a unifying theory, J. Fluid Mech. 407 (2000) 27–56.
[19] S. Grossmann, D. Lohse, Thermal convection for large Prandtl numbers, Phys. Rev. Lett. 86 (2001) 3316–3319.
[20] B.I. Shraiman, E.D. Siggia, Heat transport in high-Rayleigh-number convection, Phys. Rev. A 42 (6) (1990) 3650–3653.
[21] M. Lesieur, Turbulence in Fluids, Springer-Verlag, Dordrecht, 2008.
[22] R.J.A.M. Stevens, E.P. van der Poel, S. Grossmann, D. Lohse, The unifying theory of scaling in thermal convection: the updated prefactors, J. Fluid Mech. 730 (2013) 295–308.
[23] S. Bhattacharya, M.K. Verma, A. Bhattacharya, Predictions of Reynolds and nusselt numbers in turbulent convection using machine-learning models, Phys. Fluids 34 (2) (2022).

[24] M.K. Verma, A. Kumar, A. Pandey, Phenomenology of buoyancy-driven turbulence: recent results, New J. Phys. 19 (2017) 025012.
[25] R.J. Samuel, M. Bode, J.D. Scheel, K.R. Sreenivasan, J. Schumacher, No sustained mean velocity in the boundary region of plane thermal convection, J. Fluid Mech. 996 (2024) A49.
[26] R.H. Kraichnan, Turbulent thermal convection at arbitrary Prandtl number, Phys. Fluids 5 (1962) 1374–1389.
[27] D. Lohse, O. Shishkina, Ultimate Rayleigh-Bénard turbulence, Rev. Modern Phys. 96 (3) (2024) 035001.
[28] W.V.R. Malkus, The heat transport and spectrum of thermal turbulence, Proc. R. Soc. Lond. A 225 (1954) 196–212.
[29] X. Chavanne, F. Chillà, B. Chabaud, B. Castaing, B. Hebral, Turbulent Rayleigh-Bénard convection in gaseous and liquid he, Phys. Fluids 13 (2001) 1300–1320.
[30] X. He, D. Funfschilling, H. Nobach, E. Bodenschatz, G. Ahlers, Transition to the ultimate state of turbulent Rayleigh-Bénard convection, Phys. Rev. Lett. 108 (2012) 024502.
[31] X. Zhu, V. Mathai, R.J.A.M. Stevens, R. Verzicco, D. Lohse, Transition to the ultimate regime in two-dimensional Rayleigh-Bénard convection, Phys. Rev. Lett. 120 (2018) 144502.
[32] J.J. Niemela, L. Skrbek, K.R. Sreenivasan, R.J. Donnelly, Turbulent convection at very high Rayleigh numbers, Nature 404 (2000) 837–840.
[33] P. Urban, P. Hanzelka, T. Kralik, V. Musilová, A. Srnka, L. Skrbek, Effect of boundary layers asymmetry on heat transfer efficiency in turbulent Rayleigh-Bénard convection at very high Rayleigh numbers, Phys. Rev. Lett. 109 (2012) 154301.
[34] K.P. Iyer, J.D. Scheel, J. Schumacher, K.R. Sreenivasan, Classical 1/3 scaling of convection holds up to Ra= 10^{15}, Proc. Natl. Acad. Sci. 117 (14) (2020) 7594–7598.
[35] K.R. Sreenivasan, J.J. Niemela, Turbulent convection at very high Rayleigh numbers and the weakly nonlinear theory, Atmosphere 14 (5) (2023) 826.
[36] J.P. John, J. Schumacher, Strongly superadiabatic and stratified limits of compressible convection, Phys. Rev. Fluids 8 (10) (2023) 103505.
[37] J.P. John, J. Schumacher, Compressible turbulent convection in highly stratified adiabatic background, J. Fluid Mech. 972 (2023) R4.
[38] J.P. John, J. Schumacher, Compressible turbulent convection: The role of temperature-dependent thermal conductivity and dynamic viscosity, Phys. Fluids 36 (7) (2024).
[39] D.H. Porter, P.R. Woodward, Three-dimensional simulations of turbulent compressible convection, Astrophys. J. Suppl. Ser. 127 (1) (2000) 159.
[40] C. Ouyang, S. He, Q. Xu, Y. Luo, W. Zhang, A MacCormack-TVD finite difference method to simulate the mass flow in mountainous terrain with variable computational domain, Comput. Geosci. 52 (2013) 1–10.
[41] H.C. Yee, Upwind and Symmetric Shock-Capturing Schemes, National Aeronautics and Space Administration, Ames Research Center, 1987.
[42] D. Liang, B. Lin, R.A. Falconer, Simulation of rapidly varying flow using an efficient TVD-MacCormack scheme, Internat. J. Numer. Methods Fluids 53 (5) (2007) 811–826.
[43] J. Schmalzl, M. Breuer, U. Hansen, On the validity of two-dimensional numerical approaches to time-dependent thermal convection, Europhys. Lett. 67 (2004) 390–396.
[44] E.P. van der Poel, R.J.A.M. Stevens, D. Lohse, Comparison between two- and three-dimensional Rayleigh–Bénard convection, J. Fluid Mech. 736 (2013) 177–194.
[45] A. Pandey, M.K. Verma, A.G. Chatterjee, B. Dutta, Similarities between 2D and 3D convection for large Prandtl number, Pramana- J. Phys. 87 (2016) 13.
[46] E. Graham, Numerical simulation of two-dimensional compressible convection, J. Fluid Mech. 70 (4) (1975) 689–703.
[47] N.E. Hurlburt, J. Toomre, J.M. Massaguer, Two-dimensional compressible convection extending over multiple scale heights, Astrophys. J. 282 (1984) 557–573.
[48] J.D. Anderson, Governing equations of fluid dynamics, in: Computational Fluid Dynamics: An Introduction, 1992, pp. 15–51.
[49] R. Okuta, Y. Unno, D. Nishino, S. Hido, C. Loomis, Cupy: A NumPy-compatible library for NVIDIA GPU Calculations, in: Proceedings of Workshop on Machine Learning Systems (LearningSys) in the Thirty-First Annual Conference on Neural Information Processing Systems, NIPS, 2017.
[50] L. Dalcín, R. Paz, M. Storti, J. D'Elía, MPI for python: Performance improvements and MPI-2 extensions, J. Parallel Distrib. Comput. 68 (5) (2008) 655–662.
[51] C.R. Harris, K.J. Millman, S.J. Van Der Walt, R. Gommers, P. Virtanen, D. Cournapeau, E. Wieser, J. Taylor, S. Berg, N.J. Smith, et al., Array programming with NumPy, Nature 585 (7825) (2020) 357–362.
[52] R.J.A.M. Stevens, R. Verzicco, D. Lohse, Radial boundary layer structure and nusselt number in Rayleigh–Bénard convection, J. Fluid Mech. 643 (2010) 495–507.
[53] G. Grötzbach, Spatial resolution requirements for direct numerical simulation of the Rayleigh-Bénard convection, J. Comput. Phys. 49 (2) (1983) 241–264.
[54] P.K. Mishra, A.K. De, M.K. Verma, V. Eswaran, Dynamics of reorientations and reversals of large-scale flow in Rayleigh–Bénard convection, J. Fluid Mech. 668 (2011) 480–499.
[55] L.D. Landau, E.M. Lifshitz, Fluid mechanics, in: Course of Theoretical Physics, second ed., Elsevier, Oxford, 1987.
[56] The movies are available here. YouTube, 2024.
[57] X.-Z. Wu, A. Libchaber, Non-Boussinesq effects in free thermal convection, Phys. Rev. A 43 (1991) 2833–2839.
[58] S. Bhattacharya, R. Samtaney, M.K. Verma, Scaling and spatial intermittency of thermal dissipation in turbulent convection, Phys. Fluids 31 (2019) 075104.
[59] P.K. Mishra, M.K. Verma, Energy spectra and fluxes for Rayleigh-Bénard convection, Phys. Rev. E 81 (2010) 056316.
[60] A. Pandey, A. Kumar, A.G. Chatterjee, M.K. Verma, Dynamics of large-scale quantities in Rayleigh-Bénard convection, Phys. Rev. E 94 (2016) 053106.
[61] E.P. Van Der Poel, R. Ostilla-Mónico, R. Verzicco, D. Lohse, Effect of velocity boundary conditions on the heat transfer and flow topology in two-dimensional Rayleigh-Bénard convection, Phys. Rev. E Vol. 90 (1) (2014) 013017.
[62] M.K. Verma, P.K. Mishra, A. Pandey, S. Paul, Scalings of field correlations and heat transport in turbulent convection, Phys. Rev. E 85 (2012) 016310.

Chapter 4

On the absence of the ultimate regime in turbulent convection

In Chapter 3, we established that compressible convection exhibits a robust *classical* scaling of the Nusselt number, $\mathrm{Nu} \sim \mathrm{Ra}^{0.30}$, over a vast range of Rayleigh numbers. This finding aligns with the comprehensive study of incompressible Rayleigh-Bénard convection (RBC) by Iyer et al. (2020), who reported a scaling exponent of ≈ 0.33 up to $\mathrm{Ra} = 10^{15}$. These results strongly suggest that standard wall-bounded convective systems are dominated by a universal transport mechanism that remains close to near-classical predictions $\mathrm{Nu} \sim \mathrm{Ra}^{1/3}$ (Malkus, 1954; Priestley, 1954; Howard, 1966), resisting the transition to a steeper scaling regime even at extreme driving parameters.

However, this classical behavior is not the only outcome predicted by theory. Kraichnan (1962) famously proposed the existence of an *ultimate regime* where the boundary layers become turbulent, potentially leading to a scaling of $\mathrm{Nu} \sim \mathrm{Ra}^{1/2}$. While this regime remains elusive in standard RBC experiments and simulations, it is readily observed in periodic convection (PC)—a system where the rigid top and bottom walls are replaced by periodic boundary conditions (Lohse and Toschi, 2003; Verma et al., 2012). In PC, the absence of walls allows for unimpeded vertical transport, consistently yielding the $\mathrm{Ra}^{1/2}$ scaling and serving as a numerical realization of the ultimate regime.

The debate regarding ultimate scaling conditions was intensified by Zhu et al. (2018), who reported a transition in 2D RBC at $\mathrm{Ra} \approx 10^{13}$. They attributed this efficiency boost to *plume-ejecting regions*, observing that while velocity profiles became logarithmic globally, temperature profiles did so only locally at ejection sites. Arguing that these regions drive enhanced transport ($\mathrm{Nu} \sim \mathrm{Ra}^{0.38}$), this study raised a fundamental question: is the transition to ultimate scaling inevitable once boundary layers become turbulent, as predicted by Kraichnan?

Motivated by these conflicting observations, we investigate the hypothesis that the classical scaling arises from a delicate cancellation between positive (upward) and negative (downward) convective heat fluxes. To disentangle the roles of this flux imbalance, boundary layer structure, and global confinement, this chapter presents a comparative study. We analyze three distinct systems: standard RBC, compressible convection (CC), and periodic convection (PC). By contrasting these systems, particularly comparing the wall-bounded cases (RBC and CC) against the wall-less case (PC), we aim to isolate the specific physical mechanism that suppresses the $\mathrm{Ra}^{1/2}$ scaling in the presence of physical boundaries.

We utilized high-fidelity direct numerical simulations (DNS) to generate an extensive and rigorously validated dataset. The compressible simulations were performed using the DHARA solver, while periodic convection was simulated using the spectral code Tarang-py (Chatterjee et al., 2018). To ensure a comprehensive comparison across different flow configurations, we incorporated high-resolution RBC datasets: 2D simulations from Samuel and Verma (2024) and Samuel (2023), and 3D simulations from Bhattacharya et al. (2021a). The combined dataset covers an unprecedented range of Rayleigh numbers, reaching $\mathrm{Ra} = 10^{16}$ in 2D and $\mathrm{Ra} = 10^{13}$ in 3D. Crucially, all simulations are fully resolved; the grid spacing strictly satisfies the Grötzbach (1983) criterion within the boundary layers and resolves the Kolmogorov length scale in the bulk.

Our first major finding addresses the boundary layer hypothesis. Our 2D compressible simulations show logarithmic profiles in both velocity and temperature, resembling Zhu et al. (2018), yet heat transport scales classically as $\mathrm{Nu} \sim \mathrm{Ra}^{0.32}$. Conversely, our 3D compressible simulations display a logarithmic temperature profile but completely lack a logarithmic velocity profile. This structural disparity, combined with consistent scaling across both dimensions, demonstrates that logarithmic boundary layers can exist without enhanced heat transport, reinforcing the uncertainty surrounding the very existence of the ultimate regime in wall-bounded flows.

To understand the deeper physical reason for this resistance to ultimate scaling, we moved beyond global scaling laws and investigated the local heat flux statistics. The Nusselt number is related to the volume-averaged vertical heat flux, $\langle F_z \rangle$, by the relation

$$\mathrm{Nu} = 1 + \sqrt{\mathrm{RaPr}}\langle F_z \rangle. \tag{4.1}$$

The specific form of this flux depends on the system: for incompressible flows (RBC and PC), it is defined as $F_z = u_z T$. For CC, it explicitly accounts for density fluctuations and superadiabaticity as $F_z = \rho u_z T_{\mathrm{sa}}$, where T_{sa} is the normalized deviation from the adiabatic profile $T_A(z)$, defined as $T_{\mathrm{sa}}(\mathbf{r}) = [T(\mathbf{r}) - T_A(z)]/\epsilon$. To offer a microscopic view of the transport efficiency, we decomposed this instantaneous flux into two components: the positive heat flux F_{z+} (where $F_z > 0$), representing fluid motion aligned with the buoyancy force (hot fluid rising, cold fluid falling), and the negative heat flux F_{z-} (where $F_z < 0$), representing fluid motion opposing buoyancy (hot fluid forced downwards, cold fluid forced upwards).

In periodic convection, the absence of walls allows thermal plumes to traverse the entire domain without obstruction. Our analysis shows that transport in periodic convection is overwhelmingly dominated by F_{z+}. The probability of negative heat flux events is negligible because there are no obstacles to deflect the plumes. Consequently, the heat transport remains highly efficient, and the system naturally adheres to the free-fall scaling prediction of $\mathrm{Nu} \sim \mathrm{Ra}^{1/2}$.

In stark contrast, the presence of thermal plates in RBC and CC fundamentally alters the heat transport dynamics compared to PC. As hot ascending plumes approach the top plate, they are physically blocked and deflected downwards. Similarly, cold descending plumes are deflected upwards by the bottom plate. These deflection events force hot fluid to move against the buoyancy direction (downwards) and cold fluid to move upwards, thereby generating a significant negative heat flux (F_{z-}). Our data reveals that these negative flux events are substantial and compete with the positive heat flux (F_{z+}) generated by the buoyancy-aligned motions.

The impact of this wall-induced negative flux is critical to understanding the global scaling. In PC, the absence of walls means transport is overwhelmingly dominated by the positive component, with $\langle F_z \rangle \approx \langle F_{z+} \rangle$. Consequently, the normalized net flux remains nearly constant with Ra, naturally leading to the ultimate scaling prediction $\mathrm{Nu} \sim \sqrt{\mathrm{RaPr}}\langle F_z \rangle \sim \mathrm{Ra}^{1/2}$. However, in wall-bounded flows, the behavior is fundamentally different. For 3D RBC and CC, we observe that while both positive and negative flux components decrease with Ra, the positive flux $\langle F_{z+} \rangle$ decays faster than the negative flux $\langle F_{z-} \rangle$. This differential decay causes the net vertical heat flux $\langle F_z \rangle$ to scale approximately as $\mathrm{Ra}^{-0.2}$. When combined with the free-fall velocity scaling, this yields the observed Nusselt scaling $\mathrm{Nu} \sim \mathrm{Ra}^{1/2} \times \mathrm{Ra}^{-0.2} = \mathrm{Ra}^{0.30}$.

In 2D RBC and CC, the scenario is dynamically distinct due to the inverse energy cascade, which generates large-scale coherent structures. Here, the magnitudes of the total positive and negative fluxes are very close to each other. This tight competition results in significant fluctuations in the net heat flux $\langle F_z \rangle$ and, consequently, in the Nusselt number, as noted in recent studies (Samuel and Verma, 2024). Despite these fluctuations and dimensional differences, the time-averaged scaling remains consistent with the classical $\mathrm{Ra}^{1/3}$ scaling observed in 3D.

We further corroborated this mechanism by examining the probability density functions (PDFs) of the local vertical heat flux F_z. For PC, the PDF is highly skewed towards positive values with a mean much greater than zero, reflecting the unidirectional nature of the transport where buoyant plumes rise unimpeded. In contrast, 3D wall-bounded flows exhibit a PDF that is symmetric for small fluxes but retains a longer positive tail. Crucially, as Ra increases, this positive tail retracts, and the distribution becomes increasingly symmetric with the negative tail. In 2D simulations, the behavior is even more extreme: the PDFs exhibit heavy tails where the positive and negative sides are nearly indistinguishable. Yet, despite these structural differences, the global outcome of wall-induced suppression of heat transport remains universal.

In summary, this chapter offers new insights into the long-standing problem of turbulent convection and indicates a likely absence of the ultimate regime in standard wall-bounded flows. We demonstrate that the classical Nusselt scaling ($\mathrm{Nu} \sim \mathrm{Ra}^{1/3}$) arises primarily due to the competition between positive and negative heat fluxes induced by the thermal plates. This confirms that while the boundary layer plays a major role in confining the flow and generating negative fluxes, the direct analogy to channel flow turbulence does not apply. Even when the boundary layer exhibits logarithmic profiles, the global flux cancellation prevents the transition to the ultimate regime. We discuss these results and the statistical properties of the heat flux in detail in the following article.

PNAS RESEARCH ARTICLE | APPLIED PHYSICAL SCIENCES

On the absence of the ultimate regime in turbulent thermal convection

Harshit Tiwari[a], Lekha Sharma[a], and Mahendra K. Verma[a,b,1]

Edited by John S. Wettlaufer, Yale University, New Haven, CT; received May 26, 2025; accepted September 29, 2025 by Editorial Board Member Christopher Jarzynski

Quantifying heat transport in turbulent convection remains a challenge. The two competing models of heat transport predict that the nondimensional heat flux, known as the Nusselt number (Nu), is proportional to $\mathrm{Ra}^{1/3}$ (classical scaling) and $\mathrm{Ra}^{1/2}$ (ultimate-regime scaling), where Ra is the Rayleigh number. Some experiments and simulations report that the Nusselt number transitions from near classical scaling, $\mathrm{Ra}^{0.30}$, to a larger power law when the boundary layer turns turbulent near $\mathrm{Ra} \approx 10^{14}$. However, others find $\mathrm{Ra}^{0.30}$ scaling to continue for larger Ra. In this work, we perform a comparative study of Rayleigh-Bénard, compressible, and periodic convection in two and three dimensions using direct numerical simulations. We show that up to $\mathrm{Ra} = 10^{16}$ in two dimensions and up to $\mathrm{Ra} = 10^{13}$ in three dimensions, the positive and negative energy fluxes in Rayleigh-Bénard and compressible convection are nearly equal. However, in the distribution function, the positive fluxes have longer tails than the negative ones, and the differences between the positive and negative fluxes scale as $\mathrm{Ra}^{-0.20}$, which leads to $\mathrm{Nu} \sim \mathrm{Ra}^{0.30}$. The above robust and universal properties, even in the presence of a logarithmic layer in compressible convection, indicate a likely absence of the ultimate regime in turbulent thermal convection. In contrast, periodic convection, which is related to the ultimate regime, exhibits a predominantly positive heat flux.

turbulent convection | turbulent heat transport | ultimate regime of convection | Rayleigh–Benard convection | compressible convection

Turbulent convection, driven by heating from below and cooling from above, enhances heat transport compared to thermal conduction. It plays an important role in astrophysical systems, such as the atmospheres of planets and stars; in engineering systems, such as boilers and heat exchangers; and in the kitchen, such as tea kettles. Even though these systems have varying configurations and fluid properties, they exhibit certain universal properties. For example, stellar convection with plasmas is compressive, whereas thermal convection in Earth's oceans has nearly constant material density. Researchers have performed convection experiments and simulations on different fluids (air, water, plasmas, and helium gas) in Cartesian boxes and spherical shells with different aspect ratios. Yet, heat transport in turbulent convection follows certain universal features. In particular, the normalized rms velocity and the convective heat transport vary as approximately $(\Delta T)^{1/2}$ and $(\Delta T)^{1/3}$, respectively, where ΔT is the temperature difference between the hot and cold surfaces (1–6). In this paper, our focus is on the universal properties of heat transport. We demonstrate that the thermal boundaries induce negative heat flux, and the difference between the positive and negative heat fluxes leads to nearly classical $(\Delta T)^{1/3}$ scaling.

First, we discuss heat transport in a controlled setup called Rayleigh-Bénard convection (RBC) in which a fluid confined between two plates is heated from below and cooled at the top. RBC assumes Boussinesq approximation, according to which the fluid density is constant, except in the buoyancy term, and the fluid parameters are constant in space and time (1–6). The two nondimensional system parameters are the Rayleigh number (Ra), which is the ratio of the buoyancy term and the diffusive term, and the Prandtl number (Pr), which is the ratio of the kinematic viscosity and the thermal diffusivity. The heat transport in the flow is quantified using a nondimensional parameter Nusselt number (Nu), which is the ratio of total heat transfer and the conductive heat transfer. In 1954, based on the assumption that the heat flux is independent of box height, Priestley (7) derived that Nu is proportional to $\mathrm{Ra}^{1/3}$, which is called classical scaling. In the same year, Malkus (8) arrived at a similar scaling relation by extremizing the heat transport for various temperature profiles. Using mixing length theory, in 1962,

Significance

Thermal convection efficiently transports heat in astrophysical and engineering flows. Normally, we expect hot plumes to ascend and cold plumes to descend, resulting in a positive heat flux. This paper presents evidence that in Rayleigh-Bénard and compressible convection, the upper boundary deflects the hot plumes downward, thereby inducing a negative flux. The difference between the positive and negative heat fluxes decreases with the Rayleigh number, yielding the classical Nu scaling. These subtle features of heat flux help solve a long-standing problem in the heat transport of turbulent convection and pave the way for significantly improved heat transport models of astrophysical, atmospheric, and engineering flows.

Author affiliations: [a]Department of Physics, Indian Institute of Technology Kanpur, Kanpur 208016, India; and [b]Kotak School of Sustainability, Indian Institute of Technology Kanpur, Kanpur 208016, India

Author contributions: H.T. and M.K.V. designed research; H.T., L.S., and M.K.V. performed research; H.T., L.S., and M.K.V. contributed new reagents/analytic tools; H.T., L.S., and M.K.V. analyzed data; and H.T., L.S., and M.K.V. wrote the paper.

The authors declare no competing interest.

This article is a PNAS Direct Submission. J.S.W. is a guest editor invited by the Editorial Board.

[1]To whom correspondence may be addressed. Email: mkv@iitk.ac.in.

This article contains supporting information online at https://www.pnas.org/lookup/suppl/doi:10.1073/pnas.2513474122/-/DCSupplemental.

Published October 31, 2025.

Kraichnan (9) argued that for moderate Prandtl numbers, the boundary layer becomes turbulent at large Rayleigh numbers, leading to a scaling of Nu $\sim$ $[\mathrm{Ra}(\log \mathrm{Ra})^{-3}]^{1/2}$. The scaling Nu $\sim$ $\mathrm{Ra}^{1/2}$ is called ultimate regime scaling. Howard (10) also employed variational principles and obtained an upper bound for Nu as $\sqrt{3\mathrm{Ra}/64}$. Spiegel (11, 12) proposed that the turbulent heat flux should be independent of the molecular diffusion, which leads to Nu $\propto$ $(\mathrm{RaPr})^{1/2}$. In 1966, Howard (13) critically summarized the results of Malkus, Herring, Kraichnan, and Spiegel. In the same paper, Howard derived that Nu $\propto$ $(\mathrm{Ra})^{1/3}$ using an analytical model of diffusion and marginal stability in the turbulent boundary layer (14). See also Doering (15) for later applications of variational principles for computing upper bounds on the Nusselt number. Shraiman and Siggia (16) derived exact relations connecting Nu, Ra, and Pr, while Grossmann and Lohse (17) developed a phenomenological framework that predicts Nu scaling based on bulk and boundary-layer dissipation. See Doering (18) for a concise historical perspective.

The existence of an ultimate regime remains a central question in the field, leading to extensive experimental and numerical investigations. Up to Ra $\sim 10^{12}$, most data are consistent with the classical scaling exponent $\approx 1/3$ (1–3, 5, 17). For Ra beyond 10^{14}, using experiments and numerical simulations, Chavanne et al. (19), He et al. (20), and Zhu et al. (21) show that the Nu scaling exponent increases gradually up to 0.38 near Ra $= 10^{15}$; it is assumed that the exponent will reach 1/2 asymptotically (22, 23). However, the experimental results of Niemela et al. (24), Niemela and Sreenivasan (25), and Urban et al. (26), and the numerical simulations of Iyer et al. (27) indicate Nu $\sim$ $\mathrm{Ra}^{0.30}$ up to Ra $= 10^{16}$. Interestingly, RBC with free-slip boundary condition exhibits approximately 1/3 scaling, even though such flows are turbulent everywhere without a viscous boundary layer (28, 29). Hence, the connection between the ultimate regime and the turbulent boundary layer needs a closer examination, as articulated in a recent article by Doering (18).

The Boussinesq approximation does not hold in systems exhibiting strong density fluctuations, e.g., solar convection (4). Convection in such systems, referred to as compressible convection (CC), has been simulated by John and Schumacher (30, 31) and Tiwari et al. (32) up to Ra $\approx 10^{15}$ in two dimensions (2D) and up to Ra $\approx 10^{11}$ in three dimensions (3D). These authors report that Nu $\sim$ $\mathrm{Ra}^{0.30}$. In this paper, we extend this scaling up to Ra of 10^{16} in 2D and up to 10^{13} in 3D. We also demonstrate that a logarithmic layer is present in the viscous and thermal boundary layers of 2D compressible convection. However, the nature of the boundary layers in 3D compressible convection is uncertain. Periodic convection (PC) is another class of thermal convection, in which a fluid within a periodic box (one without walls) is subjected to a vertical temperature gradient. Lohse and Toschi (33), Verma et al. (28), and Winchester et al. (34) simulated periodic convection and reported that Nu $\sim$ $\mathrm{Ra}^{1/2}$, which aligns with the scaling of the ultimate regime.

This paper derives important insights by examining the Nusselt number scaling in a combined study of periodic, compressible, and Rayleigh-Bénard convection. While the bulk flows are turbulent at large Ra in both no-slip and free-slip versions of RBC and compressible convection, some of these systems exhibit logarithmic layers, but others do not. Still, all of them show near classical 1/3 scaling. In this paper, we compute the local heat flux $u_z(\mathbf{r})T(\mathbf{r})$, where u_z, T are the vertical velocity and temperature, respectively. Surprisingly, the heat flux takes both positive and negative values with nearly equal probabilities, but the positive flux has a longer tail in the distribution function. The positive heat flux is natural, with hot plumes ascending and cold plumes descending, but the negative flux arises due to the thermal plates. For example, a downward deflection of the hot plumes by the top plate yields negative flux. The difference between the positive and negative heat fluxes scales as $\mathrm{Ra}^{-0.20}$, which results in a correction to the Nu $\sim$ $\mathrm{Ra}^{1/2}$ scaling, yielding Nu $\sim$ $\mathrm{Ra}^{1/2-0.20}$ or Nu $\sim$ $\mathrm{Ra}^{0.30}$. Interestingly, the negative heat flux is absent in periodic convection that leads to Nu $\sim$ $\mathrm{Ra}^{1/2}$. Hence, the influence of thermal plates on the bulk flow leads to Nu $\sim$ $\mathrm{Ra}^{0.30}$ scaling, with the boundary layers appearing to play a marginal role in this phenomenon.

The structure of the paper is as follows. We take numerical data of RBC, compressible convection, and periodic convection and analyze the local heat flux and its probability distribution; the above quantities provide valuable insights into the Nu scaling. We also examine the boundary layers of compressible convection. A collective view of these systems reveals a likely absence of the ultimate regime in turbulent convection.

Results

We present all our results in this section. We start with the system and data description.

Systems and Datasets Employed. Here, we provide a brief description of the datasets used in this paper. We generate datasets for PC and CC using direct numerical simulations. However, RBC simulation datasets have been borrowed from Bhattacharya et al. (35) for 3D simulations and from Samuel and Verma (36) and Samuel (37) for 2D simulations. The details of the equations and numerical methods employed can be found in *Materials and Methods*. For the three cases (PC, RBC, CC), the Prandtl number is defined as $\mathrm{Pr} = \nu/\kappa$, whereas for RBC and PC, the Rayleigh number is defined as $\mathrm{Ra} = \alpha(\Delta T)gd^3/(\nu\kappa)$, where ν, κ, α are, respectively, the kinematic viscosity, thermal diffusivity, and the thermal expansion coefficient of the fluid, g is the acceleration due to gravity, and ΔT is the temperature difference between the thermal plates that are separated by distance d. The definition of the Rayleigh number for compressible convection differs slightly (38). The parameters specific to compressible convection are superadiabaticity (ϵ), which is the excess temperature gradient relative to the adiabatic profile, and dissipation number (D), which is the nondimensional adiabatic temperature drop. See *Materials and Methods*, Spiegel (38), Graham (39), and Schumacher and Sreenivasan (4) for the definitions of these parameters.

Periodic convection (28, 33) was simulated using a spectral code Tarang-py (40) in a $(2\pi)^2$ domain with grid points ranging from 64^2 to 1024^2, and in a $(2\pi)^3$ domain with grid points ranging from 128^3 to 256^3. The range of Ra is 10^4 to 10^8 in 2D and 10^4 to 10^7 in 3D. The Prandtl number is 1 for all the runs. In Table 1, we list the Reynolds number based on the box size ($\mathrm{Re} = UL/\nu$), the Nusselt number (Nu), the magnitudes of the average positive and negative fluxes $|\langle F_{z\pm}\rangle|$ (to be discussed below), and the resolution parameter ($\mathcal{R}_\eta = \min_i(\eta/\Delta x_i)$). In the above formulas, U, L, and ν are the rms velocity, box size, and nondimensional kinematic viscosity ($\sqrt{\mathrm{Pr}/\mathrm{Ra}}$), respectively; η is the Kolmogorov length; and Δx_i is the grid spacing in the i-th direction (41, 42). The Reynolds and Nusselt numbers for these flows are sufficiently large.

Table 1. Simulation parameters for periodic convection (P2D, P3D), RBC (R2D, R3D), and compressible convection (C2D, C3D), with 2D and 3D representing space dimensions: Rayleigh number Ra, Prandtl number Pr, grid size, aspect ratio Γ, Reynolds number Re, Nusselt number Nu, absolute values of mean positive and negative vertical heat fluxes ($|\langle F_{z+} \rangle|$, $|\langle F_{z-} \rangle|$), the von Kármán constants for the viscous and thermal boundary layers (κ_u, κ_T), and resolution parameter $\mathcal{R}_\eta$

Run	System	Ra	Pr	Grid size	Γ	Re	Nu	$\lvert\langle F_{z+}\rangle\rvert$	$\lvert\langle F_{z-}\rangle\rvert$	κ_u	κ_T	$\mathcal{R}_\eta$
1	P2D	10^4	1	64^2	1	$(9.64 \pm 0.25) \times 10^2$	92 ± 14	1.94	0.55	NA	NA	1.08
2	P2D	10^5	1	128^2	1	$(3.42 \pm 0.02) \times 10^3$	229 ± 37	2.56	0.72	NA	NA	1.23
3	P2D	10^6	1	256^2	1	$(1.05 \pm 0.03) \times 10^4$	801 ± 143	2.49	0.80	NA	NA	1.44
4	P2D	10^7	1	512^2	1	$(2.61 \pm 0.01) \times 10^4$	$2{,}103 \pm 550$	2.37	0.94	NA	NA	1.58
5	P2D	10^8	1	$1{,}024^2$	1	$(1.27 \pm 0.003) \times 10^5$	$9{,}430 \pm 2{,}500$	2.65	0.79	NA	NA	1.71
6	P3D	10^4	1	128^3	1	$(1.12 \pm 0.003) \times 10^3$	95 ± 14	1.76	0.20	NA	NA	1.11
7	P3D	10^5	1	128^3	1	$(2.99 \pm 0.02) \times 10^3$	231 ± 37	1.50	0.19	NA	NA	1.30
8	P3D	10^6	1	180^3	1	$(9.52 \pm 0.04) \times 10^3$	807 ± 68	1.48	0.21	NA	NA	1.04
9	P3D	10^7	1	256^3	1	$(2.98 \pm 0.002) \times 10^4$	$2{,}223 \pm 231$	1.38	0.20	NA	NA	1.03
10	R2D	10^9	1	$1{,}024 \times 512$	2	$(1.47 \pm 0.028) \times 10^4$	48 ± 14	0.101	0.09	-	-	1.21
11	R2D	10^{10}	1	$2{,}048 \times 1{,}024$	2	$(5.05 \pm 0.36) \times 10^4$	94 ± 29	0.108	0.102	-	-	1.24
12	R2D	10^{11}	1	$4{,}096 \times 2{,}048$	2	$(1.97 \pm 0.08) \times 10^5$	190 ± 12	0.114	0.11	-	-	1.26
13	R2D	10^{12}	1	$8{,}192 \times 4{,}096$	2	$(4.58 \pm 0.1) \times 10^5$	356 ± 17	0.099	0.098	-	-	1.14
14	R2D	10^{13}	1	$1{,}6384 \times 8{,}192$	2	$(1.16 \pm 0.02) \times 10^6$	677 ± 39	0.082	0.080	-	-	1.08
15	R2D	10^{14}	1	$12{,}288^2$	1	$(3.44 \pm 0.007) \times 10^6$	$1{,}280 \pm 130$	0.068	0.066	-	-	1.06
16	R2D	10^{15}	1	$16{,}384^2$	1	$(1.08 \pm 0.001) \times 10^7$	$2{,}875 \pm 225$	0.075	0.073	-	-	1.07
17	R2D	10^{16}	1	$32{,}768^2$	1	$(3.42 \pm 0.004) \times 10^7$	$5{,}680 \pm 380$	0.085	0.082	-	-	1.05
18	R3D	10^6	1	257^3	1	$(1.47 \pm 0.08) \times 10^2$	8.2 ± 0.9	0.056	0.041	-	-	4.92
19	R3D	10^7	1	257^3	1	$(4.91 \pm 0.14) \times 10^2$	16.3 ± 1.3	0.048	0.037	-	-	2.31
20	R3D	10^8	1	513^3	1	$(1.53 \pm 0.049) \times 10^3$	31.4 ± 2.9	0.044	0.038	-	-	2.19
21	R3D	10^9	1	$1{,}025^3$	1	$(4.7 \pm 0.092) \times 10^3$	61.2 ± 4.2	0.043	0.034	-	-	2.06
22	C2D	10^9	0.7	513^2	1	$(1.3 \pm 0.1) \times 10^4$	22 ± 2	0.026	0.019	0.93	3.7	0.82
23	C2D	10^{10}	0.7	$1{,}025^2$	1	$(4.4 \pm 0.2) \times 10^4$	46 ± 3	0.027	0.023	0.87	3.6	0.66
24	C2D	10^{11}	0.7	$2{,}049^2$	1	$(1.38 \pm 0.08) \times 10^5$	103 ± 12	0.028	0.025	0.83	3.9	0.57
25	C2D	10^{12}	0.7	$4{,}097^2$	1	$(4.7 \pm 0.2) \times 10^5$	238 ± 23	0.036	0.033	0.78	5.1	0.57
26	C2D	10^{13}	0.7	$8{,}193^2$	1	$(1.46 \pm 0.02) \times 10^6$	489 ± 35	0.036	0.035	0.69	8.6	0.56
27	C2D	10^{14}	0.7	$12{,}001^2$	0.8	$(4.04 \pm 0.05) \times 10^6$	909 ± 112	0.034	0.032	0.68	9.9	0.51
28	C2D	10^{15}	0.7	$16{,}385^2$	0.8	$(1.24 \pm 0.02) \times 10^7$	$2{,}204 \pm 220$	0.031	0.030	0.60	10	0.52
29	C2D	10^{16}	0.7	$24{,}001^2$	0.8	$(4.1 \pm 0.1) \times 10^7$	$3{,}893 \pm 510$	0.028	0.027	0.47	11	0.51
30	C3D	10^7	0.7	$33^2 \times 129$	0.25	$(3.6 \pm 0.5) \times 10^2$	5 ± 1	0.0095	0.0051	-	-	0.76
31	C3D	10^8	0.7	$65^2 \times 257$	0.25	$(1.5 \pm 0.1) \times 10^3$	14 ± 1	0.012	0.0072	-	8.8	0.76
32	C3D	10^9	0.7	$129^2 \times 513$	0.25	$(4.3 \pm 0.3) \times 10^3$	28 ± 2	0.0095	0.0063	-	10	0.72
33	C3D	10^9	0.7	513^3	1	$(6.0 \pm 0.1) \times 10^3$	27.5 ± 0.7	0.011	0.0075	-	7.1	0.72
34	C3D	10^{10}	0.7	$257^2 \times 1{,}025$	0.25	$(1.22 \pm 0.08) \times 10^4$	55 ± 3	0.0073	0.0055	-	13	0.69
35	C3D	10^{11}	0.7	$513^2 \times 2{,}049$	0.25	$(3.82 \pm 0.06) \times 10^4$	112 ± 4	0.0062	0.0046	-	16	0.66
36	C3D	10^{12}	0.7	$451^2 \times 3{,}601$	0.125	$(7.86 \pm 0.22) \times 10^4$	202 ± 34	0.0051	0.0042	-	19	0.59
37	C3D	10^{13}	0.7	$501^2 \times 5{,}001$	0.125	$(2.43 \pm 0.09) \times 10^5$	412 ± 56	0.0034	0.0025	-	24	0.55

Compressible convection was simulated using the finite-difference code Dhara (32) with grid points ranging from 513^2 to $24{,}001^2$ for 2D flows and with grid points ranging from $33^2 \times 129$ to $512^2 \times 5{,}001$ for 3D flows. We chose Ra ranging from 10^9 to 10^{16} in 2D and Ra ranging from 10^7 to 10^{13} in 3D. The aspect ratio Γ varies from 1 to 0.125 (Table 1). We chose Pr = 0.7, superadiabaticity $\epsilon = 0.1$, dissipation number $D = 0.5$, and the ratio of specific heat capacities $\gamma = 1.3$. The Reynolds number ranges from 360 to 4×10^7. Table 1 lists Ra, Pr, Re, Nu, $|\langle F_{z\pm} \rangle|$, $\mathcal{R}_\eta$, and von Kármán constants for viscous and thermal boundary layers, κ_u, κ_T, respectively, which will be discussed later.

RBC simulations were performed using the finite-difference Boussinesq code SARAS (43). All runs have Pr = 1. The Rayleigh number ranges from 10^9 to 10^{16} in 2D and from 10^6 to 10^9 in 3D. For 2D, the aspect ratio $\Gamma = 2$ up to $\mathrm{Ra} = 10^{13}$, after which Γ is unity. However, $\Gamma = 1$ for all 3D runs. The values of Re, Nu, $|\langle F_{z\pm} \rangle|$, and $\mathcal{R}_\eta$ for these runs are listed in Table 1.

Our simulations are well resolved, both in the bulk and in the boundary layers. In addition, our simulations have converged to steady states (see *Materials and Methods* and *SI Appendix* for details on numerical resolution and convergence). Next, we describe the properties of the boundary layers in turbulent convection.

Boundary Layers in Turbulent Convection. In a flow past a flat plate, the appearance of a logarithmic layer in the boundary layer signals transition to turbulence (44). Inspired by this observation, researchers have examined the boundary layers in turbulent RBC using experiments and simulations. For large Ra, Ahlers et al. (45) and He et al. (20) reported a logarithmic layer in their convection experiments with sulfur hexafluoride (SF_6). Zhu et al. (21) simulated 2D turbulent convection and reported a logarithmic layer in the viscous boundary layer with the von Kármán constant $\kappa_u \approx 0.4$. For the thermal boundary layer in 2D, Zhu et al. (21) reported a log layer with $\kappa_T \approx 4.0$ in the plume-ejecting regions, but an absence of a log layer in the plume-impacting regions. These authors relate the observed logarithmic layers to an increase in the Nu scaling exponent from 0.30 to 0.38. In contrast, Iyer et al. (27) argued that "the boundary layers remain marginally stable and continue to act as the bottleneck for global heat transport," leading to classical 1/3 scaling.

We computed the boundary layer profiles for compressible convection, which are shown in Fig. 1. Here, we plot the normalized velocity (u^+) and normalized temperature (T^+) as a function of normalized vertical height (z^+) for the Bottom plate. Refer to *SI Appendix* and books (44, 46, 47) for the definitions of u^+, T^+, z^+. We observe logarithmic layers in u^+ and T^+ for 2D flows (Fig. 1 *A* and *C*), with the von Kármán constant κ_u ranging from 0.93 to 0.47 and κ_T ranging from 3.7 to 11 (Table 1). However, u^+ in 3D flows does not show a logarithmic layer, but T^+ does. Refer to *SI Appendix* for the parameters B_u and B_T and for the boundary layer properties of the top plate. The logarithmic layer observed in 2D convection may be caused by the horizontal sweeping flow, which is analogous to the behavior of flow past a flat plate. This sweeping flow is typically absent in 3D convection, which may explain the lack of a logarithmic layer in 3D (48). Most importantly, as we show in later discussion, $\mathrm{Nu} \sim \mathrm{Ra}^{0.30}$, regardless of whether a logarithmic layer is present.

Another interesting observation is that the free-slip RBC exhibits $\mathrm{Nu} \sim \mathrm{Ra}^{0.30}$ scaling despite the flow being turbulent everywhere and lacking a viscous boundary layer (29). Note that for large Ra, the bulk flow in RBC and compressible convection are turbulent irrespective of the nature of the boundary layers. These observations appear to weaken the connection between the logarithmic layer and the ultimate regime. This led us to explore heat fluxes in turbulent convection, which is the topic of the next subsections.

Anisotropic Heat Flux and Nusselt Number Scaling. In this subsection, we discuss the temperature and velocity fields and their correlations for the PC, RBC, and CC. We take a snapshot of PC at Ra of 10^7, a snapshot of RBC at Ra of 10^9, and a snapshot of CC at Ra of 10^9 under steady state, and display their central vertical cross-sections in Fig. 2 *A*–*C*. This figure contains the vector plots of the velocity field [$\mathbf{u}(\mathbf{r})$] and the density plots of the temperature field [$T(\mathbf{r})$, $T_{\mathrm{sa}}(\mathbf{r})$]. See Eq. **23** for the definition of superadiabatic temperature, $T_{\mathrm{sa}}(\mathbf{r})$. Note that $T_{\mathrm{sa}}(\mathbf{r}) < 0$ for CC (32). We compute the vertical heat flux $F_z(\mathbf{r})$ for the three vertical cross-sections and exhibit them in Fig. 2 *D*–*F*. Note that $F_z(\mathbf{r}) = u_z(\mathbf{r})T(\mathbf{r})$ for PC and RBC, whereas $F_z(\mathbf{r}) = \rho(\mathbf{r})u_z(\mathbf{r})T_{\mathrm{sa}}(\mathbf{r})$ for CC.

Before plunging into the heat flux of turbulent convection, we discuss the flux $\mathbf{F}(\mathbf{r}) = \mathbf{u}(\mathbf{r})\phi(\mathbf{r})$ for an isotropic scalar turbulence. Here, the isotropic velocity field $\mathbf{u}(\mathbf{r})$ advects the isotropic scalar field $\phi(\mathbf{r})$. For an isotropic turbulence, the ensemble-averaged flux $\langle \mathbf{F}(\mathbf{r})\rangle = \langle \mathbf{u}(\mathbf{r})\phi(\mathbf{r})\rangle = 0$ because $\mathbf{u}(\mathbf{r}) = \mathbf{a}$ and $-\mathbf{a}$ occur with equal probability for a given $\phi(\mathbf{r})$ (49, 50). Fig. 3*A* shows that in an isotropic passive turbulence, the average vertical flux, $\langle F_z\rangle = \langle u_z T\rangle$, is zero because positive and negative u_z values occur with equal probability for a given T.

In turbulent convection, buoyancy acts along the vertical direction, which breaks the isotropy. In PC, a hot thermal plume ($T > 0$) has $u_z > 0$, whereas a cold plume ($T < 0$) has $u_z < 0$, leading to predominantly positive F_z (Figs. 2 *A* and *D* and 3*B*). Note that the horizontal heat flux in convection vanishes due to the symmetry along the horizontal. RBC and CC have very different behaviors from PC. As shown in Fig. 2 *B*, *C*, *E*, and *F*, in RBC and CC, a hot packet has both positive and negative u_z, leading to positive and negative heat fluxes (F_{z+}, F_{z-}). However, F_{z+} wins over F_{z-} that yields a net positive heat flux. We illustrate these features in Fig. 3 *C* and *D*. Two-dimensional PC, RBC, and CC have very similar behavior, except that 2D flow structures are larger in size than the 3D counterparts, which is attributed to the inverse energy cascade in 2D convection (36) (*SI Appendix*). We remark that the above features are generic and are observed all the time.

We relate the average vertical heat flux ($\langle F_z\rangle$) to the Nusselt number (Nu). The total Nu gets contributions from the positive

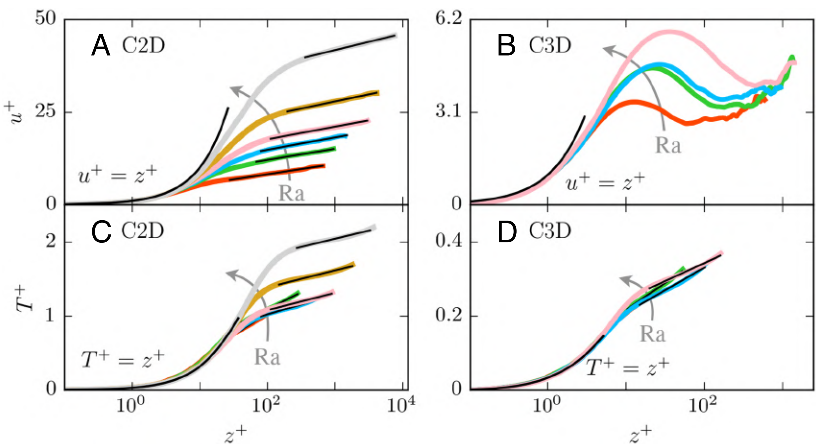

Fig. 1. For compressible convection near the *Bottom plate*, plots of u^+ vs. z^+ (*Top* row: *A* and *B*) and T^+ vs. z^+ (*Bottom* row: *C* and *D*). The *Left* column is for 2D with Ra = 10^{11} (red), 10^{12} (green), 10^{13} (blue), 10^{14} (pink), 10^{15} (golden), and 10^{16} (gray). With increasing Ra, the von Kármán constant κ_u varies from 0.83 to 0.47, whereas κ_T varies from 4 to 11. The *Right* column is for 3D convection with Ra = 10^{10} (red), 10^{11} (green), 10^{12} (blue), and 10^{13} (pink). Figure (*B*) does not exhibit a clear signature of a logarithmic layer. (*D*) For the thermal boundary layer in 3D, κ_T varies from 13 to 24.

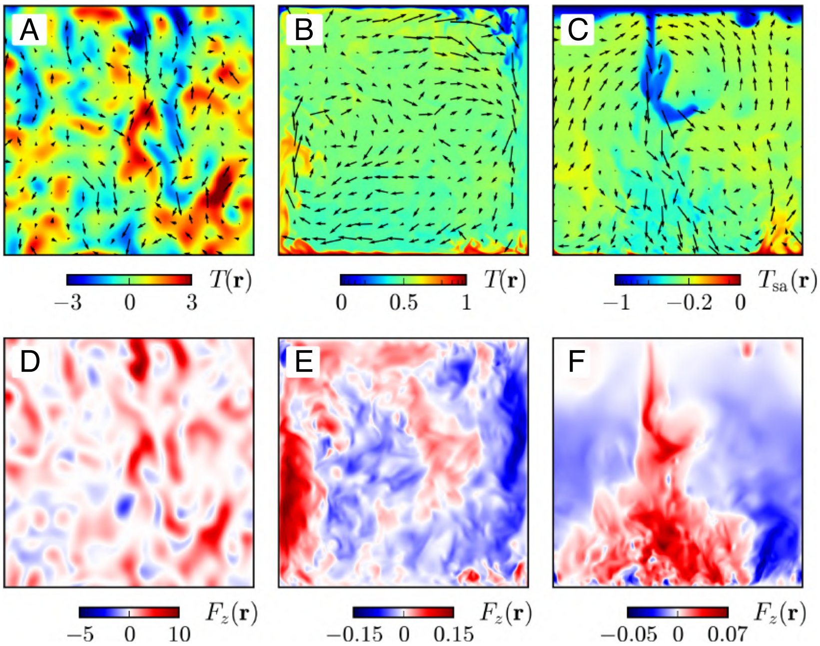

Fig. 2. Plots of the velocity and temperature fields (*A–C*), and vertical heat flux $F_z(\mathbf{r})$ (*D–F*) in the mid vertical cross-section for (*A* and *D*) 3D periodic convection (PC) with Ra = 10^7; (*B* and *E*) 3D RBC with Ra = 10^9; (*C* and *F*) 3D compressible convection (CC) with Ra = 10^9. PC exhibits predominantly positive F_z, whereas RBC and CC exhibit both positive and negative F_z.

and negative heat fluxes, $\langle F_{z\pm}\rangle$. In terms of nondimensional u_z and T (or T_{sa} for CC) (31, 32),

$$\begin{aligned}\mathrm{Nu} &= 1+\sqrt{\mathrm{RaPr}}[\langle F_{z+}\rangle+\langle F_{z-}\rangle]\\ &= 1+\sqrt{\mathrm{RaPr}}[\langle (u_zT)_+\rangle+\langle (u_zT)_-\rangle] \text{ in RBC \& PC,}\end{aligned} \quad [1]$$

$$\begin{aligned}\mathrm{Nu} &= 1+\sqrt{\mathrm{RaPr}}[\langle F_{z+}\rangle+\langle F_{z-}\rangle]\\ &= 1+\sqrt{\mathrm{RaPr}}[\langle (\rho u_zT_{\mathrm{sa}})_+\rangle+\langle (\rho u_zT_{\mathrm{sa}})_-\rangle] \text{ in CC.}\end{aligned} \quad [2]$$

In Eq. **2**, we ignore the contributions from the kinetic energy flux, which is negligible (32). Eq. **1** yields satisfactory Nu for PC, but Eqs. **1** and **2** exhibit significant fluctuations for RBC and CC, for which we compute Nu using the temperature gradient in the boundary layer as follows (5, 21, 32):

$$\mathrm{Nu} = -\frac{1}{2}\left[\left.\frac{d\langle T\rangle_{A,t}}{dz}\right|_{z=0}+\left.\frac{d\langle T\rangle_{A,t}}{dz}\right|_{z=1}\right] \text{ in RBC,} \quad [3]$$

$$\mathrm{Nu} = -\frac{1}{2}\left[\left.\frac{d\langle T_{\mathrm{sa}}\rangle_{A,t}}{dz}\right|_{z=0}+\left.\frac{d\langle T_{\mathrm{sa}}\rangle_{A,t}}{dz}\right|_{z=1}\right] \text{ in CC.} \quad [4]$$

Note that Nu computed at the boundaries using Eqs. **3** and **4** matches with those computed using Eqs. **1** and **2**, provided significant averaging is performed for the latter.

We compute Nu for PC, RBC, and CC using Eqs. **1**, **3**, and **4**, respectively. We average over 700 to 10,000 dataframes for these computations. To test Nu scaling, we fit the data with $\mathrm{Nu} = a\mathrm{Ra}^b$ using Python's polyfit function. The prefactor a and the exponent b for all the runs are listed in Table 2. Fig. 4*A* exhibits the normalized Nu, NuRa^{-b}, for periodic convection (P2D and P3D: thin and thick red lines), RBC (R2D and R3D: thin and thick green lines), and compressible convection (C2D

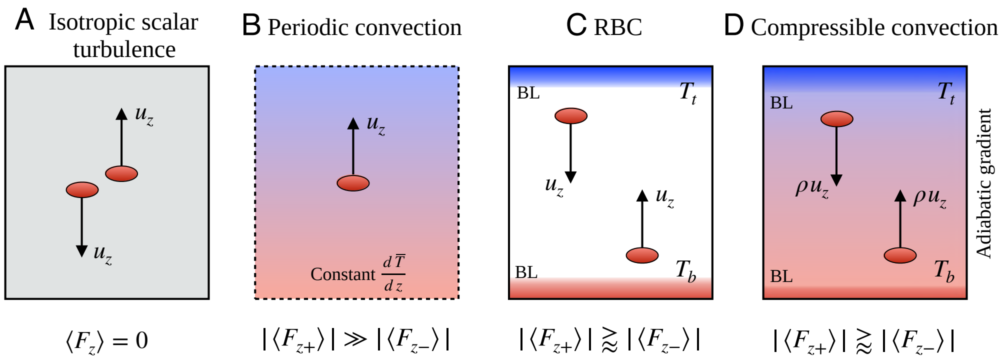

Fig. 3. Schematic diagrams illustrating heat fluxes: (*A*) In isotropic scalar turbulence, a thermal packet is equally likely to move up and down, which leads to $\langle F_z\rangle = 0$; (*B*) In periodic convection, a hot plume predominantly rises, which leads to $|\langle F_{z+}\rangle| \gg |\langle F_{z-}\rangle|$; (*C* and *D*) In RBC and compressible convection, some hot fluids have positive u_z, while others have negative u_z. This leads to $|\langle F_{z+}\rangle| \gtrapprox |\langle F_{z-}\rangle|$.

Table 2. Scaling of the Nusselt number, Nu, and absolute values of the averaged and normalized positive and negative heat fluxes ($|\langle F_{z+} \rangle|$, $|\langle F_{z-} \rangle|$) for periodic convection (P2D, P3D), RBC (R2D, R3D), and compressible convection (C2D, C3D)

System	Nu	$\|\langle F_{z+}\rangle\|$	$\|\langle F_{z-}\rangle\|$
P2D	$(0.87 \pm 0.30)\mathrm{Ra}^{(0.50 \pm 0.025)}$	$(1.79 \pm 0.35)\mathrm{Ra}^{(0.022 \pm 0.014)}$	$(0.43 \pm 0.10)\mathrm{Ra}^{(0.044 \pm 0.017)}$
P3D	$(1.23 \pm 0.32)\mathrm{Ra}^{(0.47 \pm 0.02)}$	$(2.42 \pm 0.25)\mathrm{Ra}^{(-0.030 \pm 0.008)}$	$(0.28 \pm 0.023)\mathrm{Ra}^{(0.003 \pm 0.006)}$
R2D	$(0.11 \pm 0.011)\mathrm{Ra}^{(0.29 \pm 0.003)}$	$(0.18 \pm 0.046)\mathrm{Ra}^{(-0.025 \pm 0.009)}$	$(0.16 \pm 0.043)\mathrm{Ra}^{(-0.021 \pm 0.009)}$
R3D	$(0.16 \pm 0.063)\mathrm{Ra}^{(0.28 \pm 0.022)}$	$(0.092 \pm 0.014)\mathrm{Ra}^{(-0.038 \pm 0.009)}$	$(0.045 \pm 0.007)\mathrm{Ra}^{(-0.009 \pm 0.009)}$
C2D	$(0.028 \pm 0.004)\mathrm{Ra}^{(0.32 \pm 0.005)}$	$(0.019 \pm 0.005)\mathrm{Ra}^{(0.018 \pm 0.009)}$	$(0.011 \pm 0.004)\mathrm{Ra}^{(0.033 \pm 0.011)}$
C3D	$(0.047 \pm 0.009)\mathrm{Ra}^{(0.31 \pm 0.008)}$	$(0.079 \pm 0.007)\mathrm{Ra}^{(-0.10 \pm 0.004)}$	$(0.027 \pm 0.005)\mathrm{Ra}^{(-0.070 \pm 0.008)}$

See Eqs. **1** and **2**.

and C3D: thin and thick blue lines). Clearly, $\mathrm{Nu} \sim \mathrm{Ra}^{1/2}$ for the PC, but $\mathrm{Nu} \sim \mathrm{Ra}^{0.3}$ for RBC and CC. The figure also illustrates that for a given Ra, Nu(PC) > Nu(RBC) > Nu(CC). In addition, for most cases, Nu for 3D is larger than that for 2D, possibly because of two pathways (xz and yz) for 3D flows compared to a single pathway (xz) for 2D flows. Also, Nu in 2D convection shows stronger fluctuations (or error bars) than in 3D convection, which is due to the inverse energy cascade in 2D (36). An important observation, Eqs. **1** and **2** and the Nu scaling reveal that $\langle F_z \rangle \sim \mathrm{Nu}\mathrm{Ra}^{-1/2} \sim \mathrm{Ra}^{b-1/2}$. Hence, the normalized flux decreases as $\langle F_z \rangle \sim \mathrm{Ra}^{-0.2}$ for RBC and CC, but it remains constant for PC. The *Insets* of Fig. 4*B* illustrate $\langle F_z \rangle$ for P2D, P3D, R3D, and C3D; we exclude R2D and C2D because they exhibit strong fluctuations. We will explore the reasons for such behavioral differences in PC, RBC, and CC by examining the heat fluxes $\langle F_{z\pm} \rangle$.

We compute $\langle F_{z\pm} \rangle$ using the numerical data and observe that $\langle F_{z\pm} \rangle \approx a_\pm \mathrm{Ra}^{b_\pm}$. In Fig. 4*B*, the red, green, and blue squares and circles represent positive heat fluxes in 2D and 3D, respectively, whereas pentagons and triangles represent the respective negative heat fluxes. Regarding the best-fit curves, the thin and thick solid lines represent positive fluxes for 2D and 3D, respectively. The dashed lines represent the respective negative fluxes. The plots in the figure reveal the following insights:

1. For PC, $\langle F_{z+} \rangle$ is several times larger than $\langle F_{z-} \rangle$, consistent with Figs. 2*D* and 3*B*. In addition, $\langle F_{z+} \rangle$ for 2D increases marginally with Ra, but $\langle F_{z+} \rangle$ for 3D decreases marginally with Ra.
2. In 3D RBC and CC, both $\langle F_{z+} \rangle$ and $\langle F_{z-} \rangle$ decrease with Ra, but the former decreases more rapidly than the latter. This feature leads to $\langle F_z \rangle \sim \langle F_{z+} \rangle + \langle F_{z-} \rangle \sim \mathrm{Ra}^{-0.20}$ or $\mathrm{Nu} \sim \mathrm{Ra}^{1/2-0.20} \sim \mathrm{Ra}^{0.30}$, consistent with experimental and numerical observations.
3. In 2D RBC, both $\langle F_{z+} \rangle$ and $\langle F_{z-} \rangle$ decrease marginally with Ra, with $\langle F_{z+} \rangle$ decreasing slightly faster than $\langle F_{z-} \rangle$. In CC, both $\langle F_{z+} \rangle$ and $\langle F_{z-} \rangle$ increase marginally with Ra, but $\langle F_{z-} \rangle$ increases slightly faster than $\langle F_{z+} \rangle$. However, the difference $\langle F_{z+} \rangle + \langle F_{z-} \rangle \sim \mathrm{Ra}^{-0.20}$ or $\mathrm{Nu} \sim \mathrm{Ra}^{1/2-0.20} \sim \mathrm{Ra}^{0.30}$.

Thus, a complex interplay of $\langle F_{z+} \rangle$ and $\langle F_{z-} \rangle$ yields $\mathrm{Nu} \sim \mathrm{Ra}^{0.3}$ scaling. This result is independent of the presence or absence of a logarithmic layer in the boundaries. We will continue this discussion in the next subsection.

PDF of Turbulent Convection. Further, we compute the probability distribution function (PDF) of the heat flux, $P(F_z)$, by averaging over 8 to 20 datasets. In Fig. 5, we plot $P(F_z)$ for selected Ra's among PC, CC, and RBC. Note that Fig. 5 *A*, *B*, *D*, and *F* are plotted on a semilogy scale, whereas Fig. 5 *C* and *E* are plotted on log–log scale. We chose the latter scale because $P(F_z)$ for 2D RBC and CC drops sharply with F_z. As we describe below, the $P(F_z)$ plots reveal interesting patterns and bolster the arguments for classical Nu scaling.

Periodic convection. For PC, $P(F_z)$, primarily dominated by positive F_z, is nearly Gaussian near the peak of the PDF, but it exhibits significant rightward skewness, particularly in 3D. As Ra increases, the tails of $P(F_z)$ become more extended for

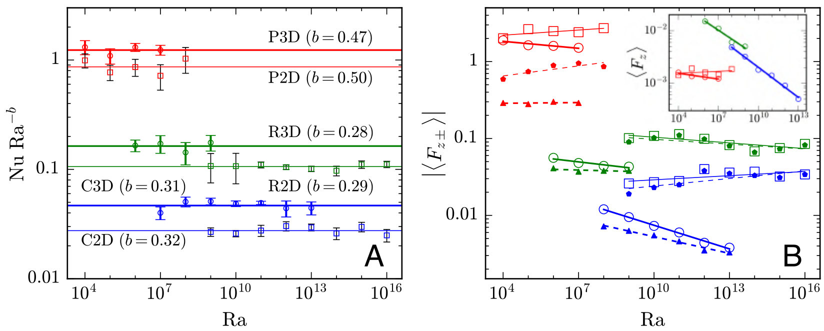

Fig. 4. (*A*) Plots of normalized Nusselt number NuRa^{-b} vs. Ra for 2D (squares, thin lines) and 3D (circles, thick lines) simulations. Red for periodic convection (P2D, P3D), green for RBC (R2D, R3D), and blue for compressible convection (C2D, C3D). Here, the symbols squares and circles represent the numerical data, while the straight lines represent the best-fit curves. (*B*) Plots of convective heat fluxes $|\langle F_{z\pm} \rangle|$ vs. Ra with the same color convention as (*A*). In (*B*), the squares and circles denote positive fluxes in 2D and 3D, respectively; the pentagons and triangles represent the respective negative fluxes; solid and dashed lines represent best-fit curves for F_{z+} and F_{z-}, respectively. The thin and thick lines distinguish between 2D and 3D curves, respectively. The *Inset* in (*B*) illustrates $\langle F_z \rangle$ scaling for P2D, P3D, R3D, and C3D; we skip R2D and C2D data because they exhibit strong fluctuations.

2D, but less extended for 3D. These observations are consistent with $|\langle F_z \rangle|$ increasing marginally with Ra in 2D, but decreasing marginally with Ra in 3D.

RBC and compressible convection. The PDFs for 3D RBC and CC, shown in Fig. 5 *D* and *F*, exhibit longer tails for F_{z+} than for F_{z-}, which leads to $\langle F_{z+} \rangle > \langle F_{z-} \rangle$ or positive Nu. As Ra increases, the tails of the PDFs shrink and the difference $\Delta P = P(F_z) - P(-F_z)$ decreases. These features lead to the decrease of $\langle F_z \rangle$ as $\mathrm{Ra}^{-0.20}$, as shown in Fig. 4*B*.

As shown in Fig. 5, the PDFs of 2D RBC and CC are more symmetric than their 3D counterparts, leading to $\Delta P = P(F_z) - P(-F_z)$ either being small or fluctuating around zero in 2D convection (see *Insets* of Fig. 5 *C* and *E*). In addition, the 2D PDFs exhibit stronger fluctuations and longer tails than 3D PDFs, primarily due to the inverse energy cascade in 2D flows (36) and due to differences in vortex dynamics in 2D and 3D (41). Consequently, $\langle F_z \rangle$ and the bulk-averaged Nu ($\mathrm{Ra}^{1/2}\langle F_z \rangle$) exhibit strong fluctuations, consistent with earlier observations by Samuel and Verma (36), Pandey and Sreenivasan (51), and Lindborg (52). Note, however, that the Nu scaling for 2D and 3D RBC and CC are very similar, even though 2D and 3D convection have different properties.

Thus, the asymmetric heat fluxes, their PDFs, and Nusselt number scaling provide a consistent picture leading to the classical Nu scaling.

Discussions

In thermal convection, we expect a hot plume to ascend and a cold plume to descend, which would yield a positive heat flux. However, our study reveals that the above dynamics occur only in PC (Fig. 3*B*). With $F_{z+} \gg F_{z-}$, Eq. **1** yields

$$\mathrm{Nu} \approx \sqrt{\mathrm{RaPr}}\langle F_{z+} \rangle \approx \sqrt{\mathrm{RaPr}}\langle (u_z T)_+ \rangle \approx \sqrt{\mathrm{RaPr}}\, u_{z,\mathrm{rms}} T_{\mathrm{rms}} \sim \sqrt{\mathrm{RaPr}}. \quad [5]$$

PC exhibits the above Nu scaling because u_z and T are strongly correlated in such flows, with the nondimensional $u_{z,\mathrm{rms}} \approx 1$ and $T_{\mathrm{rms}} \approx 1$.

In contrast, RBC and CC exhibit both positive and negative heat fluxes. The negative flux arises due to the thermal plates, e.g., the top plate deflects the hot plumes downward, leading to negative flux (Fig. 3 *C* and *D*). We find that $P(F_z)$ is symmetrical around $F_z = 0$ for small $|F_z|$, but positive F_z has a longer tail than negative F_z. Hence, $|\langle F_{z+} \rangle| \gtrsim |\langle F_{z-} \rangle|$. As shown in Fig. 4, the net $\langle F_z \rangle \sim \mathrm{Ra}^{-0.20}$, which leads to (for $\mathrm{Pr} \approx 1$)

$$\mathrm{Nu} \approx \sqrt{\mathrm{RaPr}}[\langle F_{z+} \rangle + \langle F_{z-} \rangle] \sim \sqrt{\mathrm{RaPr}}\mathrm{Ra}^{-0.20} \sim \mathrm{Ra}^{0.30}. \quad [6]$$

The above scaling for the flux correlation has been reported earlier (6, 28), and they are independent of the nature of boundary

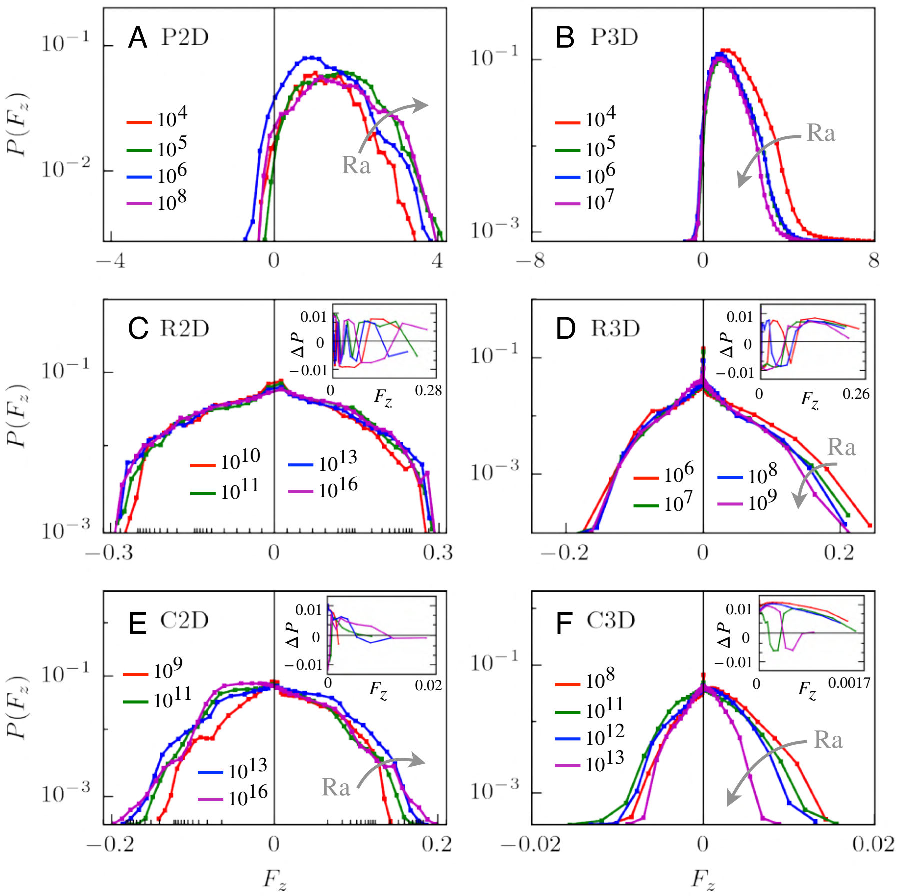

Fig. 5. Probability distribution function ($P(F_z)$) of the normalized heat flux F_z: (*A* and *B*) 2D and 3D periodic convection (P2D, P3D); (*C* and *D*) 2D and 3D RBC (R2D, R3D); and (*E* and *F*) 2D and 3D compressible convection (C2D, C3D). Subplots (*C* and *E*) are in log–log scale, while others are in semilogy scale. The *Insets* show the $\Delta P = P(F_z) - P(-F_z)$ vs. F_z plots in semilogy scale.

layers. Thus, in turbulent convection with thermal plates, $\langle u_z T \rangle$ is neither zero (as in isotropic scalar turbulence) nor $(u_z)_{\rm rms} T_{\rm rms}$ (as in periodic convection), which is a result of coexistence of F_{z+} and F_{z-}.

Many researchers (17, 20, 45) attempted to relate the possible ultimate-regime scaling in turbulent RBC to the flow past a flat plate, where the boundary layer turns turbulent near Reynolds number $\mathrm{Re}_c = 5 \times 10^5$. Using $\mathrm{Re} \approx 0.1\sqrt{\mathrm{Ra}}$ (27), the transition to turbulence in RBC is estimated to occur near $\mathrm{Ra} \approx 10^{14}$. Beyond this Ra, the boundary layers and the bulk fluid are expected to exhibit turbulent behavior. However, there are critical differences between RBC and flow past a flat plate. The boundary layer of a flat plate undergoes a transition from laminar to turbulent flow as one progresses downstream; however, such a distinct evolution is not evident in thermal convection. Also, for a flat plate, the bulk flow above the turbulent boundary layer is typically streamlined. In contrast, for $\mathrm{Ra} \gtrapprox 10^7$, the bulk flow in convection is turbulent regardless of the boundary layer's nature. Given this, the analogy between flow past a flat plate and turbulent convection is tenuous. Interestingly, the classical 1/3 scaling appears for a range of Ra (from 10^7 to 10^{16}) in RBC with no-slip and free-slip boundary conditions, with the latter flow being turbulent everywhere without any viscous boundary layer. Thus, the Nu scaling is marginally connected with the nature of the velocity boundary layer. Instead, the wall-induced $u_z T$ correlation, along with the positive and negative heat fluxes, appear to play a critical role in classical 1/3 scaling for turbulent convection.

There are several examples that need attention in view of heat flux asymmetry. Bouillaut et al. (53) and Lepot et al. (54) observed ultimate-regime scaling for convection driven by internal heat sources, internal heat sinks, and radiative heating. Turbulent convection with rough walls too exhibits ultimate-regime scaling (55). Additionally, convection driven by a horizontal pressure gradient exhibits an enhanced Nu exponent (up to 0.45) for large horizontal shear (56, 57). We conjecture that, in the above examples, the internal heat sources and sinks, horizontal shear, and rough walls increase the positive heat fluxes over the negative ones, leading to an enhancement of the Nu scaling exponent. We plan to test the above conjecture.

Conclusions

Despite extensive research, modeling heat transport in turbulent convection continues to be a significant hurdle. The two competing theories are classical Nu scaling (1/3) and ultimate-regime scaling (1/2). Some researchers argue that the Nu scaling exponent grows from 1/3 to higher values near $\mathrm{Ra} \approx 10^{14}$, where the boundary layer becomes turbulent and a logarithmic layer emerges. However, other researchers dispute these claims. As discussed in the previous section, the relation between the turbulent boundary layer and the emergence of the ultimate regime appears to be weak. In this paper, we take a different path and address this issue using turbulent heat flux (F_z).

We analyzed the positive and negative heat fluxes in 28 numerical datasets of RBC and CC whose Rayleigh numbers range from 10^6 to 10^{16}. Our analysis shows that RBC and CC exhibit both positive and negative heat fluxes, with a nearly symmetric PDF of heat flux, $P(F_z)$. A small asymmetry in $P(F_z)$ results in a net heat flux scaling of $\langle F_z \rangle \sim \mathrm{Ra}^{-0.20}$, which leads to $\mathrm{Nu} \sim \mathrm{Ra}^{1/2-0.20} \sim \mathrm{Ra}^{0.30}$. This phenomenon is quite robust, especially considering that the boundary layer in compressible convection simulations exhibits a logarithmic layer, while those in RBC simulations are uncertain. This robust classical scaling aligns with the models presented by Malkus (8) and Priestley (7). We expect the above heat flux behavior to persist for extreme Ra's (e.g., 10^{20} and beyond), but testing this conjecture will require enormous computing resources.

In contrast, periodic convection has an asymmetric heat flux with a dominant positive component. Periodic convection exhibits $\mathrm{Nu} \sim \mathrm{Ra}^{1/2}$, similar to that in the ultimate regime. We associate the difference between the 1/2 and 1/3 Nu scaling to the thermal plates. For example, the upper plate deflects the hot plumes downward, which yields negative heat flux. Absence of such wall effects in periodic convection yields dominantly positive heat flux. Thus, our paper clearly contrasts isotropic scalar turbulence, periodic convection, RBC, and compressible convection (Fig. 3).

In summary, this paper offers important insights into a long-standing problem of turbulent convection, indicating a likely absence of the ultimate regime. We demonstrate that the classical Nu scaling possibly occurs due to the positive and negative heat fluxes induced by thermal plates. Note, however, that convection with rough walls or internal heat sources and sinks yields ultimate-regime scaling. It would be interesting to explore how these factors affect heat fluxes. In addition, analyzing asymmetric momentum fluxes around airplane wings, in pipes, and in nozzles may provide valuable insights into the drag reduction and relaminarization observed in such systems (44, 58).

Materials and Methods

In this section, we briefly describe the numerical methods used to simulate periodic convection, RBC, and compressible convection.

Periodic Convection. We simulate 2D periodic convection in a $(2\pi)^2$ periodic box and 3D convection in a $(2\pi)^3$ periodic box for the parameters listed in Table 1. We solve the following nondimensionalized equations numerically (28, 33):

$$\frac{\partial \mathbf{u}}{\partial t} + \mathbf{u} \cdot \nabla \mathbf{u} = -\nabla p + T'\hat{z} + \sqrt{\frac{\mathrm{Pr}}{\mathrm{Ra}}} \nabla^2 \mathbf{u}, \quad [7]$$

$$\frac{\partial T'}{\partial t} + \mathbf{u} \cdot \nabla T' = u_z + \frac{1}{\sqrt{\mathrm{Ra\,Pr}}} \nabla^2 T', \quad [8]$$

$$\nabla \cdot \mathbf{u} = 0, \quad [9]$$

where temperature $T = \overline{T} + T'$ with $\overline{T} = 1 - z/(2\pi)$ as the linear background profile and T' as perturbation. The Rayleigh number and Prandtl number are defined as

$$\mathrm{Ra} = \frac{d\overline{T}}{dz} \frac{\alpha g d^4}{\nu \kappa}, \quad \mathrm{Pr} = \frac{\nu}{\kappa}, \quad [10]$$

where α is the thermal expansion coefficient, ν is the kinematic viscosity, κ is the thermal diffusivity, g is the gravitational acceleration, d is the height of the box, and $d\overline{T}/dz$ is the mean temperature gradient. The velocity field $\mathbf{u}$ and the temperature fluctuations T' satisfy periodic boundary conditions.

The above equations are solved numerically using the pseudospectral GPU-enabled code Tarang-py (40). We employ the fourth-order Runge–Kutta (RK4) time-stepping scheme, as well as hypodiffusive term $10^{-2}\nabla^{-1}$ and hyperdiffusive term $10^{-8}\nabla^8$ to both $\mathbf{u}$ and T' in order to stabilize the elevator modes (34, 59). All our simulations are well resolved, with $\mathcal{R}_\eta > 1$ in each case. Refer to Table 1 for the simulation parameters, Re, Pr, Nu, $\mathcal{R}_\eta$, etc.

Rayleigh-Bénard Convection. The 2D RBC datasets have been taken from Samuel and Verma (36) and Samuel (37), whereas the 3D datasets have been taken from Bhattacharya et al. (35). The above authors solved the following nondimensionalized equations:

$$\frac{\partial \mathbf{u}}{\partial t} + \mathbf{u}\cdot\nabla\mathbf{u} = -\nabla p + T\hat{z} + \sqrt{\frac{\text{Pr}}{\text{Ra}}}\nabla^2\mathbf{u}, \quad [11]$$

$$\frac{\partial T}{\partial t} + \mathbf{u}\cdot\nabla T = \frac{1}{\sqrt{\text{Ra Pr}}}\nabla^2 T, \quad [12]$$

$$\nabla\cdot\mathbf{u} = 0, \quad [13]$$

where $\mathbf{u}$, p, and T are the velocity, pressure, and temperature fields, respectively. Here, a fluid is confined between two horizontal plates separated by a unit distance. The horizontal extent of the fluid is Γ, the aspect ratio. The bottom and top plates are maintained at temperatures 1 and 0, respectively. The Rayleigh number and Prandtl number for RBC are defined as

$$\text{Ra} = \frac{\alpha(\Delta T)gd^3}{\nu\kappa}, \quad \text{Pr} = \frac{\nu}{\kappa}, \quad [14]$$

where ΔT is the imposed temperature difference across the plates. Ra, Pr, Γ, Re, Nu, $\mathcal{R}_\eta$, etc. are listed in Table 1.

Samuel and Verma (36), Samuel (37), and Bhattacharya et al. (35) employed the finite-difference code SARAS (43). The solver uses a multigrid method for the pressure-Poisson equation and a second-order Crank-Nicolson scheme for time stepping. For the top and bottom boundaries, both 2D and 3D runs employ no-slip boundary conditions for the velocity field and conducting boundary conditions for the temperature field. However, for the side walls, the 2D simulations employ periodic boundaries, while the 3D simulations employ no-slip and adiabatic boundary conditions. For all the runs, the grid spacing is smaller than the Kolmogorov length scale $\eta = \langle \nu^3/\epsilon_u\rangle^{1/4}$, where $\epsilon_u = (\nu/2)\langle(\partial_i u_j + \partial_j u_i)^2\rangle$ is the kinetic energy dissipation rate. This condition ensures that the resolution parameter $\mathcal{R}_\eta > 1$, as listed in Table 1. The boundary layers are well resolved with at least 5 grid points, satisfying the Grötzbach criterion (60).

Compressible Convection. We simulate compressible convection in a box of dimension $\Gamma\times 1$ in 2D and $\Gamma\times\Gamma\times 1$ in 3D. The bottom plate is maintained at unit temperature, whereas the top plate at $1 - D - \epsilon$, where ϵ and D are the superadiabaticity and the dissipation number, defined below

$$\epsilon = \frac{d}{T_b}\left(\frac{\Delta T}{d} - \frac{g}{C_p}\right), \quad D = \frac{gd}{T_b C_p}. \quad [15]$$

The Rayleigh number and Prandtl number are defined as (38, 39)

$$\text{Ra} = \frac{\epsilon g d^3}{\nu\kappa}, \quad \text{Pr} = \frac{\nu}{\kappa}. \quad [16]$$

The horizontal plates are maintained at a constant temperature (conducting boundary condition). In addition, we set $\mathbf{u} = 0$ on the horizontal plates. Periodic boundary condition is applied for the vertical walls. We solve the following nondimensional equations in conservative form (38, 39):

$$\frac{\partial\rho}{\partial t} + \frac{\partial}{\partial x_i}(\rho u_i) = 0, \quad [17]$$

$$\frac{\partial}{\partial t}(\rho u_i) + \frac{\partial}{\partial x_j}(\rho u_i u_j + \delta_{ij}p - \tau_{ij}) = -\frac{1}{\epsilon}\rho\delta_{iz}, \quad [18]$$

$$\frac{\partial E}{\partial t} + \frac{\partial}{\partial x_i}\left(u_i(E+p) - \frac{1}{\epsilon D\sqrt{\text{Ra Pr}}}\frac{\partial T}{\partial x_i} - u_j\tau_{ij}\right) = 0, \quad [19]$$

where $\mathbf{u}$ and T are the nondimensional velocity and temperature fields, respectively; and ρ is the nondimensional density field. The nondimensional pressure for an ideal gas is

$$p = (\gamma - 1)\frac{\rho T}{\gamma\epsilon D}, \quad [20]$$

where $\gamma = C_p/C_v$ is the ratio of specific heat capacities. The viscous stress tensor is given by

$$\tau_{ij} = \sqrt{\frac{\text{Pr}}{\text{Ra}}}\left(\partial_j u_i + \partial_i u_j - \frac{2}{3}\partial_m u_m \delta_{ij}\right), \quad [21]$$

and the total energy density is

$$E = \rho\left(\frac{u^2}{2} + \frac{T}{\gamma\epsilon D} + \frac{z}{\epsilon}\right). \quad [22]$$

Note that the background adiabatic profile is $T_A(z) = 1 - Dz$, and the superadiabatic temperature is defined as

$$T_{\text{sa}}(\mathbf{r}) = \frac{T(\mathbf{r}) - T_A(z)}{\epsilon}, \quad [23]$$

which measures the deviation of temperature from the adiabatic state, normalized by the superadiabaticity. Refer to Spiegel (38) and Graham (39) for details on compressible equations.

We solve Eqs. **17**–**19** using the finite-difference solver Dhara (32), which employs the MacCormack-TVD (Total Variation Diminishing) scheme on a collocated grid (61, 62). The MacCormack scheme is second-order accurate in both space and time (61). A nonuniform tangent-hyperbolic grid is employed in the z-direction to enhance resolution near the boundaries, while uniform grids are used in the x and y directions. At the top and bottom plates, second-order forward and backward finite differences are used to evaluate boundary values, respectively. The general conservative form of the governing equations is written as

$$\frac{\partial Q}{\partial t} + \frac{\partial F_i}{\partial x_i} = S_i, \quad [24]$$

where Q is a generic conserved variable; F_i is the flux; and S_i is the source term in the i-direction. Using operator splitting, Eq. **24** is decomposed into three one-dimensional subproblems, each solved using the MacCormack predictor–corrector approach. The TVD correction is added to suppress spurious oscillations and preserve monotonicity in steep-gradient regions (62). For further details, see ref. 32.

All our simulations are well resolved, with the resolution parameter $\mathcal{R}_\eta = \min_i(\eta(z)/\Delta x_i) > 0.5$ (30, 63) (Table 1). The Kolmogorov length scale is given by $\eta(z) = (\nu^3\langle\rho\rangle/\langle S_{ij}\tau_{ij}\rangle)^{1/4}$, where $S_{ij} = (\partial_i u_j + \partial_j u_i)/2$ is the strain-rate tensor. For all our runs, the boundary layers are resolved with at least 7 grid points, thus satisfying the Grötzbach criterion (60). For our numerical simulations, we fix $\gamma = 1.3, D = 0.5, \epsilon = 0.1, \text{Pr} = 0.7$, and vary Ra from 10^9 to 10^{16} for 2D, and from 10^7 to 10^{13} for 3D. See Table 1 for details. We perform our parallel runs on several GPUs that enable high-resolution simulations in a reasonable time. For instance, our largest 3D simulation on $501^2 \times 5{,}001$ grid ran for 10 d on the Kotak school's server (with 8 NVIDIA H100 GPUs), while the largest 2D run on $24{,}001^2$ grid ran for 20 d on two nodes of Sophia (with 8 NVIDIA A100 GPUs each) at Argonne National Laboratory.

Data, Materials, and Software Availability. Data and scripts are available at Zenodo (64).

ACKNOWLEDGMENTS. We thank K. R. Sreenivasan and Jörg Schumacher for valuable comments and suggestions and for careful reading of the manuscript. We thank Roshan Samuel and Shashwat Bhattacharya for providing the Rayleigh-Bénard convection datasets, and Rajesh Ranjan, Dhananjay Singh, and Sanjiva Lele for valuable discussions. Simulations were performed on the Argonne Leadership Computing Facility through the Director's Discretionary Program, and on the High-Performance Computing cluster of the Kotak School of Sustainability, Indian Institute of Technology Kanpur. L.S. thanks Indian Institute of Technology Kanpu for the Institute Postdoctoral Fellowship. Part of this work was done in the Center for Turbulence Research, Stanford University, where M.K.V. was a Visiting Senior Fellow. Part of this work was supported by Anusandhan National Research Foundation, India (Grant Nos. SERB/PHY/2021522 and SERB/PHY/2021473), and the J. C. Bose Fellowship (SERB /PHY/2023488).

1. E. D. Siggia, High Rayleigh number convection. *Annu. Rev. Fluid Mech.* **26**, 137–168 (1994).
2. G. Ahlers, S. Grossmann, D. Lohse, Heat transfer and large scale dynamics in turbulent Rayleigh-Bénard convection. *Rev. Mod. Phys.* **81**, 503–537 (2009).
3. D. Lohse, K. Q. Xia, Small-scale properties of turbulent Rayleigh-Bénard convection. *Annu. Rev. Fluid Mech.* **42**, 335–364 (2010).
4. J. Schumacher, K. R. Sreenivasan, Colloquium: Unusual dynamics of convection in the Sun. *Rev. Mod. Phys.* **92**, 041001 (2020).
5. F. Chillà, J. Schumacher, New perspectives in turbulent Rayleigh-Bénard convection. *Eur. Phys. J. E* **35**, 58 (2012).
6. M. K. Verma, *Physics of Buoyant Flows: From Instabilities to Turbulence* (World Scientific, Singapore, 2018).
7. C. Priestley, Convection from a large horizontal surface. *Aust. J. Phys.* **7**, 176–201 (1954).
8. W. V. R. Malkus, The heat transport and spectrum of thermal turbulence. *Proc. R. Soc. Lond. A* **225**, 196–212 (1954).
9. R. H. Kraichnan, Turbulent thermal convection at arbitrary Prandtl number. *Phys. Fluids* **5**, 1374–1389 (1962).
10. L. N. Howard, Heat transport by turbulent convection. *J. Fluid Mech.* **17**, 405–432 (1963).
11. E. A. Spiegel, A generalization of the mixing-length theory of turbulent convection. *Astrophys. J.* **138**, 216 (1963).
12. E. A. Spiegel, Convection in stars: I. Basic Boussinesq convection. *Annu. Rev. Astron. Astrophys.* **9**, 323–352 (1971).
13. L. N. Howard, "Convection at high Rayleigh number" in *Applied Mechanics: Proceedings of the Eleventh International Congress of Applied Mechanics Munich (Germany) 1964*, H. Görtler, Ed. (Springer, 1966), pp. 1109–1115.
14. P. P. Shevkar *et al*., Hierarchical network of thermal plumes and their dynamics in turbulent Rayleigh-Bénard convection. *Proc. Natl. Acad. Sci. U.S.A.* **122**, e2502972122 (2025).
15. C. R. Doering, F. Otto, M. G. Reznikoff, Bounds on vertical heat transport for infinite-Prandtl-number Rayleigh-Bénard convection. *J. Fluid Mech.* **560**, 229–241 (2006).
16. B. I. Shraiman, E. D. Siggia, Heat transport in high-Rayleigh-number convection. *Phys. Rev. A* **42**, 3650–3653 (1990).
17. S. Grossmann, D. Lohse, Scaling in thermal convection: A unifying theory. *J. Fluid Mech.* **407**, 27–56 (2000).
18. C. R. Doering, Turning up the heat in turbulent thermal convection. *Proc. Natl. Acad. Sci. U.S.A.* **117**, 9671–9673 (2020).
19. X. Chavanne, F. Chillà, B. Chabaud, B. Castaing, B. Hebral, Turbulent Rayleigh-Bénard convection in gaseous and liquid He. *Phys. Fluids* **13**, 1300–1320 (2001).
20. X. He, D. Funfschilling, H. Nobach, E. Bodenschatz, G. Ahlers, Transition to the ultimate state of turbulent Rayleigh-Bénard convection. *Phys. Rev. Lett.* **108**, 024502 (2012).
21. X. Zhu, V. Mathai, R. J. A. M. Stevens, R. Verzicco, D. Lohse, Transition to the ultimate regime in two-dimensional Rayleigh-Bénard convection. *Phys. Rev. Lett.* **120**, 144502 (2018).
22. D. Lohse, O. Shishkina, Ultimate Rayleigh-Bénard turbulence. *Rev. Mod. Phys.* **96**, 035001 (2024).
23. O. Shishkina, D. Lohse, Ultimate regime of Rayleigh-Bénard turbulence: Subregimes and their scaling relations for the Nusselt vs Rayleigh and Prandtl numbers. *Phys. Rev. Lett.* **133**, 144001 (2024).
24. J. J. Niemela, L. Skrbek, K. R. Sreenivasan, R. J. Donnelly, Turbulent convection at very high Rayleigh numbers. *Nature* **404**, 837–840 (2000).
25. J. J. Niemela, K. R. Sreenivasan, The use of cryogenic helium for classical turbulence: Promises and hurdles. *J. Low Temp. Phys.* **143**, 163–212 (2006).
26. P. Urban *et al*., Effect of boundary layers asymmetry on heat transfer efficiency in turbulent Rayleigh-Bénard convection at very high Rayleigh numbers. *Phys. Rev. Lett.* **109**, 154301 (2012).
27. K. P. Iyer, J. D. Scheel, J. Schumacher, K. R. Sreenivasan, Classical 1/3 scaling of convection holds up to $\mathrm{Ra} = 10^{15}$. *Proc. Natl. Acad. Sci. U.S.A.* **117**, 7594–7598 (2020).
28. M. K. Verma, P. K. Mishra, A. Pandey, S. Paul, Scalings of field correlations and heat transport in turbulent convection. *Phys. Rev. E* **85**, 016310 (2012).
29. A. Pandey, M. K. Verma, Scaling of large-scale quantities in Rayleigh-Bénard convection. *Phys. Fluids* **28**, 095105 (2016).
30. J. P. John, J. Schumacher, Strongly superadiabatic and stratified limits of compressible. *Phys. Rev. Fluids* **8**, 103505 (2023).
31. J. P. John, J. Schumacher, Compressible turbulent in highly stratified adiabatic background. *J. Fluid Mech.* **972**, R4 (2023).
32. H. Tiwari, L. Sharma, M. K. Verma, Compressible turbulent convection at very high Rayleigh numbers. *Int. J. Heat Mass Transf.* **242**, 126821 (2025).
33. D. Lohse, F. Toschi, Ultimate state of thermal convection. *Phys. Rev. Lett.* **90**, 034502 (2003).
34. P. Winchester, V. Dallas, P. D. Howell, Two-dimensional Rayleigh-Bénard convection without boundaries. *J. Fluid Mech.* **998**, A27 (2024).
35. S. Bhattacharya, M. K. Verma, R. Samtaney, Prandtl number dependence of the small-scale properties in turbulent Rayleigh-Bénard convection. *Phys. Rev. Fluids* **6**, 063501 (2021).
36. R. Samuel, M. K. Verma, Bolgiano-Obukhov scaling in two-dimensional Rayleigh-Bénard convection at extreme Rayleigh numbers. *Phys. Rev. Fluids* **9**, 023502 (2024).
37. R. Samuel, "Simulations of Rayleigh-Bénard convection at extreme Rayleigh numbers," PhD thesis (2023). https://www.researchgate.net/publication/391520596_PhD_Thesis.
38. E. A. Spiegel, Convective instability in a compressible atmosphere. *I. Astrophys. J.* **141**, 1068–1090 (1965).
39. E. Graham, Numerical simulation of two-dimensional compressible. *J. Fluid Mech.* **70**, 689–703 (1975).
40. A. G. Chatterjee *et al*., Scaling of a Fast Fourier Transform and a pseudo-spectral fluid solver up to 196608 cores. *J. Parallel Distrib. Comput.* **113**, 77–91 (2018).
41. U. Frisch, *Turbulence: The Legacy of A. N. Kolmogorov* (Cambridge University Press, Cambridge, 1995).
42. M. Lesieur, *Turbulence in Fluids* (Springer-Verlag, Dordrecht, 2008).
43. R. Samuel *et al*., SARAS: A general-purpose PDE solver for fluid dynamics. *J. Open Sour. Softw.* **6**, 2095 (2021).
44. P. Moin, W. R. Chan, *Fundamentals of Turbulent Flows* (Cambridge University Press, 2024).
45. G. Ahlers *et al*., Logarithmic temperature profiles in turbulent Rayleigh-Bénard convection. *Phys. Rev. Lett.* **109**, 114501 (2012).
46. H. Schlichting, K. Gersten, *Boundary-Layer Theory* (Springer, 2016).
47. S. B. Pope, *Turbulent Flows* (Cambridge University Press, Cambridge, 2000).
48. R. J. Samuel, M. Bode, J. D. Scheel, K. R. Sreenivasan, J. Schumacher, No sustained mean velocity in the boundary region of plane thermal convection. *J. Fluid Mech.* **996**, A49 (2024).
49. G. K. Batchelor, *The Theory of Homogeneous Turbulence* (Cambridge University Press, Cambridge, 1953).
50. D. C. Leslie, *Developments in the Theory of Turbulence* (Clarendon Press, Oxford, 1973).
51. A. Pandey, K. R. Sreenivasan, Transient and steady convection in two dimensions. *J. Fluid Mech.* **1015**, A42 (2025).
52. E. Lindborg, Scaling in two-dimensional Rayleigh-Bénard convection. arXiv [Preprint] (2025). http://arxiv.org/abs/2506.13213 (Accessed 29 July 2025).
53. V. Bouillaut, B. Flesselles, B. Miquel, S. Aumaître, B. Gallet, Velocity-informed upper bounds on the convective heat transport induced by internal heat sources and sinks. *Philos. Trans. R. Soc. A* **380**, 20210034 (2022).
54. S. Lepot, S. Aumaître, B. Gallet, Radiative heating achieves the ultimate regime of thermal convection. *Proc. Natl. Acad. Sci. U.S.A.* **115**, 8937–8941 (2018).
55. P. E. Roche, B. Castaing, B. Chabaud, B. Hebral, Observation of the 1/2 power law in Rayleigh-Bénard convection. *Phys. Rev. E* **63**, 045303(R) (2001).
56. S. Pirozzoli, M. Bernardini, R. Verzicco, P. Orlandi, Mixed convection in turbulent channels with unstable stratification. *J. Fluid Mech.* **821**, 482–516 (2017).
57. C. W. Hamman, P. Moin, "Numerical experiments in thermal convectionwith and without mean shear" (Tech. Rep. TF-170, Department of Mechanical Engineering, Stanford University, 2023).
58. R. Narasimha, K. R. Sreenivasan, Relaminarization of fluid flows. *Adv. Appl. Mech.* **19**, 221–309 (1979).
59. E. Calzavarini *et al*., Exponentially growing solutions in homogeneous Rayleigh-Bénard convection. *Phys. Rev. E* **73**, 035301 (2006).
60. G. Grötzbach, Spatial resolution requirements for direct numerical simulation of the Rayleigh-Bénard convection. *J. Comput. Phys.* **49**, 241–264 (1983).
61. Wesseling, *Principles of Computational Fluid Dynamics* (Springer-Verlag, Berlin Heidelberg, ed. 1, 2000).
62. C. Ouyang, S. He, Q. Xu, Y. Luo, W. Zhang, A MacCormack-TVD finite difference method to simulate the mass flow in mountainous terrain with variable computational domain. *Comput. Geosci.* **52**, 1–10 (2013).
63. S. Jagannathan, D. A. Donzis, Reynolds and Mach number scaling in solenoidally-forced compressible turbulence using high-resolution direct numerical simulations. *J. Fluid Mech.* **789**, 669–707 (2016).
64. H. Tiwari, L. Sharma, M. K. Verma, Repository for on the absence of the ultimate regime in turbulent thermal convection. [Zenodo] (2025). https://doi.org/10.5281/zenodo.16914627 (Accessed 20 August 2025).

Supporting Information for

On the Absence of the Ultimate Regime in Turbulent Thermal Convection

Harshit Tiwari, Lekha Sharma, and Mahendra K. Verma

Mahendra K. Verma
E-mail: mkviitk.ac.in

This PDF file includes:

Supporting text
Figs. S1 to S5
Tables S1 to S2
SI References

Supporting Information Text

This section contains additional discussions on boundary layers, heat fluxes in two dimensions, and convergence tests, along with five figures and two tables. The table and figure captions are self-contained and provide the necessary context. This material acts only as a supplement to the main text.

Boundary layers in Turbulent Compressible Convection

In turbulent systems, boundary layers develop adjacent to the solid plates. The boundary layer profiles are often expressed in wall units: the friction velocity scale $u_\tau = \sqrt{\tau_w/\rho}$, wall temperature scale $T_\tau = -\kappa\, \partial_z \langle T\rangle_{A,t}|_{z=0} / u_\tau$, and length scale ν/u_τ, where $\tau_w = \mu\, \partial_z \langle u\rangle_{A,t}|_{z=0}$ is the wall shear stress, $\langle u\rangle_{x,t} = \langle\sqrt{u_x^2}\rangle_{x,t}$ in 2D, $\langle u\rangle_{A,t} = \langle\sqrt{u_x^2+u_y^2}\rangle_{A,t}$ in 3D, and ν and κ are the viscous and thermal diffusivities, respectively. In the above expressions, $\langle.\rangle_{x,t}$ and $\langle.\rangle_{A,t}$ denote the horizontal-time and planar-time averages (1–3). Using these variables, the nondimensionalized velocity, temperature, and vertical height z are $u^+ = \langle u\rangle_{A,t}/u_\tau$, $T^+ = (T_b - \langle T\rangle_{A,t})/T_\tau$, and $z^+ = u_\tau z/\nu$, respectively, where T_b is the temperature at the bottom plate.

According to the boundary layer theory (2, 3), there are two distinct regions:

$$\text{Viscous sublayer region } (z^+ < 5): \quad u^+ = z^+, \qquad T^+ = z^+, \tag{1}$$

$$\text{Log-law region } (z^+ > 50): \quad u^+ = \frac{1}{\kappa_u}\ln z^+ + B_u, \quad T^+ = \frac{1}{\kappa_T}\ln z^+ + B_T. \tag{2}$$

In these formulas, κ_u and κ_T are the von Kármán constants for the viscous and thermal boundary layers, respectively; and B_u and B_T are constants that depend on the flow configuration and boundary conditions. For pipe and channel flows, empirical and numerical studies reveal that κ_u varies from 0.39 to 0.41, and $B_u \approx 5.0$ for the viscous boundary layers (2, 4, 5). However, for the thermal boundary layers, κ_T and B_T often vary with the Prandtl and Reynolds number. Yaglom and Kader (6–8) argued that for Prandtl number near unity, κ_T ranges from 0.46 to 0.6 depending on the Reynolds number.

In the main text, we focused on the mean velocity and temperature profiles for compressible convection *near the bottom boundary*. In this Supplementary Material, we present the corresponding profiles *near the top wall*. The properties of the boundary layer near the top and bottom are similar, with minor differences, which are highlighted here. Figure S1(a,b) shows the mean velocity profiles $u^+(z^+)$ near the top boundary for both 2D and 3D simulations. For 2D compressible convection, the top plate exhibits a logarithmic layer, with κ_u decreasing from 0.96 at $\mathrm{Ra} = 10^9$ to 0.32 at $\mathrm{Ra} = 10^{16}$ (see Table S1). The above logarithmic layer is attributed to the shear flow present in the 2D flow. Note that κ_u for the top boundary is lower than that for the bottom boundary, indicating a stronger gradient and turbulence near the top boundary than the bottom boundary. In addition, the 3D velocity profile near the top boundary does not exhibit a clear logarithmic region, possibly due to the absence of a shear layer in 3D (9).

In Fig. S1(c,d), we plot the temperature profiles $T^+(z^+)$ near the top boundary. These plots exhibit a logarithmic layer in both 2D and 3D, similar to the bottom wall. The values of κ_T range from 4 to 12 for 2D and from 3.2 to 7.9 for 3D. Compared to the bottom boundary, on the whole, κ_T for the top boundary is larger for the 2D flows and smaller for the 3D flows. Also note that all four plots clearly show a viscous sublayer, with best-fit functions represented by black curves for $z^+ \lessapprox 2$. Lastly, Taylor-Couette flow and RBC have certain similarities, including in the boundary layers. However, these discussions are beyond the scope of this paper (10, 11).

Anisotropic Heat Fluxes in 2D Convection

We consider a snapshot of 2D periodic convection (PC) at Ra of 10^8, a snapshot of 2D RBC at Ra of 10^{14}, and a snapshot of 2D compressible convection (CC) at Ra of 10^{13} during the steady state, and display them in Fig. S2(a,b,c). The figure displays the vector plots of the velocity field $\mathbf{u}(\mathbf{r})$ and the density plots of the temperature field $[T(\mathbf{r}), T_{\mathrm{sa}}(\mathbf{r})]$, whereas Fig. S2(d,e,f) exhibits the vertical heat flux $F_z(\mathbf{r})$. As in 3D convection, periodic convection is dominated by positive F_z, but RBC and compressible convection have both positive and negative F_z's. However, compared to 3D convection, 2D convection exhibits stronger patches of positive and negative heat fluxes due to the inverse energy cascade in 2D (12, 13). These features are consistent with the wider tails in PDF's for F_z $[P(F_z)]$ in 2D than in 3D (see Fig. 5 of the main text).

Numerical Resolution and Convergence Tests

To ensure that our simulations at high Reynolds numbers are well-resolved, we performed detailed resolution and convergence tests. To accelerate convergence to a statistically steady state, for each case, we first conduct a simulation at a lower Ra, and then interpolate its final state onto a finer grid to initialize the subsequent higher-Ra run, repeating this procedure iteratively. For each run, we monitor the resolution parameter $\mathcal{R}_\eta = \min_i(\eta/\Delta x_i)$ and the number of grid points in the top and bottom boundary layers $(N_t^{\mathrm{BL}}, N_b^{\mathrm{BL}})$. Here, η is the Kolmogorov length; and Δx_i is the grid spacing in the i-th direction. We list these quantities in Table S2 (also see Table 1 of the main text). All our runs satisfy the resolution criteria, with $\mathcal{R}_\eta > 1$ for periodic convection and RBC, and $\mathcal{R}_\eta > 0.5$ for compressible convection (14, 15). Furthermore, the boundary layers are resolved with at least 7 grid points, thereby satisfying the Grötzbach criterion (16). The grid resolutions used in our simulations are comparable to those employed in previous high Reynolds number numerical studies (17, 18). For completeness and reproducibility, we also report in Table S2 a set of additional parameters: root-mean-square velocity U, normalized Nusselt number NuRa^{-b}, average time step $\langle\Delta t\rangle$, and the total simulation time t_{run} in free-fall units.

To test whether our simulations have reached a steady state, we plot the time series of root-mean-square velocity U and normalized Nusselt number NuRa^{-b} for the periodic and compressible convection for 10 free-fall times, where b is the exponent for Nu. For 3D and 2D periodic convection, after an initial transient, U (Fig. S3(a,c)) and NuRa^{-b} (Fig. S3(b,d)) are nearly constant, thus indicating convergence to statistical steady state. In periodic convection, the errors in U are below 17% while the errors in NuRa^{-b} are below 11%. The time series of 3D and 2D compressible convection exhibits similar behaviour (Fig. S4) with errors below 13% in U and below 20% in NuRa^{-b}. The total time of simulation t_{run} in 3D compressible runs is comparable to the past numerical study of 3D RBC by Iyer et al. (17). In compressible convection, we further verify grid independence at $\mathrm{Ra} = 10^{13}$ by comparing results on $501^2 \times 5001$ and $601^2 \times 6001$ grids (Fig. S5); both U and Nu converge to the nearly same value, independent of the grid resolution.

Regarding RBC, we refer the reader to Bhattacharya et al. (19) for details on the numerical resolution and convergence of the 3D RBC datasets, and to Samuel and Verma (20) and Samuel (21) for the corresponding 2D RBC datasets. It is well established in the literature that 3D RBC reaches statistical convergence more readily, with the root-mean-square velocity U converging in several free-fall times (17, 22). In contrast, for 2D RBC, Pandey et al. (13) and Lindborg (22) showed that the velocity field evolves more slowly than the thermal field, with the former converging exponentially slowly with time. Samuel and Verma (20) and Samuel (21) moved to higher resolution progressively, which leads to relatively faster convergence. Note, however, that the Nusselt number, which is the focus of this paper, exhibits relatively weaker fluctuations.

Table S1. For compressible convection C2D, C3D: Table exhibiting the von Kármán constants κ_u, κ_T for the viscous and thermal boundary layers near the top plate. It also lists the additive constants (B_u, B_T) near the top and bottom plates. Also see Table 1 of the manuscript.

System	Ra	Γ	$\kappa_{u,\mathrm{top}}$	$\kappa_{T,\mathrm{top}}$	$B_{u,\mathrm{top}}$	$B_{T,\mathrm{top}}$	$B_{u,\mathrm{bottom}}$	$B_{T,\mathrm{bottom}}$
C2D	10^9	1	0.96	4.1	6.2	0.25	2.7	-0.34
C2D	10^{10}	1	0.61	8.6	23	0.22	3.1	-0.63
C2D	10^{11}	1	0.48	8.5	14	0.31	2.7	-0.15
C2D	10^{12}	1	0.43	8	23	0.50	6.1	0.18
C2D	10^{13}	1	0.36	7.4	26	0.96	8.1	0.49
C2D	10^{14}	0.8	0.32	12	33	0.80	11	0.62
C2D	10^{15}	0.8	0.34	12	40	1.1	16	0.93
C2D	10^{16}	0.8	0.32	8	73	2.7	28	1.4
C3D	10^8	0.25	–	3.2	–	0.20	–	-0.07
C3D	10^9	0.25	–	3.6	–	0.22	–	-0.04
C3D	10^9	1	–	3.4	–	0.25	–	-0.11
C3D	10^{10}	0.25	–	4.6	–	0.37	–	0.04
C3D	10^{11}	0.25	–	5.7	–	0.41	–	0.07
C3D	10^{12}	0.125	–	5.1	–	0.53	–	0.09
C3D	10^{13}	0.125	–	7.9	–	0.60	–	0.15

Table S2. Additional parameters for periodic convection (P2D, P3D) and compressible convection (C2D, C3D): root-mean-square velocity U, normalized Nusselt number NuRa^{-b} (b = exponent for Nu), average time step $\langle \Delta t \rangle$, total time of the simulation t_{run} in free-fall time units, and the number of grid points in the top and bottom boundary layers (N_t^{BL}, N_b^{BL}).

Run	System	Ra	Pr	Grid Size	Γ	U	NuRa^{-b}	$\langle \Delta t \rangle$	t_{run}	N_t^{BL}	N_b^{BL}
1	P2D	10^4	1	64^2	1	1.5 ± 0.2	1.1 ± 0.1	1.0×10^{-2}	100	NA	NA
2	P2D	10^5	1	128^2	1	1.7 ± 0.1	1.1 ± 0.1	1.0×10^{-2}	100	NA	NA
3	P2D	10^6	1	256^2	1	1.7 ± 0.3	1.0 ± 0.1	1.0×10^{-2}	100	NA	NA
4	P2D	10^7	1	512^2	1	1.6 ± 0.2	0.9 ± 0.1	1.0×10^{-2}	100	NA	NA
5	P2D	10^8	1	1024^2	1	2.0 ± 0.1	1.0 ± 0.1	5.0×10^{-3}	100	NA	NA
6	P3D	10^4	1	128^3	1	1.8 ± 0.2	1.43 ± 0.07	1.0×10^{-2}	100	NA	NA
7	P3D	10^5	1	128^3	1	1.5 ± 0.1	1.24 ± 0.04	1.0×10^{-2}	100	NA	NA
8	P3D	10^6	1	180^3	1	1.5 ± 0.1	1.36 ± 0.06	1.0×10^{-2}	100	NA	NA
9	P3D	10^7	1	256^3	1	1.5 ± 0.1	1.46 ± 0.05	1.0×10^{-2}	100	NA	NA
10	C2D	10^9	0.7	513^2	1	0.34 ± 0.03	0.031 ± 0.004	7.5×10^{-4}	1150	32	11
11	C2D	10^{10}	0.7	1025^2	1	0.37 ± 0.02	0.030 ± 0.003	3.5×10^{-4}	1150	32	11
12	C2D	10^{11}	0.7	2049^2	1	0.37 ± 0.03	0.032 ± 0.005	1.2×10^{-4}	1150	30	10
13	C2D	10^{12}	0.7	4097^2	1	0.39 ± 0.03	0.036 ± 0.006	5.5×10^{-5}	400	31	10
14	C2D	10^{13}	0.7	8193^2	1	0.37 ± 0.03	0.034 ± 0.007	2.8×10^{-5}	100	34	10
15	C2D	10^{14}	0.7	12001^2	0.8	0.35 ± 0.02	0.029 ± 0.006	2.0×10^{-5}	72	28	9
16	C2D	10^{15}	0.7	16385^2	0.8	0.33 ± 0.02	0.036 ± 0.006	1.0×10^{-5}	27	25	8
17	C2D	10^{16}	0.7	24001^2	0.8	0.34 ± 0.02	0.029 ± 0.005	8.0×10^{-6}	19	23	7
18	C3D	10^7	0.7	$33^2 \times 129$	0.25	0.10 ± 0.02	0.037 ± 0.005	2.0×10^{-3}	1100	28	9
19	C3D	10^8	0.7	$65^2 \times 257$	0.25	0.13 ± 0.01	0.045 ± 0.004	2.0×10^{-3}	1100	32	12
20	C3D	10^9	0.7	$129^2 \times 513$	0.25	0.11 ± 0.01	0.046 ± 0.003	8.0×10^{-4}	200	31	11
21	C3D	10^9	0.7	513^3	1	0.16 ± 0.02	0.045 ± 0.001	8.0×10^{-4}	120	32	11
22	C3D	10^{10}	0.7	$257^2 \times 1025$	0.25	0.10 ± 0.01	0.044 ± 0.002	4.0×10^{-4}	250	30	10
23	C3D	10^{11}	0.7	$513^2 \times 2049$	0.25	0.10 ± 0.01	0.043 ± 0.001	2.0×10^{-4}	79	29	9
24	C3D	10^{12}	0.7	$451^2 \times 3601$	0.125	0.066 ± 0.002	0.039 ± 0.006	1.0×10^{-4}	26	23	8
25	C3D	10^{13}	0.7	$501^2 \times 5001$	0.125	0.064 ± 0.003	0.039 ± 0.005	8.0×10^{-5}	11	21	7

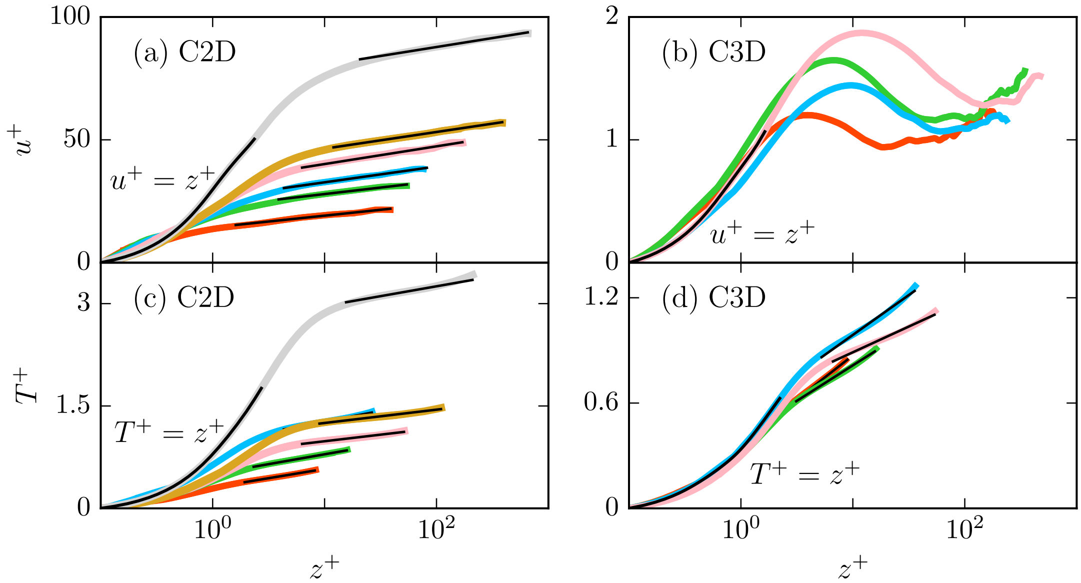

Fig. S1. Near the **top plate** of compressible convection, plots of u^+ vs. z^+ in the viscous boundary layers (top row: a,b), and T^+ vs. z^+ in the thermal boundary layers (bottom row: c,d). The left column is for 2D with Ra = 10^{11} (red), 10^{12} (green), 10^{13} (blue), 10^{14} (pink), 10^{15} (golden), and 10^{16} (gray). With increasing Ra, κ_u varies from 0.48 to 0.32, whereas κ_T varies from 8 to 11. The right column is for 3D with Ra = 10^{10} (red), 10^{11} (green), 10^{12} (blue), and 10^{13} (pink). Figure (b) does not exhibit a clear signature of the logarithmic layer. (d) For the thermal boundary layer in 3D, κ_T varies from 3.2 to 7.9.

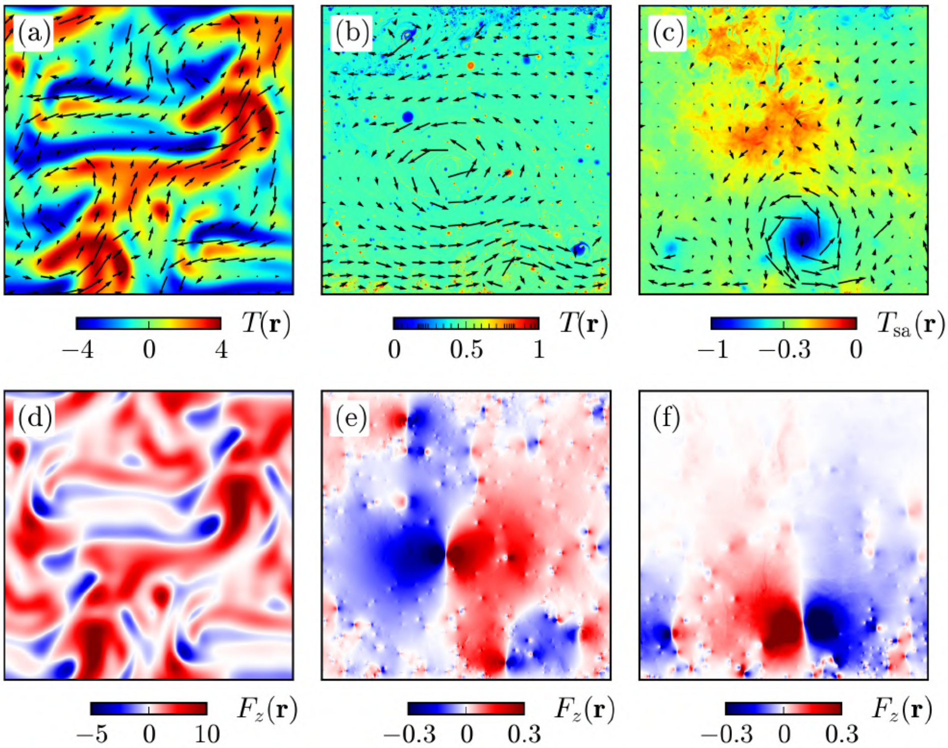

Fig. S2. For **2D convection**, plots of the velocity and temperature fields (top row), and vertical heat flux $F_z(\mathbf{r})$ (bottom row) for (a,d) 2D periodic convection with Ra = 10^8; (b,e) 2D RBC with Ra = 10^{14}; (c,f) 2D compressible convection with Ra = 10^{13}. Periodic convection exhibits predominantly positive F_z, whereas RBC and compressible convection exhibit both positive and negative F_z.

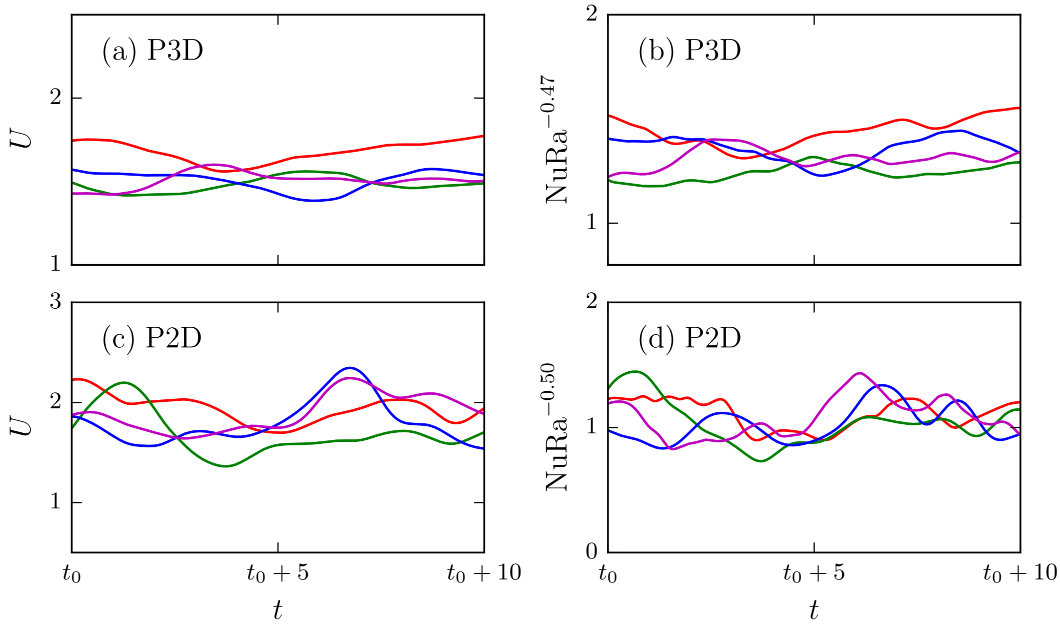

Fig. S3. For **periodic convection**, time series of the root-mean-square velocity U (a,c) and normalized Nusselt number NuRa^{-b} (b,d) during statistically steady state. The top row is for 3D at Ra $= 10^4$ (red), 10^5 (green), 10^6 (blue), and 10^7 (magenta). The bottom row is for 2D at Ra $= 10^5$ (red), 10^6 (green), 10^7 (blue), and 10^8 (magenta).

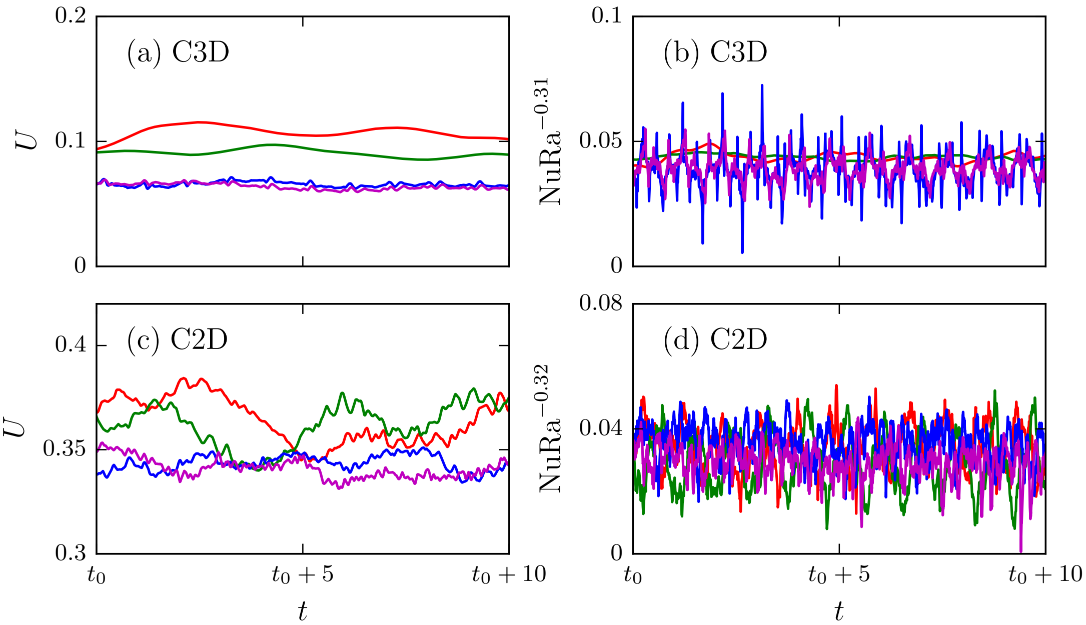

Fig. S4. For **compressible convection**, time series of the root-mean-square velocity U (a,c) and normalized Nusselt number NuRa^{-b} (b,d) during statistically steady state. The top row is for 3D at Ra $= 10^{10}$ (red), 10^{11} (green), 10^{12} (blue), and 10^{13} (magenta). The bottom row is for 2D at Ra $= 10^{13}$ (red), 10^{14} (green), 10^{15} (blue), and 10^{16} (magenta).

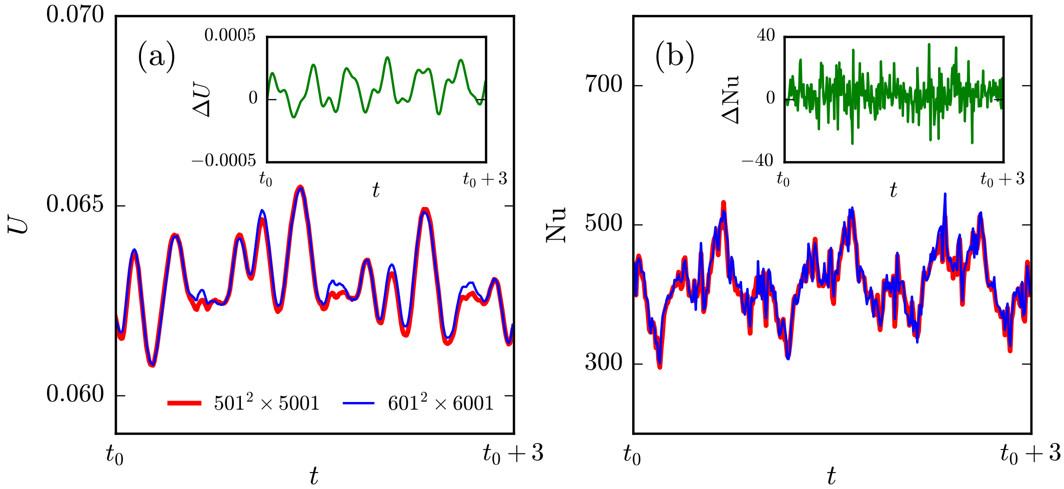

Fig. S5. For **3D compressible convection**, time series of the root-mean-square velocity U (a) and Nusselt number Nu (b) with Ra $= 10^{13}$ on grids $501^2 \times 5001$ (red) and $601^2 \times 6001$ (blue). Both U and Nu converge to similar values, confirming grid independence of our numerical simulations. The insets show their respective differences ΔU and $\Delta \mathrm{Nu}$ between the $601^2 \times 6001$ and $501^2 \times 5001$ grids. We took the final output of our $501^2 \times 5001$ grid resolution (highest 3D run), used it to perform two new simulations: on the same grid ($501^2 \times 5001$), and on the $601^2 \times 6001$ grid. We observed that the two runs yield similar results, but with some errors. The error in U is less than 1%, but the error in Nu is around 10%.

References

1. T Von Karman, Turbulence and skin friction. *J. Aero. Sci.* **1**, 1–20 (1934).
2. H Schlichting, K Gersten, *Boundary-layer theory.* (springer), (2016).
3. P Moin, WR Chan, *Fundamentals of Turbulent Flows.* (Cambridge University Press), (2024).
4. I Marusic, et al., Wall-bounded turbulent flows at high Reynolds numbers: Recent advances and key issues. *Phys. Fluids* **22**, 065103 (2010).
5. AJ Smits, BJ McKeon, I Marusic, High–Reynolds number wall turbulence. *Annu. Rev. Fluid Mech.* **43**, 353–375 (2011).
6. AM Yaglom, BA Kader, Heat and mass transfer between a rough wall and turbulent fluid flow at high Reynolds and Peclet numbers. *J. Fluid Mech.* **62**, 601–623 (1974).
7. AM Yaglom, Similarity laws for constant-pressure and pressure-gradient turbulent wall flows. *Ann. Rev. Fluid Mech.* **11**, 505–540 (1979).
8. BA Kader, Temperature and concentration profiles in fully turbulent boundary layers. *Int. J. Heat Mass Transf.* **24**, 1541–1544 (1981).
9. RJ Samuel, M Bode, JD Scheel, KR Sreenivasan, J Schumacher, No sustained mean velocity in the boundary region of plane thermal convection. *J. Fluid Mech.* **996**, A49 (2024).
10. FH Busse, The twins of turbulence research. *Physics* **5**, 4 (2012).
11. S Grossmann, D Lohse, C Sun, High-Reynolds Number Taylor-Couette Turbulence. *Annu. Rev. Fluid Mech.* **48**, 53–80 (2016).
12. EP van der Poel, RJAM Stevens, K Sugiyama, D Lohse, Flow states in two-dimensional Rayleigh-Bénard convection as a function of aspect-ratio and Rayleigh number. *Phys. Fluids* **24**, 085104 (2012).
13. A Pandey, KR Sreenivasan, Transient and steady convection in two dimensions. *J. Fluid Mech.* **1015**, A42 (2025).
14. S Jagannathan, DA Donzis, Reynolds and Mach number scaling in solenoidally-forced compressible turbulence using high-resolution direct numerical simulations. *J. Fluid Mech.* **789**, 669–707 (2016).
15. JP John, J Schumacher, Strongly superadiabatic and stratified limits of compressible convection. *Phys. Rev. Fluids* **8**, 103505 (2023).
16. G Grötzbach, Spatial resolution requirements for direct numerical simulation of the Rayleigh-Bénard convection. *J. Comput. Phys.* **49**, 241–264 (1983).
17. KP Iyer, JD Scheel, J Schumacher, KR Sreenivasan, Classical 1/3 scaling of convection holds up to $\mathrm{Ra} = 10^{15}$. *Proc. Natl. Acad. Sci.* **117**, 7594–7598 (2020).
18. X Zhu, V Mathai, RJAM Stevens, R Verzicco, D Lohse, Transition to the Ultimate Regime in Two-Dimensional Rayleigh-Bénard Convection. *Phys. Rev. Lett.* **120**, 144502 (2018).
19. S Bhattacharya, MK Verma, R Samtaney, Prandtl number dependence of the small-scale properties in turbulent Rayleigh-Bénard convection. *Phys. Rev. Fluids* **6**, 063501 (2021).
20. R Samuel, MK Verma, Bolgiano-Obukhov scaling in two-dimensional Rayleigh-Bénard convection at extreme Rayleigh numbers. *Phys. Rev. Fluids* **9**, 023502 (2024).
21. R Samuel, Ph.D. thesis (2023).
22. E Lindborg, Scaling in two-dimensional Rayleigh-Bénard convection. *arXiv preprint arXiv:2506.13213* (2025).

Chapter 5

Direct numerical simulations of compressible turbulence

In the preceding chapters, we investigated the scaling laws for global heat and momentum transport in compressible convection using the MacCormack-TVD finite difference scheme. As demonstrated in Chapter 2 (Sec. 2.6.1), this second-order approach is well-suited for accurately determining global bulk quantities, such as the Nusselt (Nu) and Reynolds (Re) numbers, while maintaining high computational efficiency. This strategy enabled us to access extreme Rayleigh numbers in the subsonic regime, where the turbulent Mach number (M_t) remained below 0.3. The turbulent Mach number is the ratio of the root-mean-square velocity to the average speed of sound ($M_t = U/\langle c_s \rangle$), and it quantifies the intrinsic compressibility of the turbulent field.

However, astrophysical flows often transcend these subsonic limits. In astrophysical settings such as stellar interiors and molecular clouds, the driving forces are vigorous enough to generate supersonic velocities ($M_t > 1$), leading to the formation of strong shocks and complex acoustic interactions. To accurately resolve these discontinuities without inducing non-physical oscillations, a more robust numerical framework is essential. Furthermore, even in the absence of shocks, high-fidelity spectral studies of compressible turbulence require schemes with minimal numerical dissipation and dispersion. In this chapter, we detail the development of a high-order finite volume module within our in-house solver, DHARA. We describe the implementation of advanced reconstruction schemes, specifically the weighted essentially non-oscillatory (WENO) (Jiang and Shu, 1996; Borges et al., 2008) and targeted essentially non-oscillatory (TENO) (Fu et al., 2016) methods, which are designed to handle both strong shocks and fine-scale turbulent fluctuations. We illustrate how DHARA has been architected as a modular, general-purpose fluid solver that retains the massive GPU scalability demonstrated earlier while extending its applicability to this broader class of complex flow problems. Finally, we demonstrate the robustness of this new framework through a high-resolution (1024^3) direct numerical simulation of supersonic turbulence at $M_t = 3.0$, showcasing the solver's ability to capture intense shocklets and paving the way for future investigations into the scaling laws of highly compressible flows.

5.1 Motivation for high-order finite volume methods

The study of compressible turbulence presents a dual challenge: the solver must robustly handle discontinuities (shocks) while accurately resolving small-scale turbulent fluctuations. In the convection simulations presented in this thesis, the flow remained largely subsonic, with fields dominated by broad thermal plumes. For such flows, the second-order MacCormack-TVD scheme provides a good balance between accuracy and computational cost, yielding converged statistics for bulk quantities like heat flux. However, when the turbulent Mach number increases into the supersonic regime ($M_t > 1$), or when the objective shifts from global scalars to detailed spectral energy transfers, low-order difference schemes face significant limitations.

The primary motivation for adopting a finite volume (FV) approach lies in its rigorous conservation properties. In the FV formulation, the rate of change of a conserved quantity within a cell is exactly equal to the net flux across its boundaries. This ensures that mass, momentum, and energy are conserved to machine precision, a property that is critical for long-time integrations of turbulent statistics. Unlike finite difference formulations, which can suffer from metric errors on distorted meshes, FV methods are naturally extensible to complex geometries, offering a pathway to simulate realistic engineering and astrophysical configurations in the future.

Furthermore, accurate resolution of the inertial and dissipation ranges in turbulence requires high-order spatial discretization. Traditional second-order schemes (like MacCormack or standard central differences) introduce numerical dispersion errors that can contaminate the small scales. Conversely, standard shock-capturing schemes (like first-order upwind) introduce excessive numerical diffusion, which artificially dampens the turbulent cascade and makes it impossible to distinguish between physical viscosity and numerical error (Pirozzoli, 2011; Fu et al., 2016). This distinction is vital for our ongoing work on supersonic turbulence, where we analyze inter-modal energy transfers using the mode-to-mode formalism (Singh et al., 2025). To reliably compute these scale-to-scale fluxes, the numerical scheme must resolve the flow features with high spectral fidelity, minimizing the numerical viscosity that otherwise plagues compressible simulations.

The development of high-order shock-capturing schemes has evolved significantly over the past few decades to address these conflicting requirements of stability and accuracy. The foundation was laid by Harten (1983) and co-workers (Harten et al., 1987) with the essentially non-oscillatory (ENO) schemes, which selected the smoothest stencil to avoid oscillations across discontinuities. Jiang and Shu (1996) generalized this concept into the weighted ENO (WENO) framework, which utilizes a convex combination of all candidate stencils to achieve higher order accuracy in smooth regions while maintaining non-oscillatory behavior near shocks. While the classic WENO scheme proved robust, it was found to be too dissipative for direct numerical simulations of turbulence. This led to the development of improved variants such as WENO-Z by Borges et al. (2008), which employs a global smoothness indicator to recover the optimal order of accuracy at critical points, thereby significantly reducing numerical dissipation and improving the resolution of shear layers and turbulent eddies.

Despite these improvements, traditional WENO schemes can still struggle to distinguish between high-frequency turbulent fluctuations and actual discontinuities, potentially clipping physical peaks (Pirozzoli, 2011). To address this, Fu et al. (2016) introduced the targeted essentially non-oscillatory (TENO) family of schemes. TENO schemes employ a sharp stencil selection strategy that effectively separates smooth scales from non-smooth discontinuities. By completely excluding high-roughness stencils rather than assigning them small weights, TENO schemes virtually eliminate the background numerical dissipation in smooth regions. This property makes them particularly well-suited for simulating broadband turbulence, where preserving the integrity of the inertial range is paramount.

We have implemented high-order reconstruction schemes, specifically WENO and TENO, within the DHARA framework. In this chapter, we focus on the rigorous validation of these methods against canonical benchmarks to verify their accuracy and stability. We demonstrate that these schemes (up to seventh-order accuracy) significantly minimize numerical dissipation, ensuring the spectral fidelity required to resolve complex flow features in the high-Mach number regime. By integrating these capabilities, we transform DHARA from a specialized convection solver into a versatile platform capable of simulating highly compressible, shock-laden flows, laying the computational groundwork for comprehensive turbulence studies.

Finally, the choice of the numerical flux function is critical for the solver's generality. We employ the Kurganov-Tadmor (KT) semi-discrete central-upwind scheme (Kurganov and Tadmor, 2000; Kurganov and Levy, 2000). Unlike traditional Riemann solvers such as Roe or Harten-Lax-van Leer-Contact (HLLC) that require complex, equation-dependent characteristic decompositions, the KT scheme is *Riemann-solver-free*. It relies solely on the local maximum wave speeds to compute fluxes, combining the simplicity of central schemes with the stability of upwind methods. This makes it highly robust and allows DHARA to easily support diverse physical systems, ranging from ideal hydrodynamics to magnetohydrodynamics (MHD) and moist convection, without rewriting the core flux kernel.

In the following section, we detail the mathematical formulation of the finite volume framework implemented in DHARA, including the specific implementations of these WENO and TENO reconstruction steps. We present these formulations for completeness and to document the specific algorithms used in this work. For a more comprehensive theoretical treatment of Riemann solvers and finite volume methods, the reader is referred to standard texts such as Toro (2009) and LeVeque (2002), as well as the original papers cited above. We begin with the discretization of the general convection-diffusion equation. This general starting point is chosen because the compressible Navier-Stokes equations—which govern the flows of interest in this thesis—constitute a system of hyperbolic conservation laws (in the inviscid limit) augmented by parabolic viscous terms. Consequently, they can be cast exactly into the general conservative form described below.

5.2 Finite volume discretization for convection-diffusion equations

We consider a system of N convection–diffusion equations with source terms in n dimensions, written in conservative form as

$$\frac{\partial \mathbf{q}}{\partial t} + \sum_{\alpha=1}^{n} \frac{\partial \mathbf{F}^{\alpha}}{\partial x_{\alpha}} = \sum_{\alpha=1}^{n} \frac{\partial \mathbf{G}^{\alpha}}{\partial x_{\alpha}} + \mathbf{S}, \tag{5.1}$$

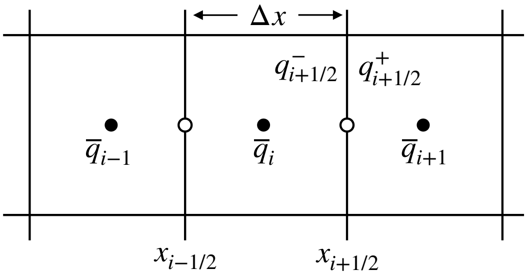

FIGURE 5.1: Schematic of the finite volume discretization on a 1D uniform grid.

where $\mathbf{q}(\mathbf{x}, t)$ is a column vector containing N conserved variables, and the index $\alpha = 1, 2, \ldots, n$ denotes the spatial directions (e.g., x, y, z in 3D). Here, $\mathbf{F}^\alpha(\mathbf{q})$ represents the nonlinear convection flux in the α-direction, $\mathbf{G}^\alpha(\mathbf{q}, \partial_\alpha \mathbf{q})$ is the corresponding dissipation flux, and $\mathbf{S}(\mathbf{q}, \mathbf{x}, t)$ is a general source term. This general formulation directly encapsulates the governing equations for compressible convection presented in Chapter 1 (see Eqs. 1.17-1.19), where the state vector $\mathbf{q}$ corresponds to the conserved density, momentum, and total energy.

For clarity, we illustrate the finite volume discretization in one spatial dimension on a uniform grid (see Fig. 5.1). The conserved variable is denoted by q, with corresponding convective flux F, diffusive flux G, and source term S. Integrating the governing equation over the control volume $[x_{i-1/2}, x_{i+1/2}]$ yields the semi-discrete form

$$\frac{\mathrm{d}\overline{q}_i}{\mathrm{d}t} = -\frac{1}{\Delta x}\left(F_{i+1/2} - F_{i-1/2}\right) + \frac{1}{\Delta x}\left(G_{i+1/2} - G_{i-1/2}\right) + \overline{S}_i, \tag{5.2}$$

where $\overline{q}_i$ is the cell-averaged value in cell i, and $\Delta x = x_{i+1/2} - x_{i-1/2}$ is the cell width. To advance the solution in time, we require the values of the fluxes at the cell interfaces, namely $F_{i\pm 1/2}$ and $G_{i\pm 1/2}$. These interface fluxes are not directly known, since the finite volume method evolves only the cell-averaged quantities $\overline{q}_i$. Therefore, we must reconstruct pointwise values of the solution near the interfaces using the surrounding cell averages. This step is referred to as *reconstruction*, and its accuracy and stability are crucial to the overall scheme.

A critical step in the finite volume method is the reconstruction of the solution at the cell interfaces. Since the solution within each cell is represented only by its volume average $\overline{q}_i$, the value at the interface $x_{i+1/2}$ is discontinuous. We therefore reconstruct two distinct values at each interface: the left-biased state, denoted as $q^-_{i+1/2}$, which is extrapolated from the cell center x_i towards the right boundary of the cell, and the right-biased state, denoted as $q^+_{i+1/2}$, which is extrapolated from the neighboring cell center x_{i+1} towards its left boundary. In a smooth flow, the difference $q^+_{i+1/2} - q^-_{i+1/2}$ is on the order of the grid spacing, but near shocks or discontinuities, this jump becomes significant. These reconstructed states serve as inputs to the numerical flux function, $F_{i+1/2} = \mathcal{F}(q^-_{i+1/2}, q^+_{i+1/2})$, which typically employs a Riemann solver or a central scheme to resolve the jump and compute the stable convective flux across the interface. Similarly, the diffusive flux $G_{i+1/2}$ is evaluated by approximating the gradients at the interface using these reconstructed values.

In higher dimensions, the governing equation (5.1) is discretized in each spatial direction separately. For example, in two dimensions, the semi-discrete form becomes

$$\frac{\mathrm{d}\overline{q}_{i,j}}{\mathrm{d}t} = -\frac{1}{\Delta x}\left(F^x_{i+1/2,j} - F^x_{i-1/2,j}\right) - \frac{1}{\Delta y}\left(F^y_{i,j+1/2} - F^y_{i,j-1/2}\right) \tag{5.3}$$

$$+\frac{1}{\Delta x}\left(G^x_{i+1/2,j} - G^x_{i-1/2,j}\right) + \frac{1}{\Delta y}\left(G^y_{i,j+1/2} - G^y_{i,j-1/2}\right) + \overline{S}_{i,j}. \tag{5.4}$$

Here, the interface fluxes $F^{x,y}_{i\pm1/2,j}$ and $F^{x,y}_{i,j\pm1/2}$ again require reconstruction in the x and y directions respectively. The method readily extends to three or more spatial dimensions in a dimension-by-dimension fashion, provided the coordinate directions are orthogonal and the grid is structured.

5.2.1 Kurganov and Tadmor semi-discrete scheme

To compute the convective fluxes $F_{i\pm1/2}$ in Eq. (5.2), we adopt the central-upwind semi-discrete scheme of Kurganov and Tadmor (2000). This method combines high-resolution interface reconstruction with local wave speed estimates to evolve the solution in a conservative and stable manner.

Given reconstructed left and right states $q^-_{i+1/2}$ and $q^+_{i+1/2}$ at interface $x_{i+1/2}$, the numerical flux is defined as:

$$F_{i+1/2} = \frac{1}{2}\left[F(q^-_{i+1/2}) + F(q^+_{i+1/2})\right] - \frac{a_{i+1/2}}{2}\left(q^+_{i+1/2} - q^-_{i+1/2}\right), \tag{5.5}$$

where $a_{i+1/2}$ is the local maximum wave speed at the interface, computed as

$$a_{i+1/2} = \max\left(|\lambda_{\max}(q^-_{i+1/2})|,\ |\lambda_{\max}(q^+_{i+1/2})|\right). \tag{5.6}$$

Here, $\lambda_{\max}(q)$ denotes the largest eigenvalue in magnitude of the Jacobian $\partial F/\partial q$ evaluated at the reconstructed state q. The first term in Eq. (5.5) provides a centered average of the fluxes, while the second term introduces dissipation proportional to the jump across the interface and the local signal speed.

The diffusive flux $G_{i+1/2}$ in Eq. (5.2) is computed using centered differences or higher-order approximations of $\partial_\alpha q$, which can also be constructed using reconstructed interface values. In multiple dimensions, the KT flux is applied in each direction separately. For example, in 2D, the numerical convective fluxes are computed as

$$F^x_{i+1/2,j} = \frac{1}{2}\left[F^x(q^-_{i+1/2,j}) + F^x(q^+_{i+1/2,j})\right] - \frac{a^x_{i+1/2,j}}{2}\left(q^+_{i+1/2,j} - q^-_{i+1/2,j}\right), \tag{5.7}$$

$$F^y_{i,j+1/2} = \frac{1}{2}\left[F^y(q^-_{i,j+1/2}) + F^y(q^+_{i,j+1/2})\right] - \frac{a^y_{i,j+1/2}}{2}\left(q^+_{i,j+1/2} - q^-_{i,j+1/2}\right), \tag{5.8}$$

where $q^\pm_{i+1/2,j}$ are the reconstructed left and right states at the x-interface $x_{i+1/2}$, $q^\pm_{i,j+1/2}$ are the reconstructed bottom and top states at the y-interface $y_{j+1/2}$, and $a^x_{i+1/2,j}$ and $a^y_{i,j+1/2}$ are the local maximum propagation speeds in x and y directions respectively. These expressions for F^x and F^y are substituted into Eq. (5.4) to evolve the solution in time.

We use the explicit third-order strong stability-preserving Runge–Kutta scheme (eSSPRK3) to evolve the semi-discrete system in time (Gottlieb et al., 2001). This scheme maintains stability for hyperbolic conservation laws and is widely used in combination with high-resolution finite volume methods like the Kurganov–Tadmor scheme. Given the semi-discrete update equation

$$\frac{\mathrm{d}\overline{q}_i}{\mathrm{d}t} = \mathcal{L}(\overline{q}_i), \tag{5.9}$$

where $\mathcal{L}(\cdot)$ represents the spatial operator (e.g., from Eq. (5.2) or (5.4)), the eSSPRK3 scheme advances the solution from time t^n to t^{n+1} as

$$\overline{q}_i^{(1)} = \overline{q}_i^n + \Delta t\mathcal{L}(\overline{q}_i^n), \quad \overline{q}_i^{(2)} = \frac{3}{4}\overline{q}_i^n + \frac{1}{4}\left(\overline{q}_i^{(1)} + \Delta t\mathcal{L}(\overline{q}_i^{(1)})\right), \tag{5.10}$$

$$\overline{q}_i^{n+1} = \frac{1}{3}\overline{q}_i^n + \frac{2}{3}\left(\overline{q}_i^{(2)} + \Delta t\mathcal{L}(\overline{q}_i^{(2)})\right). \tag{5.11}$$

This scheme achieves third-order accuracy in time while preserving strong stability, provided the time step Δt satisfies a suitable CFL (Courant–Friedrichs–Lewy) condition. Specifically, the time step is computed as

$$\Delta t = C_0 \min\left(\frac{\Delta x}{\max(|\Lambda_x|)}, \frac{\Delta y}{\max(|\Lambda_y|)}\right), \tag{5.12}$$

where $\max(|\Lambda_x|)$ and $\max(|\Lambda_x|)$ represent the maximum absolute values of the characteristic wave speeds in the x and y directions, respectively, over the entire computational domain at a given time. The constant $C_0 \leq 1$ is a user-defined CFL number that ensures numerical stability. In this study, we set $C_0 = 0.5$ for all simulations.

In the original Kurganov–Tadmor scheme, a linear reconstruction of cell-averaged $\overline{q}_i$ is used to calculate the left and right states at the $x_{i+1/2}$ interface as

$$q^-_{i+1/2} = \overline{q}_i + \frac{1}{2}\phi_i, \qquad q^+_{i+1/2} = \overline{q}_{i+1} - \frac{1}{2}\phi_{i+1}, \tag{5.13}$$

where ϕ_i is the limited slope in cell i, constructed from the left and right differences:

$$\phi_L = \overline{q}_i - \overline{q}_{i-1}, \qquad \phi_R = \overline{q}_{i+1} - \overline{q}_i. \tag{5.14}$$

Several slope limiters can be employed to control spurious oscillations near discontinuities, such as Minmod, Superbee, and Van Leer. In this work, we use the Van Albada limiter to define the slope

$$\phi_i = \mathcal{V}(\phi_L, \phi_R) = \frac{\phi_L \phi_R\,(\phi_L + \phi_R)}{\phi_L^2 + \phi_R^2 + \varepsilon}, \tag{5.15}$$

where $\varepsilon \ll 1$ is a small parameter (e.g., 10^{-20}) added to avoid division by zero. This reconstruction yields second-order accuracy in smooth regions while ensuring total variation diminishing (TVD) properties in the presence of sharp gradients or discontinuities.

To achieve higher spatial accuracy, the Kurganov–Tadmor scheme can be extended by employing high-order nonlinear reconstruction methods. We describe several such schemes in the next subsection.

5.2.2 High-order reconstructions

To achieve high-order spatial accuracy, we tested several nonlinear reconstruction schemes that are widely used in the literature, including *Weighted Essentially Non-Oscillatory* (WENO) (Jiang and Shu, 1996; Borges et al., 2008), *Central WENO* (CWENO) (Levy et al., 2000; Kurganov and Levy, 2000) and *Targeted Essentially Non-Oscillatory* (TENO) (Fu et al., 2016) schemes. We describe several such schemes below.

5.2.2.1 CWENO reconstruction

We construct a third-order accurate central weighted essentially nonoscillatory (CWENO) reconstruction, as proposed by (Levy et al., 2000), by building a single quadratic polynomial in each cell. This polynomial is formed as a nonlinear convex combination of two one-sided linear polynomials and one centered quadratic polynomial, using only the local cell averages. The left reconstructed state evaluated at $x_{i+1/2}$ is given by

$$q^-_{i+1/2} = A_i + \frac{\Delta x}{2} B_i + \frac{(\Delta x)^2}{8} C_i, \tag{5.16}$$

where A_i, B_i, and C_i are the coefficients of the combined quadratic polynomial reconstructed in cell i

$$A_i = \overline{q}_i - \frac{\omega_c}{12}(\overline{q}_{i+1} - 2\overline{q}_i + \overline{q}_{i-1}), \tag{5.17}$$

$$B_i = \frac{1}{\Delta x}\left[\omega_R(\overline{q}_{i+1} - \overline{q}_i) + \omega_C \frac{(\overline{q}_{i+1} - \overline{q}_{i-1})}{2} + \omega_L(\overline{q}_i - \overline{q}_{i-1})\right], \tag{5.18}$$

$$C_i = 2\omega_C \frac{(\overline{q}_{i+1} - 2\overline{q}_i + \overline{q}_{i-1})}{\Delta x^2}. \tag{5.19}$$

The nonlinear weights ω_k are computed as:

$$\omega_k = \frac{\alpha_k}{\sum_j \alpha_j}, \quad \text{where} \quad \alpha_k = \frac{c_k}{(\varepsilon + \beta_k)^2}, \tag{5.20}$$

with linear weights $c_L = c_R = 1/4$, $c_C = 1/2$ and a small parameter $\varepsilon = 10^{-6}$ used to avoid division by zero. The smoothness indicators β_k are

$$\beta_L = (\overline{q}_i - \overline{q}_{i-1})^2, \tag{5.21}$$

$$\beta_R = (\overline{q}_{i+1} - \overline{q}_{i-1})^2, \tag{5.22}$$

$$\beta_C = \frac{13}{3}(\overline{q}_{i+1} - 2\overline{q}_i + \overline{q}_{i-1})^2 + \frac{1}{4}(\overline{q}_{i+1} - \overline{q}_{i-1})^2. \tag{5.23}$$

5.2.2.2 WENO-Z reconstruction

To achieve high-order accuracy near discontinuities while maintaining non-oscillatory behavior, we employ the weighted essentially non-oscillatory (WENO-Z) reconstruction schemes proposed by (Borges et al., 2008). These schemes improve upon the classical WENO method by incorporating a global smoothness indicator that recovers the optimal order of accuracy at critical points (Jiang and Shu, 1996).

For the fifth-order accurate WENO5-Z reconstruction, the left state at the interface $x_{i+1/2}$ is computed as a nonlinear convex combination of three third-order polynomials

$$P_0 = \frac{1}{3}\overline{q}_{i-2} - \frac{7}{6}\overline{q}_{i-1} + \frac{11}{6}\overline{q}_i, \tag{5.24}$$

$$P_1 = -\frac{1}{6}\overline{q}_{i-1} + \frac{5}{6}\overline{q}_i + \frac{1}{3}\overline{q}_{i+1}, \tag{5.25}$$

$$P_2 = \frac{1}{3}\overline{q}_i + \frac{5}{6}\overline{q}_{i+1} - \frac{1}{6}\overline{q}_{i+2}. \tag{5.26}$$

The final reconstructed value is given by

$$q_{i+1/2}^{-} = \omega_0 P_0 + \omega_1 P_1 + \omega_2 P_2, \tag{5.27}$$

where the nonlinear weights ω_k are defined as

$$\omega_k = \frac{\alpha_k}{\sum_j \alpha_j}, \quad \alpha_k = c_k\left(1 + \frac{\tau_5}{\beta_k + \varepsilon}\right). \tag{5.28}$$

Here, the optimal linear weights are $c_0 = 0.1, c_1 = 0.6, c_2 = 0.3$, and we set $\varepsilon = 10^{-40}$ to avoid division by zero. The smoothness indicators β_k are given by

$$\beta_0 = \frac{13}{12}(\overline{q}_{i-2} - 2\overline{q}_{i-1} + \overline{q}_i)^2 + \frac{1}{4}(\overline{q}_{i-2} - 4\overline{q}_{i-1} + 3\overline{q}_i)^2, \tag{5.29}$$

$$\beta_1 = \frac{13}{12}(\overline{q}_{i-1} - 2\overline{q}_i + \overline{q}_{i+1})^2 + \frac{1}{4}(\overline{q}_{i-1} - \overline{q}_{i+1})^2, \tag{5.30}$$

$$\beta_2 = \frac{13}{12}(\overline{q}_i - 2\overline{q}_{i+1} + \overline{q}_{i+2})^2 + \frac{1}{4}(3\overline{q}_i - 4\overline{q}_{i+1} + \overline{q}_{i+2})^2. \tag{5.31}$$

A key feature of the WENO-Z formulation is the global smoothness indicator, $\tau_5 = |\beta_0 - \beta_2|$, which enhances accuracy near smooth extrema by measuring the difference between the smoothest and roughest stencils.

For simulations requiring even higher spectral resolution, we extend this formulation to the seventh-order WENO7-Z scheme. This reconstruction utilizes four candidate polynomials ($P_k, k = 0, 1, 2, 3$) defined over five-point stencils. The nonlinear weights are computed analogously using the optimal linear weights $c = [1/35, 12/35, 18/35, 4/35]$ and a higher-order global smoothness indicator $\tau_7 = |\beta_0 - \beta_3|$. This allows WENO7-Z to achieve sharper resolution of small-scale turbulent structures compared to its fifth-order counterpart.

5.2.2.3 TENO reconstruction

The TENO (targeted essentially nonoscillatory) scheme uses the same candidate polynomials $P_k(x_{i+1/2})$ and smoothness indicators β_k as in WENO5-Z and WENO7-Z. However, instead of directly using nonlinear weights for reconstruction, TENO employs a sharp stencil selection strategy (Fu et al., 2016). The preliminary nonlinear weights ω_k are computed similarly to WENO-Z. Then, a cutoff function is applied

$$\tilde{\omega}_k = \begin{cases} 1, & \omega_k \geq C_T, \\ 0, & \text{otherwise}, \end{cases} \tag{5.32}$$

where $C_T = 10^{-7}$ in this study. Only stencils with $\tilde{\omega}_k = 1$ are used in the final reconstruction, which ensures optimal order in smooth regions and avoids contributions from nonsmooth stencils near discontinuities.

With the mathematical formulation of these high-order schemes established, we now turn to their practical implementation within our computational framework.

5.3 DHARA architecture and implementation

The numerical algorithms described in this chapter are implemented within DHARA, the high-performance fluid solver framework introduced in § 2.4. While the initial application focused on compressible convection using MacCormack-TVD scheme, DHARA has been architected as a highly modular, general-purpose fluid solver. Its object-oriented design allows for the seamless integration of distinct discretization strategies—in this case, the shock-capturing finite volume schemes required for supersonic turbulence—while retaining the underlying infrastructure for parallelization, memory management, and I/O.

As detailed previously, the solver leverages the Python ecosystem for flexibility, utilizing `NumPy` for CPU-based operations and `CuPy` for GPU acceleration. This dual-backend approach ensures that the same high-level Python code executes efficiently across diverse hardware architectures. For the computationally intensive finite volume reconstruction steps (e.g., WENO/TENO) and flux computations, we employ custom `CuPy ElementwiseKernel` functions to fuse operations and maximize memory throughput on NVIDIA and AMD GPUs.

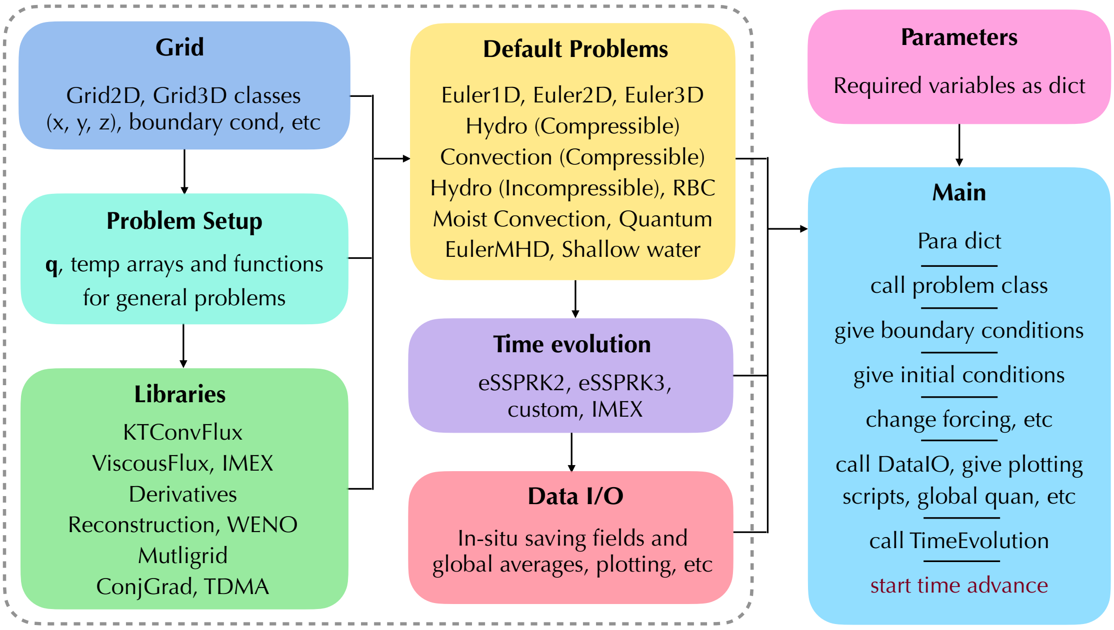

FIGURE 5.2: Schematic of the modular architecture of DHARA, illustrating the abstraction of physical models and numerical schemes.

The architecture is organized into distinct modular blocks, as illustrated in Fig. 5.2. This separation of concerns allows for the seamless integration of different physical models and numerical schemes. The primary components are:

- **Parameters:** This block acts as the central configuration hub. It manages the simulation parameters via dictionaries, ensuring that all required variables are defined and accessible.
- **Grid:** Manages the discretization of the spatial domain and boundary conditions. It encapsulates classes for various spatial dimensions (`Grid1D`, `Grid2D`, `Grid3D`), storing mesh properties such as cell centers (x, y, z), interface locations, and metric terms. It handles a variety of boundary conditions, including periodic, Dirichlet, and Neumann, which can be applied selectively to different domain boundaries.
- **Default Problems (Physics Modules):** This block defines the specific physics being simulated. It contains specialized classes for a wide range of physical systems, including:
  - **Fluid Dynamics:** `Euler` (1D/2D/3D), `Hydro` (Compressible/Incompressible), `Convection` (Compressible), `RBC` (Rayleigh-Bénard Convection) and `Shallow Water` equations.

  - **Complex Physics:** `MHD` (Magnetohydrodynamics), `Moist Convection` (Compressible) and `Quantum` (Gross–Pitaevskii equation).

  For the current study, we utilize the compressible `Euler` and `Hydro` modules, which leverage generic setup utilities to initialize flow fields and forcing terms.

- **Libraries (Numerical Kernel):** This core block contains the implementation of the spatial discretization operators and linear solvers. It provides the fundamental building blocks for the simulations:
  - **Fluxes & Derivatives:** Implements the Kurganov-Tadmor central-upwind scheme (`KTConvFlux`), viscous flux computations (`ViscousFlux`), and standard high-order derivative operators.
  - **Reconstruction:** Classes for high-order spatial reconstruction, including `WENO5Z`, `WENO7Z`, and `TENO` schemes.
  - **Solvers:** Optimized iterative solvers for implicit operations, including `Multigrid`, `ConjGrad` (Conjugate Gradient), and `TDMA` (Tri-Diagonal Matrix Algorithm).

- **Time Evolution:** Manages the temporal integration of the system. It supports a variety of schemes, including explicit Strong Stability Preserving Runge–Kutta methods (`eSSPRK2`, `eSSPRK3`), as well as Implicit-Explicit (`IMEX`) schemes for stiff problems.

- **Data I/O:** Handles the simulation output, capable of performing in-situ saving of 3D fields, computing global averages on the fly, and generating visualization-ready data.

- **Main Driver:** The `Main` block orchestrates the entire workflow. It instantiates the specific problem class, applies the initial and boundary conditions, configures forcing terms, and initializes the `Data I/O` system. Finally, it calls the `Time Evolution` module to advance the simulation.

To run a specific simulation, such as forced compressible turbulence, the `Hydro3D` class is initialized with a dictionary of input parameters. The user then specifies the requisite boundary and initial conditions, along with any external forcing terms, within the problem setup. The Main driver subsequently coordinates the interaction between the Grid, Libraries, and Time Evolution modules to execute the simulation, ensuring efficient resource utilization on the target hardware.

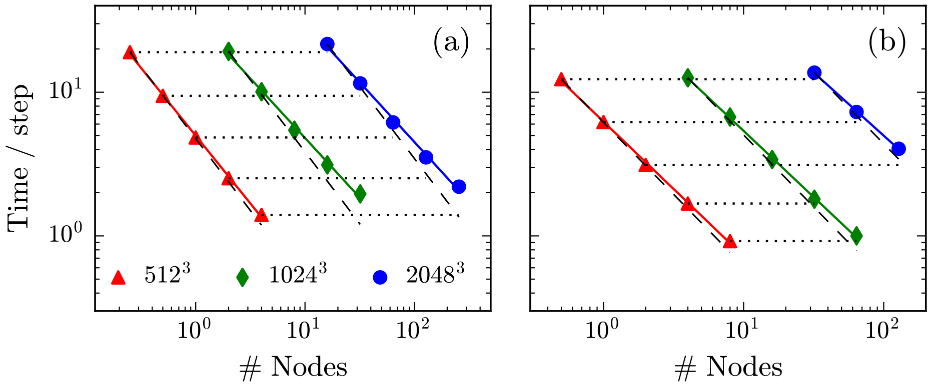

FIGURE 5.3: Scalability of DHARA on GPUs of (a) Frontier and (b) Polaris for 3D decaying compressible turbulence using TENO7 reconstruction. The figure shows the time taken per timestep vs. the number of nodes, demonstrating strong and weak scaling.

5.3.1 Computational performance

To verify that the finite volume implementation maintains the high scalability observed in our earlier finite-difference benchmarks (see Section 2.5), we performed a scaling analysis on two leadership-class systems: Frontier (OLCF) and Polaris (ALCF).

On both Frontier and Polaris, we conducted scaling tests for 3D decaying compressible turbulence using the TENO7 reconstruction scheme. The grid size was varied from 512^3 to 2048^3, with the number of nodes increased from 1 to 256 on Frontier and from 1 to 128 on Polaris. Figure 5.3(a, b) shows the average time per timestep as a function of the number of nodes on Frontier and Polaris, respectively. The reported time is averaged over several timesteps. We observe that the time taken $t \propto n^{-1}$, where n is the number of nodes, thus indicating strong scaling for DHARA in both systems. In addition, the code shows good weak scaling because the time taken remains unchanged when the grid size and number of nodes are increased proportionally. This demonstrates that DHARA achieves high scalability and efficient utilization of GPU resources across diverse architectures.

Beyond scalability, we also characterize the computational cost associated with each reconstruction scheme to guide the choice of method for large-scale production runs. Table 5.1 presents the wall-clock time per timestep for a 128^3 simulation of 3D deccaying compressible turbulence, executed on a single NVIDIA A100 GPU on Polaris. The parameters for this benchmark were $\mathrm{Re} = 10^3$, $M_0 = 0.5$, $\gamma = 1.4$, and $\mathrm{Pr} = 0.7$. The MacCormack-TVD scheme, which is a finite difference method with a compact stencil, serves as a baseline for comparison and is evidently the most computationally efficient. For the finite volume implementations, time integration was performed using the second-order explicit Strong

TABLE 5.1: Computational cost per timestep for various reconstruction schemes on a single NVIDIA A100 GPU (Polaris). The benchmark simulation corresponds to 3D decaying compressible turbulence at 128^3 resolution, with $\mathrm{Re} = 10^3, M_0 = 0.5, \gamma = 1.4$, and $\mathrm{Pr} = 0.7$.

Scheme	**Time per timestep (s)**
MacCormack-TVD (Finite Difference)	0.072
Linear	0.082
CWENO3-Z	0.14
WENO5-Z	0.20
TENO5	0.24
WENO7-Z	0.34
TENO7	0.39

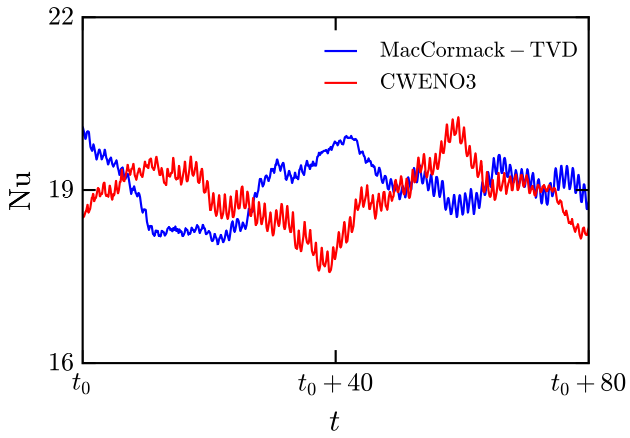

FIGURE 5.4: Temporal evolution of Nu using the MacCormack-TVD scheme (blue) and CWENO3 scheme (red) at $\mathrm{Ra} = 10^9$ and $\mathrm{Pr} = 0.1$ for 2D convection. Both schemes yield similar results, validating the consistency of the solvers.

Stability Preserving Runge-Kutta (eSSPRK2) method. While the simple linear reconstruction scheme (0.082 s) incurs only a marginal overhead compared to the baseline, the cost rises significantly for the high-order shock-capturing schemes. This increase is primarily driven by the computationally intensive characteristic decomposition and the calculation of complex nonlinear smoothness indicators required for the reconstruction step. Consequently, the robust TENO7 scheme (0.39 s) is approximately 5.4× more expensive than the MacCormack-TVD baseline. However, despite this substantial computational premium, the advanced TENO7 scheme is indispensable for the supersonic flows discussed later in this chapter, where its superior spectral resolution and stability are critical for resolving shock structures.

5.3.2 Consistency check: MacCormack-TVD vs. CWENO3

We perform a direct comparison between the finite difference MacCormack-TVD scheme used in the earlier chapters and the finite volume CWENO3 scheme to verify the consistency of our results for compressible convection. Figure 5.4 shows the temporal evolution of the Nusselt number, Nu, computed using both schemes for 2D convection at $\mathrm{Ra} = 10^9$ and $\mathrm{Pr} = 0.1$. The time-averaged values are $\mathrm{Nu} = 19.69 \pm 0.75$ for the MacCormack–TVD scheme and $\mathrm{Nu} = 18.95 \pm 0.51$ for the CWENO3 scheme. These results demonstrate quantitative agreement between the two methods, confirming that global quantities like Nu reported in the main text are robust and independent of the specific numerical discretization.

Having established the baseline consistency of the finite volume framework for compressible convection in subsonic regime ($M_t < 1$), we now proceed to validate the high-order reconstruction algorithms necessary for shock-dominated regimes. The following section details the performance of these schemes across a suite of canonical compressible flow benchmarks.

5.4 Comparison of reconstruction schemes

To assess the performance of the different reconstruction schemes implemented in our compressible fluid solver, DHARA, we performed several benchmark studies, including the well-known isentropic vortex, Kelvin-Helmholtz instability, and supersonic Taylor-Green vortex (TGV).

5.4.1 Isentropic Vortex

We consider the well-known isentropic vortex problem in two dimensions (Nonomura et al., 2010; Song et al., 2024), a standard benchmark for assessing the accuracy and dissipation characteristics of numerical schemes solving the two-dimensional Euler equations.

The governing equations are the two-dimensional compressible Euler equations in conservative form

$$\partial_t \mathbf{q} + \partial_x \mathbf{F}^x(\mathbf{q}) + \partial_y \mathbf{F}^y(\mathbf{q}) = \mathbf{0}, \tag{5.33}$$

where the conserved variable vector $\mathbf{q}$ and the inviscid fluxes in the x- and y-directions, $\mathbf{F}^x$ and $\mathbf{F}^y$, are given by

$$\mathbf{q} = \begin{bmatrix} \rho \\ \rho u_x \\ \rho u_y \\ E_T \end{bmatrix}, \quad \mathbf{F}^x(\mathbf{q}) = \begin{bmatrix} \rho u_x \\ \rho u_x^2 + p \\ \rho u_x u_y \\ u_x(E_T + p) \end{bmatrix}, \quad \mathbf{F}^y(\mathbf{q}) = \begin{bmatrix} \rho u_y \\ \rho u_x u_y \\ \rho u_y^2 + p \\ u_y(E_T + p) \end{bmatrix}. \tag{5.34}$$

Here, ρ is the density, u_x and u_y are the velocity components in the x- and y-directions, p is the pressure, and the total energy density is given by

$$E_T = \frac{p}{\gamma - 1} + \frac{1}{2}\rho(u_x^2 + u_y^2), \tag{5.35}$$

where γ is the adiabatic index. The diffusive flux vector $\mathbf{G}^\alpha$ vanishes for the Euler equations, i.e., $\mathbf{G}^\alpha = \mathbf{0}$.

We perform the isentropic vortex test for $\gamma = 1.4$ on a square domain $x, y \in [-6, 6]$, with periodic boundary conditions in both directions. The initial conditions are given by

$$\rho(x, y, t = 0) = \left[1 - \frac{\epsilon^2(\gamma - 1)}{4\alpha} \exp\left(2\xi(1 - x^2 - y^2)\right)\right]^{\frac{1}{\gamma - 1}}, \tag{5.36}$$

$$p(x, y, t = 0) = \frac{1}{\gamma}\rho^\gamma, \tag{5.37}$$

$$u_x(x, y, t = 0) = V_0 + \epsilon y \exp\left(\xi(1 - x^2 - y^2)\right), \tag{5.38}$$

$$u_y(x, y, t = 0) = -\epsilon x \exp\left(\xi(1 - x^2 - y^2)\right), \tag{5.39}$$

where ϵ denotes the vortex strength, ξ controls the vortex width, and V_0 is the uniform background flow in the x-direction. In this setup, the vortex is convected at a constant velocity $V_0 = 0.5$, and due to the periodic domain, it returns to its original position at time $t = 24$. This makes the test particularly suitable for verifying a scheme's ability to preserve smooth vortex structures over long times without introducing artificial diffusion.

We consider two cases with different vortex widths: $\xi = 0.204$ and $\xi = 1.2$, while fixing the perturbation amplitude to $\epsilon = 0.3$ in both cases. The former corresponds to a broad and smooth vortex, whereas the latter results in a sharper, more compact structure that is more susceptible to numerical diffusion. We compare the performance of several high-order reconstruction schemes on a coarse 32^2 grid. These comparisons are shown in Fig. 5.5, where we plot the normalized pressure error along the x-axis at $y = 0$ for both

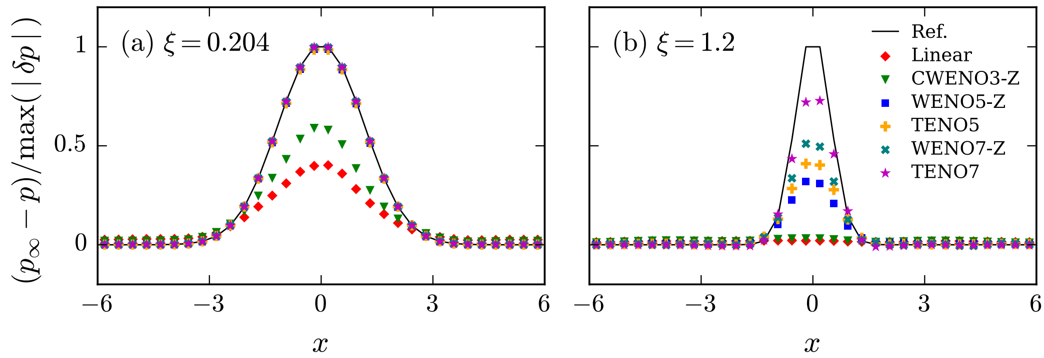

FIGURE 5.5: Normalized pressure error along the x-axis at $y = 0$ for the isentropic vortex test at $t = 24$. Results are shown for (a) a broad vortex with $\xi = 0.204$ and (b) a sharp vortex with $\xi = 1.2$.

vortex configurations. For the broad vortex ($\xi = 0.204$), the higher-order reconstructions–WENO5-Z, TENO5, WENO7-Z, and TENO7–capture the vortex well, while Linear and CWENO3-Z reconstruction introduce large diffusion. For the sharp vortex ($\xi = 1.2$), all schemes show noticeable diffusion, but TENO7 yields the least dissipative result.

5.4.2 Kelvin-Helmholtz Instability

We solve the two-dimensional compressible Euler equations to study the classical Kelvin-Helmholtz (KH) instability (Zhou, 2024). The initial condition consists of a shear layer in the horizontal velocity field and a small perturbation in the vertical velocity to trigger instability. The flow is initialized as follows

$$\rho(x, y, t = 0) = \begin{cases} 1 & \text{if } |y| > 0.25, \\ 2 & \text{if } |y| \leq 0.25, \end{cases} \tag{5.40}$$

$$p(x, y, t = 0) = 2.5, \tag{5.41}$$

$$u_x(x, y, t = 0) = \begin{cases} 0.5 & \text{if } |y| > 0.25, \\ -0.5 & \text{if } |y| \leq 0.25, \end{cases} \tag{5.42}$$

$$u_y(x, y, t = 0) = -\epsilon \sin(2\pi n x), \tag{5.43}$$

with parameters $\gamma = 1.4$, $\epsilon = 0.01$, and $n = 2$. The domain is $[-0.5, 0.5]^2$ with periodic boundary conditions in both directions.

This setup leads to the growth of perturbations at the shear interface ($y = \pm 0.25$), which eventually roll up into characteristic Kelvin-Helmholtz vortices as shown in Fig. 5.6. At

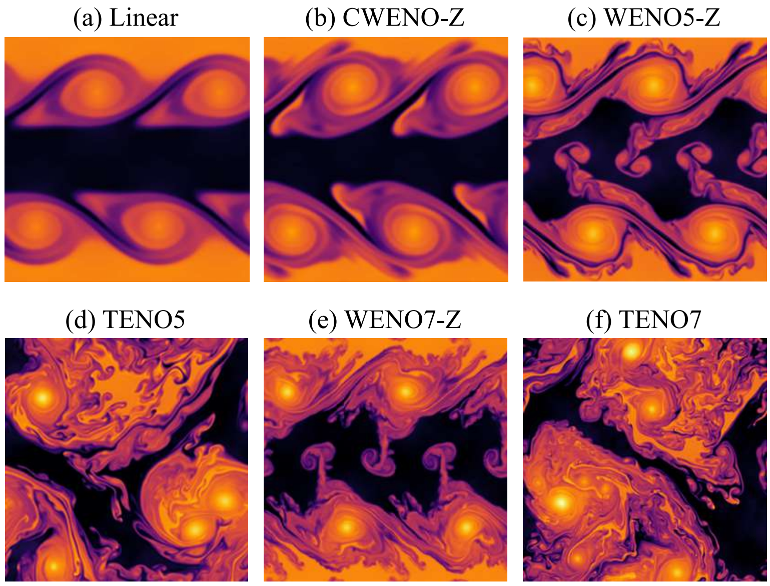

FIGURE 5.6: Density field ρ at $t = 5$ for the Kelvin-Helmholtz instability on a 512^2 grid using different reconstruction schemes. Dark regions indicate heavier fluid, while light regions correspond to lighter fluid.

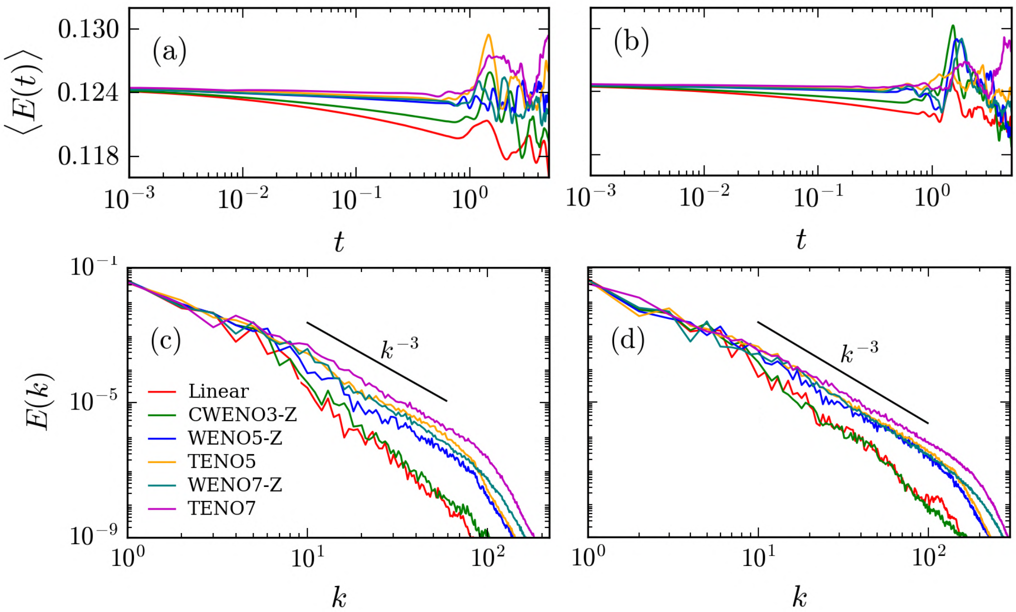

FIGURE 5.7: Kelvin-Helmholtz instability diagnostics. (a), (b): Time evolution of volume-integrated kinetic energy $E(t)$ for resolutions 512^2 and 1024^2, respectively. (c), (d): Velocity power spectrum at $t = 5$ showing $E_k \sim k^{-3}$ scaling for higher-order reconstructions.

time $t = 5$, we compare the density fields obtained using different reconstruction schemes. The higher-order TENO5 and TENO7 schemes clearly capture the roll-up of the shear layer and reveal small-scale vortex structures due to their low numerical dissipation and sharp resolution capabilities. In contrast, the Linear and CWENO3-Z schemes exhibit excessive diffusion, which suppresses the growth of fine-scale features and leads to a smeared interface.

To further quantify the quality of resolution, we analyze the kinetic energy $E = (u_x^2+u_y^2)/2$ evolution and the velocity power spectrum $E_k(k)$ in Fig. 5.7. Subplots (a) and (b) display the time evolution of the volume-averaged kinetic energy for two resolutions: 512^2 and 1024^2, respectively. These are compared with San and Kara (2015). The TENO-based reconstructions retain more kinetic energy over time, indicating lower dissipation compared to Linear and CWENO3-Z schemes. Subplots (c) and (d) show the velocity power spectrum E_k at $t = 5$ for the same grid resolutions. For WENO and TENO schemes, the spectrum follows the characteristic k^{-3} power law from Kraichnan–Batchelor–Leith (KBL) theory (Kraichnan, 1967; Batchelor, 1969; Leith, 1971), demonstrating accurate capturing of turbulent cascade and small-scale dynamics. In contrast, Linear and CWENO3-Z schemes show steep energy decay due to dissipative errors, failing to resolve the correct spectral behavior.

5.4.3 Supersonic Taylor-Green vortex

To validate our compressible Navier–Stokes solver in three dimensions, we simulate the well-known supersonic Taylor–Green vortex (TGV) (Brachet et al., 1983), which serves as a canonical test for studying transition to turbulence, compressibility effects, and dissipation characteristics of high-order schemes in complex flows.

The governing equations are the three-dimensional, non-dimensional compressible Navier–Stokes equations in conservative form (Kida and Orszag, 1990)

$$\partial_t \mathbf{q} + \nabla \cdot \mathbf{F}(\mathbf{q}) = \nabla \cdot \mathbf{G}(\mathbf{q}, \nabla \mathbf{q}), \tag{5.44}$$

where the vector of conserved variables $\mathbf{q}$, inviscid fluxes $\mathbf{F}$, and viscous fluxes $\mathbf{G}$ are defined as

$$\mathbf{q} = \begin{bmatrix} \rho \\ \rho u_x \\ \rho u_y \\ \rho u_z \\ E_T \end{bmatrix}, \quad \mathbf{F}^\alpha = \begin{bmatrix} \rho u_\alpha \\ \rho u_\alpha u_x + \delta_{\alpha x} p \\ \rho u_\alpha u_y + \delta_{\alpha y} p \\ \rho u_\alpha u_z + \delta_{\alpha z} p \\ u_\alpha (E_T + p) \end{bmatrix}, \quad \mathbf{G}^\alpha = \begin{bmatrix} 0 \\ \tau_{\alpha x} \\ \tau_{\alpha y} \\ \tau_{\alpha z} \\ u_j \tau_{\alpha j} + q_\alpha \end{bmatrix}. \tag{5.45}$$

Here, $\alpha \in \{x, y, z\}$ represents the spatial direction, and δ_{ij} is the Kronecker delta. The total energy per unit volume, E_T, is given by

$$E_T = \frac{p}{\gamma - 1} + \frac{1}{2}\rho u_k u_k. \tag{5.46}$$

The viscous stress tensor components, τ_{ij}, are defined for a Newtonian fluid as

$$\tau_{ij} = \mu' \left(\frac{\partial u_i}{\partial x_j} + \frac{\partial u_j}{\partial x_i} \right) - \frac{2}{3}\mu' \left(\nabla \cdot \mathbf{u} \right) \delta_{ij}. \tag{5.47}$$

The conductive heat flux term, q_i, follows Fourier's law

$$q_i = \frac{\mu'}{M_0^2 \mathrm{Pr}(\gamma - 1)} \frac{\partial T}{\partial x_i}, \tag{5.48}$$

where μ' is the non-dimensional viscosity, Pr is the Prandtl number, and M_0 is the reference Mach number. The system is closed with the ideal gas equation of state, $p = \rho T / (\gamma M_0^2)$.

The non-dimensional viscosity $\mu'(T)$ is modeled using *Sutherland's law*:

$$\mu'(T) = \frac{1}{\mathrm{Re}_0} T^{3/2} \frac{1 + S}{T + S}. \tag{5.49}$$

Here, S is the non-dimensional Sutherland constant, defined as the ratio of the Sutherland temperature T_S to the reference temperature T_{ref}. We set $S = 0.9$ following Lusher and Sandham (2021); for air ($T_S \approx 110.4$ K), this value implies a low reference temperature ($T_{\mathrm{ref}} \approx 122$ K), which is characteristic of the high-altitude conditions often encountered in supersonic boundary layer studies.

The initial condition is adapted from the classical incompressible Taylor–Green vortex and extended to the compressible case (Lusher and Sandham, 2021; Chapelier et al., 2024). The domain is $[-\pi, \pi]^3$ with periodic boundary conditions in all directions. The initial

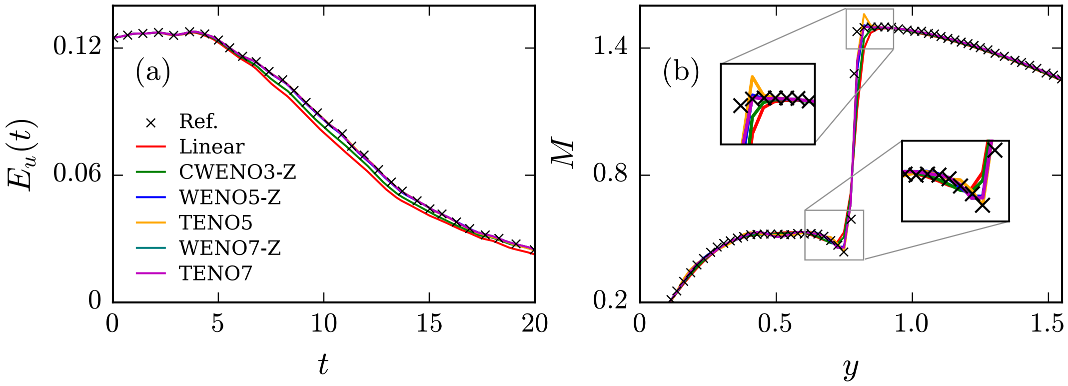

FIGURE 5.8: Case study using supersonic Taylor–Green vortex simulation. (a) Time evolution of the volume-averaged kinetic energy $E_u(t)$ for different reconstruction schemes. (b) Instantaneous Mach number profile M along the y-axis at $x = z = 0$ at time $t = 2.5$. The reference points (Ref.) in both subplots corresponds to a benchmark solution computed at 2048^3 resolution from Chapelier et al. (2024).

velocity, pressure, and density are

$$u_x(x, y, z, t = 0) = \sin(x)\cos(y)\cos(z), \tag{5.50}$$

$$u_y(x, y, z, t = 0) = -\cos(x)\sin(y)\cos(z), \tag{5.51}$$

$$u_z(x, y, z, t = 0) = 0, \tag{5.52}$$

$$p(x, y, z, t = 0) = 1 + \frac{1}{16}\left[\cos(2x) + \cos(2y)\right]\left[2 + \cos(2z)\right], \tag{5.53}$$

$$\rho(x, y, z, t = 0) = 1. \tag{5.54}$$

We consider $M_0 = 1.25$, $\gamma = 1.4$, $\mathrm{Re}_0 = 1600$, $\mathrm{Pr} = 0.71$ and grid size of 256^3 for all runs. We track the time evolution of the volume-averaged kinetic energy E_u, which is plotted in Fig. 5.8 (a) for various reconstruction schemes. In addition, we evaluate the instantaneous Mach number $M(y)$ along the y-axis at $x = z = 0$, which is shown at $t = 2.5$ in Fig. 5.8 (b). The results are compared against the high-resolution 2048^3 reference data provided in Chapelier et al. (2024). The kinetic energy plot for 5^{th} and 7^{th} order WENO and TENO schemes shows good agreement with the reference data. Lower-order schemes, such as Linear and CWENO3-Z show slight differences from the reference data. Further, looking at the Mach number $M(y)$ distribution, we notice the best agreement with the WENO7-Z and TENO7 schemes.

Having validated the accuracy and robustness of the TENO7 scheme against canonical benchmarks, we now proceed to demonstrate its efficacy in a production environment. In the following section, we describe the direct numerical simulation (DNS) of forced compressible turbulence. We outline the numerical setup, including the implementation of the large-scale stochastic forcing, and detail the parameters for a high-resolution (1024^3) simulation in the highly supersonic regime ($M_t = 3.0$), which serves as a capability demonstration for the solver's shock-capturing performance.

5.5 Direct numerical simulations of supersonic turbulence

Supersonic turbulence is of fundamental interest in astrophysics (Carroll, 2006; Elmegreen and Scalo, 2004; Mac Low and Klessen, 2004), space physics, and high-speed aerodynamics (von Kármán, 2003). Prime examples include supernovae explosions, star formation in molecular clouds (Krumholz and McKee, 2005; Padoan and Nordlund, 2011), inertial confinement fusion (Fujisawa, 2021), and hypersonic propulsion (Ingenito and Bruno, 2010). However, despite this significance, the mechanisms of energy transfer in supersonic flows remain poorly understood. Unlike incompressible turbulence, which is dominated by solenoidal eddies and local energy transfer, supersonic flows involve intricate interactions among shocks, acoustic modes, and nonlinear advection. These interactions lead to fundamentally distinct physical behaviors, where the scaling laws of the velocity spectra are significantly altered by the presence of strong density fluctuations and shocklets (Kritsuk et al., 2007; Schmidt et al., 2009; Federrath, 2013).

The structural difference between subsonic and supersonic regimes is profound. In the incompressible limit, the flow is characterized by Kolmogorov's $k^{-5/3}$ spectrum and distinct vortex tubes. However, as the turbulent Mach number (M_t) exceeds unity, compression regions and shocks become the prominent features. The presence of a compressive velocity component and pressure dilatation fundamentally distinguishes the dynamics of compressible turbulence from the incompressible regime (Kida and Orszag, 1990; Sarkar, 1992). Numerical studies suggest that while the solenoidal component may retain Kolmogorov-like scaling, the compressive component steepens towards a k^{-2} scaling, characteristic of Burgers turbulence (Wang et al., 2013; Schmidt and Grete, 2019). Furthermore, the energy transfer pathways become complex, with kinetic energy being exchanged not just between scales, but also between solenoidal and compressive modes, and eventually converted into internal energy through pressure-dilatation work.

To unravel these complex interaction mechanisms, direct numerical simulations (DNS) are indispensable. While large eddy simulations (LES) and lower-order methods like the piecewise parabolic method (PPM) (Colella and Woodward, 1984) have provided valuable insights into scaling laws, they often rely on numerical dissipation or subgrid-scale models that can obscure the fine-scale physics of intermittency and energy transfer. To capture the full range of turbulent scales—from the energy-containing eddies down to the dissipation range—it is necessary to solve the full compressible Navier-Stokes equations with high spatial resolution and high-order, low-dissipation numerical schemes. DNS allows for the precise calculation of inter-scale energy fluxes and mode-to-mode transfers, which are critical for validating theoretical frameworks like those proposed by Aluie (2011) and Singh et al. (2025).

We perform high-resolution DNS of forced supersonic turbulence on a uniform Cartesian grid with 1024^3 collocation points. The computational domain is a cubic box of length 2π with periodic boundary conditions applied in all three spatial directions. We solve the non-dimensional compressible Navier-Stokes equations described in Sec. 5.4.3 (Eqs. 5.44 and 5.45) with an external forcing term included. For these simulations, we assume a constant dynamic viscosity μ, which implies that the non-dimensional viscosity simplifies to $\mu' = 1/\mathrm{Re}_0$, where Re_0 is the reference Reynolds number. To maintain a statistically stationary turbulent state against viscous dissipation, a large-scale external forcing term $\mathbf{F}'$ is added to the momentum and energy equations. The specific formulation of this forcing is detailed below.

5.5.1 External forcing

To sustain the turbulence, we employ a stochastic forcing method based on a generalized Ornstein–Uhlenbeck (OU) process, following the formulation of Schmidt et al. (2009). This approach evolves the forcing field in Fourier space, ensuring that the energy injection is random yet temporally correlated, which mimics realistic astrophysical driving mechanisms. The time evolution of the Fourier-transformed forcing vector $\hat{\mathbf{F}}'(\mathbf{k}, t)$ is governed by the following stochastic differential equation

$$\mathrm{d}\hat{\mathbf{F}}'(\mathbf{k}, t) = g_\zeta \left[\underbrace{-\frac{\hat{\mathbf{F}}(\mathbf{k}, t) U_0}{\sqrt{\pi/2}}\,\mathrm{d}t}_{\text{damping}} + \underbrace{2U_0^2 \left(\frac{2U_0 \sigma^2(\mathbf{k})}{\sqrt{\pi/2}} \right)^{1/2} \mathbf{P}_\zeta(\mathbf{k}) \cdot \mathrm{d}\mathcal{W}_t}_{\text{stochastic injection}} \right]. \tag{5.55}$$

Here, U_0 is the characteristic velocity scale, which serves as a primary control parameter for the forcing amplitude. The term $\mathrm{d}\mathcal{W}_t$ represents a vector-valued Wiener process with zero mean and variance $\mathrm{d}t$. The first term on the right-hand side acts as a linear damping term inversely proportional to the large-eddy turnover time ($\tau \sim L/U_0$), ensuring the forcing field retains memory of its previous state.

The spectral distribution of the injected energy is determined by the profile function $\sigma(k)$, defined as

$$\sigma(k) \propto (k - k_{\text{min}})^2(k_{\text{max}} - k)^2, \tag{5.56}$$

for wavenumbers in the range $k_{\text{min}} \leq k \leq k_{\text{max}}$, and zero otherwise. In our simulations, we set $k_{\text{min}} = 1$ and $k_{\text{max}} = 3$, resulting in peak forcing at $k_0 = 2$. This corresponds to an integral length scale of approximately $\ell \sim \pi$, or half the domain size.

A critical feature of this framework is the ability to control the nature of the driving force—specifically, the ratio of solenoidal (vortical) to compressive (dilatational) modes—via the projection operator $\mathbf{P}_\zeta(\mathbf{k})$. This operator is defined in terms of the projection parameter $\zeta \in [0, 1]$ as

$$\mathbf{P}_{\zeta,ij}(\mathbf{k}) = \underbrace{\zeta\left(\delta_{ij} - \frac{k_i k_j}{k^2}\right)}_{\text{Solenoidal}} + (1-\zeta)\underbrace{\frac{k_i k_j}{k^2}}_{\text{Compressive}}, \tag{5.57}$$

where δ_{ij} is the Kronecker delta. Setting $\zeta = 1$ results in purely solenoidal (divergence-free) forcing, while $\zeta = 0$ yields purely compressive (curl-free) forcing. Finally, to ensure that the total energy injection rate remains consistent regardless of the chosen solenoidal-compressive mix, the amplitude is scaled by the normalization factor g_ζ

$$g_\zeta = \frac{1}{\sqrt{1 - 2\zeta + 3\zeta^2}}. \tag{5.58}$$

5.5.2 Demonstration of solver robustness

To demonstrate the capability of the developed solver in handling extreme compressibility, we present a high-resolution (1024^3) direct numerical simulation of supersonic turbulence. The simulation targets a high turbulent Mach number of $M_t \approx 3.0$, a regime where standard numerical schemes often fail due to the presence of strong shocks and steep gradients.

The simulation is driven by predominantly solenoidal forcing ($\zeta = 2/3$) with a characteristic velocity scale of $U_0 = 0.3$. To resolve the finest scales of the flow, the reference Reynolds number is set to $\text{Re}_0 = 5 \times 10^3$. This configuration yields a statistically stationary state with a Taylor-microscale Reynolds number of $\text{Re}_\lambda \approx 220$. We define Re_λ as

$$\text{Re}_\lambda = \left(\frac{5}{3\langle\mu\rangle\epsilon}\right)^{1/2} \langle\rho\rangle U^2, \tag{5.59}$$

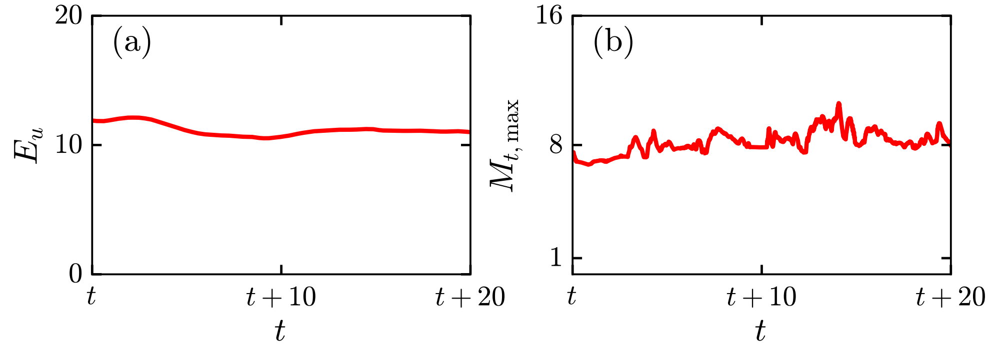

FIGURE 5.9: Time evolution of the (a) total kinetic energy E_u and (b) the maximum local Mach number $M_{t,\max}$ for the $M_t = 3.0$ simulation. The statistics are shown for the stationary regime. Note the strong intermittency in $M_{t,\max}$, reflecting the formation of localized strong shocks.

where $\epsilon = -\langle u_j \partial_j \tau_{ij} \rangle$ is the mean viscous dissipation rate (Jagannathan and Donzis, 2016). To prevent thermal runaway and mimic the efficient radiative cooling of astrophysical environments, the gas is modeled as effectively isothermal with $\gamma = 1.00001$. The simulation is evolved for more than 40 large-eddy turnover times ($t_{\text{eddy}} = l_0/U_0$) to ensure a statistically stationary state. Figure 5.9 presents the time series of the total kinetic energy, E_u, and the maximum local Mach number, $M_{t,\max}$, during the stationary phase. While E_u remains relatively stable, indicating a balance between forcing and dissipation, $M_{t,\max}$ exhibits significant fluctuations, frequently spiking well above the mean. These excursions correspond to intermittent bursts of intense compression and shock formation, characteristic of high-Mach-number turbulence.

To ensure the fidelity of these results, we strictly verify that the grid resolution satisfies the Kolmogorov resolution criterion. The Kolmogorov length scale is defined as

$$\eta = \left(\frac{\langle \mu \rangle^3}{\epsilon \langle \rho \rangle^2} \right)^{1/4}, \tag{5.60}$$

where $\langle \mu \rangle$ and $\langle \rho \rangle$ are the domain-averaged viscosity and density, and ϵ is the mean viscous dissipation rate. For the presented case, we maintain a resolution ratio of $\eta/\Delta x > 1.3$, confirming that both the shock structures and the viscous dissipation range are well-resolved.

Figure 5.10 visualizes the instantaneous flow field for this $M_t = 3.0$ case, offering a qualitative validation of the solver's robustness. This snapshot corresponds to the statistically stationary regime analyzed in Fig. 5.9, where the stability of the total kinetic energy confirms the balance between forcing and dissipation. Concurrently, the large fluctuations

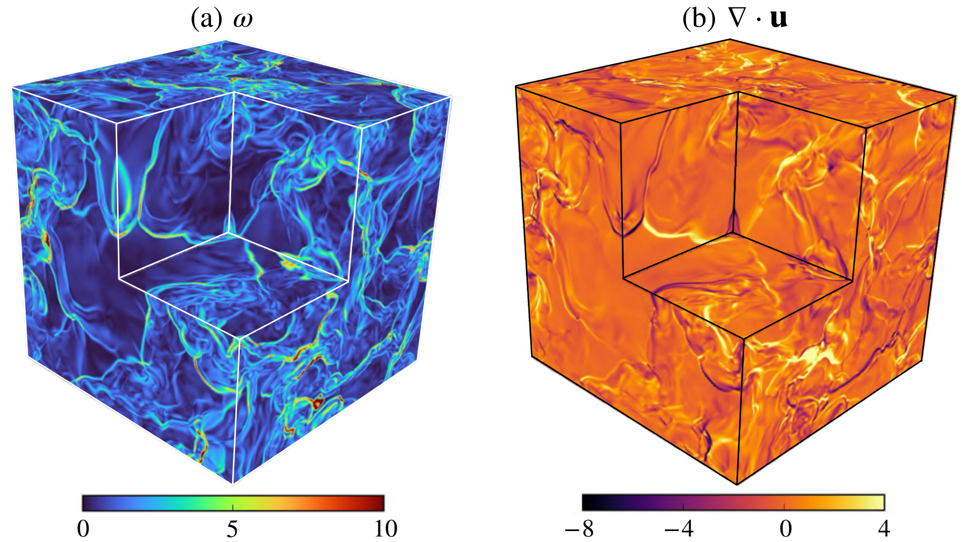

FIGURE 5.10: Instantaneous flow structures in supersonic turbulence ($M_t = 3.0$) during the statistically stationary state. Panel (a) shows the vorticity magnitude, $\omega = |\nabla \times \mathbf{u}|$, revealing intense vortex tubes. Panel (b) shows the velocity divergence, $\nabla \cdot \mathbf{u}$, highlighting the asymmetry between narrow, shock-compressed regions (blue/dark) and broad expansion regions (red/light).

observed in the maximum local Mach number (Fig. 5.9) are spatially manifested here as intermittent bursts of intense compression and localized shock formation.

The structural signature of supersonic turbulence is clearly visible in the velocity divergence field shown in Fig. 5.10(b). A stark asymmetry exists between regions of compression and expansion. The flow is dominated by strong, thin, sheet-like regions of negative divergence, identified as shocklets, where the local Mach number significantly exceeds the mean M_t. These are interspersed with broader, smoother regions of positive divergence or expansion. The TENO7 scheme effectively resolves these sharp discontinuities and captures density jumps of several orders of magnitude within just a few grid cells without introducing spurious numerical oscillations. This precise capture of the shock width is critical as it prevents the artificial smearing of energy that would otherwise contaminate the spectral transfer analysis.

Simultaneously, the vorticity magnitude in Fig. 5.10(a) reveals a complex network of intense, filamentary vortex tubes. Unlike subsonic turbulence, where fine-scale eddies are distributed somewhat uniformly, here we observe a distinct spatial organization where intense vorticity is increasingly concentrated in the vicinity of shock structures. This localization is a physical consequence of baroclinic torque acting at curved shock fronts, which generates vorticity that is subsequently amplified by vortex stretching (Lele, 1994; Federrath, 2013). The ability of the solver to capture this interaction, where solenoidal cascades develop from compressive seeds, demonstrates its suitability for investigating the complex mode-to-mode energy transfers characteristic of the supersonic regime.

5.6 Summary

In this chapter, we have established a robust computational framework designed to address the challenges of simulating compressible turbulence in the supersonic regime. By extending the DHARA solver with a high-order finite volume module, we successfully integrated the Riemann-solver-free Kurganov-Tadmor scheme with advanced reconstruction algorithms, specifically the weighted and targeted essentially non-oscillatory methods. The implementation leverages the modular Python-CuPy architecture to maintain the massive scalability required for leadership-class GPU clusters. Through rigorous validation against canonical benchmarks such as the isentropic vortex and the supersonic Taylor-Green vortex, we demonstrated that the seventh-order TENO scheme significantly minimizes numerical dissipation. This accuracy is essential for resolving fine-scale turbulent structures while simultaneously preventing spurious oscillations near strong discontinuities.

Building on this validation, we presented a high-resolution direct numerical simulation of forced supersonic turbulence at a turbulent Mach number of 3.0. This capability demonstration confirmed the robustness of the solver in handling extreme compressibility and intermittent shock formation. The qualitative analysis of the flow field revealed the complex interplay between shocklets and vorticity, including the generation of solenoidal modes from compressive seeds via baroclinic torque. These results validate the suitability of DHARA for high-fidelity research into astrophysical and high-speed aerodynamic flows. The numerical infrastructure developed here lays the foundation for subsequent investigations into the scaling laws and inter-scale energy transfer mechanisms that govern shock-dominated turbulence.

Chapter 6

Summary and outlook

6.1 Summary

Turbulent thermal convection drives the dynamics of diverse natural systems, ranging from the fluid cores of planets to the outer layers of stars and the Earth's atmosphere. Despite over a century of research into the fundamental model of Rayleigh-Bénard convection (RBC), the asymptotic behavior of heat transport at extreme driving strengths remains a subject of intense debate. A central question in this field, first posed by Kraichnan (1962), is whether the heat transport efficiency, quantified by the Nusselt number (Nu), transitions to an *ultimate regime* ($\mathrm{Nu} \sim \mathrm{Ra}^{1/2}$) at sufficiently high Rayleigh numbers (Ra), or if it remains bounded by the classical scaling ($\mathrm{Nu} \sim \mathrm{Ra}^{1/3}$). This question becomes even more intricate when compressibility is taken into account. While most theoretical and numerical works rely on the Boussinesq approximation, astrophysical and geophysical flows are often characterized by significant density stratification and acoustic waves. Understanding how compressibility alters the scaling laws of turbulence is therefore not just a theoretical curiosity, but a necessity for accurate stellar and planetary modeling.

This thesis endeavors to bridge the gap between these fundamental questions and the complex reality of compressible flows. Tackling the multiscale physics of compressible convection in extreme regimes requires a computational framework that is both robust and highly scalable. To this end, we developed DHARA, a high-performance general fluid solver architected for modern GPU-accelerated supercomputers. By leveraging a Python interface for modular flexibility and the `CuPy` library to execute high-performance computations on GPUs, DHARA allowed us to perform direct numerical simulations (DNS) of compressible convection at unprecedented resolutions, reaching $\mathrm{Ra} = 10^{16}$ in two dimensions and 10^{13} in three dimensions.

Using this framework, we addressed the open question of scaling laws in compressible convection. Although the strong density stratification renders the bulk flow adiabatic and fundamentally different from the isothermal bulk of standard RBC, our simulations revealed a remarkable robustness of the classical scaling. We observed that the Nusselt number follows $\mathrm{Nu} \sim \mathrm{Ra}^{0.30}$ and the Reynolds number scales as $\mathrm{Re} \sim \mathrm{Ra}^{0.50}$ across the entire range of parameters explored. This suggests that the fundamental machinery of thermal convection—specifically the interplay between boundary layers and thermal plumes—remains resilient to compressibility effects, provided the flow remains subsonic.

To provide a mechanistic explanation for the persistence of classical scaling, we conducted a comparative study of vertical heat flux across standard RBC, compressible convection, and periodic convection. By decomposing the vertical heat flux into positive (buoyancy-aligned) and negative (buoyancy-opposing) components, we isolated the impact of confinement. We found that periodic convection, which lacks thermal plates, is dominated by positive heat flux and consequently follows the ultimate scaling $\mathrm{Nu} \sim \mathrm{Ra}^{1/2}$. In stark contrast, the rigid plates in RBC and compressible convection physically deflect energetic plumes, inducing significant negative heat fluxes that compete with the positive transport. Crucially, our analysis revealed that in wall-bounded flows, the positive heat flux decays faster with Ra than the negative flux. This differential decay causes the net asymmetry to diminish as $\mathrm{Ra}^{-0.20}$, which effectively corrects the theoretical ultimate scaling ($\mathrm{Ra}^{1/2}$) down to the observed classical scaling ($\mathrm{Nu} \sim \mathrm{Ra}^{0.30}$). This global cancellation mechanism is so dominant that it suppresses the transition to the ultimate regime even when the local boundary layers appear turbulent; specifically, we observed logarithmic mean temperature and velocity profiles in 2D compressible convection, yet the global heat transport remained strictly confined to the classical scaling law.

Finally, recognizing that natural flows often transcend subsonic limits, we extended the capabilities of DHARA to handle shock-dominated regimes. We implemented high-order finite volume methods, specifically weighted and targeted essentially non-oscillatory (WENO /TENO) schemes, to accurately capture sharp discontinuities while minimizing numerical dissipation. This development transformed the solver from a specialized convection code into a general-purpose tool for high-speed flows, enabling us to perform high-fidelity spectral analyses of compressible turbulence and study inter-modal energy transfers.

6.2 Scope for future work

The work presented in this thesis opens several avenues for future research, ranging from the expansion of the computational framework to fundamental inquiries into the nature of turbulent transport. We outline two primary directions below.

6.2.1 Future studies with DHARA

The modular architecture of DHARA allows for the seamless integration of diverse physical models, enabling us to extend our inquiries beyond classical fluid dynamics. A key area of development is the implementation of a Gross-Pitaevskii equation (GPE) module to simulate quantum turbulence, allowing us to draw parallels between classical vortex dynamics and quantized vortices in superfluids. Furthermore, we aim to bridge the gap between idealized convection and atmospheric science by implementing a moist convection module. By introducing phase changes and latent heat release into a Rayleigh-Bénard-like setup, we can simulate the Earth's troposphere to understand how moisture and compressibility interact to modify the classical dry convection scaling laws. Additionally, we are extending the solver to higher dimensions, specifically four-dimensional (4D) RBC, to rigorously test statistical mechanics predictions regarding transient behaviors and scaling exponents in hyperspace.

On the computational front, we are focusing on further optimizing the core kernels to leverage the full potential of next-generation hardware. This involves rewriting critical compute-intensive routines using optimized CUDA raw kernels to minimize latency and maximize memory throughput. Simultaneously, we are incorporating immersed boundary methods (IBM) to handle complex, non-rectangular geometries. This capability is essential for simulating flow past obstacles or rough boundaries, which is directly relevant to high-performance computing (HPC) applications in engineering.

6.2.2 Unravelling the mechanisms of heat flux scaling

While we have established that wall-induced negative fluxes suppress heat transport, a deeper understanding of the asymptotic behavior requires pushing the simulations to even more extreme regimes. Leveraging the computational efficiency and super-linear scaling of DHARA on the Shaheen III supercomputer (at KAUST), we are currently performing massive-scale simulations of three-dimensional compressible convection reaching Rayleigh numbers up to $\mathrm{Ra} = 10^{15}$. These runs aim to verify whether the decay of the normalized net heat flux continues indefinitely or if a saturation point exists. Concurrently, we are investigating the Prandtl number (Pr) dependence of the positive and negative fluxes. Understanding how the competition between these fluxes varies with fluid properties will be crucial for developing a unified theory of heat transport applicable across diverse regimes.

A critical frontier lies in applying this flux decomposition framework to non-standard convective systems that defy the classical scaling limits. Experimental and numerical evidence suggests that the ultimate regime is accessible in configurations such as internally heated or radiatively driven convection (Bouillaut et al., 2022; Lepot et al., 2018), as well as in flows over rough boundaries (Roche et al., 2001). Similarly, the imposition of strong horizontal shear has been shown to enhance the Nusselt exponent significantly, reaching values up to 0.45 (Pirozzoli et al., 2017; Hamman and Moin, 2023). We hypothesize that these forcing mechanisms fundamentally alter the global flux budget, either by disrupting the recirculation pathways that generate negative flux or by energetically boosting the upward transport of thermal plumes. However, the precise physical mechanism responsible for this preferential enhancement of the positive heat flux remains to be understood. We plan to systematically investigate these regimes in the future.

Bibliography

Ahlers, G., Bodenschatz, E., Funfschilling, D., Grossmann, S., He, X., Lohse, D., Stevens, R. J. A. M., and Verzicco, R. (2012). Logarithmic Temperature Profiles in Turbulent Rayleigh-Bénard Convection. *Phys. Rev. Lett.*, 109(11):114501.

Ahlers, G., Bodenschatz, E., and He, X. (2014). Logarithmic temperature profiles of turbulent Rayleigh–Bénard convection in the classical and ultimate state for a Prandtl number of 0.8. *J. Fluid Mech.*, 758:436–467.

Ahlers, G., Grossmann, S., and Lohse, D. (2009). Heat transfer and large scale dynamics in turbulent Rayleigh-Bénard convection. *Rev. Mod. Phys.*, 81(2):503–537.

Aluie, H. (2011). Compressible turbulence: the cascade and its locality. *Phys. Rev. Lett.*, 106(17):174502.

Anders, E. H. and Brown, B. P. (2017). Convective heat transport in stratified atmospheres at low and high Mach number. *Phys. Rev. Fluids*, 2(8):083501.

Anderson, J. D. (1992). *Computational Fluid Dynamics: An Introduction.* Springer.

Anderson, J. D. (1995). *Computational Fluid Dynamics: The Basics with Applications.* McGraw-Hill, New York.

Balachandar, S., Yuen, D. A., and Reuteler, D. (1993). Viscous and adiabatic heating effects in three-dimensional compressible convection at infinite Prandtl number. *Phys. Fluids A*, 5(11):2938–2945.

Batchelor, G. K. (1953). *The Theory of Homogeneous Turbulence.* Cambridge University Press, Cambridge.

Batchelor, G. K. (1969). Computation of the energy spectrum in homogeneous two-dimensional turbulence. *Phys. Fluids*, 12(12):II–233.

Bercovici, D., Schubert, G., and Glatzmaier, G. A. (1992). Three-dimensional convection of an infinite-Prandtl-number compressible fluid in a basally heated spherical shell. *J. Fluid Mech.*, 239:683–719.

Bhattacharya, S., Verma, M. K., and Bhattacharya, A. (2022). Predictions of Reynolds and Nusselt numbers in turbulent convection using machine-learning models. *Phys. Fluids*, 34(2).

Bhattacharya, S., Verma, M. K., and Samtaney, R. (2021a). Prandtl number dependence of the small-scale properties in turbulent Rayleigh-Bénard convection. *Phys. Rev. Fluids*, 6:063501.

Bhattacharya, S., Verma, M. K., and Samtaney, R. (2021b). Revisiting Reynolds and Nusselt numbers in turbulent thermal convection. *Phys. Fluids*, 33:015113.

Borges, R., Carmona, M., Costa, B., and Don, W. S. (2008). An improved weighted essentially non-oscillatory scheme for hyperbolic conservation laws. *J. Comput. Phys.*, 227(6):3191–3211.

Bouillaut, V., Flesselles, B., Miquel, B., Aumaître, S., and Gallet, B. (2022). Velocity-informed upper bounds on the convective heat transport induced by internal heat sources and sinks. *Phil. Trans. R. Soc. A*, 380(2225):20210034.

Brachet, M. E., Meiron, D. I., Orszag, S. A., Nickel, B. G., Morf, R. H., and Frisch, U. (1983). Small-scale structure of the taylor–green vortex. *J. Fluid Mech.*, 130:411–452.

Calzavarini, E., Doering, C. R., Gibbon, J. D., Lohse, D., Tanabe, A., and Toschi, F. (2006). Exponentially growing solutions in homogeneous Rayleigh-Bénard convection. *Phys. Rev. E*, 73(3):035301.

Carlsson, M., De Pontieu, B., and Hansteen, V. H. (2019). New view of the Solar Chromosphere. *Annu. Rev. Astron. Astrophys.*, 57(1):189–226.

Carroll, B. W. (2006). *An Introduction to Modern Astrophysics*. Pearson, 2nd edition.

Castaing, B., Gunaratne, G., Kadanoff, L. P., Libchaber, A., and Heslot, F. (1989). Scaling of hard thermal turbulence in Rayleigh-Bénard convection. *J. Fluid Mech.*, 204:1–30.

Cattaneo, F., Brummell, N. H., Toomre, J., Malagoli, A., and Hurlburt, N. E. (1991). Turbulent compressible convection. *Astrophys. J.*, 370:282–294.

Chandrasekhar, S. (1961). *Hydrodynamic and Hydromagnetic Stability*. Oxford University Press, Clarendon.

Chapelier, J.-B., Lusher, D. J., Van Noordt, W., Wenzel, C., Gibis, T., Mossier, P., Beck, A., Lodato, G., Brehm, C., Ruggeri, M., et al. (2024). Comparison of high-order numerical methodologies for the simulation of the supersonic taylor–green vortex flow. *Phys. Fluids*, 36(5).

Chatterjee, A. G., Verma, M. K., Kumar, A., Samtaney, R., Hadri, B., and Khurram, R. (2018). Scaling of a Fast Fourier Transform and a pseudo-spectral fluid solver up to 196608 cores. *J. Parallel Distrib. Comput.*, 113:77–91.

Chavanne, X., Chillà, F., Chabaud, B., Castaing, B., and Hebral, B. (2001). Turbulent Rayleigh-Bénard convection in gaseous and liquid He. *Phys. Fluids*, 13(5):1300–1320.

Chillà, F. and Schumacher, J. (2012). New perspectives in turbulent Rayleigh-Bénard convection. *Eur. Phys. J. E*, 35(7):58.

Chorin, A. J. and Marsden, J. E. (1993). *A Mathematical Introduction to Fluid Mechanics*. Springer-Verlag, New York.

Christensen-Dalsgaard, J., Dappen, W., Ajukov, S. V., et al. (1996). The Current State of Solar Modeling. *Science*, 272(5266):1286–1292.

Colella, P. and Woodward, P. R. (1984). The piecewise parabolic method (ppm) for gas-dynamical simulations. *J. Comput. Phys.*, 54(1):174–201.

Costa, P. (2018). A FFT-based finite-difference solver for massively-parallel direct numerical simulations of turbulent flows. *Computers & Mathematics with Applications*, 76(8):1853–1862.

Dalcín, L., Paz, R., Storti, M., and D'Elía, J. (2008). MPI for Python: Performance improvements and MPI-2 extensions. *J. Parallel Distrib. Comput.*, 68(5):655–662.

Datta, K., Murphy, M., Volkov, V., Williams, S., Carter, J., Oliker, L., Patterson, D., Shalf, J., and Yelick, K. (2008). Stencil computation optimization and auto-tuning on state-of-the-art multicore architectures. In *Proceedings of the 2008 ACM/IEEE conference on Supercomputing*, pages 1–12. IEEE Press.

Doering, C. R. (2020a). Absence of evidence for the ultimate regime in two-dimensional Rayleigh-Bénard convection. *Phys. Rev. Lett.*, 124:094502. Comment on Zhu et al. (2018).

Doering, C. R. (2020b). Turning up the heat in turbulent thermal convection. *Proc. Natl. Acad. Sci.*, 117(18):9671–9673.

Doering, C. R., Otto, F., and Reznikoff, M. G. (2006). Bounds on vertical heat transport for infinite-Prandtl-number Rayleigh–Bénard convection. *J. Fluid Mech.*, 560:229–241.

Dongarra, J., Beckman, P., Moore, T., Ahern, P., et al. (2011). The international exascale software project roadmap. *The International Journal of High Performance Computing Applications*, 25(1):3–60.

Dongarra, J. and Keyes, D. (2024). The co-evolution of computational physics and high-performance computing. *Nature Reviews Physics*, 6:621–627.

Elmegreen, B. G. and Scalo, J. (2004). Interstellar turbulence I: Observations and processes. *Annu. Rev. Astron. Astrophys.*, 42(1):211–273.

Federrath, C. (2013). On the universality of supersonic turbulence. *Mon. Not. R. Astron. Soc.*, 436(2):1245–1257.

Federrath, C., Roman-Duval, J., Klessen, R. S., Schmidt, W., and Mac Low, M.-M. (2010). Comparing the statistics of interstellar turbulence in simulations and observations-Solenoidal versus compressive turbulence forcing. *Astron. Astrophys.*, 512:A81.

Frisch, U. (1995). *Turbulence: The Legacy of A. N. Kolmogorov.* Cambridge University Press, Cambridge.

Fritts, D. C. and Alexander, M. J. (2003). Gravity wave dynamics and effects in the middle atmosphere. *Rev. Geophys.*, 41(1).

Fu, L., Hu, X. Y., and Adams, N. A. (2016). A family of high-order targeted eno schemes for compressible-fluid simulations. *J. Comput. Phys.*, 305:333–359.

Fujisawa, A. (2021). Review of plasma turbulence experiments. *Proc. Jpn. Acad., Ser. B*, 97(3):103–119.

Glatzmaiers, G. A. and Roberts, P. H. (1995). A three-dimensional self-consistent computer simulation of a geomagnetic field reversal. *Nature*, 377(6546):203–209.

Gottlieb, S., Shu, C.-W., and Tadmor, E. (2001). Strong stability-preserving high-order time discretization methods. *SIAM Rev.*, 43(1):89–112.

Gough, D. O. (1969). The anelastic approximation for thermal convection. *J. Atmos. Sci.*, 26:448–456.

Graham, E. (1975). Numerical simulation of two-dimensional compressible convection. *J. Fluid Mech.*, 70(4):689–703.

Grete, P., O'Shea, B. W., Beckwith, K., Schmidt, W., and Christlieb, A. (2017). Energy transfer in compressible magnetohydrodynamic turbulence. *Phys. Plasmas*, 24(9):092311.

Grossmann, S. and Lohse, D. (2000). Scaling in thermal convection: a unifying theory. *J. Fluid Mech.*, 407:27–56.

Grossmann, S. and Lohse, D. (2001). Thermal convection for large Prandtl numbers. *Phys. Rev. Lett.*, 86(1):3316–3319.

Grötzbach, G. (1983). Spatial resolution requirements for direct numerical simulation of the Rayleigh-Bénard convection. *J. Comput. Phys.*, 49(2):241–264.

Hager, G. and Wellein, G. (2010). *Introduction to High Performance Computing for Scientists and Engineers*. CRC Press, Boca Raton.

Hamman, C. W. and Moin, P. (2023). Numerical experiments in thermal convection with and without mean shear. Technical Report TF-170, Department of Mechanical Engineering, Stanford University.

Hansen, C. J., Kawaler, S. D., and Trimble, V. (2012). *Stellar Interiors: Physical Principles, Structure, and Evolution*. Springer-Verlag, New York.

Harris, C. R., Millman, K. J., Van Der Walt, S. J., et al. (2020). Array programming with NumPy. *Nature*, 585(7825):357–362.

Harten, A. (1983). High resolution schemes for hyperbolic conservation laws. *J. Comput. Phys.*, 49(3):357–393.

Harten, A., Engquist, B., Osher, S., and Chakravarthy, S. R. (1987). Uniformly high order accurate essentially non-oscillatory schemes, iii. *Journal of Computational Physics*, 71(2):231–303.

He, X., Funfschilling, D., Nobach, H., Bodenschatz, E., and Ahlers, G. (2012). Transition to the Ultimate State of Turbulent Rayleigh-Bénard Convection. *Phys. Rev. Lett.*, 108(2):024502.

Hennebelle, P. and Falgarone, E. (2012). Turbulent molecular clouds. *Astron. Astrophys. Rev.*, 20:1–58.

Hirsch, C. (2007). *Numerical Computation of Internal and External Flows: The Fundamentals of Computational Fluid Dynamics*, volume 1. Butterworth-Heinemann, Oxford.

Homann, H., Dreher, J., and Grauer, R. (2007). Impact of the floating-point precision and interpolation scheme on the results of DNS of turbulence by pseudo-spectral codes. *Computer Physics Communications*, 177(7):560–565.

Houze, Jr., R. A. (1993). *Cloud Dynamics*. Academic Press, San Diego.

Howard, L. N. (1963). Heat transport by turbulent convection. *J. Fluid Mech.*, 17:405–432.

Howard, L. N. (1966). Convection at high Rayleigh number. In *Applied Mechanics: Proc. of the Eleventh Int. Cong. of Applied Mechanics Munich (Germany) 1964*, pages 1109–1115. Springer.

Hurlburt, N. E., Toomre, J., and Massaguer, J. M. (1984). Two-dimensional compressible convection extending over multiple scale heights. *Astrophys. J.*, 282:557–573.

Hurlburt, N. E., Toomre, J., and Massaguer, J. M. (1986). Nonlinear compressible convection penetrating into stable layers and producing internal gravity waves. *Astrophys. J.*, 311:563–577.

Incropera, F. P., DeWitt, D. P., Bergman, T. L., and Lavine, A. S. (2007). *Fundamentals of Heat and Mass Transfer*. John Wiley & Sons, 6th edition.

Ingenito, A. and Bruno, C. (2010). Physics and regimes of supersonic combustion. *AIAA J.*, 48(3):515–525.

Ingersoll, A. P. (1990). Atmospheric Dynamics of the Outer Planets. *Science*, 248(4953):308–315.

Iyer, K. P., Scheel, J. D., Schumacher, J., and Sreenivasan, K. R. (2020). Classical 1/3 scaling of convection holds up to $\mathrm{Ra} = 10^{15}$. *Proc. Natl. Acad. Sci.*, 117(14):7594–7598.

Jagannathan, S. and Donzis, D. A. (2016). Reynolds and Mach number scaling in solenoidally-forced compressible turbulence using high-resolution direct numerical simulations. *J. Fluid Mech.*, 789:669–707.

Jarvis, G. T. and Mckenzie, D. P. (1980). Convection in a compressible fluid with infinite Prandtl number. *J. Fluid Mech.*, 96(3):515–583.

Jiang, G.-S. and Shu, C.-W. (1996). Efficient implementation of weighted eno schemes. *J. Comput. Phys.*, 126(1):202–228.

John, J. P. and Donzis, D. A. (2024). Strong evidence for universality in homogeneous compressible turbulence. *Phys. Fluids*, 36(10):106121.

John, J. P. and Schumacher, J. (2023a). Compressible turbulent in highly stratified adiabatic background. *J. Fluid Mech.*, 972:R4.

John, J. P. and Schumacher, J. (2023b). Strongly superadiabatic and stratified limits of compressible. *Phys. Rev. Fluids*, 8(10):103505.

John, J. P. and Schumacher, J. (2024). Compressible turbulent convection: The role of temperature-dependent thermal conductivity and dynamic viscosity. *Phys. Fluids*, 36(7).

Jones, C. A. and Kuzanyan, K. M. (2009). Compressible convection in the deep atmospheres of giant planets. *Icarus*, 204(1):227–238.

Kader, B. A. (1981). Temperature and concentration profiles in fully turbulent boundary layers. *Int. J. Heat Mass Transf.*, 24(9):1541–1544.

Käpylä, P. J. (2021). Prandtl number dependence of stellar convection: Flow statistics and convective energy transport. *Astron. Astrophys.*, 655:A78.

Keyes, D. E., McInnes, L. C., Woodward, C., Gropp, W., et al. (2013). Multiphysics simulations: Challenges and opportunities. *The International Journal of High Performance Computing Applications*, 27(1):4–83.

Kida, S. and Orszag, S. A. (1990). Energy and spectral dynamics in forced compressible turbulence. *J. Sci. Comput.*, 5:85–125.

Klöckner, A., Pinto, N., Lee, Y., Catanzaro, B., Ivanov, P., and Fasih, A. (2012). PyCUDA and PyOpenCL: A scripting-based approach to GPU run-time code generation. *Parallel Computing*, 38(3):157–174.

Kolmogorov, A. N. (1941a). Dissipation of Energy in Locally Isotropic Turbulence. *Dokl. Akad. Nauk SSSR*, 32:16–18.

Kolmogorov, A. N. (1941b). The local structure of turbulence in incompressible viscous fluid for very large Reynolds numbers. *Dokl. Akad. Nauk SSSR*, 30:301–305.

Kraichnan, R. H. (1959). The structure of isotropic turbulence at very high Reynolds numbers. *J. Fluid Mech.*, 5:497–543.

Kraichnan, R. H. (1962). Turbulent thermal convection at arbitrary Prandtl number. *Phys. Fluids*, 5(11):1374–1389.

Kraichnan, R. H. (1967). Inertial ranges in two-dimensional turbulence. *Phys. Fluids*, 10:1417–1423.

Kraichnan, R. H. (1971). Inertial-range transfer in two-and three-dimensional turbulence. *J. Fluid Mech.*, 47:525–535.

Kritsuk, A. G., Norman, M. L., Padoan, P., and Wagner, R. (2007). The statistics of supersonic isothermal turbulence. *Astrophys. J.*, 665(1):416.

Krumholz, M. R. and McKee, C. F. (2005). A general theory of turbulence-regulated star formation, from spirals to ultraluminous infrared galaxies. *Astrophys. J.*, 630(1):250.

Kurganov, A. and Levy, D. (2000). A third-order semidiscrete central scheme for conservation laws and convection-diffusion equations. *SIAM J. Sci. Comput.*, 22(4):1461–1488.

Kurganov, A. and Tadmor, E. (2000). New high-resolution central schemes for nonlinear conservation laws and convection–diffusion equations. *J. Comput. Phys.*, 160(1):241–282.

Lax, P. D. and Wendroff, B. (1960). Systems of conservation laws. *Commun. Pure Appl. Math.*, 13(2):217–237.

Lee, S., Lele, S. K., and Moin, P. (1993). Direct numerical simulation of isotropic turbulence interacting with a weak shock wave. *J. Fluid Mech.*, 251:533–562.

Leith, C. (1971). Atmospheric predictability and two-dimensional turbulence. *J. Atmos. Sci.*, 28(2):145–161.

Lele, S. K. (1994). Compressibility effects on turbulence. *Annu. Rev. Fluid Mech.*, 26:211–254.

Lepot, S., Aumaître, S., and Gallet, B. (2014). Radiative heating achieves the ultimate regime of thermal convection. *Proc. Natl. Acad. Sci. U.S.A.*, 111(30):10665–10670.

Lepot, S., Aumaître, S., and Gallet, B. (2018). Radiative heating achieves the ultimate regime of thermal convection. *Proc. Natl. Acad. Sci.*, 115(36):8937–8941.

Lesieur, M. (2008). *Turbulence in Fluids*. Springer-Verlag, Dordrecht.

Leslie, D. C. (1973). *Developments in the theory of turbulence*. Clarendon Press, Oxford.

LeVeque, R. J. (2002). *Finite Volume Methods for Hyperbolic Problems*. Cambridge University Press, Cambridge.

Levy, D., Puppo, G., and Russo, G. (2000). Compact central weno schemes for multidimensional conservation laws. *SIAM J. Sci. Comput.*, 22(2):656–672.

Li, X.-M., He, J.-D., Tian, Y., Hao, P., and Huang, S.-D. (2021). Effects of Prandtl number in quasi-two-dimensional Rayleigh–Bénard convection. *J. Fluid Mech.*, 915:A60.

Liang, D., Lin, B., and Falconer, R. A. (2007). Simulation of rapidly varying flow using an efficient TVD-MacCormack scheme. *Int. J. Numer. Methods Fluids*, 53(5):811–826.

Libchaber, A., Laroche, C., and Fauve, S. (1982). Period doubling cascade in mercury, a quantitative measurement. *Phys. Rev. Lett.*, 48(11):712–715.

Lindborg, E. (2023). Another comment on claims of a transition to the ultimate regime of heat transfer. *arXiv preprint arXiv:2303.00030*.

Lindborg, E. (2025). Scaling in two-dimensional Rayleigh-Bénard convection. *arXiv preprint arXiv:2506.13213*.

Liu, X. and Zhong, S. (2013). Analyses of marginal stability, heat transfer and boundary layer properties for thermal convection in a compressible fluid with infinite Prandtl number. *Geophys. J. Int.*, 194(1):125–144.

Lohse, D. and Shishkina, O. (2024). Ultimate Rayleigh-Bénard turbulence. *Rev. Mod. Phys.*, 96(3):035001.

Lohse, D. and Toschi, F. (2003). Ultimate state of thermal convection. *Phys. Rev. Lett.*, 90(3):034502.

Lohse, D. and Xia, K.-Q. (2010). Small-scale properties of turbulent Rayleigh–Bénard convection. *Annu. Rev. Fluid Mech.*, 42(1):335–364.

Lorenz, E. N. (1963). Deterministic nonperiodic flow. *J. Atmos. Sci.*, 20(2):130–141.

Lusher, D. J. and Sandham, N. D. (2021). Assessment of low-dissipative shock-capturing schemes for the compressible taylor–green vortex. *AIAA J.*, 59(2):533–545.

Mac Low, M.-M. and Klessen, R. S. (2004). Control of star formation by supersonic turbulence. *Rev. Mod. Phys.*, 76(1):125.

MacCormack, R. W. (1969). The effect of viscosity in hypervelocity impact cratering. In *AIAA Hypervelocity Impact Conference*, pages 69–354, Cincinnati, Ohio. American Institute of Aeronautics and Astronautics. AIAA Paper 69-354.

Malkus, W. V. R. (1954). The Heat Transport and Spectrum of Thermal Turbulence. *Proc. R. Soc. Lond. A*, 225(1):196–212.

Manga, M. and Weeraratne, D. (1999). Experimental study of non-Boussinesq Rayleigh–Bénard convection at high Rayleigh and Prandtl numbers. *Phys. Fluids*, 11(10):2969–2976.

Miesch, M. S. (2005). Large-Scale Dynamics of the Convection Zone and Tachocline. *Living Rev. Sol. Phys.*, 2(1):1.

Miesch, M. S., Elliott, J. F., Toomre, J., Clune, T. L., Glatzmaier, G. A., and Gilman, P. A. (2000). Three-dimensional spherical simulations of solar convection. i. differential rotation and pattern of convection. *Astrophys. J.*, 532(1):593–615.

Moffat, A. F. and Robert, C. (1994). Clumping and mass loss in hot star winds. *Astrophys. J.*, 421:310–313.

Moin, P. and Chan, W. R. (2024). *Fundamentals of Turbulent Flows*. Cambridge University Press.

Moin, P. and Mahesh, K. (1998). Direct numerical simulation: data to knowledge creation. *Annu. Rev. Fluid Mech.*, 30(1):539–578.

Narasimha, R. and Sreenivasan, K. R. (1979). Relaminarization of fluid flows. *Adv. Appl. Mech.*, 19:221–309.

Niemela, J. J., Skrbek, L., Sreenivasan, K. R., and Donnelly, R. J. (2000). Turbulent convection at very high Rayleigh numbers. *Nature*, 404:837–840.

Niemela, J. J. and Sreenivasan, K. R. (2006). The use of cryogenic helium for classical turbulence: promises and hurdles. *J. Low Temp. Phys.*, 143(5-6):163–212.

Nonomura, T., Iizuka, N., and Fujii, K. (2010). Freestream and vortex preservation properties of high-order weno and wcns on curvilinear grids. *Comput. Fluids*, 39(2):197–214.

Okuta, R., Unno, Y., Nishino, D., Hido, S., and Loomis, C. (2017). CuPy: A NumPy-Compatible Library for NVIDIA GPU Calculations. In *Proc. Workshop on Machine Learning Systems (LearningSys) in The Thirty-first Annual Conference, NeurIPS.*

Ouyang, C., He, S., Xu, Q., Luo, Y., and Zhang, W. (2013). A MacCormack-TVD finite difference method to simulate the mass flow in mountainous terrain with variable computational domain. *Comput. Geosci.*, 52:1–10.

Padoan, P. and Nordlund, Å. (2011). The star formation rate of supersonic magnetohydrodynamic turbulence. *Astrophys. J.*, 730(1):40.

Pal, P., Wahi, P., Paul, S., Verma, M. K., Kumar, K., and Mishra, P. K. (2009). Bifurcation and chaos in zero-Prandtl-number convection. *EPL*, 87(5):54003.

Pandey, A., Schumacher, J., and Sreenivasan, K. R. (2021a). Non-Boussinesq convection at low Prandtl numbers relevant to the Sun. *Phys. Rev. Fluids*, 6(10):100503.

Pandey, A., Schumacher, J., and Sreenivasan, K. R. (2021b). Non-Boussinesq low-Prandtl-number convection with a temperature-dependent thermal diffusivity. *Astrophys. J.*, 907(1):56.

Pandey, A. and Sreenivasan, K. R. (2025). Transient and steady convection in two dimensions. *J. Fluid Mech.*, 1015:A42.

Pandey, A. and Verma, M. K. (2016). Scaling of large-scale quantities in Rayleigh-Bénard convection. *Phys. Fluids*, 28(9):095105.

Parker, E. N. (1955). Hydromagnetic Dynamo Models. *Astrophys. J.*, 122:293.

Pathak, M., Sharma, L., Tiwari, H., and Verma, M. K. (2025). Variation of convective heat flux imbalance with Prandtl number. *CTR Annu. Res. Briefs*, pages 263–274.

Pirozzoli, S. (2011). Numerical methods for high-speed flows. *Annu. Rev. Fluid Mech.*, 43:163–194.

Pirozzoli, S., Bernardini, M., Verzicco, R., and Orlandi, P. (2017). Mixed convection in turbulent channels with unstable stratification. *J. Fluid Mech.*, 821:482–516.

Pope, S. B. (2000). *Turbulent Flows*. Cambridge University Press, Cambridge.

Porter, D. H. and Woodward, P. R. (2000). Three-dimensional simulations of turbulent compressible convection. *Astrophys. J. Suppl. Ser.*, 127(1):159.

Porter, D. H., Woodward, P. R., and Pouquet, A. (1998). Inertial range structures in decaying compressible turbulent flows. *Phys. Fluids*, 10(1):237–245.

Priestley, C. (1954). Convection from a large horizontal surface. *Aust. J. Phys.*, 7(1):176–201.

Radice, D., Abdikamalov, E., Ott, C. D., Mösta, P., Couch, S. M., and Roberts, L. F. (2018). Turbulence in core-collapse supernovae. *J. Phys. G: Nucl. Part. Phys.*, 45(5):053003.

Ricard, Y., Alboussière, T., Labrosse, S., Curbelo, J., and Dubuffet, F. (2022). Fully compressible convection for planetary mantles. *Geophys. J. Int.*, 230(2):932–956.

Roche, P.-E., Castaing, B., Chabaud, B., and Hebral, B. (2001). Observation of the 1/2 power law in Rayleigh-Bénard convection. *Phys. Rev. E*, 63(4):045303(R).

Saffman, P. G. (1968). In Zabusky, N. J., editor, *Topics in Nonlinear Physics*, pages 485–614. Springer-Verlag, Berlin.

Sakurai, Y. and Ishihara, T. (2024). Direct numerical simulations of compressible turbulence in a periodic box: Effect of isothermal assumptions on turbulence statistics. *Phys. Fluids*, 36(8):085152.

Salvesen, G., Beckwith, K., Simon, J. B., O'Neill, S. M., and Begelman, M. C. (2014). Quantifying energetics and dissipation in magnetohydrodynamic turbulence. *Mon. Not. R. Astron. Soc.*, 438(2):1355–1376.

Samuel, R. (2023). *Simulations of Rayleigh-Bénard Convection at Extreme Rayleigh Numbers*. PhD thesis.

Samuel, R., Bhattacharya, S., Asad, A., Chatterjee, S., Verma, M. K., Samtaney, R., and Anwer, S. F. (2021). SARAS: A general-purpose PDE solver for fluid dynamics. *J. Open Source Softw.*, 6(64):2095.

Samuel, R., Samtaney, R., and Verma, M. K. (2022). Large-eddy simulation of Rayleigh–Bénard convection at extreme Rayleigh numbers. *Phys. Fluids*, 34(7).

Samuel, R. and Verma, M. K. (2024). Bolgiano-Obukhov scaling in two-dimensional Rayleigh-Bénard convection at extreme Rayleigh numbers. *Phys. Rev. Fluids*, 9(2):023502.

Samuel, R. J., Bode, M., Scheel, J. D., Sreenivasan, K. R., and Schumacher, J. (2024). No sustained mean velocity in the boundary region of plane thermal convection. *J. Fluid Mech.*, 996:A49.

San, O. and Kara, K. (2015). Evaluation of riemann flux solvers for weno reconstruction schemes: Kelvin–helmholtz instability. *Comput. Fluids*, 117:24–41.

Sarkar, S. (1992). The pressure–dilatation correlation in compressible flows. *Physics of Fluids A: Fluid Dynamics*, 4(12):2674–2682.

Scheel, J. D. and Schumacher, J. (2016). Global and local statistics in turbulent convection at low Prandtl numbers. *J. Fluid Mech.*, 802:147–173.

Schlichting, H. and Gersten, K. (2016). *Boundary-layer theory*. Springer.

Schmalzl, J., Breuer, M., and Hansen, U. (2004). On the validity of two-dimensional numerical approaches to time-dependent thermal convection. *Europhys. Lett.*, 67(3):390–396.

Schmidt, W., Federrath, C., Hupp, M., Kern, S., and Niemeyer, J. C. (2009). Numerical simulations of compressively driven interstellar turbulence-i. isothermal gas. *Astron. Astrophys.*, 494(1):127–145.

Schmidt, W. and Grete, P. (2019). Kinetic and internal energy transfer in implicit large-eddy simulations of forced compressible turbulence. *Phys. Rev. E*, 100(4):043116.

Schumacher, J. and Sreenivasan, K. R. (2020). Colloquium: Unusual dynamics of convection in the Sun. *Rev. Mod. Phys.*, 92(4):041001.

Sharma, L., Pathak, M., Tiwari, H., and Verma, M. K. (2025). Prandtl number dependence in turbulent compressible convection. *Phys. Rev. Fluids*, 10(11):114611.

Shevkar, P. P., Samuel, R. J., Zinchenko, G., Bode, M., Schumacher, J., and Sreenivasan, K. R. (2025). Hierarchical network of thermal plumes and their dynamics in turbulent rayleigh–bénard convection. *Proc. Natl. Acad. Sci.*, 122(32):e2502972122.

Shishkina, O., Emran, M. S., Grossmann, S., and Lohse, D. (2017). Scaling relations in large-Prandtl-number natural thermal convection. *Phys. Rev. Fluids*, 2(10):103502.

Shishkina, O. and Lohse, D. (2024). Ultimate Regime of Rayleigh-Bénard Turbulence: Subregimes and Their Scaling Relations for the Nusselt vs Rayleigh and Prandtl Numbers. *Phys. Rev. Lett.*, 133(14):144001.

Shishkina, O. and Wagner, C. (2008). Analysis of sheet-like thermal plumes in turbulent Rayleigh–Bénard convection. *J. Fluid Mech.*, 599:383–404.

Shraiman, B. I. and Siggia, E. D. (1990). Heat transport in high-Rayleigh-number convection. *Phys. Rev. A*, 42(6):3650–3653.

Siggia, E. D. (1994). High Rayleigh number convection. *Annu. Rev. Fluid Mech.*, 26(1):137–168.

Singh, D., Tiwari, H., Sharma, L., and Verma, M. K. (2025). Mathematical formulation of mode-to-mode energy transfers and energy fluxes in compressible turbulence. *Phys. Rev. Fluids*, 10(11):114609.

Singh, H. P. and Chan, K. L. (1993). A study of the three-dimensional turbulent compressible convection in a deep atmosphere at various Prandtl numbers. *Astron. Astrophys.*, 279:107–118.

Song, H., Ghate, A. S., Matsuno, K. V., West, J. R., Subramaniam, A., and Lele, S. K. (2024). A robust compact finite difference framework for simulations of compressible turbulent flows. *J. Comput. Phys.*, 519:113419.

Spiegel, E. A. (1962). On the Malkus theory of turbulence. *Mécanique de la Turbulence*, pages 181–201.

Spiegel, E. A. (1963). A Generalization of the Mixing-Length Theory of Turbulent Convection. *Astrophys. J.*, 138:216.

Spiegel, E. A. (1965). Convective instability in a compressible atmosphere. I. *Astrophys. J.*, 141:1068–1090.

Spiegel, E. A. (1971). Convection in stars: I. Basic Boussinesq convection. *Annu. Rev. Astron. Astrophys.*, 9:323–352.

Spiegel, E. A. and Veronis, G. (1960). On the Boussinesq approximation for a compressible fluid. *Astrophys. J.*, 131:442.

Spruit, H. C., Nordlund, A., and Title, A. M. (1990). Solar convection. *Annu. Rev. Astron. Astrophys.*, 28(1):263–303.

Sreenivasan, K. R. and Niemela, J. J. (2023). Turbulent convection at very high Rayleigh numbers and the weakly nonlinear theory. *Atmosphere*, 14(5):826.

Stevens, R. J. A. M., Lohse, D., and Verzicco, R. (2011). Prandtl and Rayleigh number dependence of heat transport in high Rayleigh number thermal convection. *J. Fluid Mech.*, 688:31–43.

Stevens, R. J. A. M., van der Poel, E. P., Grossmann, S., and Lohse, D. (2013). The unifying theory of scaling in thermal convection: the updated prefactors. *J. Fluid Mech.*, 730:295–308.

Strang, G. (1968). On the construction and comparison of difference schemes. *SIAM J. Numer. Anal.*, 5(3):506–517.

Tannehill, J. C., Anderson, D. A., and Pletcher, R. H. (1997). *Computational Fluid Mechanics and Heat Transfer.* Taylor & Francis, Washington, DC.

Tilgner, A. (1996). High-Rayleigh-number convection in spherical shells. *Phys. Rev. E*, 53(5):4847.

Tiwari, H., Sharma, L., and Verma, M. K. (2025a). Compressible turbulent convection at very high Rayleigh numbers. *Int. J. Heat Mass Transf.*, 242:126821.

Tiwari, H., Sharma, L., and Verma, M. K. (2025b). On the absence of the ultimate regime in turbulent thermal convection. *Proc. Natl. Acad. Sci.*, 122(44):e2513474122.

Tiwari, H., Sharma, L., and Verma, M. K. (2025c). Repository for on the absence of the ultimate regime in turbulent thermal convection [data set], doi:https://doi.org/10.5281/zenodo.16914627.

Toomre, J., Brummell, N., Cattaneo, F., and Hurlburt, N. E. (1990). Three-dimensional compressible convection at low Prandtl numbers. *Comput. Phys. Commun.*, 59(1):105–117.

Toro, E. F. (2009). *Riemann Solvers and Numerical Methods for Fluid Dynamics: A Practical Introduction*. Springer-Verlag Berlin Heidelberg, Berlin, Heidelberg, 3rd edition.

Urban, P., Hanzelka, P., Kralik, T., Musilová, V., Srnka, A., and Skrbek, L. (2012). Effect of Boundary Layers Asymmetry on Heat Transfer Efficiency in Turbulent Rayleigh-Bénard Convection at Very High Rayleigh Numbers. *Phys. Rev. Lett.*, 109(15):154301.

Van Der Poel, E. P., Ostilla-Mónico, R., Verzicco, R., and Lohse, D. (2014). Effect of velocity boundary conditions on the heat transfer and flow topology in two-dimensional Rayleigh-Bénard convection. *Phys. Rev. E*, 90(1):013017.

van der Poel, E. P., Stevens, R. J. A. M., and Lohse, D. (2013). Comparison between two- and three-dimensional Rayleigh–Bénard convection. *J. Fluid Mech.*, 736:177–194.

Verhoeven, J., Wiesehöfer, T., and Stellmach, S. (2015). Anelastic versus fully compressible turbulent Rayleigh–Bénard convection. *Astrophys. J.*, 805(1):62.

Verma, M. K. (2018). *Physics of Buoyant Flows: From Instabilities to Turbulence*. World Scientific, Singapore.

Verma, M. K., Kumar, A., and Pandey, A. (2017). Phenomenology of buoyancy-driven turbulence: recent results. *New J. Phys.*, 19:025012.

Verma, M. K., Mishra, P. K., Pandey, A., and Paul, S. (2012). Scalings of field correlations and heat transport in turbulent convection. *Phys. Rev. E*, 85(1):016310.

Von Karman, T. (1934). Turbulence and skin friction. *J. Aero. Sci.*, 1(1):1–20.

von Kármán, T. (2003). Compressibility effects in aerodynamics. *J. Spacecr. Rockets*, 40(6):992–1011.

Wan, Z.-H., Wang, Q., Wang, B., Xia, S., Zhou, Q., and Sun, D.-J. (2020). On non-Oberbeck–Boussinesq effects in Rayleigh–Bénard convection of air for large temperature differences. *J. Fluid Mech.*, 889:A10.

Wang, J., Yang, Y., Shi, Y., Xiao, Z., He, X. T., and Chen, S. (2013). Cascade of Kinetic Energy in Three-Dimensional Compressible Turbulence. *Phys. Rev. Lett.*, 110(21):214505.

Wesseling (2000). *Principles of Computational Fluid Dynamics.* Springer-Verlag, Berlin Heidelberg, first edition.

Winchester, P., Dallas, V., and Howell, P. D. (2024). Two-dimensional rayleigh–bénard convection without boundaries. *J. Fluid Mech.*, 998:A27.

Woodward, P. and Colella, P. (1984). The numerical simulation of two-dimensional fluid flow with strong shocks. *J. Comput. Phys.*, 54(1):115–173.

Wu, X.-Z. and Libchaber, A. (1991). Non-boussinesq effects in free thermal convection. *Phys. Rev. A*, 43:2833–2839.

Wulf, W. A. and McKee, S. A. (1995). Hitting the memory wall: implications of the obvious. *ACM SIGARCH Computer Architecture News*, 23(1):20–24.

Yaglom, A. M. (1979). Similarity laws for constant-pressure and pressure-gradient turbulent wall flows. *Annu. Rev. Fluid Mech.*, 11:505–540.

Yaglom, A. M. and Kader, B. A. (1974). Heat and mass transfer between a rough wall and turbulent fluid flow at high Reynolds and Peclet numbers. *J. Fluid Mech.*, 62(3):601–623.

Yee, H. C. (1987). *Upwind and symmetric shock-capturing schemes.* National Aeronautics and Space Administration, Ames Research Center.

Zank, G. P. and Matthaeus, W. H. (1991). The equations of nearly incompressible fluids. I - hydrodynamics, turbulence, and waves. *Phys. Fluids A*, 3(1):69–82.

Zhang, Y. and Zhou, Q. (2024). Low-Prandtl-number effects on global and local statistics in two-dimensional Rayleigh–Bénard. *Phys. Fluids*, 36(1).

Zhou, Y. (1993). Interacting scales and energy transfer in isotropic turbulence. *Phys. Fluids A*, 5(10):2511–2524.

Zhou, Y. (2021). Turbulence theories and statistical closure approaches. *Phys. Rep.*, 935:1–117.

Zhou, Y. (2024). *Hydrodynamic Instabilities and Turbulence: Rayleigh–Taylor, Richtmyer–Meshkov, and Kelvin–Helmholtz Mixing*. Cambridge University Press, Cambridge.

Zhu, X., Mathai, V., Stevens, R. J. A. M., Verzicco, R., and Lohse, D. (2018). Transition to the Ultimate Regime in Two-Dimensional Rayleigh-Bénard Convection. *Phys. Rev. Lett.*, 120(14):144502.

Zhu, X., Stevens, R. J. A. M., Verzicco, R., and Lohse, D. (2017). Roughness-facilitated local 1/2 scaling does not imply the onset of the ultimate regime of thermal convection. *Phys. Rev. Lett.*, 119:154501.